# Development and Characterisation of Nanotemplated Carbon Monoliths in Analytical Chemistry

By

**Xiaoyun He**

Student number: 59114983

Under the Supervision of

Dr. Ekaterina P. Nesterenko (ISSC, DCU)

Dr. Dermot Brabazon (ISSC, DCU),

Prof. Pavel N. Nesterenko (Across, University of Tasmania) and

Prof. Brett Paull (Across, University of Tasmania)

A thesis submitted to Dublin City University for consideration for

The degree of:

**Doctor of Philosophy**

Dublin City University

School of Chemical Sciences

February 2014

# Declaration

 I hereby certify that this material, which I now submit for assessment on the programme of study leading to the award of Ph.D. is entirely my own work, that I have exercised reasonable care to ensure that the work is original, and does not to the best of my knowledge breach any law of copyright, and has not been taken from the work of others save and to the extent that such work has been cited and acknowledged within the text of my work.

Signed: _____

ID No.: 59114983

Date: _____

# Table of Contents

**Chapter 4 Porous Carbon Monoliths as Multifunctional Adsorbents for Organic Pollutants** .......................................................................................................**115**

# List of Abbreviations

| | |
|---|---|
| 0D | zero-dimensional |
| 1D | one-dimensional |
| 2D | two-dimensional |
| 3D | three-dimensional |
| 3DOM | 3D ordered macroporous |
| 3DOM/m | 3DOM with controllable mesoporosity |
| AC | activated carbon |
| ACN | acetonitrile |
| AIBN | azobisisobutyronitrile |
| APS | 3-aminopropyl silica |
| APTES | 3-aminopropyltriethoxysilane |
| ATR-FTIR | attenuated total reflectance Fourier transform infrared spectra |
| BDD | boron doped diamond |
| BET | Brunauer-Emmett-Teller |
| BJH | Barrett–Joyner–Halenda |
| BPA | bisphenol A |
| $C_{60}$ | fullerene $C_{60}$ |
| CAs | carbon aerogels |
| CM blank | carbon monolith blank |
| CMs | carbon monoliths |
| CNTs | carbon nanotubes |
| CV | cyclic voltammetry |
| CW | continuous wave mode |
| DESs | deep eutectic solvents |
| DMF | *N-N*, dimethylformamide |
| EDX | energy-dispersive X-ray |
| $FeCl_3$ | ferric chloride |
| FE-SEM | field emission scanning electron microscope |
| FMS | fullerene $C_{60}$ modified silica gels |

| | |
|---|---|
| FT-IR | Fourier transform infrared |
| GCE | glassy carbon electrode |
| GO | graphene oxide |
| $H_2O_2$ | hydrogen peroxide |
| HETP | the height equivalent to a theoretical plate |
| HF | hydrofluoric acid |
| HPLC | High performance liquid chromatography |
| HTC | Hydrothermal carbonisation |
| I.D. | Inner diameter |
| ILs | ionic liquids |
| IPA | 2-propanol |
| IUPAC | the International Union of Pure and Applied Chemistry |
| $K_3Fe(CN)_6$ | potassium hexacyanoferrate (III) |
| $K_4Fe(CN)_6 \cdot 3H_2O$ | potassium hexacyanoferrate(II) trihydrate |
| LC | liquid chromatography |
| LCMs | laser cut carbon monoliths |
| LCMs | laser sectioned carbon monoliths |
| MB | methylene blue |
| MeOH | methanol |
| MHC | monolithic hierarchically porous carbon |
| MSDN | detonation nanodiamonds |
| MWCNTs | multi-walled carbon nanotubes |
| n/a | not applicable |
| $NH_4OH$ | ammonium hydroxide |
| NMR | nuclear magnetic resonance |
| NTCM | nanotemplated carbon monolith/monolithic rod |
| ODS | octaldecylsiloxane-bond silica |
| OMR | a well-ordered hexagonal or cubic mesoporous structure (*Im-3m*) |
| PAHs | polyaromatic hydrocarbons |
| PB@G | prussian blue-in-graphene |
| PBS | phosphate buffer solution |

| | |
|---|---|
| PEEK | polyether ether ketone |
| PEO–PPO–PEO | poly(propylene oxide)–poly(ethylene oxide)–poly(propylene oxide) |
| PGC | porous graphitic carbon |
| PIPS | polymerisation-induced phase separation |
| PMMA | poly(methacrylate) |
| PS-DVB | polymerisation of styrene and divinylbenzene |
| RF | resorcinol-formaldehyde |
| RP-HPLC | reversed-phase high performance liquid chromatography |
| RP-LC | reversed phase liquid chromatography |
| RT | room temperature |
| SCMs | scalpel cut carbon monoliths |
| SE | standard error |
| SEM | scanning electron microscopy |
| SMCA | silica modified carbon aerogels |
| $SnO_2$ | tin oxide |
| SPE | solid phase extraction |
| SPME | solid phase microextraction |
| TEM | tunneling electron microscopy |
| TG | thermogravimetric |
| TGA | thermogravimetric analysis |
| uHPLC | ultra-high-performance liquid chromatography |
| XPS | X-ray photoelectron spectroscopy |

# List of Figures

# List of Tables

# List of Publications

1. **Porous Graphitized Carbon Monolith as Electrode Material for Probing Direct Bioelectrochemistry**, <u>Xiaoyun He</u>, Lin Zhou, Ekaterina P. Nesterenko, Pavel N. Nesterenko, Brett Paull, Jesse O. Omamogho, Jeremy D. Glennon, and John H. T. Luong, *Analytical Chemistry,* **84** (2012)*,* 2351-2357.

2. **Fabrication and Characterization of Nanotemplated Carbon Monolithic Material,** <u>Xiaoyun He</u>, Ekaterina P. Nesterenko, Pavel N. Nesterenko, Dermot Brabazon, Lin Zhou, Jeremy D. Glennon, John H.T. Luong, and Brett Paull, *ACS Applied Materials & Interfaces,* **5** (2013), 8572-8580.

3. **Adsorption and Desorption of Methylene Blue on Porous Carbon Monoliths and Nanocrystalline Cellulose,** <u>Xiaoyun He</u>, Keith B. Male, Pavel N. Nesterenko, Dermot Brabazon, Brett Paull, and John H.T. Luong, *ACS Applied Materials & Interfaces,* **5** (2013), 8796-880.

4. **Nano-particle modified stationary phases for high-performance liquid chromatography,** Ekaterina P. Nesterenko, Pavel N. Nesterenko, Damian Connolly, <u>Xiaoyun He</u>, Patrick Floris, Emer Duffy and Brett Paull, *Analyst,* **138** (2013), 4229-4254.

5. **Liquid phase pulsed laser ablation: a route to fabricate different carbon nanostructures,** Ahmed Al-Hamaoy, Evans Chikarakara, Hussein Jawad; Kapil Gupta, Dinesh Kumar, M.S. Ramachandra Rao, Satheesh Krishnamurthy, Muhammad Morshed, Eoin Fox, Dermot Brougham, <u>Xiaoyun He</u>, Mercedes Vazquez and Dermot Brabazon, *Applied Surface Science,* available online 25 September 2013, in press

6. **Focussed ion beam serial sectioning and imaging of monolithic materials for 3D reconstruction and morphological parameter evaluation,** Mercedes Vazquez, David Moore, <u>Xiaoyun He</u>, Aymen Ben Azouz, Ekaterina Nesterenko, Pavel Nesterenko, Brett Paull and Dermot Brabazon, *Analyst,* **139** (2014), 99-104.

# List of Poster Presentations

1. **Characterisation of C$_{60}$ Fullerene-modified Silica for the Preparation of Carbon Monoliths**, <u>Xiaoyun He</u>, Ekaterina Nesterenko, Damian Connolly, Norma Scully, Jeremy Glennon and Brett Paull. *The annual Analytical Research Forum (ARF),* University of Loughborough, UK, 26-29 July 2010.

2. **Preparation and characterisation of C$_{60}$-fullerene-modified silica template particles for the preparation of graphitic carbon monoliths**, <u>Xiaoyun He</u>, Ekaterina Nesterenko, Damian Connolly, Jesse O. Omamogho, Jeremy Glennon, Brendan Twamley, Maurice Burke, Pavel Nesterenko and Brett Paull. *28$^{th}$ International Symposium on Chromatography (ISC),* Valencia Conference Centre, Spain, 12-16 September, 2010.

3. **Preparation and characterisation of C$_{60}$-fullerene-modified silica template particles for the preparation of graphitic carbon monoliths,** <u>Xiaoyun He</u>, Ekaterina Nesterenko, Damian Connolly, Jesse O. Omamogho, Jeremy Glennon, Brendan Twamley, Maurice Burke, Pavel Nesterenko and Brett Paull. *UNSCR 2$^{nd}$ Annual Symposium,* Dublin City University, Ireland, 29 September, 2010.

4. **Fabrication and Characterisation of a Novel C$_{60}$-Fullerene Modified Macro/Mesoporous Graphitic Carbon Monolith,** <u>Xiaoyun He</u>, Ekaterina Nesterenko, Lin Zhou, Jeremy Glennon, Pavel Nesterenko, and Brett Paull. *6$^{th}$ biennial Conference on Analytical Sciences in Ireland (CASi),* Dublin City University, 21-22 Feb 2011.

5. **Fabrication and Characterisation of Porous Graphitic Carbon Monoliths Using C$_{60}$-Fullerene Modified Silica Gel Templates,** <u>Xiaoyun He</u>, Ekaterina Nesterenko, Lin Zhou, Jeremy Glennon, Pavel Nesterenko, and Brett Paull. *36$^{th}$ International Symposium on High-Performance Liquid Phase Separations and Related Techniques (HPLC),* Budapest, Hungary, 19-23 June, 2011.

6.  **Carbon and polymer monolith focussed ion beam serial sectioning and imaging for 3D surface reconstruction and morphological parameter evaluation**, Aymen BenAzouz, <u>Xiaoyun He</u>, Mercedes Vazquez, Ekaterina P. Nesterenko, David Collins, Brett Paull, and Dermot Brabazon. *36<sup>th</sup> International Symposium on High-Performance Liquid Phase Separations and Related Techniques (HPLC),* Budapest, Hungary, 19-23 June, 2011.

7.  **A novel porous nanotemplated carbon monolithic rod for solid-phase extraction of phenols,** <u>Xiaoyun He</u>, Ekaterina P. Nesterenko, Pavel N. Nesterenko, Dermot Brabazon and Brett Paull. *38<sup>th</sup> International Symposium on High-Performance Liquid Phase Separations and Related Techniques (HPLC)*, Anaheim, California, USA, 16-21 June, 2012.

8.  **Centrifugal microfluidic disc integrating carbon monoliths for solid-phase micro-extraction,** Mercedes Vázquez, Emer Duffy, <u>Xiaoyun He</u>, Elizaveta Vereshchagina, Jens Ducrée, Ekaterina P. Nesterenko, Pavel N. Nesterenko, Dermot Brabazon and Brett Paull, *39<sup>th</sup> International Symposium on High-Performance Liquid Phase Separations and Related Techniques (HPLC)*, Amsterdam, The Netherlands, 16-20 June, 2013.

# List of Oral Presentations

1. **Application of metallic and carbonaceous nano-particle modified phases in micro-extraction and liquid chromatography,** Brett Paull, Pavel N Nesterenko, Damian Connolly, Ekaterina P Nesterenko, Hassan Alwael, David Collins, Anton Peristyy, Emmer Duffy and <u>Xiaoyun He</u>. *38th International Symposium on High Performance (HPLC),* Anaheim, California, USA, 16-21 June, 2012. (Invited talk)

2. **Porous graphitic nano-templated carbon monolith: preparation, characterisation and application as extraction sorbent,** <u>Xiaoyun He</u>, Ekaterina P Nesterenko, Pavel N Nesterenko, Dermot Brabazon and Brett Paull, *The Analytical Research Forum (ARF),* University of Durham, UK, 2-4 July, 2012.

3. **Production of Nano-templated Porous Graphitised Carbon Monoliths and their Physical and Electrochemical Characterisation**, <u>Xiaoyun He</u>, Ekaterina P. Nesterenko, Lin Zhou, Jeremy D. Glennon, John H.T. Luong, Pavel N. Nesterenko, Dermot Brabazon, and Brett Paull, *7th CASi Conference on Analytical Science, Ireland (CASi),* University College Cork, Ireland 1-2 July, 2013.

4. **Solid phase micro-extraction on centrifugal microfluidic disc integrating carbon monolithic stationary phases,** Mercedes Vázquez, <u>Xiaoyun He</u>, Emer Duffy, Elizaveta Vereshchagina, Jens Ducrée, Ekaterina P. Nesterenko, Pavel N. Nesterenko, Dermot Brabazon and Brett Paull, *20th International Symposium on Electro- and Liquid Phase-Separation Techniques (ITP 2013),* Tenerife, Canary Island, Spain, 6-9 October, 2013.

5. **Porous graphitic carbon monoliths embedded with nanodiamonds and other temperature induced nanocarbons,** Emer Duffy, <u>Xiaoyun He</u>, Ekaterina P. Nesterenko, Satheesh Krishnamurthy, Dermot Brabazon, Pavel N. Nesterenko and Brett Paull, *12th international conference on Frontiers of polymers and advanced materials (12th ICFPAM)*, Auckland, New Zealand, 8-13 December, 2013.

# List of honours and awards

1. **RSC travel grant** received for presenting my poster at the annual Analytical Research Forum (ARF), University of Loughborough, U*K,* 26-29 July 2010.

2. **RSC travel grant** received for the attending the annual Analytical Research Forum (ARF), University of Durham, UK, 2-4 July 2012.

3. **A best oral presentation prize** received at the annual Analytical Research Forum (ARF), University of Durham, UK, 2-4 July 2012.

4. **1<sup>st</sup> poster prize** at Faculty Research Day, represented for School of Mechanical and Manufacturing Engineering, 12 September, 2012.

# Acknowledgements

First and foremost, I would like to express my sincere gratitude to my supervisor Prof. Brett Paull, for offering me the opportunity to undertake the PhD and for all his guidance and advice over my four years PhD period of time. Many thanks also go to Dr. Dermot Brabazon and Prof. Pavel N. Nesterenko and for all their valuable advice and supervision.

I would also like to express my deep appreciation to all the other excellent people who I have had the privilege of working with over the last few years, especially to Dr. Ekaterina P. Nesterenko for her valuable mentorship. I would like to thank her for her elaborative instructions in every detail of my research work. Without all my supervisors' help, my PhD thesis will never be in shape.

My many thanks also go to all the technical staff and postgraduates of the School of Chemical Sciences, especially Dr. Brendan Twamley for helping me on FE-SEM, SEM and EDX imaging and providing helpful advice. I would also like to thank the technical staff in the National Centre for Sensor Research (NCSR), especially, Mr. Stephen Fuller for his great help on HPLC systems, Mr. Maurice Burke for his valuable technical support and assistance on Raman Spectroscopy. In the meantime, I would like to acknowledge all my colleagues in the Irish Separation Science Cluster (ISSC) group and my friends who helped me through difficult times and made my life in Dublin more delightful.

Last but not least, I would like to thank my family and friends for their endless continuous encouragements and all the sacrifices they did to help me to get to this point. Their love is beyond words.

# Abstract

A novel approach has been developed to fabricate a hierarchical nanotemplated carbon monolithic rod (NTCM) by using $C_{60}$-fullerene modified silica fullerene $C_{60}$ ($C_{60}$) modified silica gels (FMS) as hard templates and resorcinol-formaldehyde (RF) copolymer as carbon precursor. The influence of using the $C_{60}$ modified template was systematically studied using various physiochemical characterisation techniques in comparison with the unmodified counterpart carbon monolith blank (CM blank). This carbon/carbon monolithic composite, NTCM, possessed a higher specific surface area of 435 $m^2$ $g^{-1}$ with an integrated open hierarchical porous structure consisting of a tri-modal pore distribution. Due to its high surface area, high pore volume and graphite-like nature, it was used to modify the surfaces of boron doped diamond electrodes for hydrogen peroxide detections. The separation of three phenols on an in-house prepared CM blank column in reversed phase liquid chromatography demonstrated that this type carbon monolith has good selectivity for small polar aromatic compounds and poor separation efficiency due to strong affinity between the analytes and stationary phase. Subsequently, CM blank and NTCM in a rod form were tested as SPE sorbents for phenols adsorption. The adsorption kinetics showed that the CMs had good selectivity with very slow adsorption kinetics and lower adsorption capacity than the other common carbonaceous sorbent reported due to the capillary diffusion effect in the broad cross-section of the sorbents. Then the ground CM blank and NTCM powders were used for the adsorption of methylene blue (MB) in aqueous environment. Their adsorption kinetics, Langmuir isotherms, pH and temperature effects were intensely studied. The overall kinetics of both sorbents in a powder form showed much faster than in the rod form. The experimental results showed ground CM blank was a significantly better sorbent material for MB removal in water than NTCM with good reusability. For obtaining carbon monoliths of required shape for actual applications, $CO_2$ laser ablation in a continuous mode was used to cut two CM blank and NTCM rods under control conditions to produce discs with controlled dimensions. Adsorption studies confirmed the changes in surface chemistry and morphology in these resultant laser cut carbon monolithic discs (LCMs). The results showed laser cut is a good technique for cutting the fragile and porous carbon monoliths with intriguing structure and morphology.

# Chapter 1

# Literature Review

*"Learning never exhausts the mind."*

Leonardo da Vinci

## 1.1 Introduction

In recent years, there has been a growing interest in the synthesis of porous carbon materials, which are widely used in adsorbents [1-8], energy storage [9-11], fuel cells [12, 13], catalyst supports [14-16] and separation [17]. Several reviews covering synthesis, properties, and applications of porous carbonaceous materials are available [18-22]. According to the International Union of Pure and Applied Chemistry (IUPAC) recommendation, porous carbon materials can be classified into three types based on their pore sizes: microporous < 2 nm, 2 nm < mesoporous < 50 nm, and macroporous > 50 nm. Hierarchical porous carbon materials should be characterised by the presence of macropores along with micro- and /or mesopores. Trimodal porous materials have all three levels of pores. Among them, carbon monolithic materials hold several fascinating properties including high specific surface areas, uniform and tuneable 3D interconnected porous structure, good chemical and thermal stability. These properties usually lead to several distinct advantages such as high flow-through permeability, rapid heat and mass transfer, good electronic conductivity, high molecular interaction efficiency and ease of handling [23, 24]. Moreover, it is often necessary to formulate them in a particular shape directly (rods, discs or any shapes at the macroscopic level) and integrated structure in contrast to their powdered counterparts. Traditionally, monolithic materials are usually composed of either silica or polymer and developed mainly for separation science since the early 1990's [25-27]. They can be defined as a single piece of material with a continuous interconnected porous structure. The first carbon monolithic column used for the high performance liquid chromatography (HPLC) was developed by Guiochon's group in 2003. They demonstrated that it can be an alternative adsorbent to silica and organic polymer based monolithic column material. It can overcome the limited silica resistance to hydrolysis due to the silanol effects and the problem of polymer swelling in the presence of organic solvents. Today, these features along with the development of synthetic methods paved an even broader way for potentially using such carbon-based monolithic materials in analytical chemistry applications, such as adsorption, separation and electrodes for detection and quantitative analysis. However, as emerging adsorbent materials, they have received only limited attention from analytical chemists. Therefore, the work presented in this thesis mainly focused on the development and characterisation

of novel nanotemplated carbon monolithic materials, and exploring their applications in electrode support materials and adsorption.

In this chapter, the progress of chemical synthesis of carbon monoliths and their applications in the area of analytical chemistry in the last ten years is presented. The key for all of these synthetic methods is 'pores designing', which generally involves choosing the suitable template or solvent for creating the controlled pores, using the correct chemical approach to incorporate the template (either hard or soft or dual templates) and precursor mixture together, followed by carbonisation and finally chemical removal of the template. Furthermore, desirable carbon morphologies and structures can be achieved by using various precursors which are prepared via either thermal polymerisation or drying process (evaporation, supercritical or freeze drying) and carbonisation which are listed in Section 1.3. For clarity, these methods are classified into hard template (non-sacrificial template), soft template (a sacrificial template), dual template (a combination of hard and soft template) and other new synthesis approaches (non-template and the others). In each category, synthesis strategies and resultant materials are discussed in Section 1.3. Many efforts including development of unique polymerisation systems (solvent and/or precursor, conditions), precise pore controlling (pore orders, shapes and sizes (uniform or and multimodal)) and surface modification have been examined to enhance their structure and applications. The potential applications in the area of analytical chemistry are discussed in Section 1.4. Finally, some main characterisation techniques used for confirmation of the physiochemical properties of carbon monolithic materials are also briefly mentioned in Section 1.5.

## 1.2 Carbon in general

The sixth element, carbon, has always been considered fascinating by many material scientists and organic chemists owing to its versatility and unique properties. It can not only bond to the other elements both electronegatively and electropositively by covalent bonds but also bond to itself to form single, double or triple bonds with different hybrid orbitals $sp^3$, $sp^2$, sp, respectively. The most well-known carbon allotropes include

diamond, graphite and charcoal which are usually naturally occurring carbon materials. Accompanied with modern science and technology, various nanostructured carbon materials have been synthesised which cover the entire range of dimensionalities, from zero-dimensional (0D) (fullerenes, nanodiamonds, quantum dot, spheres), to one-dimensional (1D) (carbon nanotubes (CNTs), fibres, tubes and wires), over two-dimensional (2D) (graphene sheets, film and membrane) and three-dimensional structures (3D) (fullerite, CNT ropes and carbon monoliths). The term 'carbon monoliths' used here, belongs to the family of porous carbon materials but with interconnected porous structure and macroscopic shape. Depending on their hybridisation state and atomic arrangement, the major carbon allotropes are summarised in Figure 1.1 [28].
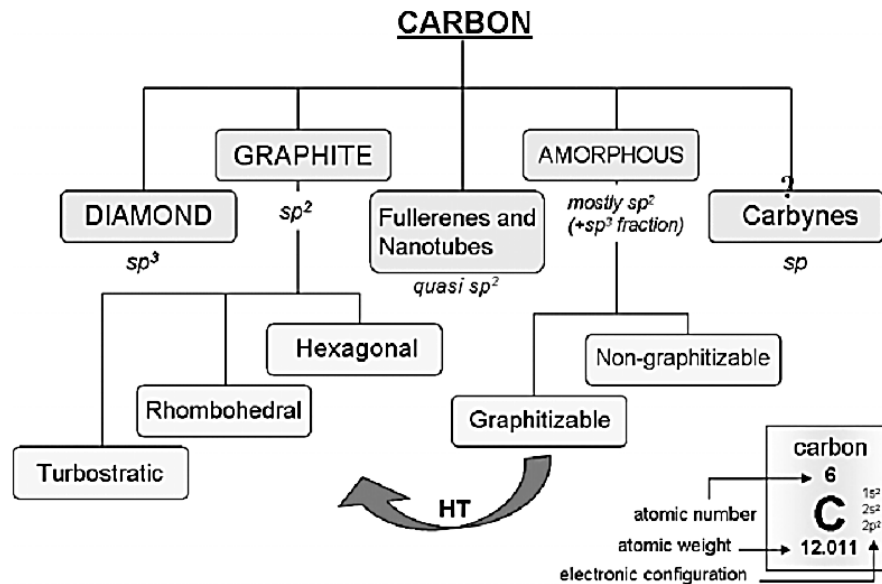


**Figure 1.1:** *Allotropes of the element carbon (Reproduced from: [28]).*

Amorphous carbon (or 'non-graphitic'), is usually prepared by pyrolysis of a carbon source, such as organic polymer or hydrocarbon precursors at a temperature below 1500 $^{o}$C, for example, carbon black, carbon fibre and most of porous carbons. They are composed with roughly planar layers with mostly sp$^2$ hybridisation carbons. In fact, they also have a crystalline structure, but they are in the short range and consequently lack

stacking direction [28]. Therefore, they still inherit good electric/thermal conductivity and thermal/chemical stability. Moreover, they usually have a higher surface area than the crystallised carbon, such as diamond, graphite, fullerene and CNTs.

## 1.3 Synthesis of carbon monolith

Originally porous carbon materials were prepared by carbonisation of various hydrocarbons such as wood, phenol resin [29], and a copolymer of styrene and divinylbenzene [30] etc. These carbon materials generally possessed irregular structures and exhibited small pores or broad pore size distributions, which limited their applications. In the past decades, many synthetic strategies emerged for the design and fabrication of porous carbon materials with a well-defined morphology, a suitable pore size, a suitable composition (functional groups and crystallinity) and a narrow pore size distribution in order to enhance their performance. Moreover, strong mechanical and hydrolytic stability, thermal stability, homogeneous surfaces, and an eliminated microporous structure for high mass transfer are also essential [31]. Many concepts and synthetic strategies for development of porous carbon powder materials are slowly adapted to fabricate the carbon monoliths.

### 1.3.1 Hard template

In general, carbon monoliths can be fabricated by extrusion, or directly, by wet chemistry (sol-gel process or thermal polymerisation). The hard template approach, also known as nanocasting or exotemplating is a more effective route to preparation of porous materials with finely tuned pore size, structure, highly controlled morphology, determined by the chosen template. Most of the nanocasting processes developed to date use different hard templates [32]. The so-called nanocasting process involves using a porous hard template as a mould and filling another material into a relevant structure on the length scale of nanometre; removing the initial mould to obtain negative replicas. If the voids are not of a nanometre scale in any dimension, it is known as casting process [33]. The general hard template synthetic routes for porous carbons can be summarised in the following steps [20, 34, 35]:

1.  Preparation of inorganic template, such as silica sol, zeolites, anodic alumina membranes, and various mesoporous silica materials, especially silica monolith.
2.  Introduction of carbon source into the void of templates through techniques, such as impregnation, infiltration or chemical vapour deposition (depending on the type of template used), to form a carbon/template precursor.
3.  Carbonisation under controlled conditions such as temperature, inert gas flow or additives.
4.  Removal of the inorganic templates using alkaline or HF solutions.

From the above procedure it can be noted that due to the nature of the template it does not sacrifice during the carbonisation and an extra step is required for removing it.

### 1.3.1.1 Replicas from silica spheres

One of the most successful examples of a hard templating strategy was developed by Knox and Gilbert for the production of commercially available porous graphitic carbon in 1979 [36]. Hypercarb® is the trade name of 100% porous graphitic carbon (PGC) which was commercialised by Thermo Electron Corporation in 1988 [37]. Almost thirty years later, it is still one of the most popular carbon stationary phases for liquid chromatography and solid phase extraction (SPE) [31]. For the fabrication of such stationary phases, the high-porosity HPLC grade silica gel used as a template is impregnated with a phenol-formaldehyde mixture and then heated to 80-160 °C to induce polymerisation. The precursor is then pyrolysed under inert atmosphere (nitrogen) at 1000 °C. Thus, highly porous amorphous carbon known as carbon black is produced (Figure 1.2 (a)). The silica template is then removed by a hot potassium carbonate aqueous solution. The resultant material is graphitised at 2340°C under inert atmosphere (argon). The high temperature treatment eliminates surface functions, produces a structural rearrangement and removes the micropores. After cooling down to 1000°C, the argon is replaced by hydrogen to induce a reaction between hydrogen and free radicals which present at the carbon surface for deactivating the surface to render it more uniform. The final porous graphitic carbon is shown in Figure 1.2 (b).
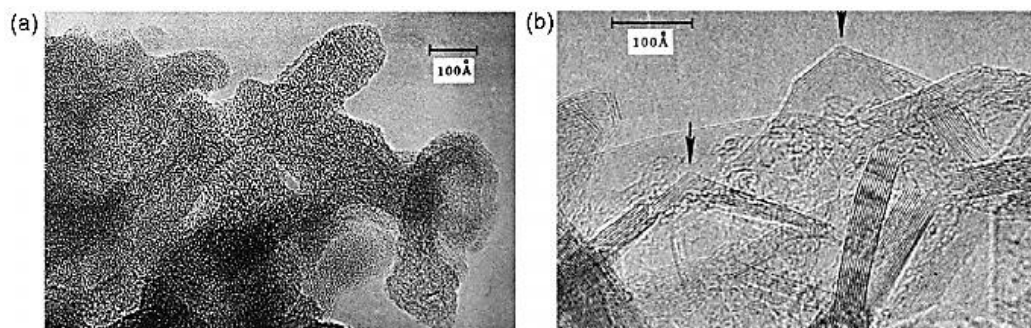
***Figure 1.2:*** *High-resolution scanning electron microscopy (SEM) images of (a) amorphous carbon obtained at 1000 ℃ and (b) PGC after graphitisation at 2340 ℃ (Reproduced from [38]).*

The physiochemical aspect of PGC and its application as a stationary phase will be discussed in detail in Section 1.4.1.1. However, PGC is a carbonaceous particle with a disordered pore structure which is restricted to manipulate or chemically functionalise its pore network [39]. This master approach was extended to the unitisation of different ordered inorganic hard templates to produce novel carbon monolithic materials, especially on more controllable structures and morphology. Guiochon's group first reported a graphitised carbon monolith column for HPLC in 2003 [40]. Their synthesis process involved impregnation of HPLC grade mesoporous silica particles in a phenolic carbon precursor, following with pyrolysis under inert atmosphere, then dissolution of silica template and metal catalyst by hydrofluoric acid [40]. Later, Eltmimi *et al.* from our group followed the same fashion for the fabrication of carbon monolith modified with gold nanoparticle [17]. The performance of these resultant carbon monoliths used as HPLC stationary phases will be discussed in Section 1.5.1. The orientation of silica beads in such a process was only dependant on their gravities which was a lack of controlling of the voids between silica beads resulting in random order of macropores.

In order to have more control of the arrangement of inorganic spheres, Klepel and his co-workers reported an alternative route to obtain hard templating materials with defined shape, so called 'powder pressing' [34]. Both commercially available zeolite and mesoporous silica were used as raw materials. They were each mixed with sucrose powder with a certain ratio and pressed at a pressure of 10 MPa for 30 min. All carbon

precursors were calcined in nitrogen at 800 ℃ for 3 h and followed with hydrofluoric acid (40%) treatment. For silica/sucrose carbon precursor, a minimum 50 wt% sucrose powder was needed as a binder between silica particles to form stable monoliths. However, nitrogen adsorption isotherms of carbon materials obtained from this template (silica/sucrose) showed the amount of sucrose binder was inversely proportional to the porosity of the carbon monolith decrease. They observed the pressing procedure caused a moderate porosity decrease for both materials. The template pore filling degree was low and an unstable carbon framework was consequently formed. The porosity and the mechanical stability of the resulting carbon monolith are low though a relatively high surface area (800 – 1600 $m^2$/g depending on the amount of sucrose dosed) was obtained.

### 1.3.1.2 Replicas from silica monoliths

Tanaka *et al.* developed a silica monolith with a hierarchical bimodal porosity (meso- and macropores) and full interconnectivity using a classic sol-gel process [41]. The preparation of this silica monolith consists of sequential hydrolysis and polycondensation of tetramethoxysilane in acidic solution, in the presence of a suitable porogen (e.g. polyacrylic acid, polyethylene oxide), followed by the maceration of the gel in a basic condition for the formation of suitable mesopores [41]. Merck commercialised this type of silica monolith for HPLC columns, under the brand name Chromolith®, consequently ending the monopoly era of the conventional packed columns with 4.6 mm inner diameter (I.D.) with 5 μm and 10 μm fully porous silica/polymer particles, which lasted for a quarter of a century (1975–2000) [27]. Since early 2000, silica monoliths have been widely used from separation science to material science. Many material scientists used such silica monoliths as templates and furfuryl alcohol or sucrose as a carbon precursor to produce carbon monolithic replicas with well-controlled porosity [23, 42, 43]. Such a nanocasting approach is now the most common one for fabrication of multiple modal porous carbon monoliths. Unlike the silica spherical template, it is a one piece silica rod with rigid hierarchical porous network. Lindén's group prepared a series of hierarchical porous carbon monolith replicas with wormhole-like mesopores and macropores, as shown in Figure 1.3 [42, 44-46]. Shi *et al.* adapted their methodology and prepared a carbon monolith with trimodal

pores and co-continuous structure using a hierarchical silica monolith as template and sucrose as a carbon source [43]. Noticeably, the carbon monoliths replicated from meso- and macropores silica monoliths possess the following unique features: positive replication of the silica framework on the micrometre scale and negative replication on the nanometre scale. For nanocasting, porosity accessibility and thermal stability are the key important factors to take into consideration on preparation of a template monolith.

Recently, a more eco-friendly and cost-effective hydrothermal nanocasting method using a commercially available amino-functionalised silica monolith as a template was developed to synthesise hierarchically porous monolithic carbons by Titirici and co-workers [47]. They emphasised the great versatility of their method using a series of biomass derived precursors (glucose, sucrose and xylose). The resultant carbon monoliths possessed very high surface area as measured by Brunauer-Emmett-Teller (BET) technique and pore volume up to 1426 $m^2$ $g^{-1}$ and 3.097 $cm^3$ $g^{-1}$, respectively.
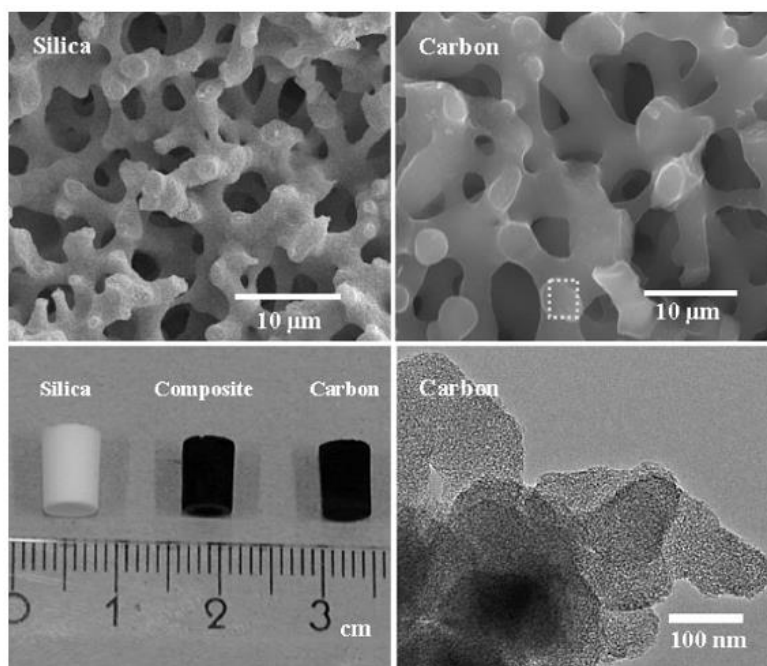


**Figure 1.3:** *SEM images (upper), photograph (lower left), and tunnelling electron microscopy (TEM) image (lower, right) of silica and carbon monolith (Reproduced from [32]).*

However, the macro- or mesopores in above mentioned carbon monolithic replicas are not size controlled. Zhao's group synthesised a large-diameter-sized mesoporous carbon monoliths with a bicontinuous cubic structure of *Ia3d* symmetry by using periodic mesoporous silica monoliths as hard templates and acidified sucrose as carbon sources, as shown in Figure 1.4 [48].
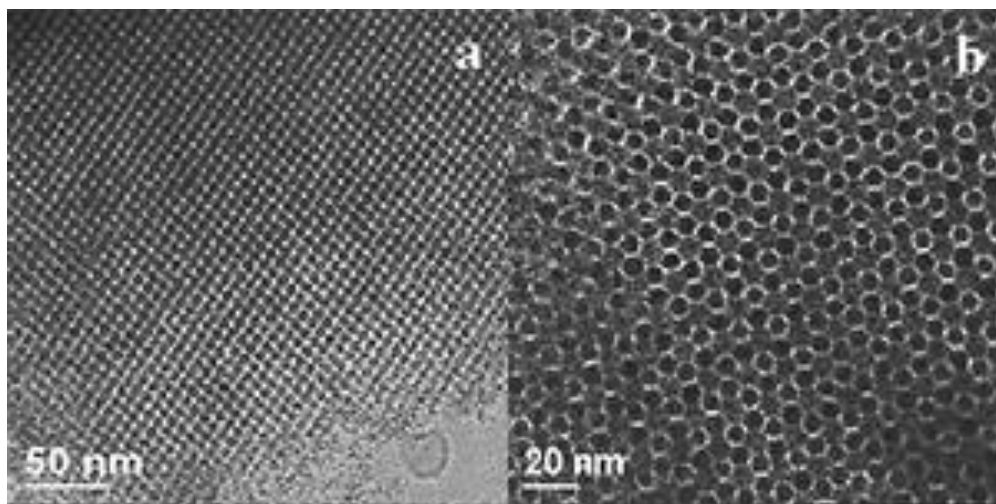


*Figure 1.4:* *TEM images of mesoporous carbon monolith with bicontinuous cubic mesostructure of Ia3d symmetry: along the (a) [110], (b) [111] directions (Reproduced by [48]).*

### 1.3.1.3 Replicas from colloidal crystals

Inverse opals or 3D ordered macroporous (3DOM) structure is possible to obtain by using a colloidal crystal template (colloidal silica or polymeric spheres) which are able to self-assemble into a periodic structure consisting of close packed uniform particles. The resultant carbon monoliths usually replicate this structure after the template is removed and subsequently have a high degree of periodicity in three dimensions. A recent review of 3DOM with various compositions (silica, carbon and metals) was published by Stein *et al.* which covered recent advances in controlling both the internal structure of 3DOMs, their external morphology, and their possible functionalities [49]. Several groups synthesised macroporous carbon with colloidal templating and cost effective sucrose and phenol resin [50-52]. Again the synthetic process is similar to the above mentioned but the templating materials are different. These macroporous carbon

monoliths also exhibited high specific surface area with large pore volumes. For instance, macroporous active carbon synthesised using an acidified aqueous solution of sucrose as a carbon precursor and $SiO_2$ colloidal crystals as hard template showed well-ordered, close-packed uniformed spherical macropores with a microporous framework, a total pore volume of 0.16 $cm^3$/g, and a BET surface area of 408 $m^2$/g [51]. Ordered mesoporous carbons reported to date usually have pore diameters well below 10 nm whereas 3DOM monolithic carbon prepared by colloidal-crystal template is usually above 100 nm. There was a gap in pore sizes between 10 and 100 nm [50]. A 3DOM with 62 nm spherical pores with periodic structures was reported by Kang and co-works which fill the pore size gap [50]. The details of the carbon monolith prepared from colloidal crystals that were eliminated during carbonisation will be discussed in Section 1.3.2.2.

So far, the self-assembly between block copolymer surfactants and carbon precursors via the hydrogen bonding interactions to achieve ordered mesoporous carbon monolith has been extensively explored. However, the success of hydrogen bonding induced self-assembly can only produce a narrow range of mesopores (3-10 nm). To achieve well-ordered porosity in either micropores range (< 2 nm) or large scale of mesopores (10-50 nm) still remains a challenge [35, 50]. In addition most of current syntheses are usually required for a minimum of a day at an acid or base catalysed polymerisation and precise controlled self-assembly soft template. Therefore, new polymerisation systems are in high demand to save preparation time and simplify the process. Moreover, hierarchical structured monolithic carbon materials would be more appropriate for application in the area of analytical chemistry, such as flow through devices for low pressure separations, rapid electrochemical detection and efficient adsorbents [53-55].

To date, the hard template approaches have been extensively explored by either nanocasting or exotemplating using thermal stable porous templates to obtain the carbonaceous replicas. The template used usually predominates the morphology and structure of the resulted carbon monoliths. However it still remains a challenge to introduce finely tuned porous structures for the resultant carbon monolith using these

approaches. The major disadvantage associated with this method are (1) an extra step of hard template preparation is required; (2) the fidelity and reproducibility of the precursor mixture to fulfil the nanostructure of the hard template is hard to control; (3) high temperature carbonisation might cause shrinkage and destroy the structural integrity of the replicating scaffolds and (4) template removal using heated NaOH and HF is needed. The soft template or dual template methods can alternatively be a solution for some of these issues.

## 1.3.2 Soft template

In recent years, great progress has been achieved on the synthesis of ordered mesoporous carbon materials with various symmetries using self-assembly of amphiphilic block copolymers/copolymer and surfactants as templates, also known as soft templates [56-58]. These templates have also been applied extremely successfully to the preparation of carbon monolith [59, 60]. Unlike the fussy and time consuming multistep hard template synthetic procedure, the soft templates are sacrificed as porogens during carbonisation and subsequently shorten the synthesis duration. However, it remains a great challenge to prepare carbon monoliths with highly ordered porosity, especially for producing mesopores in periodic arrangement, due to the meticulous requirements.

Three key points are required as shown below for designing of experiments using a soft template:

1. An ideal matching interaction between the carbon precursors and the porogen is required, which allows a stable micelle nanostructure to be formed by self-assembling;
2. The micelle structure should be retained during the drying/curing process, but must be able to decompose during carbonisation;
3. The carbon precursor is required to form a highly cross-linked polymer that maintains the rigid micelle nanostructure during pyrolysis or extract the soft template.

The presence of each one of these requirements is essential to the achievement of a monolithic carbon exhibiting properly developed mesoporosity.

### 1.3.2.1 Self-assemble copolymer templates

Huang *et al*. fabricated carbon monoliths with hierarchical porosities using triblock poly(propylene oxide)–poly(ethylene oxide)–poly(propylene oxide) (PEO–PPO–PEO) copolymers of Pluronic F127 and P123 as double soft templates, and phenolic resols (phenol : formaldehyde 1:4) as carbon precursors, as shown in Figure 1.5 [60]. The mixture with molar ratio between resols and soft template was about 46:1 and followed by one-step hydrothermal polymerisation with the presence of a base catalyst at 100 ℃ for 10 h, as shown in Figure 1.5 [60].
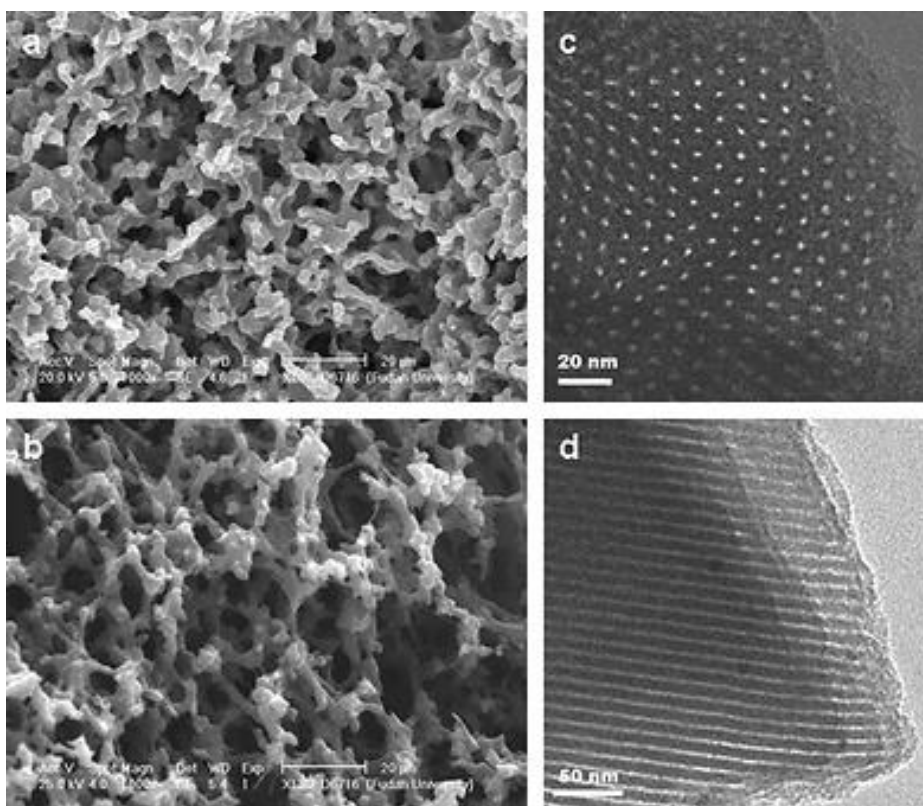


***Figure 1.5:*** *SEM image of the (a) as-synthesised and (b) calcined monolith samples. TEM images of the hierarchical carbon monolith with its ordered hexagonal mesostructure viewed from the (c) [10] and (d) [11] directions (Reproduced from [60]).*

Both SEM and TEM images (Figure 1.5) showed the resultant carbon monoliths with an ordered 2D hexagonal mesoporous structure and with an approximately 3nm uniform pore size which was confined in a 3D irregular interconnected macroporous framework (~ 3 $\mu$m) [60]. The hierarchical porosities were formed through the organic-organic self-assembling of amphiphilic triblock copolymers and phenolic precursors upon carbonisation. The resultant carbon monoliths were thermally stable and crack-free with a high yield of around 90 wt% (based on the carbon precursor) [60]. They suggested that this one step hydrothermal synthesis approach had potential to be scaled up for industrial production of mesoporous carbonaceous materials [60].

Later, Xiao *et al.* also prepared an extraordinary thermal/mechanical stable carbon monolith with a well-ordered hexagonal or cubic mesoporous structure (*Im-3m*) (OMR) via hydrothermal polymerisation at even high temperature and longer time (200 and 260 ℃ for more than 17 h) under alkaline conditions [61]. They also carefully studied the mesopores formation mechanism between the resol and surfactants mesopores due to the hydrogen bonding in the resultant OMR by ^{1}H nuclear magnetic resonance (NMR) spectroscopy [61]. They assumed that F127 induced self-assembly of the resol precursor with surfactants in the initial stage for generation of basic mesostructure [61]. The degree of cross-linking was increased and the surfactant F127 became dispersible when high temperature was applied to hydrothermal polymerisation [61]. Well-ordered mesostructures were still retained in the final products although most of F127 was thermally degraded, as shown in Figure 1.6 [61].
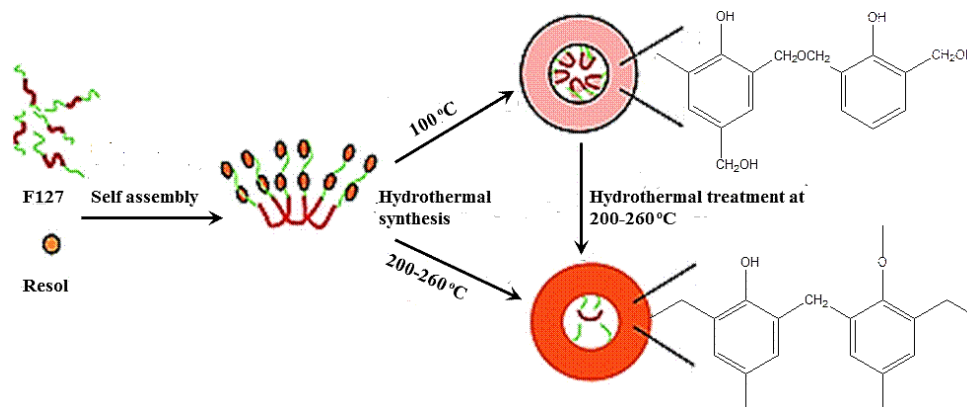


***Figure 1.6:*** *Proposed mechanism for the formation of OMR-n samples (Reproduced from [61]).*

At the same time, very light and highly conductive (2.5 S/cm) carbon aerogels showing a 3D continuous macro-/microporous structure have been prepared through $PPO_{15}$-$PEO_{22}$-$PPO_{15}$ block copolymer assisted RF polymerisation route [62]. More information about carbon aerogels will be described in Section 1.3.4.1 [62].

Dai and Liang prepared a meso-/macroporous carbon monolith by polymerisation-induced spinodal decomposition shown in Figure 1.7 [63]. Spinodal decomposition is a well-developed polymerisation-induced phase separation (PIPS) method for the preparation of low micrometre range macroporous polymers [63]. Polymerisation-induced spinodal decomposition was conducted in glycolic solutions of phloroglucinol/formaldehyde copolymer and triblock copolymer Pluronic F127 to synthesise bicontinuous macroporous morphologies with micro-domains from 0.5 to 6 $\mu$m [63]. The polymeric materials were further carbonised at elevated temperature up to 850 °C to yield bimodal carbon monoliths after the thermal decomposition of the soft template. The bimodal porous structure of the resultant carbon monoliths was derived from the dual phase separation in which spinodal decomposition and microphase separation occurred simultaneously. More examples of carbon monoliths fabricated by PIPS method without using F127 will be described in Section 1.3.4, Chapter 1.
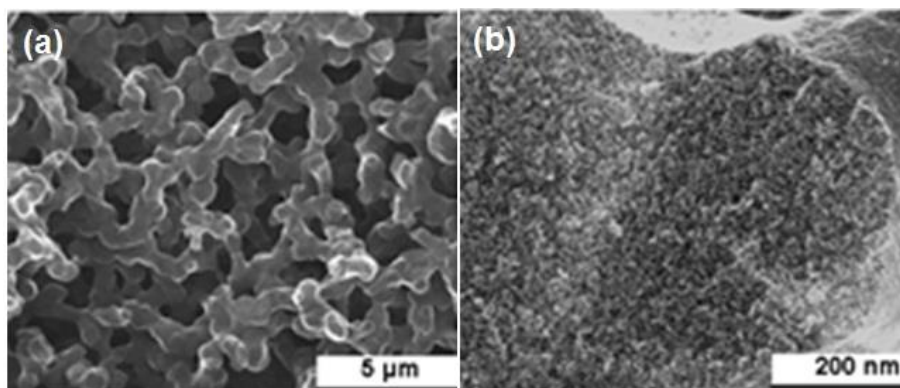


**Figure 1.7:** *Microstructure of one of the resultant carbon monolith fabricated in triethylene glycol: (a) Bicontinuous macroporous network and (b) mesopores on the skeleton (Reproduced from the [63]).*

### 1.3.2.2 Colloidal crystal templates

Stein group synthesised 3DOM monoliths of hard carbon via a RF sol-gel process using poly (methacrylate) (PMMA) colloidal crystal templates, as shown in Figure 1.8 [9]. This is an exceptional example which is unlike the other conventional 3DOM procedure using inorganic templates which normally require an extra step to remove. The template used here was thermally removed. Their synthetic procedure is involved: preparations of PMMA via an emulsifier free emulsion polymerisation technique and closely packing the resultant spheres by gravitational settling, as shown in Figure 1.8(a) [9]. RF polymer was used as a source of active carbon which infiltrated into the templates under the assistance of vacuum [9]. The mixture of the template-RF-sol composite was agitated in a sealed polyethylene bottle at $85^{\circ}$C for three days and then dried at $85^{\circ}$C in the same container with the lid open. The RF gel was pyrolysed at $900^{\circ}$C for 2 h under nitrogen flow, and PMMA spheres were thermally decomposed. The resultant 3DOM samples showed inverse opal geometry with ~ 285 nm pores, ~ 10 nm wall thickness and BET specific surface area of 326 $m^2$/g. The application of this material will be discussed in Section 1.5.3. However, those carbon sources did not provide an ordered mesoporous structure. The 3DOM with ordered mesopore and macropore structure that can be achieved by introducing another template composite will be discussed in Section 1.3.3 using both colloidal template and surfactant.
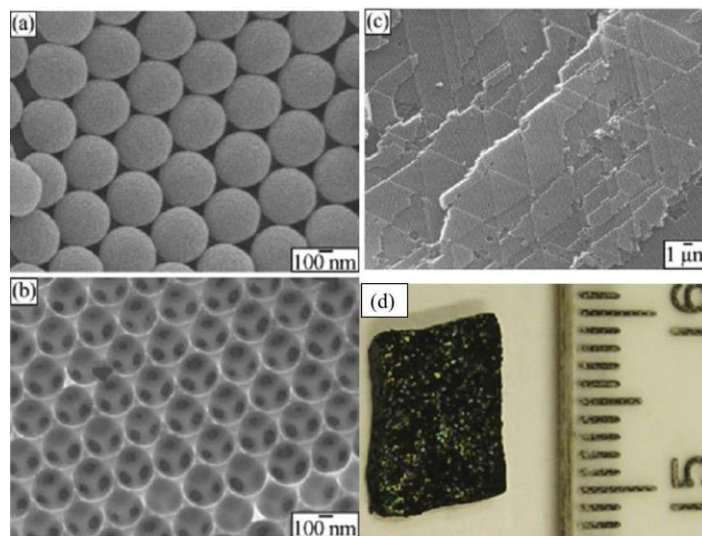


***Figure 1.8:*** *SEM images of (a) PMMA colloidal crystal template used to prepare 3DOM*

*carbon sample (as shown in Figure 1.8), (b) 3DOM carbon sample at higher magnification to show the macroporous structure, (c) 3DOM carbon sample at lower magnification to show the long-range periodicity of the sample and (d) photograph of monolithic 3DOM carbon sample (Reproduced from [9]).*

So far, the self-assembly between block copolymer surfactants and carbon precursors via the hydrogen bonding interactions to achieve ordered mesoporous carbon monolith has been extensively explored. However, the success of hydrogen bonding induced self-assembly can only produce a narrow range of mesopores (3-10 nm). To achieve well-ordered porosity in either micropores range (< 2 nm) or large scale of mesopores (10-50 nm) still remains a challenge [35, 50]. In addition most of current syntheses are usually required for a minimum of a day at an acid or base catalysed polymerisation and precise controlled self-assembly soft template. Therefore, new polymerisation systems are in high demand to save preparation time and simplify the process. Moreover, hierarchical structured monolithic carbon materials would be more appropriate for application in the area of analytical chemistry, such as flow through devices for low pressure separations, rapid electrochemical detection and efficient adsorbents [53-55].

## 1.3.3 Dual template

The dual templating approach is a combination of both hard and soft template for tailing macro- and mesopores, respectively. Hard templates usually provide a high degree of control over porous structures. Simultaneously, soft templates generate great variety of the micelle nanostructures. Many researchers employed such approaches to create an interdependent and interactive module for achieving a controlled hierarchical structure in an effective manner. Wang and co-workers prepared a monolithic hierarchically porous carbon (MHC) by a dual templating approach using a porous silica monolith and triblock copolymers F127 as shown in Figure 1.9 [64]. Their experimental results showed that F127 has a strong influence on increasing specific surface area and formation of mesopores in carbon materials. They treated this monolithic surface with strong acid to gain superwetting, more details will be mentioned in Section. 1.4.2.
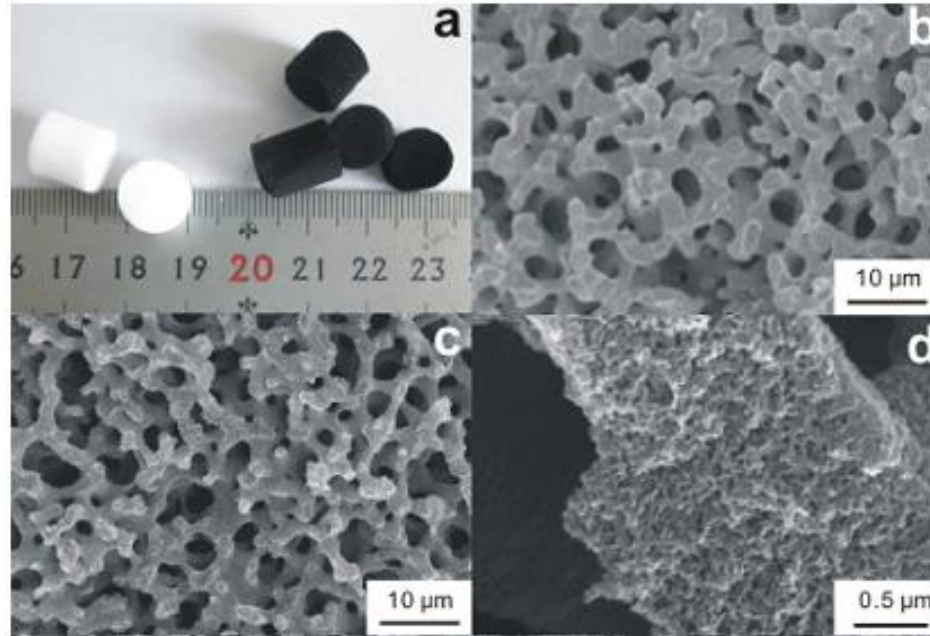
**Figure 1.9:** *(a) Photograph of the monoliths of hierarchically porous silica template and as-prepared carbon monoliths (MHC), (b) SEM image of silica showing interconnected macroporous structure (c) SEM image of MHC as-synthesised, owning replicated structure of the silica template, (d) image of (c) with higher magnification, showing abundant mesopore on the skeleton (Reproduced from [64]).*

However, the above mentioned methods required hydrofluoric acid to remove the silica template, raising environmental issues. A silica-free direct synthesis route was developed by Stein's group [65]. Again they extended their RF/PMMA nanocasting approach, mentioned in Section 1.3.2, and produced ordered hierarchical 3DOM with controllable mesoporosity (3DOM/m) via a facile dual template consisted of PMMA and amphiphilic triblock copolymer surfactant as template, as shown in Figure 1.10 [65].
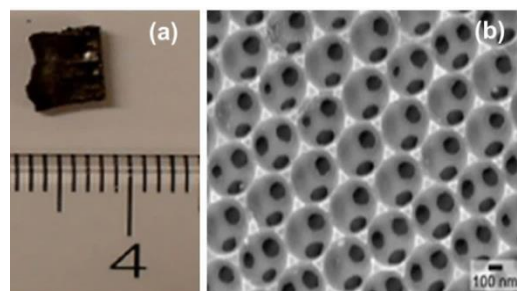


**Figure 1.10:** *(a) photograph of 3DOM/m as made and (b) SEM image of 3DOM/m carbon*

*monolith (Reproduced from [65]).*

The synthesis of 3DOM/m products includes four main steps as demonstrated in Figure 1.11: (1) infiltration of a precursor solution containing resol solution, copolymer surfactant and hydrochloric acid containing a PMMA colloidal crystal template, (2) thermal curing of the resol with surfactant micelles within the void space of the template, (3) removal of solvent under dynamic vacuum, (4) removal of template composites by carbonisation at $900^{\circ}C$ under inert atmosphere to obtain desirable glassy carbon [65]. To date, this is the first report of direct synthesis of ordered hierarchical porous carbon monolith which has completely eliminated any silica template and the use of hydrofluoric acid. Thus, this approach is safer, easier, cheaper and environmentally friendlier than any of the other nanocasting methods employing silica based templates.
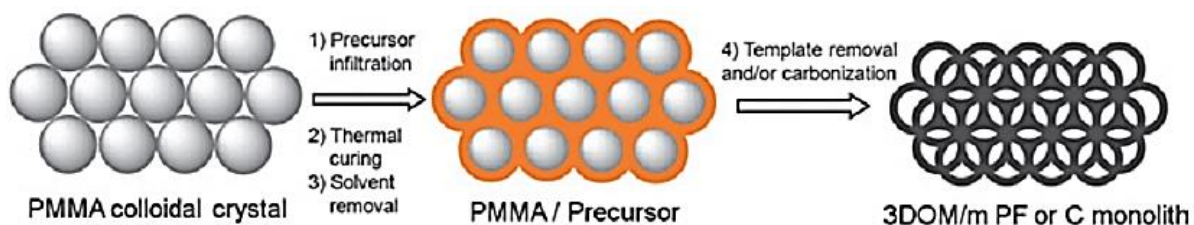


**Figure 1.11:** *Synthesis scheme of 3DOM/m phenolic resols (phenol-formaldehyde) and 3 DOM/m C monoliths (Reproduced from [65]).*

## 1.3.4 Template free and the other synthesis methods

In spite of the above mentioned, classic nanocasting and soft template approaches are quite successful, but the multi-steps and time consuming processes are unavoidable. Many researchers made tremendous efforts on simplifying the tedious process. Xu *et al.* reported mesoporous carbon monolith derived from the mixtures of phenol resin and ethylene glycol based on PIPS (Figure 1.12) [29]. Chemically induced phase separation is also known as PIPS [66, 67]. To carry out PIPS, reactive monomers are mixed with non-reactive low molecular weight or oligomeric solvents in the initial homogeneous solution [66-68]. It is crucial to select a suitable solvent to dissolve all the reactants as well as act as a porogen during the polymerisation [66-68]. A mild solvent is required to

give a homogeneous precursor mixture in the initial stage [66-68]. Phase separation will occur during polymerisation due to an immiscible solvent. The non-reactive components (usually the solvent used) are removed during the polymerisation. The polymerised reactive monomers are carbonised to form carbon monoliths under suitable conditions [29, 63]. The resulting morphology type is dependent on phase separation dynamics and reaction kinetics [68]. The influence of the amount of ethylene glycol used varying from 7.3% - 72.7% in the resin composition on the pore structure of carbonised products as demonstrated in Figure 1.12 [29].
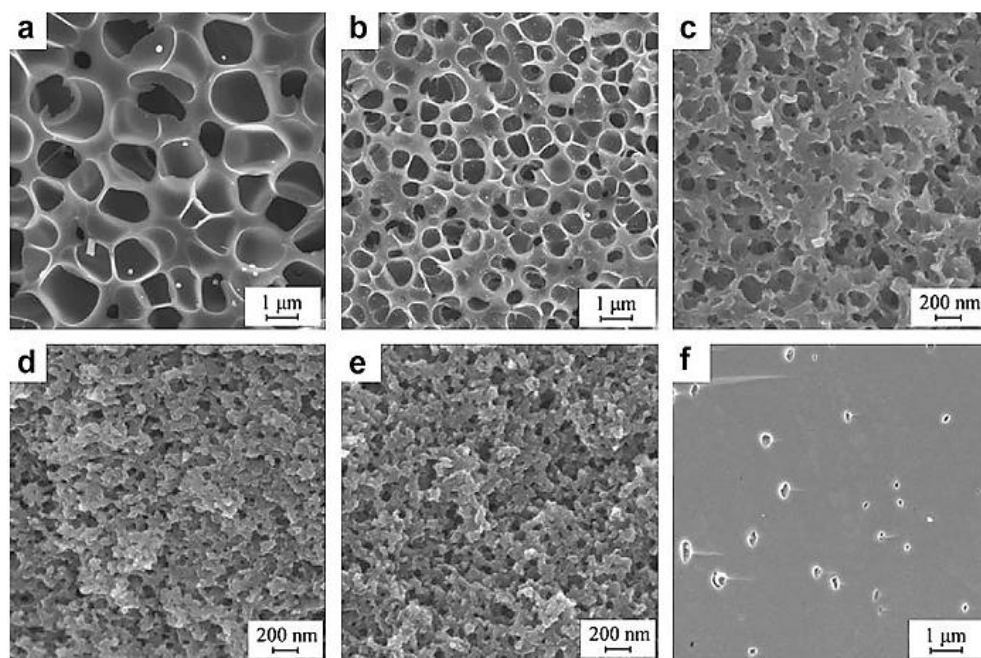


***Figure 1.12:*** *Morphologies of carbonised products prepared from the resin mixtures with different ethylene glycol content (a) 27.3%, (b) 36.4%, (c) 45.5%, (d) 54.5%, (e) 63.5% and (f) 72.7% (Reproduced from [29]).*

Tonanon and co-workers prepared a macroporous carbon monolith using ultrasonic irradiation without any template and they named it sonogel (gel treated by ultrasound at gelation stage) [69]. The preparation procedure involved mixing RF aqueous solution with a basic catalyst (sodium carbonate) and gelated at 35 $^\circ$C, ultrasonication of the mixture to speed up the reaction and yield the products, aging the resultant mixture in a cylindrical glass tube for a week at 75 $^\circ$C, then transferring the solvent to 1-butanol and

freeze-drying the RF hydrogel at -10 $^{o}$C for few hours, finally carbonisation at 750 $^{o}$C under flowing nitrogen gas to obtain the resulting carbon sonogels [69]. They suggested that the new synthesis method for 3D interconnected macroporous sonogel or carbon monolith has several advantages to the other carbon aerogel, such as reduced gelation time of the polymer monolith, reduction of the shrinkage and no template or templated removal required.

Different from the conventional RF carbon monolith, Shi *et. al* prepared a carbon monolith micro-sized in diameter as a micro-extraction fibre [30]. The preparation of the resulting carbon monolith by thermal polymerisation of styrene and divinylbenzene (PS-DVB) was rather similar to those of a PS-DVB monolithic capillary column for liquid chromatography, but without a cross-link to the inner wall of the fused silica capillary [70]. Azobisisobutyronitrile (AIBN) was used as a catalyst and the long chain alcohol as a porogens, e.g. 1-cotanol and dodecyl alcohol. The resulting carbon monolith was be used as a solid phase microextraction fibre and more details will be discussed in section 1.5.1, Chapter 1.

### 1.4.4.1 Carbon aerogels

Carbon aerogels (CAs; also named carbongels) are one of the most common methods currently used for preparation of carbon monoliths. Their synthesis is generally by sol-gel method [71] [72]. The word 'aerogel' designates wet gels that are synthesised by low-temperature traditional sol-gel chemistry and dried by supercritical conditions. If the same gels are dried by any other technique, such as evaporation or freeze drying, the resulting materials are known as xerogels or cryogels, respectively. In general, CAs are obtained by pyrolysis at temperatures above 500$^{o}$C of organic or polymer aerogels, which are mainly RF and melamine-formaldehyde based aerogels [73]. The general fabrication procedure to obtain carbon aerogels is outlined in Figure 1.13.
.
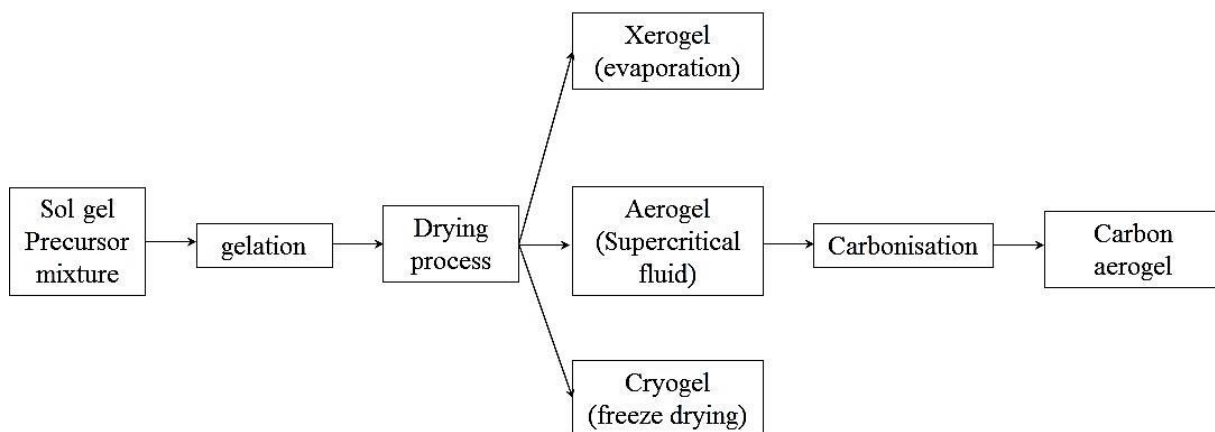
*Figure 1.13:* *A flowchart of carbon aerogels (the optional steps of aging in the mother liquor and washing after 'gel formation' and before 'drying process' are not shown in this flowchart) (Reproduced from [73]).*

The precursor mixture is usually RF based polymeric mixture with either an acidic (phosphoric, acetic or nitric acid) or basic catalyst (sodium carbonate or potassium carbonate) [74]. The chemistry of the formation of RF aerogels with either an acidic or basic conditions is outlined in Figure 1.14. These mechanisms can also apply to the thermal polymerised RF copolymer. The RF aerogel is prepared via sol-gel polycondensation of resorcinol with formaldehyde and dried by $CO_2$ supercritical fluid [75]. Of interest, the CAs obtained from RF aerogels usually are rich in micro-, meso- and/or macropores with high specific surface area (400-800 $m^2$/g) and large mesopore volume (> 0.55 $cm^3$) [73]. Since the first development of the phenolic resin type CAs by Pekala at the end of the 1980s [76], they have achieved remarkable progress in the development of monolithic carbons. The functionalised carbon aerogels will be briefly discussed in Section 1.4 by either direct synthesis or post-modification.
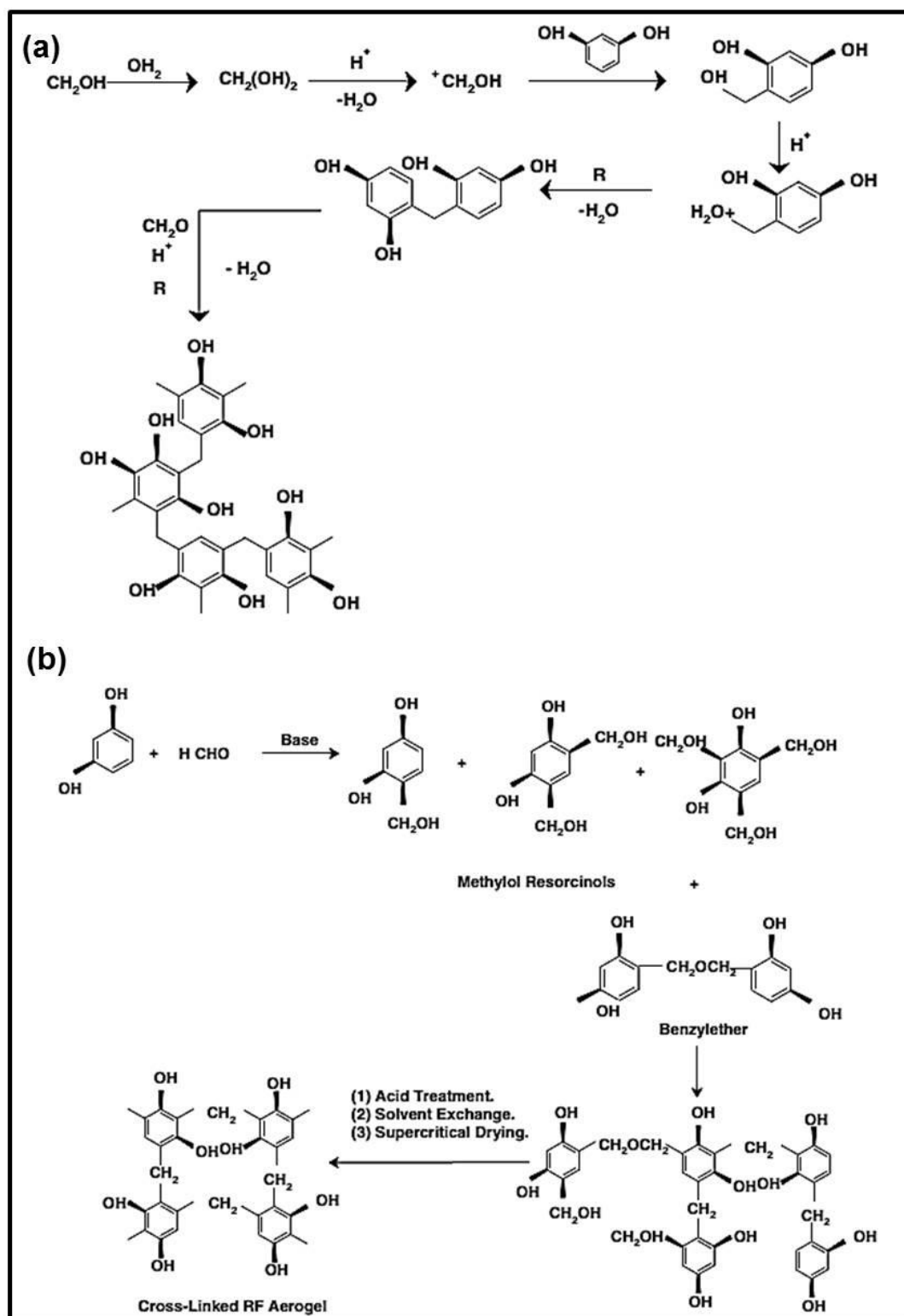
**Figure 1.14:** *Proposed mechanism for (a) acid catalysed and (b) base catalysed RF gelation (Reproduced from [77]).*

ElKhatat and Muhtaseb recently published a comprehensive review on the preparation and properties of RF organic and carbon gels and discussed how different synthesis approaches and reaction conditions affect their properties [77]. The most vital factors that affect the properties of carbon-based gels are the ratio of R/F, the type and concentration of catalyst, the time and temperature of curing, method of drying and conditions of pyrolysis. The CAs obtained from RF aerogels usually are rich in micro-, meso- and/or macropores with high specific surface area (400-800 $m^2/g$) and large mesopore volume (> 0.55 $cm^3$) [73]. Since the first development of the phenolic resin type CAs by Pekala at the end of the 1980s [76], they have achieved remarkable progress in the development of monolithic carbons. The functionalised carbon aerogels will be briefly discussed in Section 1.4 by either direct synthesis or post-modification.

Toman et al. have systematically studied the effect of the amount of resorcinol, formaldehyde, distilled water, and sodium carbonate used to control the mesoporous structure of the conventional carbon aerogels. They were able to control the radius of mesopore in the range of 2.0 to 6.1 nm by changing the mole ratio of resorcinol to sodium carbonate and the ratio of resorcinol to water in the resulted carbon aerogels. Different solvents, such as water, methanol, ethanol, tetrahydrofuran, or acetone also have an impact on the monolith density, which can vary from 0.37 to 0.87 $g/cm^3$ for carbon aerogels [78].

So far no study of the ability of deep eutectic solvents (DESs) to template the structure of the resulting carbon has been conducted. The ionic liquids (ILs) can also be used as solvent or as carbonaceous precursor, or alternatively to be structuring directing agents (template) for the fabrication of carbon aerogels with hierarchical monolithic structures because they have some special features, such as nonreactive with water, non-volatile, and biodegradable [79]. As a new class of ILs, DESs are obtained by the complexion of quaternary ammonium salts with hydrogen-bond donors (such as acids, amines, and alcohols, among others) [80, 81]. The freezing point of the mixture can be decreased, as can the melting points of the individual constituents, by means of the charge delocalisation occurring as a result of the hydrogen bonding between the halide

anion and the hydrogen-donor. Many emerging carbonaceous materials are prepared using ILs and DESs as solvents and even as carbonaceous precursors [80-83]. For example, Carriazo *et al.* prepared two precursors of resorcinol : one binary with choline chloride (molar ratio 4:1), called RC1-DES and the other ternary with urea and choline chloride (3.5:2:1), called RUC1-DES (depending on molar ratio of resorcinol : choline chloride used, 4:1 ) via formaldehyde polycondensation in DESs, as shown in Figure 1.15 [82]. Such approaches led to hierarchical porous carbon monoliths with BET surface area up to 600 $m^2$/g and narrow mesopore diameter distributions. The use of urea in the starting components enlarged the diameter of mesopores to ~ 23 nm in comparison with ~10 nm for the counterpart without urea. It subsequently introduced nitrogen into the carbon networks.
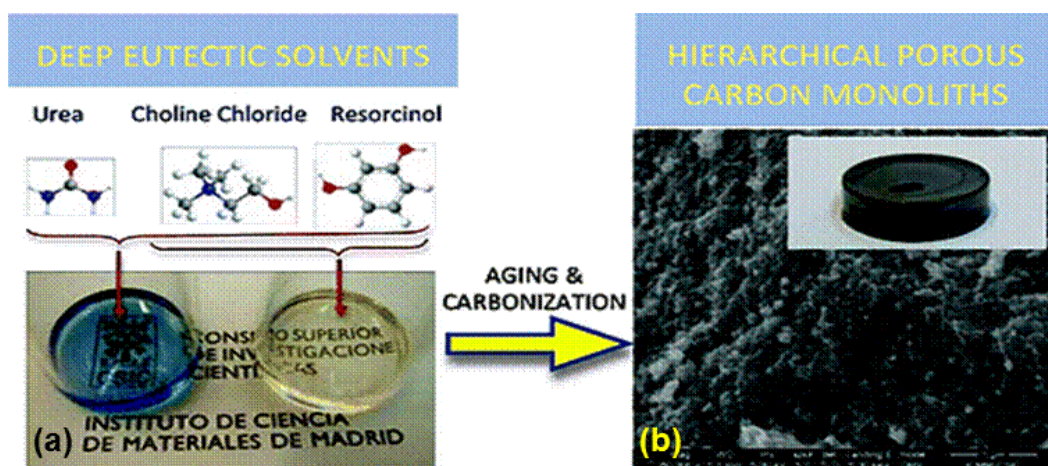


*Figure 1.15:* *(a) (Top panel) Molecules mixing with the DESs and (bottom panel) photograph of as-synthesised carbon precursors; RUC1-DES (blue) and RC1-DES (transparent) (Left hand side of the arrow) and (b) (Top right panel) photograph of as synthesised carbon monolith (Scale bar = 150 nm) with hierarchical porous structure as shown in SEM image (Scale bar = 1 µm) (Reproduced from [82]).*

A major disadvantage of the above mentioned synthetic procedure is the necessity for the use of expensive and unsustainable precursors. A greener approach for the synthesis of highly porous carbon cryogels and aerogels has been obtained *via* the hydrothermal gelation of a phenolic compound, *i.e.* phloroglucinol, with monosaccharides, *i.e.* glucose,

fructose or xylose, without any catalyst [84]. Due to the nature of these sugar-derived dried gels, the resulting carbon monolith showed trimodal porous structure with high micro-mesopore surface areas and volumes (up to 1159 m$^2$ g$^{-1}$ and 1.5 cm$^3$ g$^{-1}$ respectively), together with low density interconnected macromorphologies.

Sol-gel methods as simple and straightforward approaches have been widely used both in academic and industrial circles for obtaining of bulky porous carbons. However, this method requires a long gelation period time (> 1 days) and a laborious process, such as solvent exchange and drying. A slight variation occurring in any stage of the synthesis and preparation conditions may cause drastic changes in the texture and nanostructure [77]. Furthermore, more advanced sol-gel methods are demanded for solving the existing problem, such as the pore blockage and disposability of additive components or active sites on the surface or in the carbon skeleton.

## 1.4 Functionalisation of carbon monoliths

The utility of the carbon monolith can be promoted to the next level by surface modification in order to finely tune the interaction with guest molecules and optimise the properties of the materials in bulk or interface levels. Most approaches still rely on the knowledge gained from modification of more traditional forms of carbon (activated carbon, carbon black and glassy carbon etc.), for example, surface oxidation [85], KOH activation [86] and amination [87]. New methods of surface modification for carbon monolith have been slowly emerging along with the development of nanotechnology. It is critical to take into consideration functionalisation via direct synthesis if the heteroatoms have resistance to decomposition during the carbonisation process. Therefore, post treatments are very useful which could introduce the largest variety of surface functional groups without taking too much consideration of decomposition of functional groups during pyrolysis. Of course, there are many heteroatoms or components that are thermally stable, such as non-carbonaceous nanoparticles, suitable carbon precursors (thiophene, furan acrylonitrile and pyrrole for introduction of S, O and N groups, respectively). Post-modifications include surface oxidation by acids, KOH activation, grafting surface functional group, chemical vapour deposition and so

on. Incorporation of a secondary phase, commonly non-carbonaceous nanoparticles, into the carbon monolith framework by either direct synthesis or post-modifications has certainly gained much interest. More methods of functionalisation of the porous carbon were reviewed by Sten and his co-workers in great detail [21]. Further reviews below present a snapshot of other methods for functionalisation of carbon monoliths.

## 1.4.1 Direct synthesis

Porous carbon materials functionalised with sulfonic acid groups have been investigated due to low cost, high stability, and high activity. These environmentally friendly materials have shown wide potential in chemical production, separation/purification, and fuel cell [88-91]. Zhang *et al.* synthesised carbonaceous monoliths rich in sulfonic acid groups by one-pot hydrothermal carbonisation of the mixture of *p*-toluenessulfonic acid/glucose/resorcinol at 180 $^{o}$C [72]. Hydrothermal carbonisation process involves the dehydration of the biomass into a furan-like molecule at a low temperature (normally lower than 200 $^{o}$C) in the first step and subsequently stimulating polymerisation and carbonisations to occur at the same time [92, 93]. The catalytic results showed high activity (up to 1.65 mmol/g of sulfonic acid on the surface of resultant carbon monolith) and reusability to the initial conversion of benzaldehyde (up to 94 %) due to high surface area, large porosity and high loading of sulfonic acid on the surface. Moreover, the adsorption capacity of these activated samples for dye molecules with different sizes was much higher than the commercially activated carbons and ordered mesoporous carbons. However, a fraction of sulphuric acid leaching from the sample was observed.

A highly mesoporous carbon aerogel with controlled hydrophilicity was prepared similar to the above mentioned conventional carbon aerogel as seen in Section 1.4.4.1, except colloidal silica particles (Ludox HS-40, average ~12 nm in particle size) were used as hard templates to form ordered mesopores throughout the carbon matrix (Figure 1.16 (a)) [94]. From their rational experiments, they confirmed that the interconnected micrpores and small mesopores (10.5 nm in diameter) were formed by $CO_2$ supercritical drying whereas large mesopores (6.5 and 22.0 nm in diameter) were formed by whole or

partial colloidal silica template. Thus the silica template was embedded in an opened micro-/mesoporous structure, therefore it was much easier for HF or NaOH to penetrate into the carbon skeleton and dissolve the template. Finally the nanoporosity and hydrophilicity of the walls was increased by this controlled etching process. The water adsorption isotherms of the silica modified carbon aerogels (SMCA) at 30 $^o$C showed relative steep uptakes between $P/P_0 = 0.2$ and 0.4 in comparison to a carbon aerogel without silica template $P/P_0$ was around 0.5 without a clear adsorption hysteresis as shown Figure 1.16 (b). This difference could be due to the residue of silica template that remained in the resulting material. They suggested these carbon aerogel materials can be used as adsorbents, anodes for lithium ion batteries, electrochemical supercapacitors and solid catalyst o macromolecules.
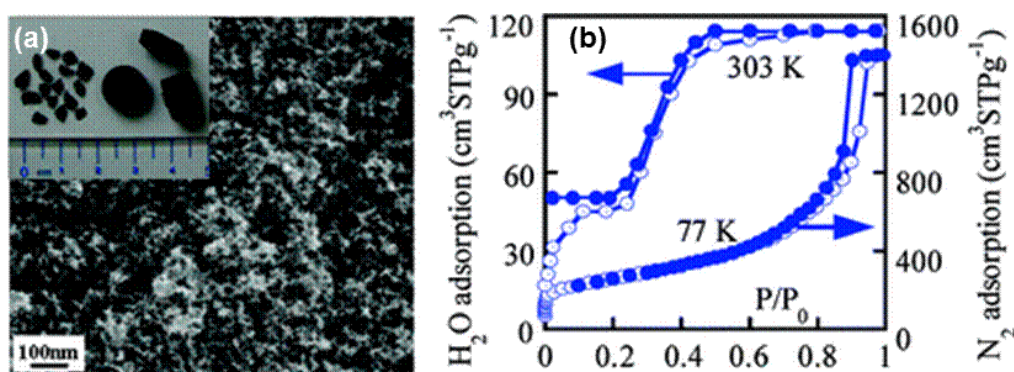


**Figure 1.16:** (a) FE-SEM image and photograph (insert) of silica modified carbon aerogels (SMCA); (b) Water adsorption (○)/desorption (●) isotherms at 30 $^o$C for SMCA and a carbon aerogel without silica template as a reference sample (Reproduced from [94]).

Alternatively, the heteroatoms can be also added in the solvent exchange step rather than in the initial mixing stage. Sepehri *et al.* chemically modified RF derived carbon cryogels with boron and nitrogen [95]. The general preparation of carbon cryogels is rather similar, as previously mentioned in Section 1.3.4.1, to carbon aerogel, except that it is dried by freeze drying. The clear aqueous solution containing resorcinol, formaldehyde and sodium carbonate (molar ration: 200:0.5:1, resorcinol : water 0.035 g/mol) was cured in a glass vial (10 mm in diameter) at 90 $^o$C for 7 days. Trifluoroacetic acid solution (pH 1.9) was used to terminate the condensation reaction of the hydrogels.

28

A 2% ammonia borane in *t*-butanol solution was then added to the hydrogels during the solvent exchange stage. All of the samples were freeze dried for a week under vacuum to achieve the final product as shown in Figure 1.17. This modified carbon aerogel showed an increased surface area and enlarged mesoporosity in comparison to its untreated counterpart. They used electric double layer supercapacitors to confirm their electrochemical properties and showed pseudocapacitive behaviour and increasing current density and capacitance.
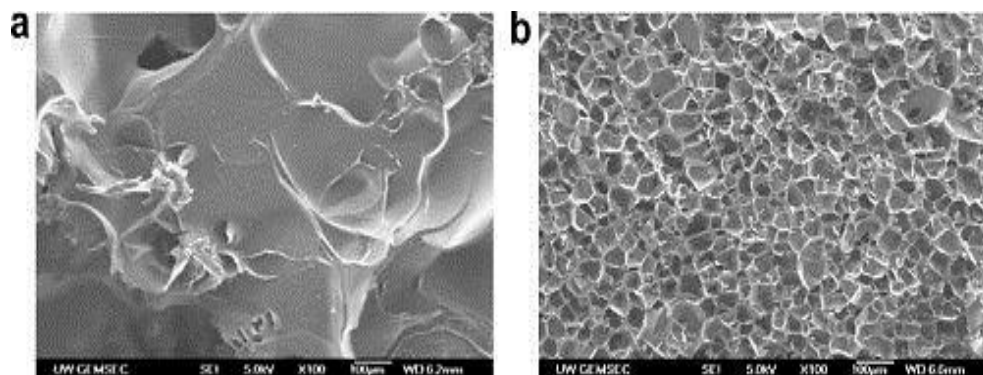


***Figure 1.17:*** *SEM of (a) unmodified carbon cryogel and (b) carbon cryogel modified with boron and nitrogen (scale bar = 100 μm) (Reproduced from [95]).*

Recently, Burn and co-workers took one step further with their previous 'phenolic-sugar' hydrothermal approach [84] and synthesised highly porous nitrogen-doped carbon aerogels from carbohydrate-based derivatives, i.e. glucose, D-(+)-glucosamine hydrochloride and N-acetyl-D-glucosamine, and phenolic compounds, i.e. phloroglucinol and cyanuric acid [96]. Noticeably, this approach did not involve any metal catalysts which exactly match the criteria of green chemistry. The resultant nitrogen rich micro-/mesoporous monolithic carbon aerogels exhibited high BET surface area and electrical conductivities of 600–700 $m^2$/g and 5–10 S/m, respectively. Moreover, it showed electrocatalysts for the oxygen reduction reaction and have many potentials including for advanced energy conversion and storage devices.

The catalytical, thermal and mechanical properties of carbon monolith can be improved by incorporation of carbonaceous nanoparticles into the carbon framework. A direct copolymerisation can not only disperse nanoparticles throughout the carbon

matrix, but also introduce unique active sites to the resultant materials. Among the other carbon allotropes, graphene and its functionalized derivatives are emerging carbon nanomaterials due to their unique and versatile properties. They can be easily used as building blocks for self-assembly to synthesise graphene-based functional materials with hierarchical microstructures. Baumann groups successfully incorporated CNTs or graphene sheets into the sol-gel reaction [97-99]. This resulted in the formation of advanced carbon-based monolithic materials with significantly improved mechanical and electrical properties. The RF precursor not only reduced the graphene oxide (GO) or CNTs but also produced carbon cross links in the graphene or CNT networks during pyrolysis. These carbon scaffolds almost maintained the similar physiochemical properties to those in the graphene sheets or CNTs networks. For example, Worsley *et al.* prepared carbon/graphene composite aerogels through sol-gel polymerisation of resorcinol and formaldehyde in an aqueous suspension of GO, and followed by the high temperature reduction of GO to graphene during pyrolysis at 1050 $^{\circ}$C (Figure 1.18) [99].
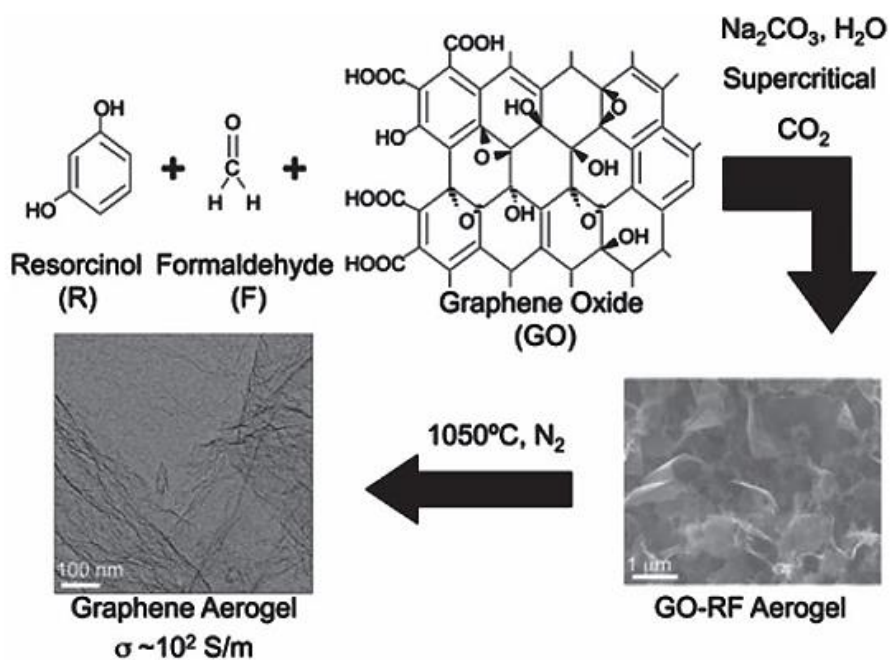


**Figure 1.18:** *The synthesis scheme for the GO-RF aerogel and graphene aerogel (Reproduced from [99]).*

Zhang *et al.* reported another means of creating graphene aerogels from hydrogel precursors by either supercritical drying or freeze drying and using L-ascorbic acid to reduce GO to graphene [100]. Noticeably, the process has no template and carbonisation involved compared with those reported by Worsley *et al.* [97]. The graphene aerogel so produced exhibited low density (12-96 mg/cm$^3$), high conductivity (~$10^2$ S/m), and developed porosity (BET surface area of 512 m$^2$/g and pore volume of 2.48 cm$^3$/g wide pore size distribution). Noteworthy is the fact that such graphene aerogel can support more than 14,000 times its own weight which was nearly twice the amount supported by the carbon nanotube counterpart (Figure 1.19).
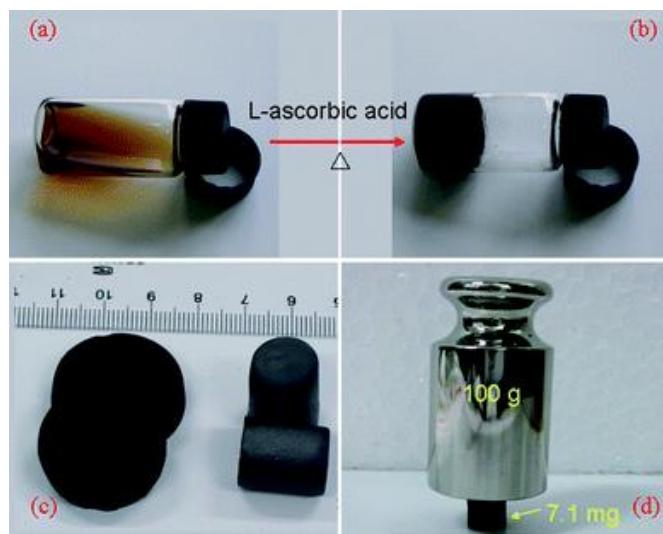


***Figure 1.19:*** *Photograph of (a) the aqueous suspension of GO, (b) the graphene hydrogel in a vial prepared by heating the mixture of GO and L-ascorbic acid without stirring; (c) the supercritical CO2 dried (left) and freeze dried (right) graphene aerogel, and (d) a graphene aerogel pillar (7.1 mg, 0.62 cm in diameter and 0.83 cm in height) supporting 100 g weights (Reproduced from [100]).*

Traditionally, the synthesis of 3D graphene assemblies relies on van der Waals forces for holding the 2D graphene sheets together, resulting in bulk properties that is no longer same as reported for individual graphene sheets [97, 99]. The recent progress in 3D carbon structures has revealed that it is possible to prepared bulk graphene or GO macroassemblyies by self-assembling method which maintain its initial properties.

Tang *et al.* reported the controlled assembly of single-layered GO into 3D macrostructures promoted by a noble-metal nanocrystal (Au, Ag, Pd, Ir, Rh, or Pt, etc.) [101]. Glucose was used as a carbon source. These macroassemblies have been utilised as fixed-bed catalyst for a Heck reaction resulting in 100% selectivity and conversion as a result of their very low density (0.03 g/cm) and excellent mechanical properties (compressive strength of 0.042 MPa and compress modulus of 0.26 MPa). Xu *et al.* prepared GO/DNA composite hydrogels by a novel and facile 3D self-assembly method [102]. The resulting hydrogels showed high mechanical strength, environmental stability, and dye-loading capacity, and self-healing property. The GO related building blocks can be further assembled with biomolecules or other species.

Several research groups also investigated the incorporation of inorganic nanoparticles onto monolithic carbon by various approaches. Interpenetrating inorganic nanoparticle-organic networks of Cu/RF aerogel was prepared by Leventis and co-works using a CuO induced one-pot synthesis [103]. Ferromagnetic nickel [104], Pt [105], Ti [106] or ZnO [107] nanoparticles can also uniformly be introduced into the 3D carbon matrix by a similar manner. In order to enhance carbon monoliths' electrical conductivity, metal salts are usually added into the initial polymer mixture as a catalyst for carbonisation [24, 40]. They tend to be reduced by carbon matrix and form metallic nanoparticles throughout the carbon skeletons. Maldonado-Hodar and co-workers investigated the changes in surface area, porosity and graphitisation of transitional metallic salts ($Cr^{3+}$, $Fe^{3+}$, $Co^{2+}$ and $Ni^{2+}$) containing carbon aerogels from the temperature range of 500 to 1800 $^{o}C$ [108]. The resultant carbon aerogels were fabricated in the conventional way as previously mentioned in Section 1.3.4.1, and showed preserved high pore volumes, surface area and increased graphitisation; consequently their electrical conductivity was also enhanced. The BET specific surface areas of those samples (300 - 400 m$^2$/g) were dramatically decreased after heat at 1400 $^oC$ (200 - 240 m$^2$/g) due to shrinkage of the microporosities. The localisation graphitisation phenomena observed that the crystalline graphite layers with the 002 lattice fringe were around metal particles. XRD result showed a mixture of $Fe_2O_3$ and Fe nanoparticles to coexist inside of the carbon matrix

which was treated at $1000^{\circ}C$. It further confirmed iron oxide was completely reduced at higher temperature ($1400^{\circ}C$).

Recently, Sevilla and Fuertes used a similar soft template approach to Huang *et al.* [60] as discussed in Section 1.3.2 (F127 as self-assemble soft templates), for synthesising macro/mesoporous carbon monoliths with a graphitic framework [24]. The modifications they made were done using poly (benzoxazine-co-resol) via polymerisation of the benzoxazine monomer obtained from condensation of resorcinol with formaldehyde in the presence of tetraethylenepentamine (Mannich reaction) as a carbon precursor and doping the polymer with a metallic salt of $Fe^{3+}$, $Ni^{2+}$ or $Co^{2+}$ as catalysts for graphitisation in order to achieve high content of graphitic carbon (>50 wt.%) in the resulting carbon monoliths for improving their electrical conductivity. The TEM image in Figure 1.20 showed that three different phases co-existed in the graphitised sample PGM-Ni-1000, which were reduced nickel nanoparticles, amorphous carbon and graphitic nanostructures. These materials possess a dual porosity made up of macropores and mesopores ($\sim$ 2 - 10 nm), their BET specific surface area of 280 - 400 $m^2$/g and pore volumeof~0.4 $cm^3$/g.
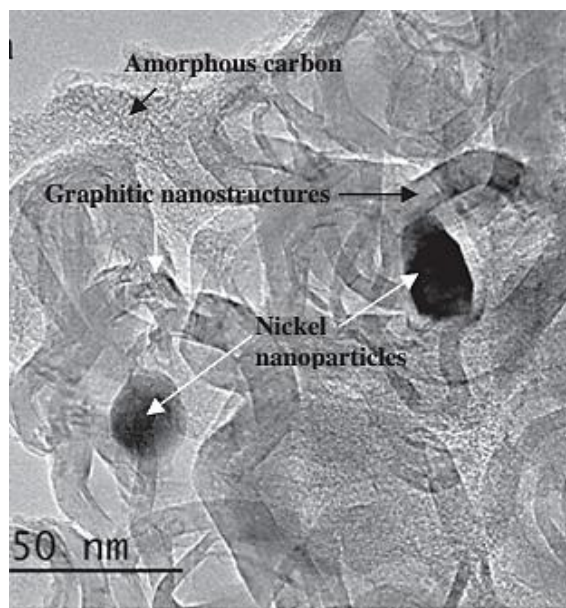


***Figure 1.20:*** *TEM image of the PGM-Ni-1000 sample (Reproduced from[24] )* .

## 1.4.2 Post-modification

Post-modification of the carbon surface is more versatile than introduction of functional groups during the synthesis of porous carbon materials since it is usually performed after the carbonisation process. However, it is rather challenging due to the chemical inertness of carbon. One of the most common approaches involves controlled oxidation of the carbon surface with oxidising solutions (nitric acid, hydrogen peroxide, permanganates and dichromates etc.) or oxidising gases (air, oxygen, ozone and nitrous oxides etc.) to introduce oxygenated functional groups, such as carboxylic acids, esters, ketone, phenol, lactone, lactol or quinones [20]. The oxygen-containing carbon samples subsequently are able to be further modified by covalent, electrostatic, and hydrogen bonding interactions. In addition, the oxidation treatment enhances the wettability of the carbon materials to the polar solvents. The strong acid treatment will also increase the fraction of micropores due to corrosion of the carbon material and consequently increase the specific surface area under the controlled conditions. However, the drawback to such oxidation process is that the resultant carbon materials have low bonding densities, and damaged surface or porous structures may result [21, 109].

Silva and co-workers were the first group to investigate the oxygenated surface groups on carbon xerogels using highly diluted $HNO_3$, by a hydrothermal method in an inert condition [110]. They found that the degree of functionalisation was dependent on the concentration of $HNO_3$ used. There was a clear correlation between the amount of oxygen functional groups and treatment conditions, including acid concentration, temperature and the amount of carbon loaded. For example, the BET specific surface area and the amount of oxygen group increased by increasing the $HNO_3$ concentration at 200 $^o$C. The above mentioned superwetting monolithic carbon monolith (Section 1.3.3) was also achieved by post-treatment of nitric acid by reflux (0.5g of pristine carbon monolith in 30 mL of 5 M $HNO_3$) [64]. More comprehensive surface chemistry study of the oxidation treatment of conventional carbon xerogels by oxygen plasma, nitric acid and diluted air was reported by Mahata *et al* [111]. Treatments with plasma created oxygen groups on the external surface of the carbon materials, whereas nitric acid and diluted air introduced oxygen groups throughout the entire carbonaceous frameworks,

including external surface and inside of the pore channels [111]. Alternatively, acid treatment can be also performed before carbonisation. A poly (divinylbenzene) (PDVB) monolithic precursor has been synthesised by living radical polymerization accompanied by spinodal decomposition [90]. It was then treated in concentrated $H_2SO_4$ at 120 $^o$C in order to prevent the dramatic shrinkage/weight loss during carbonisation stage as well as to sulfonate the carbon skeleton.

# 1.5 Applications

Porous hierarchical carbon monoliths are generally recognised as being suitable materials for numerous applications in the fields of energy storage, sensing, catalysis, and adsorption [18]. This is a consequence not only of their chemical/thermal stability and electronic conductivity but also of their high diffusion throughout the integrated structure with high surface area and high pore volume. Furthermore, those features also contribute to carbon monolithic materials a high adsorption capability and the ability to interact with active species electrochemically. Heretofore different forms of carbon were utilised for these applications, such as glassy carbon and graphitic carbon for electrodes [112] and activated carbons for catalysis [113] and adsorption [114]. Carbon materials with designed porosity (i.e. tuneable surface area, pore-size distribution, and pore accessibility) can add enormous benefit to the development of advanced adsorbents. In addition, the wall or the surface composition of carbon materials can be also modified to enhance their adsorption performance. This section emphasises applications of carbonaceous monoliths, particularly in analytical chemistry, such as adsorption, separation and sensors.

# 1.5.1 Adsorption and separation

Carbon based materials are one of the most common sorbents in both gas-solid and liquid-solid environments. SPE and liquid chromatography (LC) play very important roles in analytical chemistry. The sorbent materials used in SPE are quite similar to those packed in HPLC columns in most of the cases. SPE is one of the most widespread sample preparation techniques for extraction and pre-concentration of non-volatile

liquid samples in recent years [115-117]. For analysis of environmental, biological and pharmaceutical samples, sample pre-treatment is needed either to remove the matrix or preconcentrate the target analytes to the detection limit for the instruments [118, 119]. Solid phase microextraction (SPME), which evolved from SPE, was first developed by Pawliszyn [120]. Carbon and carbon related materials as sorbent materials in analytical processes have been reviewed by many scientists previously [121-123]. Namera carried out the most updated review of monolithic materials for sample preparation in 2011 and only two types of carbon monolithic materials were mentioned for liquid extraction [124]. The first example was a PS-DVB type carbon monolith was used as a microextraction fibre for phenol extraction and its extraction efficiency was compared to other commercial SPME fibres, which was prepared by Zhi-Guo Shi and co-workers [30]. The synthesis method of PS-DVB type carbon fibre was previously mentioned in Section 1.3.4. According to Shi *et al.* study, it showed higher extraction capacity, faster extraction time and longer lifespan compared with the commercial SPME fibres, due to the superior pore connectivity and high surface area. These factors resulted from its monolithical bimodal porous substructure and carbonaceous composition. The second example, MonoTrap$^®$ RCC18 was an endcapped $C_{18}$ silica monolithic rod coated with active carbon and which could be considered as a new generation carbon/silica monolith hybrid material which is commercially available from GL Science [125]. It is completely engineering free, i.e. no need to use pump, cartridge or manifold, and furthermore no need for conditioning therefore various sampling methods can be applied such as passive sampling, headspace gas chromotography sampling and agitation. It is useful for polar hydrophobic components with low to medium boiling points if it is used for thermal desorption.

Chromatography has become an important tool in organic and biochemical research over the last few decades for qualitative and quantitative analysis. Liquid chromatography among all the other types of chromatography (gas and supercritical fluid) is the predominant technique widely used in modern analytical separations. Currently liquid chromatography is most commonly performed as HPLC. Even ultra-high-performance liquid chromatography (uHPLC) depends on the particle size within

the column. Innovations in LC are most often boosted by the development of new column technologies both through the creation of surface modifications and compositions as well as in the new formats. Silica and polymer based monolithic HPLC with continuous macro-/mesoporous network showed high column efficiency and low pressure drop which is more suitable than the other conventional columns for fast separations [25, 126]. These resulted from their large and fully opened flow-through pores (macropores) and mesopore-rich skeleton. Thus they have higher permeability and shorter diffusion path length [27]. Unlike the silica and polymer monolithic sorbents (see Section 1.3.1.2 for more details), as alternative sorbent materials, carbon monoliths are still in the exploratory stage of their development to be used as HPLC media. Carbonaceous nanoparticles modified stationary for HPLC was reviewed by our group [123], thus the stationary phases consists of pure porous carbon or carbon modified with the other heterogenous atoms are focused on in this thesis. So far only Liang *et al.* [40] and Eltmimi *et al.* [17] have attempted to prepare and use carbon monolithic columns for HPLC. Both groups adapted Knox's process to produce porous graphitised carbon rods for HPLC (see Section 1.3.1.1 for more information about synthesis method). Their product was examined by SEM, Raman spectroscopy, X-ray diffraction and BET adsorption isotherm and they revealed the highly interconnected bimodal porous structure, porosity, and broad pore sized distributed mesopores and the partially graphitised nature. The carbon monolithic rod was cladded in heat-shrinkable Teflon tubing and then glued into a stainless steel or polyether ether ketone (PEEK) column before HPLC evaluation. The flow-through channels in Liang's column consisted of interconnected macropores ~ 10 μm in diameter throughout the skeleton. It showed a high permeability equivalent to that of a bundle of 7.5 μm capillary tubes, but the efficiency for the separation was poor, with a minimum value of the height equivalent to a theoretical plate (HETP) of 73.5 μm. The chromatogram of the separation of n-alkylbenzenes obtained from the aforementioned column is shown in Figure 1.21.
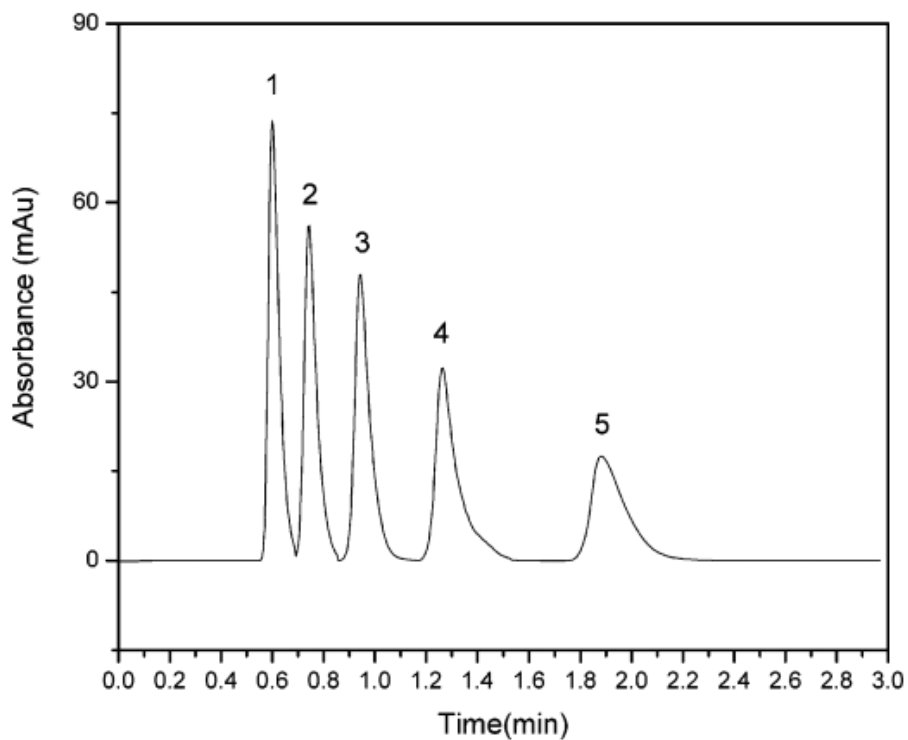
**Figure 1.21:** *Chromatogram of a mixture containing five alkylbenzenes in a mobile phase made of methanol (30%), dichloromethane (69%), and n-hexane (1%). The elution order is (1) toluene, (2) ethylbenzene, (3) propylbenzene, (4) butylbenzene, and (5) amylbenzene (Reproduced from [40]).*

The chromatographic retention mechanism of carbon is complicated, which is much different from those reversed phase liquid chromatography (RP-LC) packing materials (i.e. non-polar phases) [37]. The nonpolar carbon surface has much higher transfer energy than octaldecylsiloxane-bond silica (ODS) phases [37]. Therefore the conventional RP-LC mobile phases are too weak to be used. Strong solvents having a high polarisability and/or quadrupole moment are needed [127]. Liang and Dai used a mixed organic solvent containing methanol (30 %), dichloromethane (69 %) and n-hexane (1%) as mobile phase [40]. Eltmimi modified a similar porous carbon monolithic rod as Liang's one with gold micro-particles followed by 6-mercaptohexanoic acid for ion-exchange properties evaluation. However, his results showed limited suitability for the efficient separation of small molecules. Noticeably, none of them carbonised their carbon rods above 2200 $^{o}$C nor treated them with hydrogen gas during the cooling stage of the carbonisation as per Knox method due to

38

restriction of the temperature limit from the laboratory furnace [27]. Therefore the resultant materials were only partially graphitised with the presence of micropores. Micropores have negative adsorption properties along with the surface oxygen group [128]. This was the cause of the poor separation efficiency achieved.

Investigations into the suitability of functionalised glassy carbon and porous graphitic-carbon particles with diazonium salts as stationary phases for chromatography, including electrochemically modulated liquid chromatography have also been conducted in 2001. Many scientists suggested a carbon monolithic column would be an ideal stationary phase to use for this application due to its interconnected framework providing a more homogeneous electroproperty than a packed column [40]. However, there is not any literature reported on this application to date.

It is rather chanllenging for the conventional carbonaceous sorbent to adsorb either extremely large or small molecules. As aforementioned post treatment with strong acids (Secton 1.4.2) for improving the wettability of the carbon monolithic surface and subsequently to enlarge the pore size. This allows the access of large biomolecules to activated sites. The adsorption of biomolecules including cytochrome C, histidine, catechin, vitamin E, and the endocrine disrupter nonylphenol onto ordered mesoporous carbons has been studied [129-131]. Surface modification/acitivation also helpe the small molecules such as $CO_2$ and $H_2$ to be capatured [132, 133].

### 1.5.1.1 Commercially available carbon based sorbents

One of the commercially available carbon sorbents, PGC is turbostratic graphite, composed of intertwined graphitic ribbons (Figure 1.2 (b)) while the successive graphitic layers are not oriented regularly. PGC exhibits very low surface oxygen content (0.14%) when examined by X-ray photoelectron spectroscopy (XPS), which is largely distributed over phenol, carbonyl, carboxylic acid, lactone and quinine groups [37]. However, according to most literature, it has a largely homogeneous surface, minimum defects associated with oxygen active sites after the high temperature thermal

treatment. This material is physically and chemically stable. The typical physical characteristics of PGC are shown in Table 1.1.

*Table 1.1:* *Typical physical properties of PGC in relation of use as HPLC stationary phases.*

| | **Physical properties** | **Requirements of being HPLC stationary phases** |
|---|---|---|
| **Particle shape** | Spherical, fully porous | No micropores |
| **Specific surface area** | 120 m$^2$/g | Retention linearity and loading capacity |
| **Median pore diameter** | 250Å | Mass transfer for wide range of analytes shapes and sizes |
| **Pore volume** | 0.7 m$^3$/g | |
| **Mean particle diameters** | 3, 5, 7, and 30 $\mu$m depending on a template used | Packing bed uniformity |
| **Porosity** | 75% | Mass transfer within particles |
| **% C** | 100% | Chemical stability |
| **Mechanical strength** | > 400 bar | Operational particle stability; pressure gradients in packing process |

PGC can be used as a chromatographic stationary phase as well as a SPE sorbent. It has been utilised to provide solutions to a wide range of what might be considered extreme separation conditions in HPLC as compared with reversed phases sorbents [134]. They are stable throughout the entire pH range 1-14 [135], and are nearly insensitive to aggressive mobile phases and operation conditions [37]. Its compatibility with all solvent systems enables separation of a wide range of polarities within a single chromatographic run. Even 100% aqueous solution can be applied with PGC, while their application with $C_{18}$ (alkyl-) bonded silica phase will cause stationary phase collapse and retention time shift [135]. It is also a suitable stationary phase to meet the requirements for the area of high temperature liquid chromatography which attracts increased interest. Apart from its applications to reversed-phase separations, it was discovered that PGC provides unique retention and separation of ionised and highly

polar compounds [136]. The surface of PGC is stereo-selective which benefits from the planar nature of graphite [137, 138]. Furthermore, enantiomer (chiral separation) can also separate by PGC using optically active modifiers contained mobile phase [139]. Therefore it has the capability to separate geometric isomers [140, 141], sugars, carbohydrates, glycosides and other closely related compounds [142, 143].

## 1.5.2 Sensors

Besides graphene and carbon nanotubes, porous carbon materials have attracted considerable interest in electrode modification owing to their high surface area, good electronic conductivity, chemical inertness, large potential window, and high electrocatalytic activity for many important redox reactions. Porous carbons, especially those with suitable size pore size allowing the analytes to access, are suitable for using as electrode modifiers due to their controlled morphology, electrical conductivity and large surface areas [144]. Moreover, their biofriendly surface and meso-/macropore can accommodate relatively large guest species, such as enzymes and other biomolecules. Adsorption of enzymes on porous carbon might have potential applications in biosensing, biosensing enzymatic catalysis, bioreactor and biofuel cells [144]. Carbon monoliths owing to their interconnected porous structure and large mass transfer will be suitable to use as electrodes or electrode supported materials.

For the first time 3D porous and redox-active prussian blue-in-graphene (PB@G) aerogels with mass ratios of graphene to PB from 2.5:1 to 1:0.5 have been fabricated [53]. This has been carried out by means of supercritical fluid drying of hydrogel precursors. These have been synthesised by co-reduction of graphene oxide and $FeCl_3$ with L-ascorbic acid as the reducing agent in the presence of ferricyanide. PB is a very well-known coordination compound, which has a good electrochemical activity towards hydrogen peroxide ($H_2O_2$). $H_2O_2$ is a very important biomarker produced in many biological and environmental processes. The PB@G aerogels obtained are light weight (45–60 mg cm$^{-3}$) with a large BET surface area (316–601 m$^2$ g$^{-1}$) and excellent conductivity (up to 38 S m$^{-1}$). The PB@G aerogel modified electrode has been successfully applied in $H_2O_2$ electrochemical detection, and resulted in a very low limit

of detection ($5 \times 10^{-9}$ M) and a wide linear range (0.005–4 mM) as a result of its extremely porous morphology, high specific surface area and highly electrical conductivity (Figure 1.22).
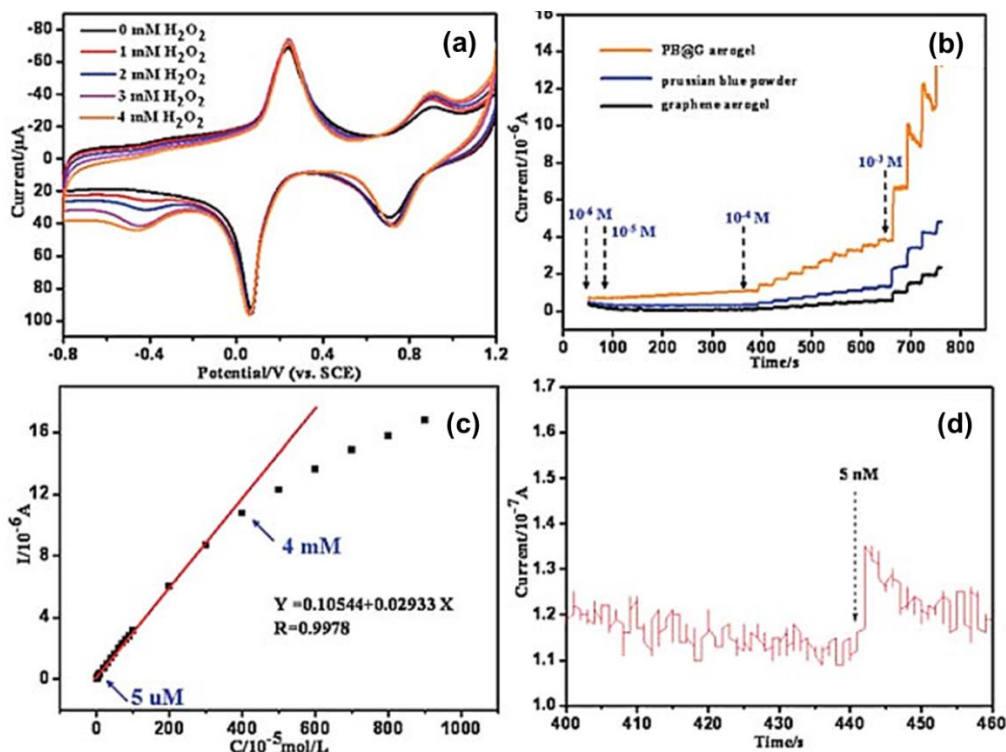


***Figure 1.22:*** *(a) cyclic voltammetry curves of the PB@G aerogel modified electrode with addition of different concentration of $H_2O_2$, (b) amperometric response curves of three kinds of electrodes at a detection potential of −0.5 V vs. SCE in a stirring PBS solutions (0.1 M, pH = 7) upon successive injection of different concentration $H_2O_2$ for each step, (c) the calibration curve for amperometric determination of $H_2O_2$, and (d) amperometric response of the PB@G aerogel modified electrode to addition of 5 nM $H_2O_2$ at −0.5 V in a stirring PBS solution (0.1 M, pH = 7) (Reproduced from [53]).*

3DOM carbon was used as the intermediate layer for the solid contact ion-selective electrode [145]. The carbon materials was connected to a metal current collector and covered with a poly(vinyl chloride) sensing membrane containing ionophore and ionic sites. The electrode was able to selectively detect $K^+$ with a detection limit of $10^{-6.2}$ M due to high ion and electric conductivity and well interconnected porous structure of

3DOM carbon. It exhibited a good resistance to interference from oxygen and light with a good long-term stability.

## 1.5.3 Other applications

Recently, carbon monoliths have gained interest as anode materials for lithium-ion batteries. The advantages of monolithic 3DOM carbon electrodes are: 1) short solid-state diffusion lengths (a few tens of nanometers) for lithium ions, 2) high surface area providing a large number of active sites for charge-transfer, 3) a well-interconnected wall structure enhanced electrical conductivity, 4) macropores allow the electrolyte penetrate easily within the 3DOM carbon matrix thus increase ionic conductivity, and 5) no need for a binder and/or a conducting agent [9]. Lee and co-work showed aforementioned PMMA templated 3DOM (see Section 1.3.2 for synthesis details) outperformed a similar but non-templated carbon electrode and an electrode prepared from spherical carbon with binder as regards to rate performance [9]. Furthermore, tin oxide ($SnO_2$) nanoparticles were used to coat the surface of 3DOM carbon by thermal decomposition for improving the energy density [9].

3DOM or the other macro-/mesoporous carbon monoliths with the promising macroporous surface area and volume together with good mechanical and electrical properties can be good candidates for the design of bioelectrocatalytic systems, such as electrodes in enzymatic fuel cells. Brun *et al.* recently successfully incorporated carbon monolithic disc onto a working electrode for the electro-oxidation of glucose after the immobilisation of a glucose oxidase-based biocatalytic mixture onto carbon support [146]. The modification improved the electrical connection between the carbon surface and the bioelectrocatalysts, which resulted in a 100 % increase in current density compared to a bare GCE with the same loading.

Carbon materials are also commonly used as catalysis support materials, especially for hosting precious-metal catalyst for organic reaction [113, 147]. Recently, nitrogen doped carbon monoliths were also developed for oxygen reduction reactions without

metal catalyst [96, 148]. These sorbents appear to be more environmentally friendly and cheaper than the precious metal incorporated porous carbons.

## 1.7 Conclusion

Tremendous progress has been made in synthesis of carbon monolithic materials with defined nanostructure and morphology, tunable surface area, and pore sizes in recent years. It also brings great opportunities for functionalisation of such materials to improve their properties for specific applications. The typical synthesis strategies for the fabrication of carbon monolith including sol-gel process, self-assembly, nanocasting, and precursor controlled pyrolysis along with suitable templates were reviewed. The common surface modification strategies were also described. This provides an opportunity to fundamentally understand the design and development of high-quality carbon monoliths to eventually meet the actual analytical applications. For optimising the existing carbon monolithic stationary phase for HPLC, polymer [149] or polyelectrolyte[150] coating can be used to block micropore and modestly reduce surface area of the sorbent for fast equilibrium if desired. The graphitisation method derived from Knox's method can be used to reduce the amount of oxygen-containing groups and improve the graphitisation degree to improve the separation efficiency of the aforementioned carbon monolithic sorbents. Carbon monoliths with finely tuned chemical composition and nanostructure can also improve the performance in sensors with better sensitivity and low detection limits. The incorporation of designed carbon monoliths with biomolecules, such as proteins, DNA and enzyme, might also provide a platform for bio-affinity adsorptions and separations.

## 1.8 References

1.  W. Cheah, S. Hosseini, M. A. Khan, T. G. Chuah, T. S. Y. Choong, Acid modified carbon coated monolith for methyl orange adsorption. *Chemical Engineering Journal* **215**, 747-754 (2013).
2.  W. Djeridi, A. Ouederni, A. D. Wiersum, P. L. Llewellyn, L. El Mir, High pressure methane adsorption on microporous carbon monoliths prepared by olives-stones. *Materials Letters* **99**, 184-187 (2013).

3. Y. G. Jin, S. C. Hawkins, C. P. Huynh, S. Su, Carbon nanotube modified carbon composite monoliths as superior adsorbents for carbon dioxide capture. *Energy Environ. Sci.* **6**, 2591-2596 (2013).

4. F. J. Liu, H. Zhang, L. F. Zhu, Y. M. Liao, F. Nawaz, X. J. Meng, F. S. Xiao, High-temperature hydrothermal synthesis of magnetically active, ordered mesoporous resin and carbon monoliths with reusable adsorption for organic dye. *Adsorption-Journal of the International Adsorption Society* **19**, 39-47 (2013).

5. M. Oschatz, L. Borchardt, I. Senkovska, N. Klein, M. Leistner, S. Kaskel, Carbon dioxide activated carbide-derived carbon monoliths as high performance adsorbents. *Carbon* **56**, 139-145 (2013).

6. T. Sun, H. Y. Fan, Z. Wang, Z. J. Wu, Hydrophobic monolithic silica with abundant pore as efficient adsorbent for organic contaminants removal. *J Mater Sci* **48**, 6713-6718 (2013).

7. C. Zhang, W. W. Tjiu, T. X. Liu, One-pot hydrothermal synthesis and reusable oil-adsorbing properties of porous carbonaceous monoliths using multi-walled carbon nanotubes as templates. *Rsc Advances* **3**, 14938-14941 (2013).

8. Z. X. Wu, P. A. Webley, D. Y. Zhao, Post-enrichment of nitrogen in soft-templated ordered mesoporous carbon materials for highly efficient phenol removal and CO2 capture. *Journal of Materials Chemistry* **22**, 11379-11389 (2012).

9. K. T. Lee, J. C. Lytle, N. S. Ergang, S. M. Oh, A. Stein, Synthesis and rate performance of monolithic macroporous carbon electrodes for lithium-ion secondary batteries. *Adv. Funct. Mater.* **15**, 547-556 (2005).

10. Z. Wang, M. A. Fierke, A. Stein, Porous Carbon/Tin (IV) Oxide Monoliths as Anodes for Lithium-Ion Batteries. *J. Electrochem. Soc.* **155**, A658-A663 (2008).

11. Y. S. Hu, P. Adelhelm, B. M. Smarsly, S. Hore, M. Antonietti, J. Maier, Synthesis of hierarchically porous carbon monoliths with highly ordered microstructure and their application in rechargeable lithium batteries with high-rate capability. *Adv. Funct. Mater.* **17**, 1873-1878 (2007).

12. V. Flexer, N. Brun, R. Backov, N. Mano, Designing highly efficient enzyme-based carbonaceous foams electrodes for biofuel cells. *Energy Environ. Sci.* **3**, 1302-1306 (2010).

13. G. S. Chai, S. B. Yoon, J.-S. Yu, J.-H. Choi, Y.-E. Sung, Ordered porous carbons with tunable pore sizes as catalyst supports in direct methanol fuel cell. *J. Phys. Chem. B* **108**, 7074-7079 (2004).

14. C. Moreno-Castilla, F. J. Maldonado-Hodar, Carbon aerogels for catalysis applications: An overview. *Carbon* **43**, 455-465 (2005).

15. J. S. Yu, S. Kang, S. B. Yoon, G. Chai, Fabrication of ordered uniform porous carbon networks and their application to a catalyst supporter. *Journal of the American Chemical Society* **124**, 9382-9383 (2002).

16. C. Moreno-Castilla, F. J. Maldonado-Hodar, Carbon aerogels for catalysis applications: An overview. *Carbon* **43**, 455-465 (2005).

17. A. H. Eltmimi, L. Barron, A. Rafferty, J. P. Hanrahan, O. Fedyanina, E. Nesterenko, P. N. Nesterenko, B. Paull, Preparation, characterisation and modification of carbon‐based monolithic rods for chromatographic applications. *Journal of Separation Science* **33**, 1231-1243 (2010).

18. J. Lee, J. Kim, T. Hyeon, Recent progress in the synthesis of porous carbon materials. *Advanced Materials* **18**, 2073-2094 (2006).
19. R. Ryoo, S. H. Joo, M. Kruk, M. Jaroniec, Ordered mesoporous carbons. *Advanced Materials* **13**, 677-681 (2001).
20. C. Liang, Z. Li, S. Dai, Mesoporous carbon materials: Synthesis and modification. *Angew. Chem.-Int. Edit.* **47**, 3696-3717 (2008).
21. A. Stein, Z. Wang, M. A. Fierke, Functionalization of Porous Carbon Materials with Designed Pore Architecture. *Advanced Materials* **21**, 265-293 (2009).
22. A. I. Cooper, Porous materials and supercritical fluids. *Advanced Materials* **15**, 1049-1059 (2003).
23. A.-H. Lu, J. H. Smatt, S. Backlund, M. Linden, Easy and flexible preparation of nanocasted carbon monoliths exhibiting a multimodal hierarchical porosity. *Microporous Mesoporous Mat.* **72**, 59-65 (2004).
24. M. Sevilla, A. B. Fuertes, Fabrication of porous carbon monoliths with a graphitic framework. *Carbon* **56**, 155-166 (2013).
25. F. Svec, Porous polymer monoliths: Amazingly wide variety of techniques enabling their preparation. *J. Chromatogr. A* **1217**, 902-924 (2010).
26. F. Švec, T. B. Tennikova, Z. Deyl, *Monolithic materials: preparation, properties, and applications, 1st ed.* (Elsevier, Amsterdam, 2003).
27. G. Guiochon, Monolithic columns in high-performance liquid chromatography. *J. Chromatogr. A* **1168**, 101-168 (2007).
28. E. H. L. Falcao, F. Wudl, Carbon allotropes: beyond graphite and diamond. *Journal of Chemical Technology & Biotechnology* **82**, 524-531 (2007).
29. S. Xu, J. Lie, G. Qiao, H. Wang, T. Lu, Pore structure control of mesoporous carbon monoliths derived from mixtures of phenolic resin and ethylene glycol. *Carbon* **47**, 2103-2111 (2009).
30. Z. G. Shi, F. Chen, J. Xing, Y. Q. Feng, Carbon monolith: Preparation, characterization and application as microextraction fiber. *J. Chromatogr. A* **1216**, 5333-5339 (2009).
31. L. Pereira, Porous graphitic carbon as a stationary phase in HPLC: Theory and applications. *Journal of Liquid Chromatography & Related Technologies* **31**, 1687-1731 (2008).
32. A. H. Lu, F. Schueth, Nanocasting: A versatile strategy for creating nanostructured porous materials. *Advanced Materials* **18**, 1793-1805 (2006).
33. F. Schüth, Endo- and exotemplating to create high-surface-area inorganic materials. *Angewandte Chemie International Edition* **42**, 3604-3622 (2003).
34. O. Klepel, H. Strauss, A. Garsuch, K. Boehme, Several ways to produce porous carbon monoliths by template assisted routes. *Mater. Lett.* **61**, 2037-2039 (2007).
35. A.-H. Lu, G. P. Hao, Q. Sun, X. Q. Zhang, W. C. Li, Chemical synthesis of carbon materials with intriguing nanostructure and morphology. *Macromol. Chem. Physic* **213**, 1107-1131 (2012).
36. J. H. Knox, M. T. Gilbert, US Patent 4263268. (1979).
37. C. West, C. Elfakir, M. Lafosse, Porous graphitic carbon: A versatile stationary phase for liquid chromatography. *J. Chromatogr. A* **1217**, 3201-3216 (2010).
38. J. H. Knox, B. Kaur, G. R. Millward, Structure and performance of porous graphitic carbon in liquid chromatography. *J. Chromatogr. A* **352**, 3-25 (1986).

39. R. J. White, V. Budarin, R. Luque, J. H. Clark, D. J. Macquarrie, Tuneable porous carbonaceous materials from renewable resources. *Chemical Society Reviews* **38**, 3401-3418 (2009).

40. C. Liang, S. Dai, G. Guiochon, A graphitized-carbon monolithic column. *Analytical Chemistry* **75**, 4904-4912 (2003).

41. H. Minakuchi, K. Nakanishi, N. Soga, N. Ishizuka, N. Tanaka, Effect of skeleton size on the performance of octadecylsilylated continuous porous silica columns in reversed-phase liquid chromatography. *J. Chromatogr. A* **762**, 135-146 (1997).

42. A. Taguchi, J. H. Smatt, M. Linden, Carbon monoliths possessing a hierarchical, fully interconnected porosity. *Advanced Materials* **15**, 1209-1211 (2003).

43. Z. G. Shi, Y. Q. Feng, L. Xu, S. L. Da, M. Zhang, Synthesis of a carbon monolith with trimodal pores. *Carbon* **41**, 2677-2679 (2003).

44. J. H. Smatt, C. Weidenthaler, J. B. Rosenholm, M. Linden, Hierarchically porous metal oxide monoliths prepared by the nanocasting route. *Chem. Mat.* **18**, 1443-1450 (2006).

45. A.-H. Lu, J. H. Smatt, M. Linden, Combined surface and volume templating of highly porous nanocast carbon monoliths. *Adv. Funct. Mater.* **15**, 865-871 (2005).

46. A.-H. Lu, J. H. Smatt, M. Linden, F. Schuth, Synthesis of carbon monoliths with a multi-modal pore system by a one step impregnation technique. *New Carbon Materials* **18**, 265-269 (2003).

47. L. Yu, N. Brun, K. Sakaushi, J. Eckert, M. M. Titirici, Hydrothermal nanocasting: Synthesis of hierarchically porous carbon monoliths and their application in lithium-sulfur batteries. *Carbon* **61**, 245-253 (2013).

48. H. F. Yang, Q. H. Shi, X. Y. Liu, S. H. Xie, D. C. Jiang, F. Q. Zhang, C. Z. Yu, B. Tu, D. Y. Zhao, Synthesis of ordered mesoporous carbon monoliths with bicontinuous cubic pore structure of Ia3d symmetry. *Chemical Communications*, 2842-2843 (2002).

49. A. Stein, F. Li, N. R. Denny, Morphological Control in Colloidal Crystal Templating of Inverse Opals, Hierarchical Structures, and Shaped Particles†. *Chem. Mat.* **20**, 649-666 (2007).

50. S. Kang, J. S. Yu, M. Kruk, M. Jaroniec, Synthesis of an ordered macroporous carbon with 62 nm spherical pores that exhibit unique gas adsorption properties. *Chemical Communications*, 1670-1671 (2002).

51. Z. B. Lei, Y. G. Zhang, H. Wang, Y. X. Ke, J. M. Li, F. Q. Li, J. Y. Xing, Fabrication of well-ordered macroporous active carbon with a microporous framework. *Journal of Materials Chemistry* **11**, 1975-1977 (2001).

52. J. S. Yu, S. B. Yoon, G. S. Chai, Ordered uniform porous carbon by carbonization of sugars. *Carbon* **39**, 1442-1446 (2001).

53. L. Chen, X. Wang, X. Zhang, H. Zhang, 3D porous and redox-active prussian blue-in-graphene aerogels for highly efficient electrochemical detection of $H_2O_2$. *Journal of Materials Chemistry* **22**, 22090-22096 (2012).

54. X. He, K. B. Male, P. N. Nesterenko, D. Brabazon, B. Paull, J. H. T. Luong, Adsorption and desorption of methylene blue on porous carbon monoliths and nanocrystalline cellulose. *ACS Appl. Mater. Interfaces* **5**, 8796-8804 (2013).

55. Y. Zhao, M.-b. Zheng, J.-m. Cao, X.-f. Ke, J.-s. Liu, Y.-p. Chen, J. Tao, Easy synthesis of ordered meso/macroporous carbon monolith for use as electrode in electrochemical capacitors. *Materials Letters* **62**, 548-551 (2008).

56. J. S. Beck *et al.*, A new family of mesoporous molecular-sieves prepared with liquid-crystal templates. *Journal of the American Chemical Society* **114**, 10834-10843 (1992).

57. C. T. Kresge, M. E. Leonowicz, W. J. Roth, J. C. Vartuli, J. S. Beck, Ordered mesoporous molecular-sieves synthesized by a liquid-crystal template mechanism. *Nature* **359**, 710-712 (1992).

58. Y. Wan, Zhao, On the Controllable Soft-Templating Approach to mesoporous silicates. *Chem. Rev.* **107**, 2821-2860 (2007).

59. Y. Meng, D. Gu, F. Q. Zhang, Y. F. Shi, H. F. Yang, Z. Li, C. Z. Yu, B. Tu, D. Y. Zhao, Ordered mesoporous polymers and homologous carbon frameworks: Amphiphilic surfactant templating and direct transformation. *Angew. Chem.-Int. Edit.* **44**, 7053-7059 (2005).

60. Y. Huang, H. Cai, D. Feng, D. Gu, Y. Deng, B. Tu, H. Wang, P. A. Webley, D. Zhao, One-step hydrothermal synthesis of ordered mesostructured carbonaceous monoliths with hierarchical porosities. *Chemical Communications*, 2641-2643 (2008).

61. F. Liu, C. Li, L. Ren, X. Meng, H. Zhang, F.-S. Xiao, High-temperature synthesis of stable and ordered mesoporous polymer monoliths with low dielectric constants. *Journal of Materials Chemistry* **19**, 7921-7928 (2009).

62. M. C. Gutierrez, F. Pico, F. Rubio, J. Manuel Amarilla, F. Javier Palomares, M. L. Ferrer, F. del Monte, J. M. Rojo, $PPO_{15}$-$PEO_{22}$-$PPO_{15}$ block copolymer assisted synthesis of monolithic macro- and microporous carbon aerogels exhibiting high conductivity and remarkable capacitance. *Journal of Materials Chemistry* **19**, 1236-1240 (2009).

63. C. Liang, S. Dai, Dual phase separation for synthesis of bimodal meso-/macroporous carbon monoliths. *Chem. Mat.* **21**, 2115-2124 (2009).

64. Y. Wang, S. Tao, Y. An, Superwetting monolithic carbon with hierarchical structure as supercapacitor materials. *Microporous Mesoporous Mat.* **163**, 249-258 (2012).

65. Z. Y. Wang, E. R. Kiesel, A. Stein, Silica-free syntheses of hierarchically ordered macroporous polymer and carbon monoliths with controllable mesoporosity. *Journal of Materials Chemistry* **18**, 2194-2200 (2008).

66. J.-P. Pascault, Rubber- and thermoplastic-modified polymer networks. Phase separation process induced by polymerization and polycondensation. *Macromolecular Symposia* **93**, 43-51 (1995).

67. J. Kiefer, H. H. Kausch, J. G. Hilborn, Synthesis of solvent-modified epoxies via Chemically Induced Phase Separation: A new approach towards void toughening of epoxies. *Polymer Bulletin* **38**, 477-483 (1997).

68. J. Kiefer, J. G. Hilborn, J. L. Hedrick, Chemically induced phase separation: a new technique for the synthesis of macroporous epoxy networks. *Polymer* **37**, 5715-5725 (1996).

69. N. Tonanon, A. Siyasukh, Y. Wareenin, T. Charinpanitkul, W. Tanthapanichakoon, H. Nishihara, S. R. Mukai, H. Tamon, 3D interconnected macroporous carbon monoliths prepared by ultrasonic irradiation. *Carbon* **43**, 2808-2811 (2005).
70. A. R. Ivanov, L. Zang, B. L. Karger, Low-attomole electrospray ionization MS and MS/MS analysis of protein tryptic digests using 20-μm-i.d. polystyrene−divinylbenzene monolithic capillary columns. *Analytical Chemistry* **75**, 5306-5316 (2003).
71. J. Biener, M. Stadermann, M. Suss, M. A. Worsley, M. M. Biener, K. A. Rose, T. F. Baumann, Advanced carbon aerogels for energy applications. *Energy Environ. Sci.* **4**, 656-667 (2011).
72. W. Zhang, H. Tao, B. Zhang, J. Ren, G. Lu, Y. Wang, One-pot synthesis of carbonaceous monolith with surface sulfonic groups and its carbonization/activation. *Carbon* **49**, 1811-1820 (2011).
73. A. C. Pierre, G. M. Pajonk, Chemistry of aerogels and their applications. *Chem. Rev.* **102**, 4243-4266 (2002).
74. H. Tamon, H. Ishizaka, M. Mikami, M. Okazaki, Porous structure of organic and carbon aerogels synthesized by sol-gel polycondensation of resorcinol with formaldehyde. *Carbon* **35**, 791-796 (1997).
75. H. Tamon, H. Ishizaka, T. Araki, M. Okazaki, Control of mesoporous structure of organic and carbon aerogels. *Carbon* **36**, 1257-1262 (1998).
76. R. W. Pekala, Organic aerogels from the polycondensation of resorcinol with formaldehyde. *J Mater Sci* **24**, 3221-3227 (1989).
77. A. M. ElKhatat, S. A. Al-Muhtaseb, Advances in tailoring resorcinol-formaldehyde organic and carbon gels. *Advanced Materials* **23**, 2887-2903 (2011).
78. D. Fairen-Jimenez, F. Carrasco-Marin, C. Moreno-Castilla, Inter- and intra-primary-particle structure of monolithic carbon aerogels obtained with varying solvents. *Langmuir* **24**, 2820-2825 (2008).
79. R. Sheldon, Catalytic reactions in ionic liquids. *Chemical Communications*, 2399-2407 (2001).
80. M. C. Gutierrez, M. L. Ferrer, C. Reyes Mateo, F. del Monte, Freeze-drying of aqueous solutions of deep eutectic solvents: a suitable approach to deep eutectic suspensions of self-assembled structures. *Langmuir* **25**, 5509-5515 (2009).
81. C. Gu, J. Tu, One-Step Fabrication of Nanostructured Ni Film with Lotus Effect from Deep Eutectic Solvent. *Langmuir* **27**, 10132-10140 (2011).
82. D. Carriazo, M. C. Gutierrez, M. Luisa Ferrer, F. del Monte, Resorcinol-based deep eutectic solvents as both carbonaceous precursors and templating agents in the synthesis of hierarchical porous carbon monoliths. *Chem. Mat.* **22**, 6146-6152 (2010).
83. M. C. Gutiérrez, F. Rubio, F. del Monte, Resorcinol-formaldehyde polycondensation in deep eutectic solvents for the preparation of carbons and carbon−carbon nanotube composites. *Chem. Mat.* **22**, 2711-2719 (2010).
84. N. Brun, C. A. Garcia-Gonzalez, I. Smirnova, M. M. Titirici, Hydrothermal synthesis of highly porous carbon monoliths from carbohydrates and phloroglucinol. *Rsc Advances* **3**, 17088-17096 (2013).

85. C. Moreno-Castilla, F. Carrasco-Marin, F. J. Maldonado-Hodar, J. Rivera-Utrilla, Effects of non-oxidant and oxidant acid treatments on the surface properties of an activated carbon with very low ash content. *Carbon* **36**, 145-151 (1998).

86. Y. Lv, F. Zhang, Y. Dou, Y. Zhai, J. Wang, H. Liu, Y. Xia, B. Tu, D. Zhao, A comprehensive study on KOH activation of ordered mesoporous carbons and their supercapacitor application. *Journal of Materials Chemistry* **22**, 93-99 (2012).

87. R. J. J. Jansen, H. van Bekkum, XPS of nitrogen-containing functional groups on activated carbon. *Carbon* **33**, 1021-1027 (1995).

88. J.-B. Lee, Y.-K. Park, O. B. Yang, Y. Kang, K.-W. Jun, Y.-J. Lee, H. Y. Kim, K.-H. Lee, W. C. Choi, Synthesis of porous carbons having surface functional groups and their application to direct-methanol fuel cells. *Journal of Power Sources* **158**, 1251-1255 (2006).

89. D. J. Malik, A. W. Trochimczuk, A. Jyo, W. Tylus, Synthesis and characterization of nanostructured carbons with controlled porosity prepared from sulfonated divinylbiphenyl copolymers. *Carbon* **46**, 310-319 (2008).

90. G. Hasegawa, K. Kanamori, K. Nakanishi, T. Hanada, Fabrication of activated carbons with well-defined macropores derived from sulfonated poly(divinylbenzene) networks. *Carbon* **48**, 1757-1766 (2010).

91. M. Kitano, K. Arai, A. Kodama, T. Kousaka, K. Nakajima, S. Hayashi, M. Hara, Preparation of a sulfonated porous carbon catalyst with high specific surface area. *Catalysis Letters* **131**, 242-249 (2009).

92. B. Hu, K. Wang, L. Wu, S.-H. Yu, M. Antonietti, M.-M. Titirici, Engineering carbon materials from the hydrothermal carbonization process of biomass. *Advanced Materials* **22**, 813-828 (2010).

93. M.-M. Titirici, M. Antonietti, N. Baccile, Hydrothermal carbon from biomass: a comparison of the local structure from poly- to monosaccharides and pentoses/hexoses. *Green Chem.* **10**, 1204-1212 (2008).

94. Y. Tao, M. Endo, K. Kaneko, Hydrophilicity-Controlled Carbon Aerogels with High Mesoporosity. *Journal of the American Chemical Society* **131**, 904-905 (2009).

95. S. Sepehri, B. B. Garcia, Q. Zhang, G. Cao, Enhanced electrochemical and structural properties of carbon cryogels by surface chemistry alteration with boron and nitrogen. *Carbon* **47**, 1436-1443 (2009).

96. N. Brun, S. A. Wohlgemuth, P. Osiceanu, M. M. Titirici, Original design of nitrogen-doped carbon aerogels from sustainable precursors: application as metal-free oxygen reduction catalysts. *Green Chem.* **15**, 2514-2524 (2013).

97. M. A. Worsley, P. J. Pauzauskie, T. Y. Olson, J. Biener, J. H. Satcher, Jr., T. F. Baumann, Synthesis of graphene aerogel with high electrical conductivity. *Journal of the American Chemical Society* **132**, 14067-14069 (2010).

98. M. A. Worsley, S. O. Kucheyev, J. D. Kuntz, T. Y. Olson, T. Y.-J. Han, A. V. Hamza, J. H. Satcher, Jr., T. F. Baumann, Carbon Scaffolds for Stiff and Highly conductive monolithic oxide-carbon nanotube composites. *Chem. Mat.* **23**, 3054-3061 (2011).

99. M. A. Worsley *et al.*, High surface area, sp(2)-cross-linked three-dimensional graphene monoliths. *Journal of Physical Chemistry Letters* **2**, 921-925 (2011).

100. X. Zhang, Z. Sui, B. Xu, S. Yue, Y. Luo, W. Zhan, B. Liu, Mechanically strong and highly conductive graphene aerogel and its use as electrodes for electrochemical power sources. *Journal of Materials Chemistry* **21**, 6494-6497 (2011).

101. Z. H. Tang, S. L. Shen, J. Zhuang, X. Wang, Noble-Metal-Promoted Three-dimensional macroassembly of single-layered graphene oxide. *Angew. Chem.-Int. Edit.* **49**, 4603-4607 (2010).

102. Y. Xu, Q. Wu, Y. Sun, H. Bai, G. Shi, Three-dimensional self-assembly of graphene oxide and DNA into multifunctional hydrogels. *ACS Nano* **4**, 7358-7362 (2010).

103. N. Leventis, N. Chandrasekaran, A. G. Sadekar, C. Sotiriou-Leventis, H. B. Lu, One-pot synthesis of interpenetrating inorganic/organic networks of CuO/resorcinol-formaldehyde aerogels: nanostructured energetic materials. *Journal of the American Chemical Society* **131**, 4576-+ (2009).

104. D.-W. Wang, F. Li, G. Q. Lu, H.-M. Cheng, Synthesis and dye separation performance of ferromagnetic hierarchical porous carbon. *Carbon* **46**, 1593-1599 (2008).

105. M. B. Dawidziuk, F. Carrasco-Marin, C. Moreno-Castilla, Influence of support porosity and Pt content of Pt/carbon aerogel catalysts on metal dispersion and formation of self-assembled Pt-carbon hybrid nanostructures. *Carbon* **47**, 2679-2687 (2009).

106. M. A. Worsley, J. D. Kuntz, P. J. Pauzauskie, O. Cervantes, J. M. Zaug, A. E. Gash, J. H. Satcher, Jr., T. F. Baumann, High surface area carbon nanotube-supported titanium carbonitride aerogels. *Journal of Materials Chemistry* **19**, 5503-5506 (2009).

107. T. Y.-J. Han, M. A. Worsley, T. F. Baumann, J. H. Satcher, Jr., Synthesis of ZnO coated activated carbon aerogel by simple sol-gel route. *Journal of Materials Chemistry* **21**, 330-333 (2011).

108. F. J. Maldonado-Hodar, C. Moreno-Castilla, J. Rivera-Utrilla, Y. Hanzawa, Y. Yamada, Catalytic graphitization of carbon aerogels by transition metals. *Langmuir* **16**, 4367-4373 (2000).

109. J. L. Bahr, J. M. Tour, Covalent chemistry of single-wall carbon nanotubes. *Journal of Materials Chemistry* **12**, 1952-1958 (2002).

110. A. M. T. Silva, B. F. Machado, J. L. Figueiredo, J. L. Faria, Controlling the surface chemistry of carbon xerogels using HNO3-hydrothermal oxidation. *Carbon* **47**, 1670-1679 (2009).

111. N. Mahata, M. F. R. Pereira, F. Suarez-Garcia, A. Martinez-Alonso, J. M. D. Tascon, J. L. Figueiredo, Tuning of texture and surface chemistry of carbon xerogels. *Journal of Colloid and Interface Science* **324**, 150-155 (2008).

112. V. Carralero Sanz, M. L. Mena, A. González-Cortés, P. Yáñez-Sedeño, J. M. Pingarrón, Development of a tyrosinase biosensor based on gold nanoparticles-modified glassy carbon electrodes: Application to the measurement of a bioelectrochemical polyphenols index in wines. *Anal. Chim. Acta* **528**, 1-8 (2005).

113. J. Matos, J. Laine, J. M. Herrmann, Synergy effect in the photocatalytic degradation of phenol on a suspended mixture of titania and activated carbon. *Applied Catalysis B-Environmental* **18**, 281-291 (1998).

114. G. Liu, J. Ma, X. Li, Q. Qin, Adsorption of bisphenol A from aqueous solution onto activated carbons with different modification treatments. *Journal of Hazardous Materials* **164**, 1275-1280 (2009).

115. I. Liska, Fifty years of solid-phase extraction in water analysis - historical development and overview. *J. Chromatogr. A* **885**, 3-16 (2000).

116. M. C. Hennion, Solid-phase extraction: method development, sorbents, and coupling with liquid chromatography. *J. Chromatogr. A* **856**, 3-54 (1999).

117. C. W. Huck, G. K. Bonn, Recent developments in polymer-based sorbents for solid-phase extraction. *J. Chromatogr. A* **885**, 51-72 (2000).

118. H. Alwael, D. Connolly, B. Paull, Liquid chromatographic profiling of monosaccharide concentrations in complex cell-culture media and fermentation broths. *Anal. Methods* **3**, 62-69 (2011).

119. E. Caro, R. M. Marcé, F. Borrull, P. A. G. Cormack, D. C. Sherrington, Application of molecularly imprinted polymers to solid-phase extraction of compounds from environmental and biological samples. *TrAC Trends in Analytical Chemistry* **25**, 143-154 (2006).

120. Z. Y. Zhang, J. Pawliszyn, Headspace solid-phase microextraction. *Analytical Chemistry* **65**, 1843-1852 (1993).

121. M. Valcarcel, S. Cardenas, B. M. Simonet, Y. Moliner-Martinez, R. Lucena, Carbon nanostructures as sorbent materials in analytical processes. *TrAC Trends in Analytical Chemistry* **27**, 34-43 (2008).

122. K. Scida, P. W. Stege, G. Haby, G. A. Messina, C. D. Garcia, Recent applications of carbon-based nanomaterials in analytical chemistry: Critical review. *Anal. Chim. Acta* **691**, 6-17 (2011).

123. E. P. Nesterenko, P. N. Nesterenko, D. Connolly, X. He, P. Floris, E. Duffy, B. Paull, Nano-particle modified stationary phases for high-performance liquid chromatography. *Analyst* **138**, 4229-4254 (2013).

124. A. Namera, A. Nakamoto, T. Saito, S. Miyazaki, Monolith as a new sample preparation material: Recent devices and applications. *Journal of Separation Science* **34**, 901-924 (2011).

125. A. Sato, M. Takeda, A simplified sample preparation technique for the analysis of off-flavor using Monotrap and TD-GC-MS-Olfactometry. *Kuki Seijo* **47**, 51-56 (2010).

126. T. Ikegami, N. Tanaka, Monolithic columns for high-efficiency HPLC separations. *Current opinion in chemical biology* **8**, 527-533 (2004).

127. H. Colin, G. Guiochon, A. Stouffi, Comparison of various systems for the separation of free sterols by high performance liquid chromatography. *Analytical Chemistry* **51**, 1661-1666 (1979).

128. M. Diack, G. Guiochon, Adsorption-isotherm and overloaded elution profiles of phenyldodecane on porous carbon in liquid-chromatography. *Analytical Chemistry* **63**, 2608-2613 (1991).

129. A. Vinu, M. Miyahara, V. Sivamurugan, T. Mori, K. Ariga, Large pore cage type mesoporous carbon, carbon nanocage: a superior adsorbent for biomaterials. *Journal of Materials Chemistry* **15**, 5122-5127 (2005).

130. A. Vinu, K. Z. Hossain, G. S. Kumar, K. Ariga, Adsorption of L-histidine over mesoporous carbon molecular sieves. *Carbon* **44**, 530-536 (2006).

131. A. Vinu, M. Miyahara, T. Mori, K. Ariga, Carbon nanocage: a large-pore cage-type mesoporous carbon material as an adsorbent for biomolecules. *Journal of Porous Materials* **13**, 379-383 (2006).

132. C. Robertson, R. Mokaya, Microporous activated carbon aerogels via a simple subcritical drying route for CO2 capture and hydrogen storage. *Microporous Mesoporous Mat.* **179**, 151-156 (2013).

133. H. Kabbour, T. F. Baumann, J. H. Satcher, Jr., A. Saulnier, C. C. Ahn, Toward new candidates for hydrogen storage: High-surface-area carbon aerogels. *Chem. Mat.* **18**, 6085-6087 (2006).

134. B. J. Bassler, R. A. Hartwick, The application of porous graphitic carbon as an HPLC stationary phase. *J. Chromatogr. Sci.* **27**, 162-165 (1989).

135. L. K. Liem, L. H. L. Choong, K. T. Woo, Porous graphitic carbon shows promise for the rapid screening partial DPD deficiency in lymphocyte dihydropyrimidine dehydrogenase in Chinese, Indian and Malay in Singapore by using semi-automated HPLC-radioassay. *Clinical Biochemistry* **35**, 181-187 (2002).

136. K. Koizumi, High-performance liquid chromatographic separation of carbohydrates on graphitized carbon columns. *J. Chromatogr. A* **720**, 119-126 (1996).

137. O. Gyllenhaal, A. Karlsson, Enantiomeric separations of amino alcohols by packed-column SFC on Hypercarb with L-(+)-tartaric acid as chiral selector. *Journal of Biochemical and Biophysical Methods* **54**, 169-185 (2002).

138. O. Gyllenhaal, A. Karlsson, Evaluation conditions for SFC of metoprolol and related amino alcohols on Hypercarb (porous graphitic carbon) with respect to structure-selectivity relations. *Chromatographia* **71**, 7-13 (2010).

139. J. H. Knox, Q. H. Wan, Chiral chromatography of amino-acids and hydroxy-acids on surface-modified porous graphite. *Chromatographia* **40**, 9-14 (1995).

140. A. Wutte, G. Gubitz, S. Friebe, G. J. Krauss, High-performance liquid-chromatography of cis-trans isomers of proline-containing dipeptides: III. Comparative-studies with different stationary phases. *J. Chromatogr. A* **677**, 186-191 (1994).

141. J. C. Reepmeyer, J. F. Brower, H. P. Ye, Separation and detection of the isomeric equine conjugated estrogens, equilin sulfate and Delta(8,9)-dehydroestrone sulfate, by liquid chromatography-electrospray-mass spectrometry using carbon-coated zirconia and porous graphitic carbon stationary phases. *J. Chromatogr. A* **1083**, 42-51 (2005).

142. M. J. Davies, K. D. Smith, R. A. Carruthers, W. Chai, A. M. Lawson, E. F. Hounsell, Use of a porous graphitized carbon column for the high-performance liquid-chromatography of oligosaccharides, alditols and glycopeptides with subsequent mass-spectrometry analysis. *Journal of Chromatography* **646**, 317-326 (1993).

143. J. Q. Fan, A. Kondo, I. Kato, Y. C. Lee, High-performance liquid-chromatography of glycopeptides and oligosaccharides on graphitized carbon columns. *Analytical Biochemistry* **219**, 224-229 (1994).

144. Y. B. S. Côme, H. Lalo, Z. Wang, G.-W. Kohring, R. Hempelmann, M. Etienne, A. Walcarius, A. Kuhn, Interest of the sol-gel approach for multiscale tailoring of porous bioelectrode surfaces. *Electroanalysis* **25**, 621-629 (2013).

145. C.-Z. Lai, M. A. Fierke, A. Stein, P. Buehlmann, Ion-selective electrodes with three-dimensionally ordered macroporous carbon as the solid contact. *Analytical Chemistry* **79**, 4621-4626 (2007).

146. N. Brun, L. Edembe, S. Gounel, N. Mano, M. M. Titirici, Emulsion-templated macroporous carbons synthesized by hydrothermal carbonization and their application for the enzymatic oxidation of glucose. *Chemsuschem* **6**, 701-710 (2013).

147. F. Rodriguez-Reinoso, The role of carbon materials in heterogeneous catalysis. *Carbon* **36**, 159-175 (1998).

148. M. Sevilla, L. Yu, T. P. Fellinger, A. B. Fuertes, M.-M. Titirici, Polypyrrole-derived mesoporous nitrogen-doped carbons with intrinsic catalytic activity in the oxygen reduction reaction. *Rsc Advances* **3**, 9904-9910 (2013).

149. N. S. Ergang, M. A. Fierke, Z. Wang, W. H. Smyrl, A. Stein, Fabrication of a fully infiltrated three-dimensional solid-state interpenetrating electrochemical cell. *Journal of the Electrochemical Society* **154**, A1135-A1139 (2007).

150. Z. Y. Wang, N. S. Ergang, M. A. Al-Daous, A. Stein, Synthesis and characterization of three-dimensionally ordered macroporous carbon/titania nanoparticle composites. *Chem. Mat.* **17**, 6805-6813 (2005).

# Chapter 2

# Fullerene C$_{60}$ Modified Silica Template

*"Do not fear mistakes. You will know failure. Continue to reach out."*

Benjamin Franklin

## Abstract

There are a number of ways to prepare fullerene $C_{60}$-functionalised silica which are presented in the literature. In this Chapter, a facile synthetic method was developed and optimised to synthesise $C_{60}$ modified silica (FMS) gels. They were prepared by direct amine addition between 3-aminopropyl silica (APS) with different particle sizes (1.38, 3 and 5 μm) and pristine $C_{60}$. Field emission SEM imaging of FMS revealed the nanoparticle coverage and size distribution, together with BET surface area analysis to probe the effect of $C_{60}$ nanoparticle grafting upon aminated silica morphology. Elemental analysis showed that batch to batch carbon loading was on average 16.0% and consequently predicted that the exact chemical structure of FMS was 2 ethylmethoxy substituents which were bonded to silica (5 μm) and that 1 ethylmethoxy substituent was unbonded after amination. This $C_{60}$ coverage was $1.937 \times 10^{-4}$ mol/g and reproducible from batch to batch with variation of $< 4\%$. The Fourier transform infrared (FT-IR) spectra further confirmed the covalent attachment and showed the signature peaks from both $C_{60}$ and aminated silica (5 μm) appeared in resultant brown particles with a slight shift in wavenumber. In addition, the hydrophobicity of FMS was increased significantly after $C_{60}$ modification which was shown by a change in contact angle measurement from $23^{o}$ to $108^{o}$. Finally, reversed-phase high performance liquid chromatography (RP-HPLC) was used as a characterisation tool for confirmation of covalent attachment of $C_{60}$ to APS (5 μm), using a series of aromatic compounds. The FMS stationary phase showed mechanical and chemical stability as well as different retention behaviour from a conventional octadecyl silica phase. 5 μm FMS was considered as the ideal $C_{60}$ functionalised silica template to be used as a nano- template.

## Aim

The aim of this work was to develop a facile synthetic method for preparation of FMS and confirm the covalent attachment between $C_{60}$ and aminated silica gels by various physiochemical characterisation techniques. The coverage of $C_{60}$ on the aminated silica had to be optimised and reproducible for use as a hard template for fabrication of carbon monolithic materials, as discussed in Chapter 3.

## 2.1 Introduction

Since the discovery of fullerenes by Kroto *et al.,* in 1985 [1], their unique structure and properties have attracted much interest within the field of analytical chemistry. The isolation and purification of fullerenes from carbon soot mixtures has always been a key procedure for obtaining these interesting compounds prior to their use in various applications [2]. HPLC is proving to be the most promising method among various proposed separation methods to separate $C_{60}$ and $C_{70}$ from carbon soots. Relatively soon after their first discovery, the retention behaviours of fullerenes in LC on various chemically bonded stationary phases was studied, and even more over the last decade [2-4]. The results have clearly indicated that phenyl ligand(s) bonded phases can interact effectively with these solutes through $\pi$-$\pi$ interactions [5].

The above earlier studies showed $C_{60}$ has specific features and dimensions, and its immobilisation onto the surface of silica or polymer particles provides novel chromatographic materials with electron-donating and –accepting surface interactions similar to those of aromatic carbons [6]. Thus, there has been growing interest in fullerene/silica hybrid materials as stationary phases for LC [7, 8] and GC [9, 10] as well as SPE [11, 12]. The interest in such hybrid materials is not limited to chromatography but also includes the potential applications in photo-electrochemistry [13] and in the advanced electronics field including photovoltaic cells, photodiodes and sensors [14].

## 2.2 Synthetic methods of $C_{60}$ bonded silica stationary phases

$C_{60}$ is a hollow cluster consisting of 60 carbons and it is the most symmetrical large molecule known. $C_{60}$ has only $sp^2$ hybridised carbon atoms, similar to graphite, but instead of being arranged in layers, these carbons are arranged in rings and fitted together like seams of a soccer ball [15, 16]. This configuration is responsible for their electrical conductivity, and their capacity to form charge-transfer complexes with compounds containing electron-acceptor groups [17]. However, this configuration is also responsible for the development of strong van der Waals' forces,

which significantly affects dispersion and solubility in water and organic solvents [18]. The simplest approach to the preparation of a $C_{60}$/silica hybrid material for use as a photo-oxidation catalyst is by impregnation of silica with $C_{60}$ [19]. Such a technique ensures only a physical adsorption of the fullerenes inside or outside a silica matrix. Those fullerenes can be easily extracted from the surface of silica by a suitable organic solvent. Accordingly, such hybrid material can really only be used in an aqueous environment. There are a number of more sophisticated synthetic approaches regarding the chemical bonding of $C_{60}$ on a silica surface. Fullerene modified stationary phases prepared for LC need to be reproducible, have high coverage of fullerene, stable binding with silica support and a narrow size distribution [8, 20, 21]. The fullerene modified silica gels (FMS) used as a hard template for fabrication of carbon monolith will be discussed in Chapter 3. Meanwhile, it is crucial to understand these approaches from the aspects of basic chemistry of $C_{60}$ fullerenes.

## 2.2.1 Basic $C_{60}$ Chemistry

Each $C_{60}$ molecule has 32 interlocking rings which are arranged to form 20 isolated hexagons and 12 pentagons [1]. All the rings are fused and all the double bonds are conjugated. $C_{60}$ and its derivatives are quite stable but not totally unreactive. It would appear to be aromatic because of its benzene-like rings' structure at first glance. However, it tends to undergo mainly electrophilic addition and cycloaddition reaction instead of electrophilic substitution reactions [14]. A myriad of $C_{60}$-based molecules, as well as many related materials have been produced using these reactions, e.g. Bingel, Bingel-Hirsch, Prato and azoalkane cycloaddition reactions [22]. The chemical reactivity of $C_{60}$ is typical of an electron-deficient olefin. $C_{60}$, in fact, reacts readily with nucleophiles and is a reactive 2p component in cycloadditions. The vast majority of reactants will attack the 6.6 ring junctions of $C_{60}$, which possess more electron density as shown in Figure 2. [17]. In most cases, the new derivatives retain the main properties of the original fullerene.
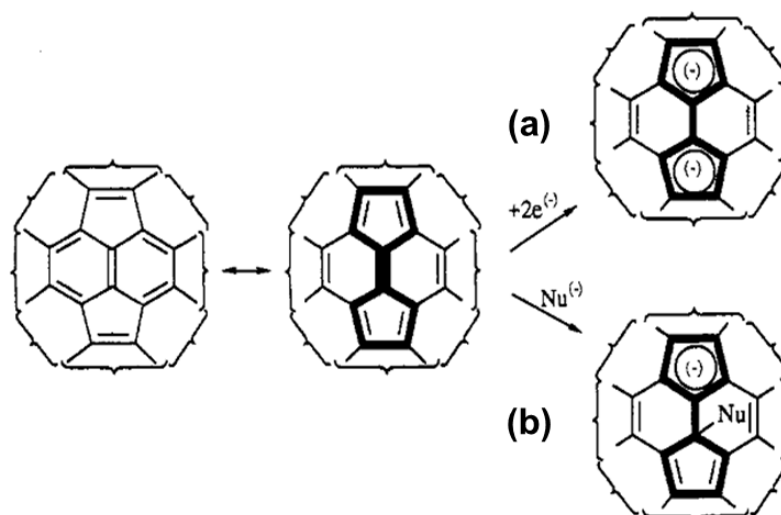
*Figure 2.1:* *Schematic of a pyracyclene unit (4nπ) in C$_{60}$ capture of up to two electrons either by (a) direct electron transfer to give a 4n + 2 π electron dianion or (b) in the form of a lone pair to give a "cyclopentadienide" monoadduct (Reproduced from [17]).*

## 2.2.2 Synthetic approaches

There are two ways to incorporate C$_{60}$ onto silica, namely functionalising the silica surface in order to react with C$_{60}$, or alternatively, functionalising both silica and C$_{60}$, so they can selectively react together.

Jinno and co-worker were the first group that introduced a C$_{60}$ bonded silica as a stationary phase for LC and evaluated the retention behaviour of various polyaromatic hydrocarbons (PAHs) [23-25]. C$_{60}$ silylmethyl was prepared by addition of a Grignard reagent, then refluxed with bare silica in the presence of pyridine or xylene [25]. The structures of these phases are shown in Figure 2.2. Their results reported not only demonstrated a different selectivity for PAHs to that of monomeric type ODS in reversed-phase LC, but also showed how retention behaviour varied among these phases. Interestingly, C-high, 2-leg type (Figure 2.2 (A)) and C-high (Figure 2.2 (B)) C$_{60}$ phases showed a molecular planarity recognition capability for these isomeric PAHs by π-π interaction, i.e. planar PAHs having a partial structure similar to that of the C$_{60}$ molecule, were retained longer than the non-planar solutes, although C$_{60}$ is spherical [26, 27]. Meanwhile, C-low, 2-leg type (Figure 2.2 (C)) and C-low, 1-leg type (Figure 2.2 (D)) did not possess such capability at all [2].
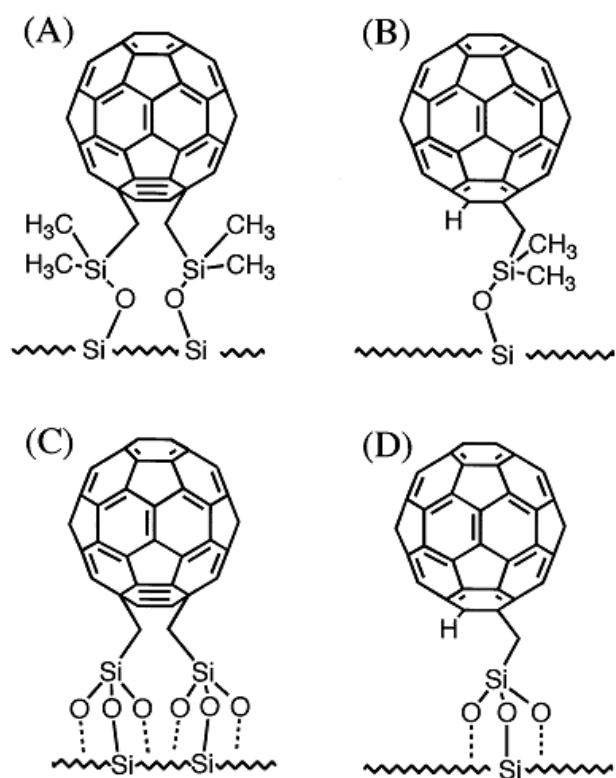
**Figure 2.2:** *Structure of the C$_{60}$ bonded phases (A) C-high, 2-leg type; (B) C-high, 1-leg type; (C) C-low, 2-leg type; and (D) C-low, 1-leg type (Reproduced from [25]).*

Another approach by Vallant *et al.* used the reaction of 3-aminopropyl silica with different functionalised fullerenes [11]. Figure 2.3 shows reaction schematics for reactions of (A) C$_{60}$-fullerenoacetic acid and (B) C$_{60}$-epoxyfullerene with APS through simple condensation and nucleophilic reaction respectively [11]. The group were the first to apply the resultant materials as an alternative to commercially available reversed-phase solid phase extraction sorbent for desalting and pre-concentration of proteins and peptide, especially phosphopeptides [11].
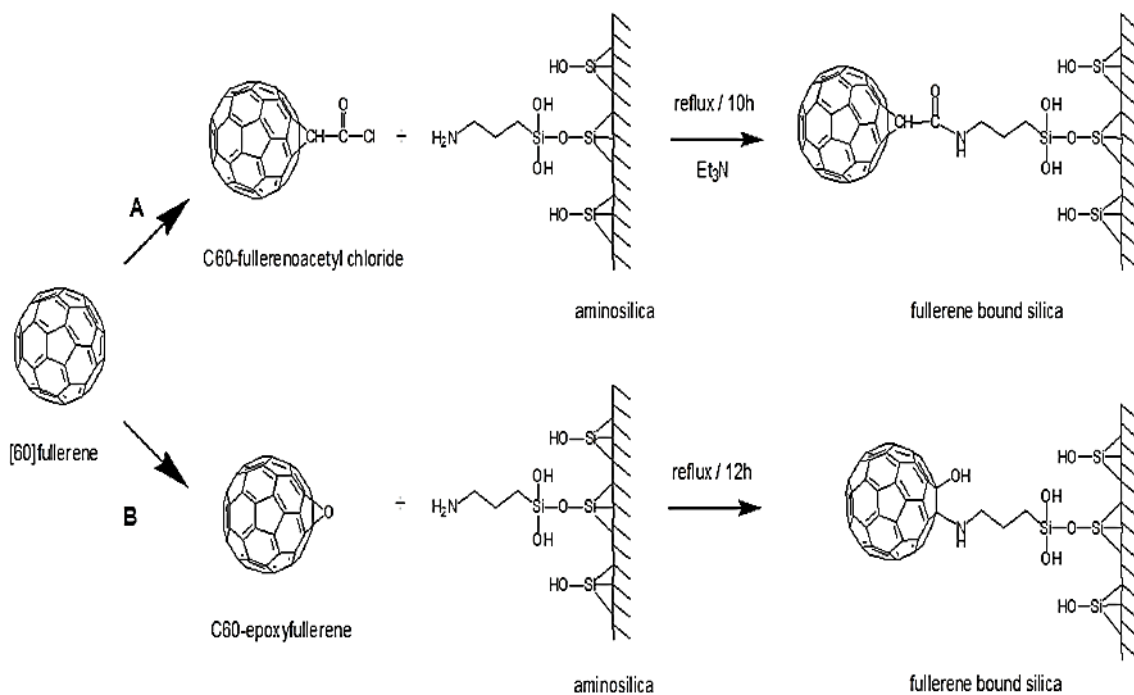
***Figure 2.3:*** *Reaction scheme showing the synthesis of fullerene-bonded silica, using (A) $C_{60}$-fullerenoacetic acid and (B) $C_{60}$-epoxyfullerene as starting material (Reproduced from [11]).*

Amine addition is another common approach. Cheng *et al.* prepared their $C_{60}$ stationary phases by simple reaction of $C_{60}$ and APS in the presence of anhydrous toluene at room temperature for 72 h under argon gas [7, 28]. Later this stationary phase was used for the separation of quinines [7] and high energetic nitroaromatic compounds [28]. Miller reviewed the reaction between aliphatic amines and $C_{60}$ and suggested that hydroaminations prefer either a 1,2- or 1,4- addition [29].

In the following Chapter, a facile synthetic method is described, which was developed and optimised to synthesise $C_{60}$ modified silica, prepared by direct amine addition between APS and pristine $C_{60}$. The covalent attachment of $C_{60}$ to aminated silica was successfully achieved as a result, confirmed by various physical and chemical characterisation techniques. Later, this FMS also served as a carbonaceous nanoparticle functionalised template for the preparation of porous carbon monoliths for adsorption and electrochemical applications, which are described in Chapter 3.

## 2.3 Experimental

### 2.3.1 Reagents and materials

$C_{60}$ Fullerene (98 wt.%), 3-aminopropyltriethoxysilane (APTES) (99 wt.%, 0.946 g/mL at 25 ℃), ammonium hydroxide ($NH_4OH$) solution (28 - 30.0 wt.%), methanol ACS reagent ($\geqslant$ 99.5 wt.%), toluene ACS reagent ($\geqslant$ 99.5 wt.%), anthracene ($\geqslant$ 99 wt.%), $p$-xylene anhydrous ($\geqslant$ 99 wt.%), benzene ($\geq$ 99.9 wt.%), phenol ($\geqslant$ 99 wt.%), naphthalene (98 wt.%) and toluene anhydrous (99.8 wt.%) were obtained from Sigma-Aldrich (Dublin, Ireland). Methanol (HPLC grade, 99.9 wt.%) and 2-propanol (HPLC grade, 99.9 wt.%) were purchased from Fisher Scientific (Dublin, Ireland). Three different types of silica templates, denoted as 1.38 μm, 3 μm and 5 μm respectively, were used. 1.38 μm 3-aminopropyl nonporous silica beads (surface area of 5 $m^2$/g, 1 mmol/g amino- group) and 3 μm silica gels (surface area of 220 $m^2$/g and pore size of 75 Å) were obtained from ISSC group (University of Cork, Ireland), and 5 μm silica gels (surface area of ~ 94.83 $m^2$/g and pore size of 15.98 nm) were supplied by Prof. Peter Myers (University of Liverpool). Deionised water (18.2 MΩ·cm) was obtained from a Milli-Q water purification system (Millipore, Ireland) water purification system. All mobile phases were filtered and degassed prior to use. All reagents were of analytical grade and used as received and without purification.

### 2.3.2 Instrumentation

Fullerene modified silica templates (FMS) were prepared using a Yellowline MST basic hotplate stirrer with temperature control probe and an IKA® RW 20 digital mechanical overhead stirrer from IKA®-Werke GmbH & Co. KG (Staufen, Germany) with a small magnetic bar (12 mm in length, 4.5 mm in diameter, PTFE coated) from Sigma-Aldrich (Dublin, Ireland). A SupelcoTM nylon membrane (0.45 μm pore size, diam. 47 mm) from Sigma-Aldrich (Dublin, Ireland) was placed in a Büchner funnel for filtration of silica particles. An EHRET thermovacuum oven from Ehret Labor and Pharmatechnik GmbH, KG (Emmendingen, Germany) was used to dry the silica particles. The surface morphology of the FMS was examined using a field emission Hitachi S-5500 scanning electron microscope (FE-SEM) (Dallas, TX, USA) at an accelerating voltage of 20 kV, providing for achieving high-resolution SEM images

of the silica surface. A surface area analyser, model TriStar II 3020 (Micromeritics Gemini, Georgia, USA) was used to measure the specific surface area and the pore volume using the nitrogen adsorption/desorption technique. A Perkin-Elmer Spectrum 100 FT-IR spectrometer (Santa Clara, CA, USA) was used for collecting attenuated total reflectance Fourier transform infrared spectra (ATR-FTIR). Elemental analysis was performed on a CE440 Elemental Analyser from Exeter Analytical (Coventry, UK). Contact angle measurements of FMS were performed using a FTÅ200 dynamic contact angle analyser (Portsmouth, VA, USA). A Waters 2965 liquid chromatography system equipped with a Waters 2487 spectrophotometric UV detector (Milford, MA, USA) was used for HPLC evaluations. The system management and data collection was controlled by Waters Empower™ 1 Chromatography Software. The in-house prepared FMS column was packed using a stirred slurry Model CPP-085 reservoir (Chemco Econo-Packer, Osaka, Japan).

## 2.3.3 Characterisation of FMS

The preparation of a silica FE-SEM sample involved depositing a drop (15 $\mu$L) of 1 mg/$\mu$L silica suspension in methanol onto the grid and allowing the solvent to evaporate prior to imaging. The suspension was sonicated for 15 min prior to casting. Typically, 20 mg of FMS was dried at 120 $^{\circ}$C under vacuum for 16 h to remove any physically adsorbed moisture before nitrogen adsorption/desorption analysis. It was then loaded into the apparatus for measurement. The specific surface area values were calculated according to the BET equation at $P/P_0$ between 0.05 and 0.2 [30]. The pore parameters (pore volumes and pore diameters) were evaluated from the desorption branches of isotherms based on Barrett–Joyner–Halenda (BJH) model. The values obtained were derived from the BET isotherm using supporting software with the instrument. The FT-IR spectra were obtained from 4 scans with a resolution of 2 cm$^{-1}$ in the spectral region of 650 – 4000 cm$^{-1}$. A background measurement was taken before the sample was loaded onto the ATR unit for measurements. Typically, 10 mg of dried sample was used for elemental analysis. The preparation of silica contact angle sample involved 1 mg/$\mu$L of silica suspension in methanol coated a glass slide and dried at 40 $^{\circ}$C in the oven for 1 hour before test and then depositing a droplet (30 $\mu$L) onto the surface of the glass slide.

## 2.3.4 Column packing and HPLC evaluation

2 mL of 0.1 g/mL of FMS (5 $\mu$m) suspension in isopropanol was packed in 5 mm × 2 mm I.D. stainless steel column. The column was packed in the ascending direction and then eluted with methanol at *ca.* 6000 psi.

All separations were carried out at ambient temperature, 1 $\mu$L of injection volume, flow rate of 0.2 mL/min and run time of 10 min in isocratic mode. The UV detector was operated at 254 nm. The column retention behaviour study was tested with 5 different ratios of methanol:water (80:20, 70:30, 60:40, 50:50 40:60 (v/v), respectively) as the mobile phase. The back pressure of FMS at equilibrium was 273 psi with 80 % methanol as mobile phase. The separation of a six aromatic mixture was performed using 40: 60, methanol:10 mM phosphoric acid (pH 2.6).  Individual stock solutions of 1000 ppm toluene, anthracene, *p*-xylene, benzene, phenol and naphthalene were prepared in methanol. Then each analyte was diluted to 100 ppm using 100 % methanol as diluent for the column retention behaviour study. A mixture containing six aromatic compounds was prepared by mixing 100 μL of each individual stock solution together and then diluted to 10 mL with 40:60 methanol : 10 m*M* phosphoric acid.

## 2.3.5 Preparation of fullerene modified silica templates

The chemical modification of the silica surface with $C_{60}$ was carried out using a standard coupling procedure, as shown in Scheme 2.1 [7, 31]. The silica gel was first reacted with APTES and the resulting aminated silica (APS) was then linked to fullerene $C_{60}$ under the described conditions to form $C_{60}$ modified silica (FMS).

***Scheme 2.1:*** *Preparation of $C_{60}$ modified APS.*
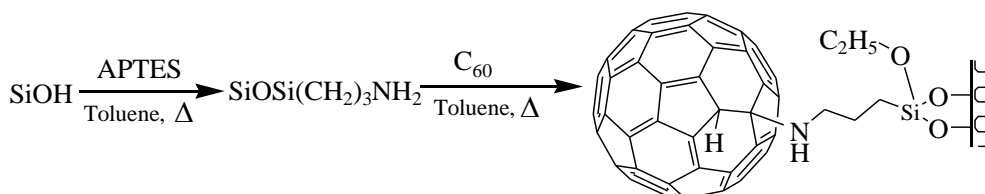
### 2.3.5.1. Hydroxylation of silica

Silica gel had to be activated before use which was first subjected to drying at 120 °C and 0.0015 psi in a vacuum oven for 16 h. The silica gel (~1.5 g) was then added to 30 mL of 10 v/v % $NH_4OH$ aqueous solution and sonicated for 10 min. The suspension was then refluxed for 6 h, and filtered with the nylon membrane. The silica gel was then washed with deionised water until the pH of filtrate was neutral. The hydrolysed silica gel was then oven dried at 80 °C for 16 h and kept in a desiccator.

### 2.3.5.2. Amination of silica

~ 1.2 g of the hydrolysed silica beads was reacted with 10 v/v% APTES (0.057 moles) in 100 mL anhydrous toluene under reflux for 5 h (110 °C). The silica gel was then filtered through a nylon membrane (0.45 $\mu$m pore size) and washed with toluene and methanol (30 mL each), respectively. The resulting APS was oven dried at 80 °C for 16 h and kept in a desiccator. The concentration of the amino groups on the silica was estimated from elemental analysis, results of which are presented in Section 2.4.4 [32].

### 2.3.5.3. Synthesis of fullerene $C_{60}$ modified silica

Fullerene $C_{60}$ (0.3 g, 0.5 moles equivalent to theoretical no. of amino groups on the surface of silica) was mixed with 1.0 g of aminated silica in a 250 mL round-bottomed flask containing 100 mL of toluene anhydrous. After sonicating for 10 min, the reaction mixture was refluxed for 16 h under continuous flow of nitrogen gas. The crude FMS was then filtered with a nylon membrane. FMS was then transferred into a thimble for soxhlation with 100 mL of toluene until the filtrate was colourless followed by chloroform and methanol (30 mL each), respectively. These obtained FMS particles were oven dried at 80 °C for 16 h and kept in a desiccator.

## 2.4 Results and discussion

### 2.4.1 Preparation of fullerene modified silica templates

Theoretically, there are 4.6 OH groups per $nm^2$ [33]. The calculation of the number of moles of APTES required for a bonding was performed as follows:

$$n = \frac{N}{N_A}$$

where n is the amount of substance (unit mole), $N$ is the nnumber of molecules or atoms, $N_A$ is Avogadro constant and expresses the number of elementary entities per mole of substance and it has the value $6.023 \times 10^{23}$/mol, and 4.6 OH groups / $nm^2$ can be convert to $4.6 \times 10^{18}$ OH groups/$m^2$.

$$n = \frac{4.6 \times 10^{18}}{6.023 \times 10^{23}} = 7.64 \times 10^{-6} \ moles / m^2$$

As an example, for 3 μm diameter silica beads with a surface area of 220 $m^2$ / g, the number of moles of OH per gram can be calculated as follows:

$7.64 \times 10^{-6}$ moles / $m^2 \times 220$ $m^2$ / g = $1.681 \times 10^{-3}$ moles/g ~ 1.681 mmol per 1 g of silica. Multiplied by the weight of silica it gives the total number of moles of silanol groups on the surface of the desired amount of silica.

Since the molar ratio of -$NH_2$ to -OH is 1:1 and $C_{60}$ to $NH_2$- is 0.5:1, 0.417 mmol of fullerene require 0.834 mmol of -$NH_2$. Therefore the gram mass of APS needed to fully react with 0.417 mmol = 0.834 mmol / 1.681 mmols/g = 0.496 g. As a result it is possible to calculate the amount of the reagent needed to modify the available silanol groups on the surface and all further calculations for modification reaction can be done using this data.

As FMS was to be used as a template for the introduction of $C_{60}$ into the macroporous wall structure during fabrication of carbon monoliths (see Chapter 3), it was crucial to choose a template which was homogeneous in size for creation of macropores and which had reasonable surface area for sufficient loading capacity of

C$_{60}$. Within the availability of both nonporous and porous materials, in-house prepared and commercially available HPLC grade silica gels were used for comparison purposes. 3 μm silica beads showed the greatest initial surface area (Table 2.2). Several adaptations were made to this preparation method which were slightly different to the literature methods [7, 31], for maximising the surface coverage of C$_{60}$. The hydroxylation step was also vital for the improvement of surface ligand loading density. H$_2$O, NH$_4$OH and HCl are the common solvents used to hydrolyse silica surfaces. 10% NH$_4$OH was chosen for hydroxylation. Ordinary grade toluene was chosen for amination of the silica because it contains approximately 0.5% H$_2$O in order to prevent the self-condensation of APTES.

***Table 2.2:*** *Reaction compositions used for the preparation of FMS$^a$ (n = 3).*

| Type and silica | APS [g] Theoretical no. of mmol of NH$_4$- /g | Amount of C$_{60}$ | % yield |
|---|---|---|---|
| 1.38 μm aminated silica beads (5 m$^2$/g, 1 mmol/g NH$_2$- groups) | ~ 1 0.834 | 0.3 g, 0.417 mmol | 98% ( 1.27 g) |
| 3 μm silica beads (220 m$^2$/g) | ~ 0.496 1.681 | 0.3 g, 0.417 mmol | 96% (0.768 g) |
| 5 μm aminated silica beads (95 m$^2$/g) | ~ 1.149 g, 0.7258 | 0.3g, 0.417 mmol | 95% (1.092 g) |

$^a$ per 100 mL of anhydrous toluene.

To optimise the reaction, various reaction conditions were attempted, including performing the process in dark or under light, with or without nitrogen, reflux or room temperature, toluene anhydrous or normal grade toluene, and magnetic stirring bar or overhead mechanical stirrer. These details have not been previously mentioned in the literature [7, 31]. Anhydrous toluene was chosen as a reaction media, being the most common solvent for C$_{60}$ functionalisation. The solubility of C$_{60}$ in toluene is only 3 mg/mL [34]. Thus with the same amount of C$_{60}$ present in the reaction, the silica which has a higher surface area will yield a lesser amount of FMS, as shown in Table 2.2, i.e. 3 μm silica beads are expected to have the highest loading density. This prediction was further investigated by FE-SEM (see Section 2.3.2).

Theoretically, the yield should be 100% for solid phase synthesis, but actually silica gel is a fine powder and it is hard to prevent loss during transfer.

The theoretical molar ratio of $C_{60}$ to amine group on silica was 0.5:1, where $C_{60}$ was in considerable excess, and after the reaction there was still $C_{60}$ in the reaction mixture. $C_{60}$ is a highly photosensitive molecule and has a rich photochemistry. In the above thermal addition reaction for FMS synthesis, the round bottom flask was exposed to light within a laboratory fume hood in order to speed up the reaction [29]. It was noticed that the colour change (from purple to reddish brown) for the reaction took longer in the dark (flask was wrapped in aluminium foil). $C_{60}$ is also very reactive under certain conditions, as discussed in Section 2.3.5.3. In order to avoid the reaction with oxygen from the air, inert gaseous conditions were needed and an overhead mechanical stirrer cannot be used due to the special glassware required. Instead a standard reflux setup was used for the reaction. Furthermore, the presence of water in toluene can also act as interference. Following many repeat runs, the reaction conditions for producing a high surface coverage FMS were identified as follows: reflux in anhydrous toluene, under continuous flow nitrogen, with the use of a small magnetic bar, with low revolution per minute in order to prevent crashing of the silica particles and operation under lab light.

## 2.4.2 Morphology

Since the size of single $C_{60}$ molecules is only ~ 0.8 nm and its cluster in organic solvent is approximately 10 nm [35], FE-SEM was used for higher resolution SEM imaging to attempt to visualise the nanometre scale species on the surface of the silica particles. The morphology of the 1.38 $\mu$m, 3 $\mu$m and 5 $\mu$m FMS was examined by FE-SEM in order to investigate the presence of covalently attached $C_{60}$ on the APS surface, as well as silica particle size distribution, as shown in Figure 2.4 (a) – (d), (e) – (h), and (i) – (l), respectively. There were some slight indications of the presence of $C_{60}$ on the surface of both nonporous and porous silica templates for all products obtained. There is a *ca.* 400 nm cluster on the surface of nonporous silica (Figure 2.4(b) – (d)) but no observation of any individual $C_{60}$ due to the limitation of the resolution on the FE-SEM. For porous silica shown in Figure 2.4(g) and (h), there is a less than 50 nm semi-transparent uneven layer on the edge of porous silica

which was deemed to be grafted $C_{60}$ which was further examined and confirmed by ATR-FTIR and elemental analysis. The phase contrast from typical amorphous silica support often confuses the search for particles with diameters below 1 nm [36]. High resolution transmission electron microscopy or TEM could be a better electron microscopic technique to measure the size of an individual fullerene molecule [35]. 5 μm of FMS (Figure 2.4(i) – (l)) showed the best particle size distribution among the three FMSs. Therefore, 5 μm FMS was considered as the ideal $C_{60}$ functionalised silica template to be used later.
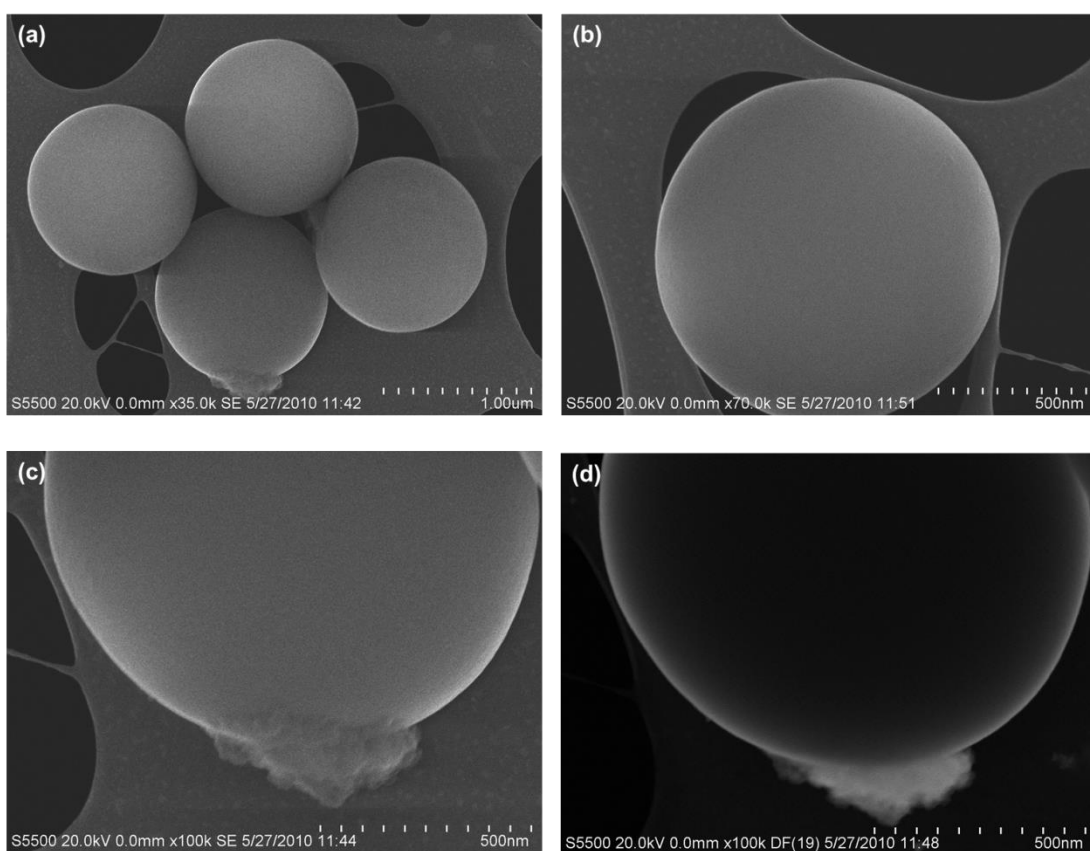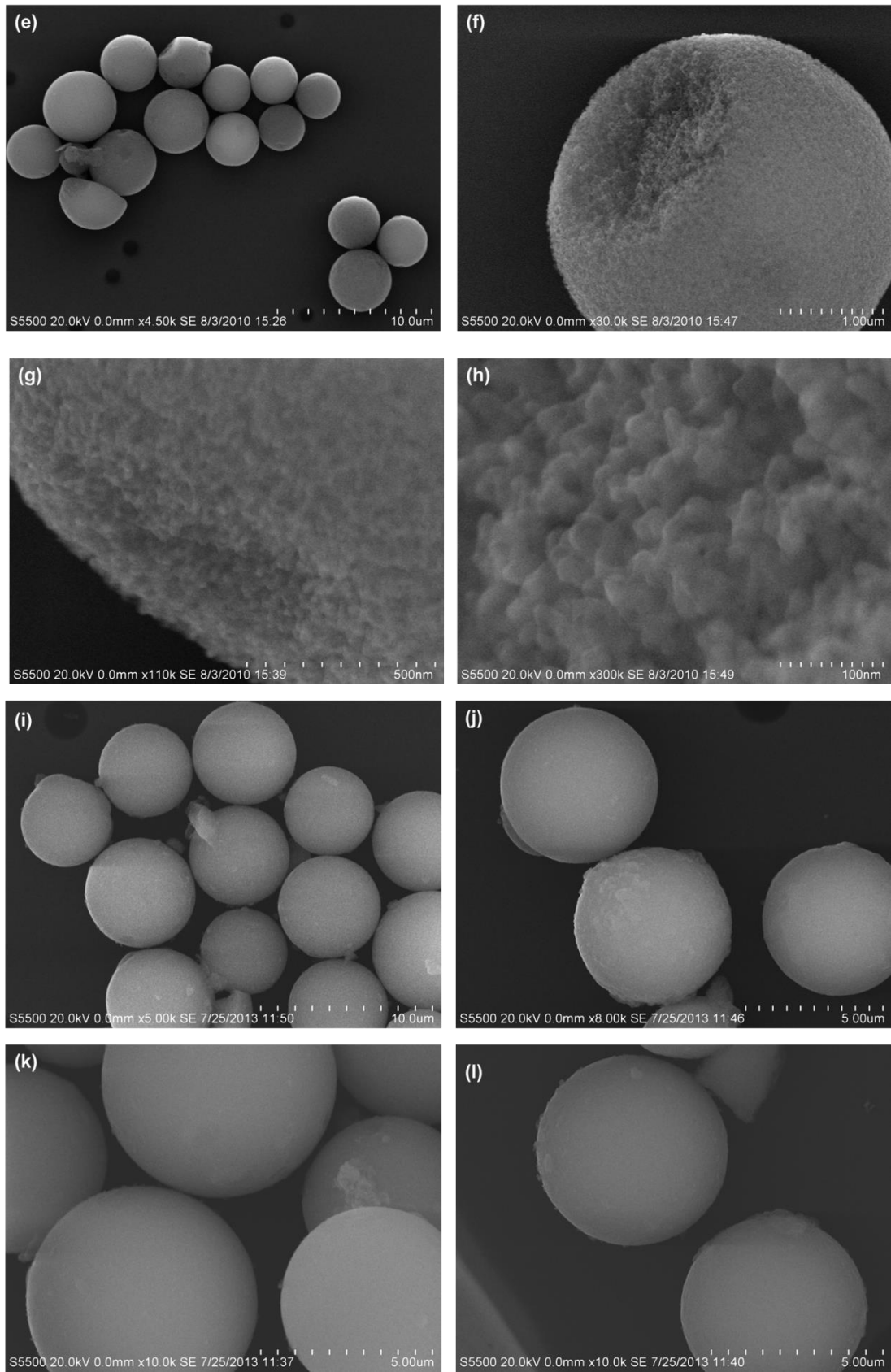
***Figure 2.4:*** *FE-SEM images of (a) – (d) 1.38μm, (e) – (h) 3μm and (i) – (l) 5 μm of FMS with different magnifications.*

## 2.4.3 Surface area and porosities

The study of surface area effects before and after immobilisation of $C_{60}$ on the surface of APS was carried out using BET analysis. The nitrogen sorption isotherm (Figure 2.5 (a) and (b)) of the APS and FMS (5 μm) showed typical type IV curves, with a sharp type A hysteresis loop, corresponding to a narrow pore size distribution. The shape of the hysteresis loop is implying ordered cylindrical mesopores open at both ends. Both isotherms at the relative pressure from 0.01 - 0.7 were almost identical, which indirectly confirmed that the covalently attached $C_{60}$ did not change the microporous structure of FMS, i.e. the microporous structure of FMS remains almost the same as its APS counterpart.
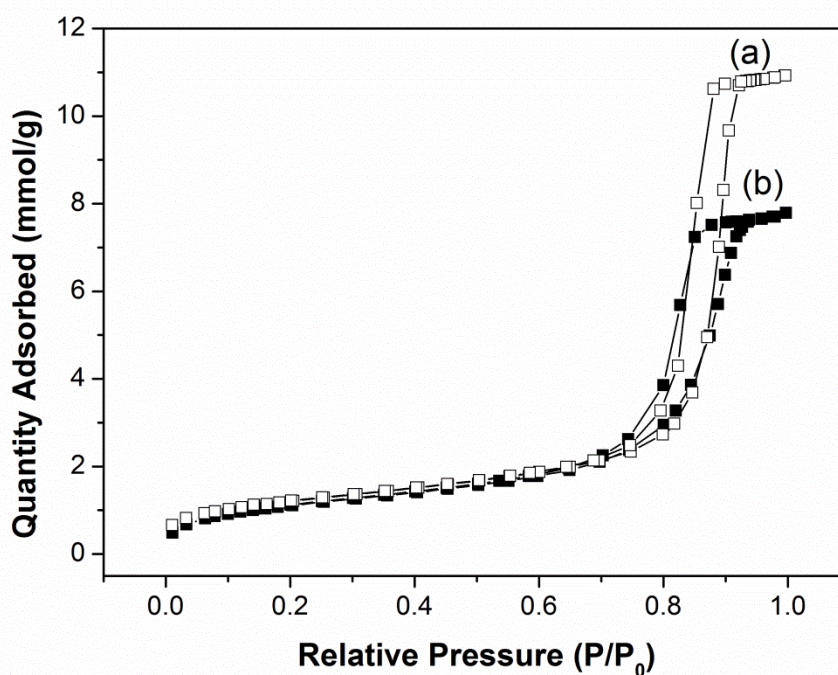


***Figure 2.5:*** *Nitrogen adsorption / desorption isotherm of (a) APS (5μm) and (b) FMS (5μm).*

The BET specific surface area of the FMS was 88.97 $m^2$, which was decreased from 94.83 $m^2$/g (APS) due to the functionalisation of $C_{60}$ onto mesoporous wall and narrowed mesopores. The average size of mesopores after $C_{60}$ attachment was reduced from 15.08 nm to 11.77 nm. Thus, it could be speculated that there is an evenly distributed ~ 1.655 nm of $C_{60}$ layer on each side of mesoporous wall. There was no obvious sign of any blockage of $C_{60}$ clusters within the mesoporous structure

otherwise its specific surface area would have decreased dramatically. This observation suggested that the washing step after the synthesis was sufficient to remove any the unreacted or physically adsorbed $C_{60}$ on the surface of FMS. The structural characteristics of APS and FMS are summarised in Table 2.3.

***Table 2.3:*** *Structural characteristics of APS and APS (5 μm).*

| Samples | $S_{BET}$[a] $(m^2\,g^{-1})$ | $V_{total}$[b] $(cm^3\,g^{-1})$ | $D_{meso}$[c] $(nm)$ | $V_{micro}$[d] $(cm^3\,g^{-1})$ |
|---------|--------|--------|--------|--------|
| APS | 94.83 | 0.38 | 15.08 | 0.0023 |
| FMS | 88.97 | 0.27 | 11.77 | -0.0023 |

[a] The BET method was used to calculate the specific surface areas at relative pressure of $P/P_o$ = 0.01-0.30. [b] Calculated by the $N_2$ amount adsorbed at the highest $P/P_o$ (~0.99). [c] The BJH method was used to calculate mesopore diameter from the adsorption branches of the isotherms. [d] Micropore volumes were calculated by the t-plot.

## 2.4.4 Covalent bonding between APS and $C_{60}$

In order to confirm every modification step, a study using ATR-IR spectroscopy was performed on three materials, $C_{60}$, APS, and the final product FMS, as shown in Figure 2.6. The spectrum of FMS (5 μm) can be representative of the other FMS at different particle sizes, and shows that the fullerenes were successfully bonded to APS, as the product clearly contains the features of both starting materials (Figure 2.6 (b)). Trace (b) revealed the appearance of a very broad peak at 1038 cm$^{-1}$ with 26 cm$^{-1}$ shift, compared with trace (a), which was due to Si-O-R bonds present within APS. The peak at 802 cm$^{-1}$ is attributed to N-C wag. The peaks at 1421 and 1178 cm$^{-1}$ are typical of pure $C_{60}$, which were still remaining in the spectrum of FMS with a very slight shift [37]. Therefore, the covalent bond C-N between $C_{60}$ and the primary amine group from APS in FMS was also confirmed.
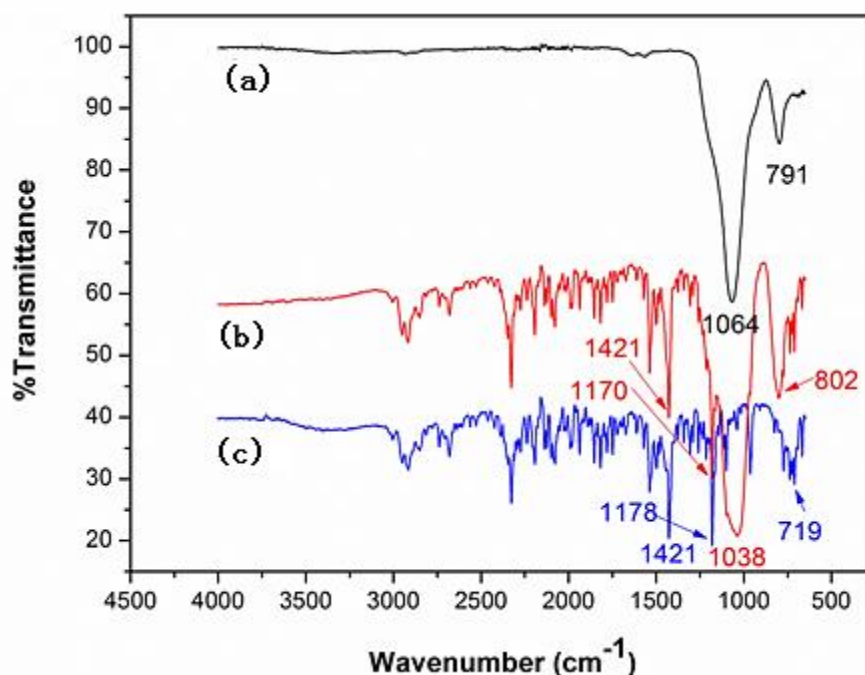
**Figure 2.6:** *FT-IR spectra (a) 5 μm APS, (b) 5 μm FMS and (c) C$_{60}$.*

## 2.4.5 C$_{60}$ loading capacity

Elemental analysis provided the percentages of carbon, nitrogen and hydrogen in the materials. Elemental analysis was carried out on two batches of APS and FMS to obtain quantitative information about the coverage of aminopropyl and C$_{60}$ ligands by calculations [38], results which are shown in *Table 2.4* - Table 2.6. As can been seen, a good reaction indicator is the amount of carbon in the sample introduced by the covalently attached C$_{60}$. For a better comparison the amount of nitrogen was normalised to the amount of carbon found in the FMS. Generally, a greater amount of carbon was found on the FMS, resulting from the carbon rich C$_{60}$ covalently attached to the surface of the APS. The loading capacity of C$_{60}$ on APS was 1.23 molecules per nm$^2$ (or 1.977 $\mu$mol/m$^2$), estimated from elemental analysis. This C$_{60}$ coverage was reproducible from batch to batch with variation of < 4%. These results were in good agreement with ATR-FTIR analysis and suggest that using the optimised reaction conditions resulted in more surface coverage on the APS surface, that compared with the literature value of 0.86 $\mu$mol/m$^2$ [39]. Thermogravimetric analysis data of C$_{60,}$ hydrolysed silica and APS will be discussed in Chapter 3 in relation to nanotemplated carbon monolith fabrication.

**Table 2.4**: *Elemental analysis of Batch 1 FMS (APS, 5 μm, porous, 95m$^2$/g according to in-house BET measurement).*

| Sample | %C | %H | %N | Surface coverage N (molecule per nm$^2$) |
|---|---|---|---|---|
| | 0.00 | 0.11 | 0.00 | 0.00 |
| APS (0.0054g) | 2.83 | 0.35 | 0.66 | 2.99[a] |
| FMS | 16.02 | 0.41 | 0.48 | 1.17[b] |

[a] no. of amino groups calculated by %N

[b] C$_{60}$ bonded on amino group calculated by %C increased

**Table 2.5:** *Elemental analysis of Batch 2 FMS (APS, 5 μm, porous, 95m$^2$/g according to in-house BET measurement).*

| Sample | %C | %H | %N | Surface coverage N (molecule per nm$^2$) |
|---|---|---|---|---|
| Silica | 0.00 | 0.12 | 0.00 | 0.00 |
| APS (0.0054g) | 2.81 | 0.32 | 0.63 | 2.85[a] |
| FMS | 16.00 | 0.40 | 0.46 | 1.23[b] |

[a] no. of amino groups calculated by %N

[b] C$_{60}$ bonded on amino group calculated by %C increased

**Table 2.6:** *Averaged elemental analysis results between two batches of FMS.*

| Sample | %C | %H | %N | Surface coverage N (molecule per nm$^2$) |
|---|---|---|---|---|
| Silica | 0.00 | 0.12 | 0.00 | 0.00 |
| APS (0.0054g) | 2.82 | 0.34 | 0.65 | 2.94[a] |
| FMS | 16.01 | 0.41 | 0.47 | 1.23[b] |

[a] no. of amino groups calculated by %N

[b] C$_{60}$ bonded on amino group calculated by %C increased

The calculations of averaged elemental analysis results in Table 2.6 are shown below.

*Surface coverage of -NH₂ on APS*

%N = 0.65%= 0.0065g /g

No. of moles of N=$\frac{0.0065g}{14\,{}^g/_{mol}}$ = 4.64 × 10⁻⁴mo/g

4.64 × 10⁻⁴mol ×6.02 10²³mol⁻¹ = 2.795 × 10²⁰ molecules/g

$\frac{2.795×10^{20}\,molecules/g}{95m^2/g}$ = 2.94 × 10¹⁸ molecules per m²= 2.94 molecules/ nm²


*Surface coverage of C₆₀ on FMS*

%C from APS = 2.82% = 0.0282 g/g

No. of moles of C from APS = $\frac{0.0282g}{12\,{}^g/_{mol}}$ = 2.35 × 10⁻³mol/g

Therefore, the molar ratio between C:N in APS = $\frac{2.35×10^{-3}\,mol/g}{4.64×10^{-4}\,mol/g}$ = 5.06 ~ 5

The chemical structure of APS is shown in Figure 2.7 according to the above ratio.
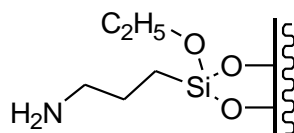


**Figure 2.7:** *The chemical structure of APS according to elemental analysis.2 ethylmethoxy substituents were bonded to silica and 1 ethylmethoxy substituent was free after amination.*


The chemical structure of FMS is predicted as shown in Figure 2.8 according to the structure of APS.
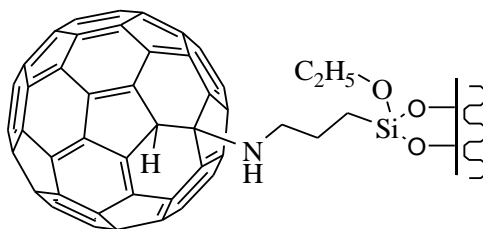


**Figure 2.8:** *The chemical structure of FMS according to elemental analysis.*


%C from FMS = 16.01% = 0.1601 g/g

No. of moles of C from FMS = $\frac{0.1601g}{12g/mol}$ = 1.33 × 10⁻² mol/g

%N from FMS = 0.47% = 4.7 × 10⁻³ g/g

No. of moles of N = $\frac{4.7×10^{-3}g}{14\,{}^g/_{mol}}$ = 3.357 × 10⁻⁴ mol/g

Therefore, N : C ratio = 1:5 in APS, no. of moles of C contributed from APS in FMS

$= 3.357 \times 10^{-4} \ mol/g \times 5 = 1.679 \times 10^{-3}$ mol/g.

No. of moles of C contributed from $C_{60}$ substituents $= 1.33 \times 10^{-2} - 1.679 \times 10^{-3} = 1.162 \times 10^{-2}$ mol/g.

There are 60 carbons in an $C_{60}$ moiety.

No of moles of $C_{60}$ from FMS $= \frac{1.162 \times 10^{-2}}{60} = 1.937 \times 10^{-4}$ mol/g

$1.937 \times 10^{-4}$ mol $\times 6.02 \ 10^{23}$ mol$^{-1} = 1.166 \times 10^{20}$ molecules/g

$\frac{1.166 \times 10^{20} molecules/g}{95 \text{m}^2/g} = 1.227 \times 10^{18}$ molecules per m$^2 \sim 1.23$ molecules/nm$^2$

Since the molar ratio of secondary amino and $C_{60}$ was 1:1, the amount of secondary amine groups can be found was $1.937 \times 10^{-4}$ mol/g.

No. of moles of primary amine group on the surface of FMS $= 3.357 \times 10^{-4}$ mol/g $- 1.937 \times 10^{-4}$ mol/g $= 1.42 \times 10^{-4}$ mol/g

Elemental analysis also revealed the total moles of nitrogen upon the FMS after modification was $3.357 \times 10^{-4}$ mol/g of the stationary phase, while the amount of $C_{60}$ on the surface of the resultant FMS was $1.937 \times 10^{-4}$ mol/g of the stationary phase. Their ratio was almost 1, therefore it was confirmed that the attachment of $C_{60}$ to the APS surface took place only through one carbon atom of $C_{60}$. Thus, the amount of primary and secondary amine groups on the surface was $1.42 \times 10^{-4}$ mol/g and $1.937 \times 10^{-4}$ mol/g, respectively, i.e. approximately 57% of primary amine groups were converted to secondary amine groups in the second modification step. Therefore, the resulting FMS phase are mixed $C_{60}$-aminopropyl phases.

## 2.4.6 Hydrophobicity

The contact angle of drop-coated 1.38 μm APS and FMS i.e., $C_{60}$ unmodified and modified silica gels were measured and are shown in Figure 2.9. APS exhibited a 23$^{\circ}$ contact angle (Figure 2.9 (a)), which was 4.7 times higher after functionalisation with $C_{60}$ (Figure 2.9 (b)), proving that material hydrophobicity significantly increased due to the nature of $C_{60}$ [34]. The contact angle obtained from APS surface was consistent with prior studies of APTES films on silicon wafer which have measured contact angles were 26$^{\circ}$ [40, 41]. The FMS as a template should therefore be more compatible with phenolic resins than APS in terms of hydrophobicity, for later fabrication of NTCM (see Chapter 3). Spin coating proves to be a better

technique for sample preparation. It provides a more even surface for contact angle measurements, but required time to establish optimum parameters, such as solvent for dispersion, rotation speed and temperature for such samples.
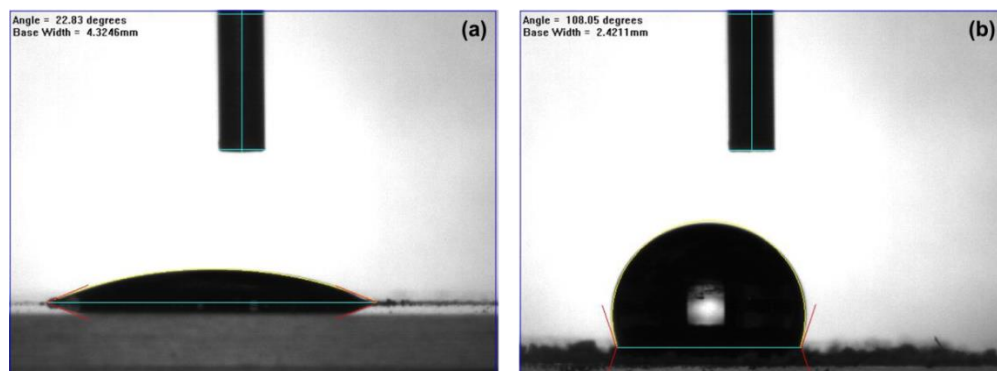


***Figure 2.9:*** *Contact angle measurement of (a) 1.38 μm APS and (b) 1.38 μm FMS.*

## 2.4.7 HPLC evaluation

The prepared stationary phase was not only used as a template for further fabrication of carbon monoliths (see Chapter 3), but was also evaluated as a stationary phase for the separation of a series of aromatic compounds by RP-LC using an in-house packed FMS column. To optimise separation conditions, the separation was first evaluated with different concentrations of methanol as mobile phases. The retention factor data for selected aromatic hydrocarbons is shown in Table 2.7.

***Table 2.7:*** *Capacity factor (k) of 5 different compositions of mobile phases (methanol: water (80:20, 70:30, 60:40, 50:50 40:60 (v/v) respectively on APS column (5 mm × 2 mm I.D.). Analytes:10 ppm of toluene, anthracene, p-xylene, benzene, phenol and naphthalene in 100% methanol. Conditions: flow rate of 0.2 mL/min at isocratic mode, injection volume 1 μL, UV detector at 254 nm and column temperature ambient.*

| [CH₃OH] Vol % | log k | | | | | |
|---|---|---|---|---|---|---|
| | toluene | anthracene | *p*-xylene | benzene | phenol | naphthalene |
| 80 | -1.11 | -0.172 | -0.946 | -1.281 | -1.193 | -0.664 |
| 70 | -0.852 | 0.196 | -0.654 | -1.032 | -1.11 | -0.375 |
| 60 | -0.52 | 0.727 | -0.3004 | -0.725 | -0.856 | -0.01 |
| 50 | -0.236 | 1.227 | 0.025 | -0.489 | -0.623 | 0.339 |
| 40 | 0.03 | 1.66 | 0.33 | -0.26 | -0.39 | 0.724 |

The data showed that the stationary phase, indeed, exhibited hydrophobic properties. Phenols are generally only weakly retained on ODS columns, but did show reasonable retention on the FMS, when a low organic solvent mobile phase was applied [42]. $C_{60}$ is expected to show preferential interactions with electron rich aromatic molecules rather than an electron deficient aromatic molecules [2]. This effect was especially pronounced for polycyclic aromatic hydrocarbons, i.e. an electron rich molecule like anthracene showed the strongest retention. The grafted $C_{60}$ has a large surface to volume ratio and a powerful $\pi - \pi$ intermolecular interaction with aromatic eluents which again differs from those in reversed-phase columns [31].
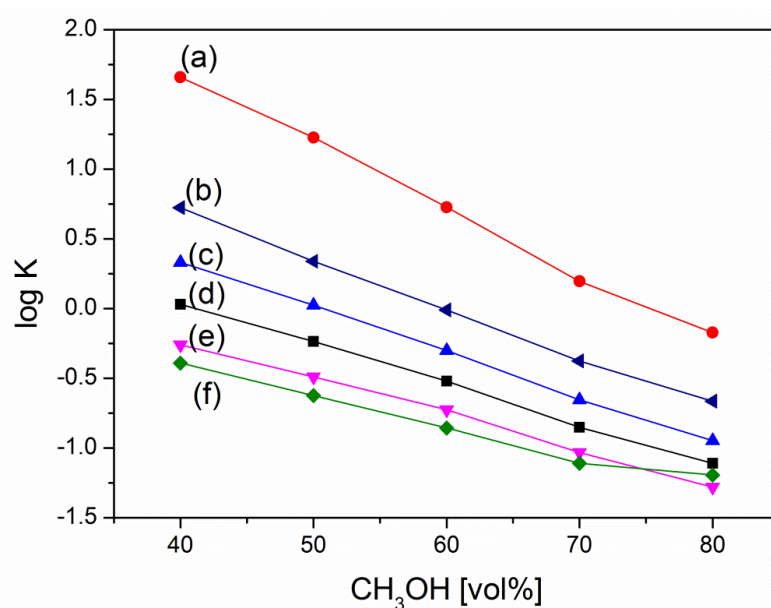


***Figure 2.10:*** *Effect of methanol content of the mobile phase on logarithm of retention factor (k) of six aromatic compounds (a) anthracene, (b) naphthalene, (c) xylene, (d) toluene, (e) benzene and (f) phenol on the column of FMS (5 mm × 2 mm I.D.). Analytes:10 ppm of toluene, anthracene, p-xylene, benzene, phenol and naphthalene in 100% methanol. Conditions: flow rate of 0.2 mL/min at isocratic mode, injection volume 1 μL, UV detector at 254 nm and column temperature ambient.*

Figure 2.10 demonstrated that the retention factors (*k*) of six aromatic compounds on FMS decreased almost linearly with an increase in the concentration of methanol in the mobile phase over the range of concentration (40 − 80%). This is because the $C_{60}$ moiety is nonpolar and tends to exhibit a hydrophobic and $\pi$-$\pi$ interaction and reversed-phase mechanism for the retention of these sample analytes, which is very

similar to PGC phases [42, 43]. According to the chemical structure of anthracene naphthalene, p-xylene, toluene, and benzene, they are polarisable but have no permanent dipoles, whereas phenol has a permanent dipole [44]. The analytes were strongly retained on the FMS column when the concentration of methanol was < 70%. The polarities of the sorbent and eluent, and additional interaction by the presence of functional groups are the most influential factors affecting retention of polar substances in LC. When the concentration of methanol was increased to 80%, log k values for phenol no longer displayed a linear trend due to enhanced hydrophilic interaction. [45].
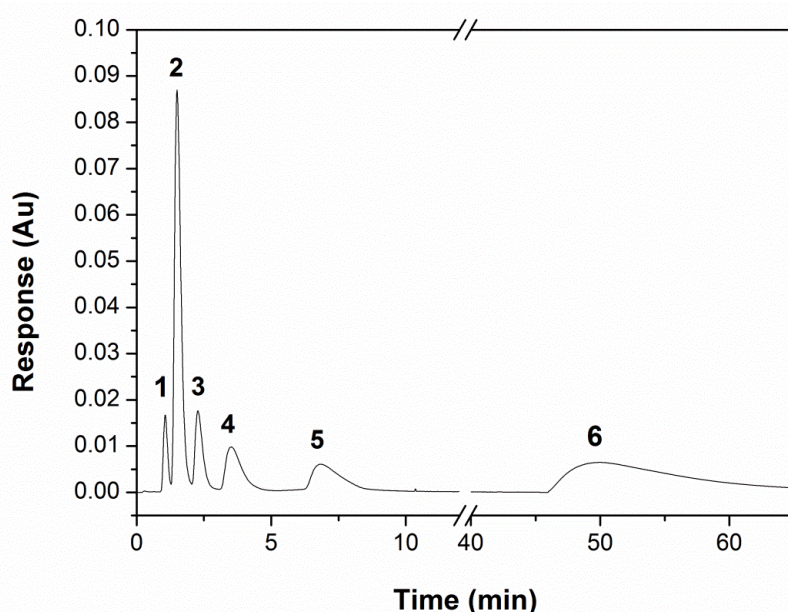


*Figure 2.11: The separation of six aromatic and heterocyclic mixed compounds on a FMS column (5 mm × 2 mm I.D.). Conditions: mobile phase 40 : 60, methanol : 10 mM phosphoric acid (pH 2.6) at flow rate of 0.2 mL/min at isocratic mode, injection volume 1 μL, UV detector at 254 nm and column temperature ambient. Peaks: (1) System peak, (2) benzene, (3) phenol, (4) toluene, (5) p-xylene and (6) naphthalene.*

A separation of a test mixture of five aforementioned aromatic compounds was obtained on the column packed with FMS shown in Figure 2.11. It showed a clear trend that the more hydrophobic the analyte the longer the retention time according to the sequence of elution of benzene, phenol, toluene and p-xylene. Naphthalene retained longest with very poor peak efficiency in RP-LC mode, which suggests the strongest $\pi$-$\pi$ interactions between stationary phase and analyte among the other

analytes. Although anthracene was also present in the separation mixture, in the above conditions its elution time was very long, ~100 minutes and peak efficiency was very low, so it was not possible to see the peak. Therefore, this in-house prepared FMS phase showed $\pi$-$\pi$ interactions and hydrophobic retention behaviour. The HPLC separation and detection with FMS phase further confirmed the success of grafting high coverage $C_{60}$ on APS.

## 2.5 Conclusion

In the work presented herein, a convenient approach for the attachment of $C_{60}$-fullerene to aminopropyl bonded silica by amine addition was successfully developed. The obtained product was fully characterised using FE-SEM, contact angle measurements, ATR-FTIR and elemental analysis. All the characterisation results confirmed the covalent attachment of fullerenes to the silica surface. Three different size silica particles with different surface areas were used for comparison. The reaction conditions for hydroxylation, amination and fullerene immobilisation on the silica surface were optimised to achieve maximum loading of $C_{60}$. A series of aromatic compounds were used as probes for the confirmation of covalent attachment of the fullerenes to 5 µm FMS which was packed within a stainless steel column and tested using RP-HPLC. The resultant stationary phase showed good mechanical, and chemical stabilities and different retention behaviour from a conventional ODS phase. All characterisation results showed the 5 µm FMS particles to be suitable carbonaceous nanotemplates for use in the fabrication of carbon monoliths.

## 2.6 References

1. H. W. Kroto, J. R. Heath, S. C. O'Brien, R. F. Curl, R. E. Smalley, C60: Buckminsterfullerene. *Nature* **318**, 162 (1985).
2. K. Jinno, R. S. o. Chemistry., *Separation of fullerenes by liquid chromatography*. (Royal Society of Chemistry, Cambridge, 1999).
3. J. M. Millar *et al.*, Chromatographic separations of fullerenes: discovery and characterization of C60 mono-epoxide. *Inorganic Chemicals and Reactions* **59**, 317 (1993).
4. J. C. Fetzer, Mechanisms of fullerene separations. *Analytical Chemistry* **76**, 342A (2004).

5.  Y. Saito, H. Ohta, K. Jinno, Design and characterization of novel stationary phases based on retention behavior studies with various aromatic compounds. *Journal of Separation Science* **26**, 225 (2003).

6.  Y. Saito, H. Ohta, K. Jinno, Peer Reviewed: Chromatographic Separation of Fullerenes. *Analytical Chemistry* **76**, 266 A (2004).

7.  C. S. Chang, T. G. Den, C. C. Chen, S. L. Lee, Stationary phases 44: Chromatographic separation of naturally occurring dehydroiso-alpha-lapachone derivatives with C-60-fullerene stationary phase. *Hrc-Journal of High Resolution Chromatography* **20**, 624 (1997).

8.  K. Jinno, K. Tanabe, Y. Saito, H. Nagashima, R. D. Trengove, Retention behavior of calixarenes with various $C_{60}$ bonded silica phases in microcolumn liquid chromatography. *Section Title: Organic Analytical Chemistry* **34**, 175 (1997).

9.  C. D. Tran, S. Challa, Fullerene-impregnated ionic liquid stationary phases for gas chromatography. *Analyst* **133**, 455 (2008).

10. L. A. Kartsova, A. A. Makarov, New fullerene-based stationary phases for gas chromatography. *Journal of Analytical Chemistry* **59**, 724 (2004).

11. R. M. Vallant *et al.*, Development and application of $C_{60}$-fullerene bound silica for solid-phase extraction of biomolecules. *Analytical Chemistry* **79**, 8144 (2007).

12. K. Boeddi *et al.*, Use of fullerene-, octadecyl-, and triaconthyl silica for solid phase extraction of tryptic peptides obtained from unmodified and in vitro glycated human serum albumin and fibrinogen. *Journal of Separation Science* **32**, 295 (2009).

13. P. Innocenzi, G. Brusatin, Fullerene-based organic-inorganic nanocomposites and their applications. *Chem. Mat.* **13**, 3126 (2001).

14. M. Prato, [60] Fullerene chemistry for materials science applications. *Journal of Materials Chemistry* **7**, 1097 (1997).

15. H. W. Kroto, J. R. Heath, S. C. O'Brien, R. F. Curl, CM: Buckminsterfullerene. *Physics & chemistry of fullerenes: a reprint collection*, 8 (1993).

16. E. H. L. Falcao, F. Wudl, Carbon allotropes: beyond graphite and diamond. *Journal of Chemical Technology & Biotechnology* **82**, 524 (2007).

17. F. Wudl, The chemical-properties of Buckminsterfullerene ($C_{60}$) and the birth and infancy fulleroids. *Accounts of Chemical Research* **25**, 157 (1992).

18. H. L. Anderson *et al.*, in *2nd International winterschool on electronic properties of novel materials, Progress in fullerene research; Chemistry*. (World Scientific , River Edge, NJ 1994),  pp. 13-18.

19. G. D. Panagiotou *et al.*, Development of [60] fullerene supported on silica catalysts for the photo-oxidation of alkenes. *Applied Catalysis A: General* **372**, 16 (2010).

20. Y. Liu, Y. Feng, S. Da, Y. Chen, Preparation and evaluation of C60 bonded silica phase for high performance liquid chromatography. *Se Pu* **16**, 115 (1998).

21. Y. Feng *et al.*, Separation of calixarenes and calixcrowns with a $C_{60}$ bonded silica stationary phase in normal-phase liquid chromatography. *Journal of Instrumental Analysis* **19**, 1 (2000).

22. F. Wudl, Fullerene materials. *Journal of Materials Chemistry* **12**, 1959 (2002).

23. Y. Saito *et al.*, Microcolumn LC separation of polycyclic aromatic hydrocarbons with a chemically bonded C60 stationary phase. *Inorganic Analytical Chemistry* **16**, 192 (1995).

24. Y. Saito *et al.*, Separation of polycyclic aromatic hydrocarbons with a C60-bonded silica phase in microcolumn liquid chromatography. *Organic Analytical Chemistry* **18**, 569 (1995).

25. K. Jinno, K. Tanabe, Y. Saito, H. Nagashima, Separation of polycyclic aromatic hydrocarbons with various C-60 fullerene bonded silica phases in microcolumn liquid chromatography. *Analyst* **122**, 787 (1997).

26. K. Jinno, K. Fukuoka, J. C. Fetzer, W. R. Biggs, Buckminsterfullerene as a stationary phase in liquid chromatography. *Journal of Microcolumn Separations* **5**, 517 (1993).

27. K. Jinno, K. Yamamoto, J. C. Fetzer, W. R. Biggs, C60 as a stationary phase for microcolumn liquid chromatographic separation of polycyclic aromatic hydrocarbons. *Journal of Microcolumn Separations* **4**, 187 (1992).

28. C.-S. Chang, C.-H. Wen, T.-G. Den, Stationary phases 45[(1)]: Chromatographic separation of high energetic materials with $C_{60}$-fullerene stationary phase. *Propellants, Explosives, Pyrotechnics* **23**, 111 (1998).

29. G. P. Miller, Reactions between aliphatic amines and [60] fullerene: a review. *Comptes Rendus Chimie* **9**, 952 (2006).

30. S. Brunauer, P. H. Emmett, E. Teller, Adsorption of gases in multimolecular layers. *Journal of the American Chemical Society* **60**, 309 (1938).

31. L. L. Gumanov, G. A. Volkov, A. V. Shastin, B. L. Korsounskii, Preparation and properties of sorbents based on silica gel containing covalently linked fullerene $C_{60}$. *Russian Chemical Bulletin* **45**, 768 (1996).

32. I. Taylor, A. G. Howard, Measurement of primary amine groups on surface-modified silica and their role in metal-binding. *Anal. Chim. Acta* **271**, 77 (1993).

33. J. Nawrocki, The silanol group and its role in liquid chromatography. *J. Chromatogr. A* **779**, 29 (1997).

34. R. S. Ruoff, D. S. Tse, R. Malhotra, D. C. Lorents, Solubility of fullerene ($C_{60}$) in a variety of solvents. *The Journal of Physical Chemistry* **97**, 3379 (1993).

35. A. Goel, J. B. Howard, J. B. Vander Sande, Size analysis of single fullerene molecules by electron microscopy. *Carbon* **42**, 1907 (2004).

36. D. M. Cox *et al.*, Characterization of $C_{60}$ and $C_{70}$ Clusters. *Journal of the American Chemical Society* **113**, 2940 (1991).

37. G. Angelini, O. Ursini, F. Cataldo, Synthesis of fullerene-silica hybrid materials. *Journal of Radioanalytical and Nuclear Chemistry* **284**, 179 (2010).

38. B. Buszewski, M. Jaroniec, R. K. Gilpin, Studies of physicochemical and chromatographic properties of mixed amino-alkylamide bonded phases. *J. Chromatogr. A* **673**, 11 (1994).

39. C. S. Chang, T. G. Den, C. C. Chen, S. L. Lee, Stationary Phases. Part 44. Chromatographic separation of naturally occurring dehydroiso-Ⱡ-lapachone derivatives with C60-fullerene stationary phase. *Section Title: Organic Analytical Chemistry* **20**, 624 (1997).

40. A. Simon, T. Cohen-Bouhacina, M. C. Porté, J. P. Aimé, C. Baquey, study of two grafting methods for obtaining a 3-aminopropyltriethoxysilane monolayer on silica surface. *Journal of Colloid and Interface Science* **251**, 278 (2002).

41. D. F. Siqueira Petri, G. Wenz, P. Schunk, T. Schimmel, An improved method for the assembly of amino-terminated monolayers on $SiO_2$ and the vapor deposition of gold layers. *Langmuir* **15**, 4520 (1999).

42. O. N. Fedyanina, P. N. Nesterenko, Regularities of Chromatographic retention of phenols on microdispersed sintered detonation nanodiamond in aqueous-organic solvents. *Russian Journal of Physical Chemistry A* **84**, 476 (2010).

43. E. Forgacs, T. Cserhati, Retention strength and selectivity of porous graphitized carbon columns. Theoretical aspects and practical applications. *Section Title: Organic Analytical Chemistry* **14**, 23 (1995).

44. E. Heftmann, *Chromatography: fundamentals and applications of chromatographic and electrophoretic methods.* (Elsevier Scientific, Amsterdam, 1983).

45. G. Marko-Varga, D. Barceló, Liquid chromatographic retention and separation of phenols and related aromatic compounds on reversed phase columns. *Chromatographia* **34**, 146 (1992).

# Chapter 3

# Nanotemplated Carbon Monolithic Material

*"The whole of science is nothing more than a refinement of everyday thinking."*

Albert Einstein

# Abstract

A novel hierarchical nanotemplated carbon monolithic rod (NTCM) was prepared using a facile nanotemplating approach. The NTCM was obtained using $C_{60}$-fullerene modified silica gels as hard templates, which were embedded in a phenolic resin containing a metal catalyst for localised graphitisation, followed by bulk carbonisation, and template and catalyst removal. TEM, SEM and BET measurements revealed that NTCM possessed an integrated open hierarchical porous structure, with a tri-modal pore distribution. This porous material also possessed a high mesopore volume and narrow mesopore size distribution. During the course of carbonisation, the $C_{60}$ bound to the aminated silica was partly decomposed, leading to the formation of micropores. The Raman signature of NTCM was very similar to that of multi-walled carbon nanotubes as exemplified by three major peaks as commonly observed for other carbon materials, i.e., the $sp^3$ and $sp^2$ carbon phases coexisted in the sample. Surface area measurements were obtained using both nitrogen adsorptions/desorption isotherms (BET) showing the NTCM material possessed an average specific surface area of 435 $m^2$/g. A carbon monolithic rod (unmodified counterpart of NTCM, CM blank) was cladded into a PEEK column (74.5 $\times$ 4 mm I.D.) to demonstrate the potential uses as a stationary phase for reversed phase chromatography. Its permeability was $6.5 \times 10^{-11}$ $cm^2$, which had good agreement with the literature value. A linear dependency of back pressure on flow rate within the range of (0.1 – 2.8 mL/min) demonstrated the excellent rigidity of this carbon monolithic rod. The separation of three phenolic compounds exhibited high selectivity and low hydraulic resistance, but poor separation efficiency. It suggested that this carbon monolithic material was not suitable to be used as a stationary phase for liquid chromatography. Electrochemical studies using NTCM modified glassy carbon or boron doped diamond (BDD) electrodes displayed quasi-reversible oxidation/reduction with ferricyanide. In addition, the BDD electrode modified with NTCM was able to detect hydrogen peroxide with a detection limit of below 300 n$M$, whereas pristine BDD electrode was not responsive to this target compound.

**Aim**

The aim of this work was to synthesise a hierarchically porous carbon monolith, using $C_{60}$ fullerene-modified silica gels as the hard agglomerated template materials, and to explore its possible potential applications in analytical sciences, either in separations or electrochemistry. Key physical and chemical features of these '*carbon in carbon*' or '*carbon on carbon*' monolithic composites needed to be fully investigated.


## 3.1 Introduction

Over the past decade or so, porous carbon materials have attracted significant attention [46-48], and have been shown to exhibit excellent potential for many cutting edge applications, including for example, catalysis supports, electrochemical double-layer capacitors, gas storage, and sorbents for separation/remediation processes. These diverse applications stem from high specific surface areas and excellent thermal/chemical stability of such porous carbon materials. It is noticeable that most of these carbon materials are usually prepared in a powder form [49, 50], thus for tailoring these materials to match a particular application, it is often necessary to formulate them in a particular macroscopic shape. Carbon monoliths (CMs) possess an integrated structure, which is much easier to apply to many of the above applications [51, 52]. Additionally, CMs often exhibit controlled pore structures, with interconnected channels within their framework, which additionally provide the benefit of high flow-through permeability. According to International Union of Pure and Applied Chemistry (IUPAC) definitions, mesoporous carbon materials possess pores within the 2 -50 nm range, microporous materials have pores of < 2 nm, whilst pore size within macroporous carbon are > 50 nm. Hierarchical pore structuring is usually achieved by various templating techniques, including the use of hard and soft templates [53, 54]. It is crucial to understand the effects of such architecture upon its physicochemical properties, surface area, mechanical strength, and surface chemistry [55].

Fabrication of CMs by various fabrication strategies has been reported by a number of authors [56-59] and more details can be found in Chapter 1 Section 1.3.1. Alvarez and Fuertes produced a carbon monolith by a "nanocasting" approach, employing a macro/mesoporous silica monolith as the sacrificial template [60]. The

resultant CM exhibited an interconnected replicated structure, with an impressive surface area of 1,800 $m^2$/g. Xu et al. also used a silica monolith as hard template together with a mixture of styrene and divinylbenzene to synthesise a CM with bimodal perfusion pores by nanocasting and phase separation [61].

Carbon-based monoliths can also be prepared via the pyrolysis of a carbon rod produced from the polymerisation of a RF copolymer on bare silica particle templates, with iron as the catalyst for localised carbonisation [55, 62]. More recently, macro/mesoporous carbon monoliths with a graphitic framework have also been prepared via co-polymerisation of resorcinol and formaldehyde, with the inclusion of a polyamine (tetraethylenepentamine) [63]. The polymers were also doped with metallic salts of Fe (III), Ni(II), or Co(II) prior to carbonisation, forming encapsulated metallic nanoparticles during the carbonisation step. Such nanoparticles effect the conversion of a fraction of amorphous carbon into graphitic domains and can be removed from carbon monoliths by acid etching.

However, despite considerable interest in carbon monoliths over the past decade or more, to-date carbon nanoparticles have not been immobilised onto and within the macroporous wall surface of such carbonaceous monolithic materials, producing '*carbon in carbon*' or '*carbon on carbon*' monolithic composites. Given the unique selectivity, and physical and chemical properties that many such carbon nanoparticles are known to possess, it is reasonable to anticipate that the use of such nanoparticles within the formation of carbon monolithic structures may result in transfer of such properties, in full or in-part, onto the resultant carbon substrate.

Therefore, this Chapter describes a new synthesis procedure for the production of monolithic hierarchically porous carbon, using a facile 'nanotemplating' process, based upon $C_{60}$ fullerene-modified silica gels as the hard agglomerated template material. Carbon rods were formed using a thermally initiated process, based on pyrolysing a precursor rod made of a mixture of phenol-formaldehyde resin and the modified silica gel. Key physical and chemical features of these hierarchically porous carbon materials were investigated, together with their potential application as stationary phases for liquid chromatograph as well as new selective electrode materials.

## 3.2 Experimental

### 3.2.1 Reagents and materials

Resorcinol (99 wt.%), formaldehyde (37 wt.% aqueous solution), hydrofluoric acid (HF) (38 - 40 wt.%), hydrogen peroxide (50 wt.%), *N-N*,dimethylformamide (DMF, anhydrous, $\geq$ 99.8 wt.%), 2-*tert*-4-methylphenol ($\geqslant$ 99 wt.%), phenol ($\geqslant$ 99 wt.%), 4-methylphenol ($\geqslant$ 99 wt.%), potassium hexacyanoferrate(III) ($K_3Fe(CN)_6$, $\geq$99.9 wt.%), potassium hexacyanoferrate(II) trihydrate ($K_4Fe(CN)_6$ • $3H_2O$, $\geq$99.9 wt.%), Nafion® NR50, graphite (powder, <20μm, synthetic), methanol (HPLC grade, $\geq$99.9%), 2-propanol (IPA, anhydrous, 99.5%), sodium phosphate monobasic and sodium phosphate dibasic were all obtained from Sigma-Aldrich (Dublin, Ireland). 1-Butanol and ferric chloride ($FeCl_3$) (99 wt.%) were obtained from Riedel-De Haen, Seelze (Hannover, Germany). FMS (5 $\mu$m, specific surface area of ~ 89 $m^2$/g and pore size of 12 nm) were in-house prepared; more details are provided in Chapter 2 Section 2.3.5. For electrochemical measurements, a 50 m$M$ phosphate buffer solution (PBS), pH 7.0, was used as the supporting electrolyte. Deionised water with a specific resistance of 18.3 MΩ.cm or greater was obtained from a Millipore Milli-Q water purification system (Millipore, Bedford, MA, USA). All reagents were of analytical grade and used as received and without further purification. 5 min general purpose epoxy and plastic weld were purchased from Permatex® (Connecticut, USA).

### 3.2.2 Instrumentation

For the formation of the carbon monoliths, a Yellowline MST basic hotplate stirrer with temperature control probe from IKA®-Werke GmbH & Co. KG (Staufen, Germany), a GFL water bath (MSC Medical Supply, Dublin, Ireland), a GSL 1300X tube furnace (MTI Co., Richmond, CA, USA), an EHRET thermovacuum oven from Ehret Labor and Pharmatechnik GmbH, KG (Emmendingen, Germany) and K12553 Gallenkamp OVA031.XX1.5 vacuum oven (Weiss Technik UK Ltd.) were used.

High-resolution SEM images of the prepared monolith surface morphologies were obtained using a Hitachi S-5500 FE-SEM (Dallas, USA) at an accelerating voltage of 10-20 kV. The surface compositions of the NTCM and morphology of

FMS were examined using a Hitachi SEM/energy-dispersive X-ray spectroscope (SEM/EDX), model VP-SEM S-3400N, equipped with a PentaFET-x3 detector which was managed by INCA microanalysis suite (Oxford, UK). High-resolution imaging for carbon monoliths was also performed by using a JOEL JEM-2100 LaB$_6$ TEM (Tokyo, Japan) operated at 200 kV. Thermogravimetric analysis (TGA) was conducted on a TA instruments TGA-Q50 analyser (New Castle, USA) from 25 $^{\circ}$C to 800 $^{\circ}$C, with a heating rate of 10 $^{\circ}$C/min under nitrogen (50 mL/min) to mimic the carbonisation process. A Micromeritics Gemini TriStar II 3020 surface area analyser (Georgia, USA), was used to measure the specific surface area and the pore volume using the nitrogen adsorption/desorption technique. Raman spectra were obtained using a Horiba JobinYvon LabRam 800HR with a CCD detector (New Jersey, USA). The argon ion laser used was the Innova 70-C-2, made by Coherent (Santa Clara, USA). The laser power was 6 mW with an excitation wavelength of 514.5 nm. A magnification of ×50 on the objective lens was used both to focus the laser beam and to collect the backscattering radiation. The exposure time of all spectra recorded was 10 s. Each spectrum was the accumulation of three scans.

A Waters 2965 liquid chromatography system equipped with a Waters 2487 spectrophotometric UV detector (Milford, MA, USA) was used for chromatographic analysis. The system management and data collection was controlled by Waters Empower™ 1 Chromatography Software.

Electrochemical characterisation was performed using a CH Instruments CHI 1040A electrochemical workstation (Austin, USA). A three-electrode system consisted of a working electrode, a BAS Ag/AgCl (3 *M* NaCl) reference electrode (West Lafayette, USA) and a platinum wire counter electrode.

## 3.2.3 Fabrication of nanotemplated carbon monolith rods

A modified procedure similar to that first reported by Liang *et al.,* and later by Eltmimi *et al.* [55, 62] was used for the preparation of the NTCM rods. FMS was synthesised as outlined in Chapter 2, Section 2.3.3. Typically, a 1 g portion of FMS particles was dispersed in ~ 1.85 mL of 1-butanol and sonicated for 1 h. Following this, 0.18 g (1.110 mmol) of FeCl$_3$ was added to the silica suspension and dissolved

by gentle agitation, after which 0.367 g (3.333 mmol) of resorcinol was added. A 0.275 mL (3.109 mmol) volume of ice cooled formaldehyde water solution was introduced dropwise into the mixture with gentle agitation. The mixture was then kept in an ice-water bath for 1 h with constant stirring. The mixture was slowly transferred into capped 5 mm I.D. glass tubes and incubated at 90 $^{\circ}$C for 16 h. Resulting crack-free phenolic resin/silica rods were removed from the glass tubes and kept in the fume hood for 72 h to allow slow evaporation of the majority of the residual solvent. Rods were dried under vacuum oven at 80 $^{\circ}$C overnight and further cured at 135 $^{\circ}$C for 4 h to complete polymerisation. The polymerised rods were then pyrolysed under the flow of nitrogen. The temperature was first ramped from room temperature to 800 $^{\circ}$C at 2.5 $^{\circ}$C/min, and then held at this temperature for 2 h to complete carbonisation. A second ramp took place from 800 to 1250 $^{\circ}$C, at a rate of 10 $^{\circ}$C/min, and this temperature was kept for another 1 h. The furnace was allowed to cool by natural convection to room temperature. Silica particles and the iron catalyst were removed from the rods by etching in concentrated HF for 6 h and subsequently washed with deionised water until neutral pH was obtained. These porous carbon rods obtained were then dried under vacuum at 80 $^{\circ}$C for 16 h. For comparison, a number of carbon monolith blank rods (CM blank) were prepared in the same manner, using the same grade of silica gel as a template, but without the presence of the surface attached $C_{60}$.

## 3.2.4 Characterisation of nanotemplated carbon monoliths

For FE-SEM sample preparations, all of CMs were prepared by slicing approximately 0.5 mm in thickness cross section of carbon monolith using a scalpel and then loading onto a normal carbon film grid. For EDX analysis, a 10 mg piece of carbon monolith was ground into fine powder in an agate mortar and then suspended in 15 μL of methanol. The suspension was sonicated 15 min and then cast onto an aluminium stub and dried overnight in the fumehood at room temperature. The use of a carbon grid was avoided in order to avoid possible carbon contamination during EDX analysis. The samples for TEM measurements were prepared with about 1 mg of pulverised carbon monolith which was dispersed in 3.5 mL of IPA and then sonicated for 30 min until a homogenous suspension was formed. 10 μL of the suspension was dropped onto a carbon-coated copper grid which allowed the solvent

to evaporate at atmospheric pressure and room temperature. A standard calibration was carried out prior to the TGA analysis. Approximately 10 mg of an intact carbon precursor or silica particles was placed within the platinum pan for analysis. Typically, a 20 mg of carbon monolith rod was dried at 120 $^\circ$C under vacuum for 16 h to remove any physically adsorbed moisture before nitrogen adsorption/desorption analysis. Then it was loaded into the apparatus for measurements.

## 3.2.5 Column cladding and HPLC evaluation

A straight CM blank rod (74.5 × 4 mm O.D., 5 $\mu$m, ~ 0.17 mg dry weight) was surface coated thoroughly with 5 Min. Permatex® general purpose epoxy and cured for 4 h at room temperature. The hardened rod was then encased in a suitable size plastic tube which was filled full with the same glue and cured overnight at room temperature. Finally the plastic tube encased carbon rod was placed in an oven at 50 $^\circ$C for 3 h to terminate the curing process. The encased rod was sealed into a pre-cut into sized PEEK HPLC column (74.5 × 10 mm I.D.) with Permatex® Plastic Weld. The configuration of the column cross section is illustrated in Figure 3.1. The resultant column was then ready to be connected to the HPLC system using standard connection.



**4 mm O.D. Carbon monlith**

**~ 1mm in thickness epoxy resin**

**6 mm I.D., 8 mm O.D., plastic tube**

**~ 1mm in thickness epoxy resin**

**10 mm I.D. PEEK column**
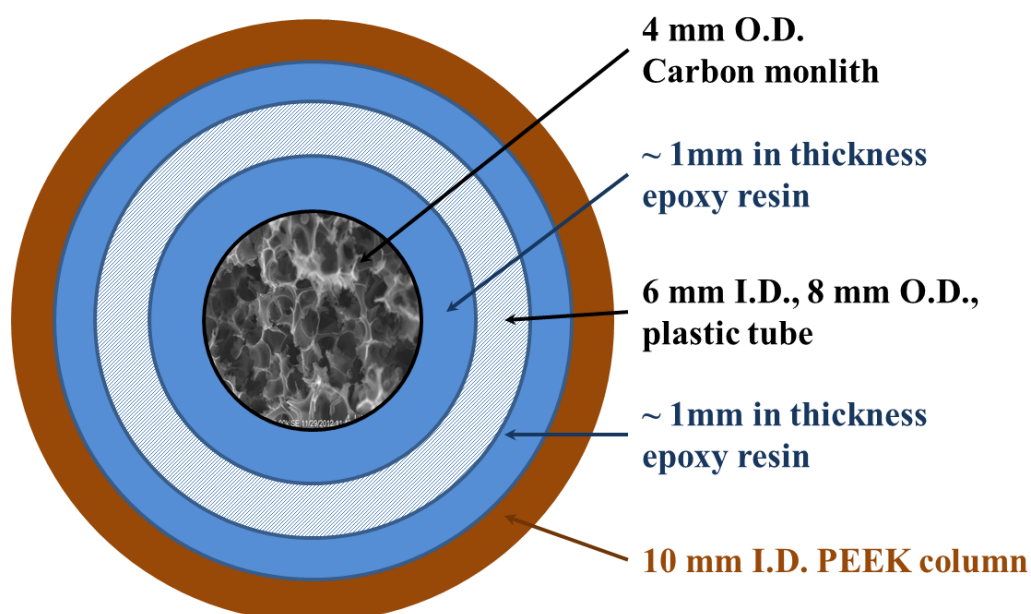
***Figure 3.1:*** *Cross-section of the CM blank column.*

**Table 3.1:** *Equations and parameters used for chromatography evaluations [64].*

| | | |
|---|---|---|
| **Resolution**<br><br>**($R_s$)** | $R_s = \left(\frac{1}{4}\right) N^{0.5} \left(\frac{a-1}{a}\right)\left(\frac{k'}{1+k'}\right)$<br><br>Where N = efficiency,<br><br>$\alpha$ = selectivity<br><br>k' = retention factor | (3.1) |
| **Efficiency**<br><br>**Or theoretical plates (N)**<br><br>**per m**<br><br>**($N/m$)** | $N/m = \dfrac{5.545(\frac{t_r}{w_{0.5}})^2}{L}$<br><br>Where $t_r$ = retention time of analyte<br><br>$w_{0.5}$ = peak width at half height in min<br><br>$L$ = length of the column in meter, 0.0745 m | (3.2) |
| **Selectivity**<br><br>**($\alpha$)** | $\alpha = \dfrac{t_{r2} - t_0}{t_{r1} - t_0}$<br><br>Where subscripts 1 and 2 refer to two analytes<br><br>$t_{r1}$ = retention time of analyte 1<br><br>$t_{r2}$ = retention time of analyte 2<br><br>$t_0$ = retention time of unretained analyte (0.88 min) | (3.3) |
| **Retention factor**<br><br>**(k')** | $k' = \dfrac{t_r - t_0}{t_0}$<br><br>Where $t_r$ = retention time of analyte<br><br>$t_0$ = retention time of unretained analyte (0.88 min) | (3.4) |
| **Permeability**<br><br>**($k_0$)** | $K_0 = \dfrac{u\eta L}{\Delta p}$<br><br>Where u = the mobile phase flow velocity (1mL/min)<br><br>$\Delta p$ = the pressure drop (Pa)<br><br>$\eta$ = the viscosity of the mobile phase (0.48 cP ~ for 90% methanol at 25 $^{\circ}$C)<br><br>L = the column length (7.45 cm) | (3.5) |

All separations were carried out at ambient temperature, 10 μL of injection volume and the UV detector was operated at 280 nm. The freshly in-house made column was washed with methanol: water mixture (90:10) at 0.2 mL/min for 300 min. The probe compounds were 2-*tert*-butyl-4-methylphenol, phenol and 4-methylphenol. A test mixture contained 0.5 mg of each analyte in 1 mL of 100% methanol. The column was tested with methanol: water (90:10) mixture as a mobile phase at flow rate of 1 mL/min in isocratic. The chromatographic performance of this in-house prepared carbon monolithic column was investigated using a series of parameters as shown in Table 3.1. The hydraulic resistance evaluation was performed using 100% methanol.

### 3.2.6 Electrochemical measurement

Electrochemical investigation of the prepared materials was carried out in order to further confirm the presence of $C_{60}$ or monolith entrapped residues. Cyclic voltammetry (CV) measurements were performed using a BAS glassy carbon electrode (GCE, 3 mm I.D, West Layette, USA) or BDD, 3 mm I.D., Winsor Scientific, UK), which were polished using 0.3 $\mu$m and then 0.05 $\mu$m alumina powder, rinsed with deionised water, sonication in absolute ethanol, and finally rinsed with deionised water once more. Each electrode was then dried under nitrogen. Finally, the GCE or BDD was cleaned using CV in a 50 m$M$ PBS, pH 7.0, between - 0.5 and +1.5 V for GCE and -1.5 to 2 V for BDD at 0.1 V/s, until a stable CV profile was obtained.

A stock suspension of graphite (1 mg/mL) was prepared by dissolving in a solution of methanol containing 0.5 % Nafion. The suspension (5 $\mu$L) was cast onto the surface of a freshly polished GCE (Graphite/Nafion/GCE) and dried at room temperature. The solvent was evaporated slowly in air, resulting in a uniform electrode film. Carbon monolithic fragments (CM blank or NTCM) were prepared via crushing of the carbon monolith rod with a ceramic mortar and pestle. Modified electrodes were then prepared in the same way as for the graphite electrode, but replacing the graphite suspension with either a suspension of $C_{60}$, crushed CM blank or crushed NTCM, producing the various composite modified electrodes, denoted as $C_{60}$/Nafion/GCE, CM blank/Nafion/GCE and NTCM/Nafion/GCE, respectively. For the fabrication of modified BDD electrodes, carbon monolithic (CM blank or NTCM) powder was dispersed in DMF (1 mg/mL) with intensive ultrasonication for 30 min. The suspension (5 $\mu$L) was cast onto the surface of a freshly polished working BDD electrode and dried at room temperature.

## 3.3 Results and discussion

### 3.3.1 Preparation of the nanotemplated carbon monolith

The RF/Fe(III) system used for the fabrication of the nanotemplated carbon monolith was also noticeably different from that used for the formation of other types of carbon monoliths [65]. The RF resin was formed via polycondensation

mechanism, induced by HCl from partially hydrolysed $FeCl_3$ [66]. Fe(III) was used, as described below, to enhance the graphitisation process at later stage of formation. In general, most phenolic resins are resistant to complete graphitisation, even at temperatures of up to 2000 °C [48]. Such a high temperature treatment will drastically reduce the mesoporosity of the glassy carbon, limiting its surface area for many applications [55]. Thus, when the RF carbon precursor is pyrolysed at temperatures up to 1250 °C, it produces a largely amorphous structure, that resembles that of turbostratic carbon. To partially circumvent these issues, in situ catalytic graphitisation, which can be obtained at a relatively low temperature, can be applied. In the present study, $FeCl_3$ serves as a catalyst for polymerisation, as well as increasing the degree of graphitisation [55]. With such an approach it was important to understand the precise combustion behaviour process taking place, which obviously affected the physical and chemical properties of the resultant carbon monolith. In this regard, a series of TGA studies were carried out [67], which were used to mimic the carbonisation/graphitisation process, to determine the composition of materials and evaluate their thermal stability up to 800 °C.

The thermogravimetric (TG) curve obtained for the FMS template material revealed four stages of weight loss. The first one occurred between 25 °C and 120 °C with a gradual weight loss of 0.3%, mainly attributed to adsorbed moisture vaporisation, a loss also seen with samples of CM blank resin, NTCM resin, as well as pure samples of $C_{60}$ (Figure 3.2 (a)). The next stage between 120 and 400 °C shows a gradual weight loss of ~0.7% for the FMS, resulting from the deamination of the secondary amino substitute. This weight loss could also attributed to the partial decomposition of the substituted $C_{60}$ molecules, as the pure $C_{60}$ showed signs of decomposition beginning at ~ 400 °C (Figure 3.2 (a), $C_{60}$). The weight loss rate for FMS reached a maximum at ~ 530 °C and ~ 700 °C, for the third and final stage, respectively, with 5% total weight loss, mainly due to the decomposition of the covalently attached $C_{60}$. However, these two temperature values were slightly shifted towards higher temperatures, compared to TGA of pure $C_{60}$, which could be related to their covalent immobilisation. Pure $C_{60}$ under inert conditions showed a total loss of approximately 67% weight at 800 °C, in full agreement with literature data [68].

The rapid weight loss of $C_{60}$ at approximately 700 °C illustrated that the sublimation /decomposition temperature was reached.
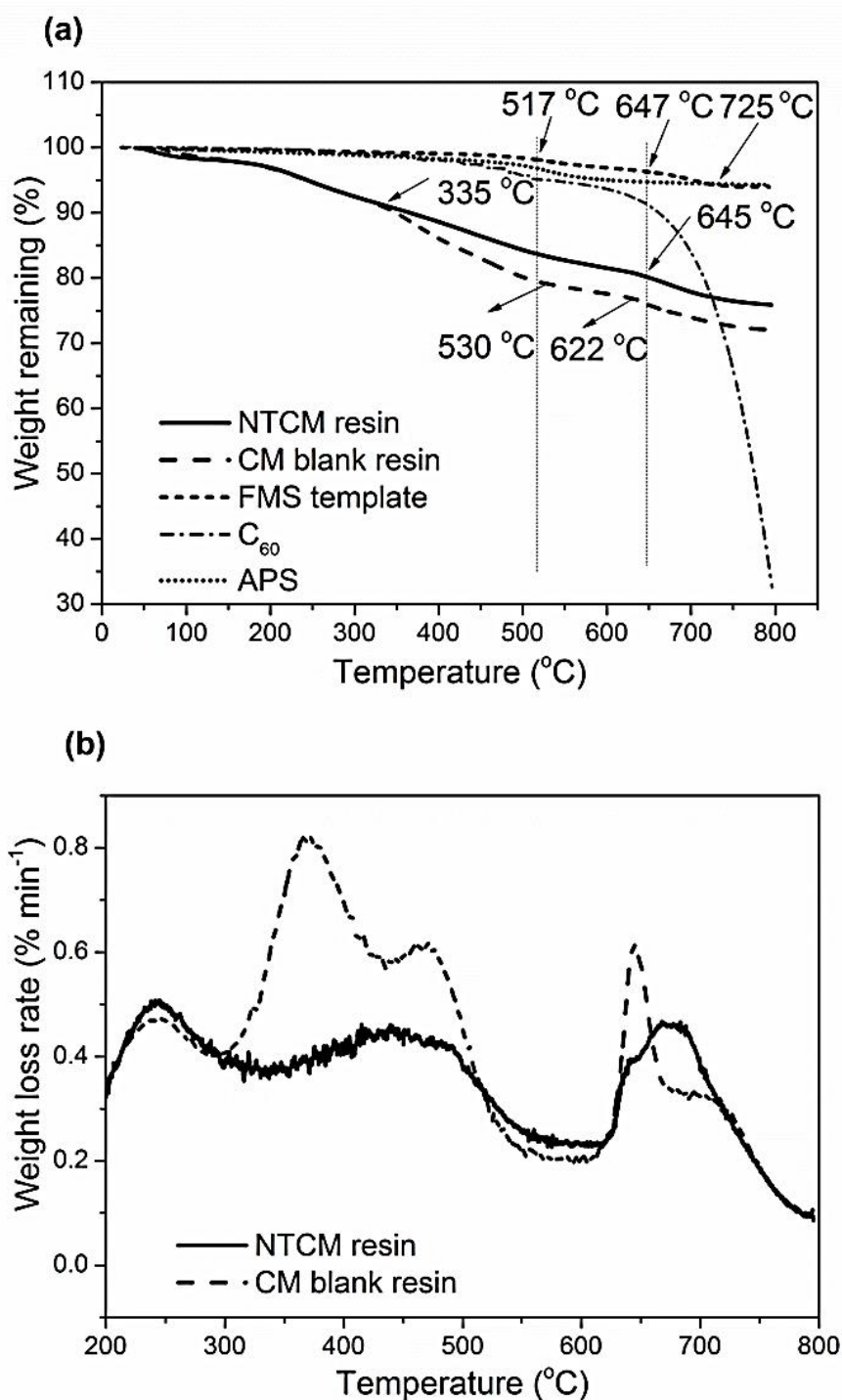


**Figure 3.2:** *Thermogravimetric curves of NTCM and CM blank precursors, FMS template, $C_{60}$ and APS. (a) Weight remaining and (b) weight loss rate.*

The TG curve for the NTCM sample (Figure 3.2 (a)) resembled closely that of the CM blank, however it displayed a lower total weight loss (~ 25%) and much lower

weight loss rates at ~ 450 ℃ and ~ 640 ℃. These differences should only arise from the presence of thermally resistant $C_{60}$. The NTCM TG curve also shows four stages of weight loss. As mentioned above, the first, between 25 ℃ and 140 ℃, with a gradual weight loss of 1.7%, was mainly attributed to vaporisation of physically adsorbed moisture, solvent residue and unreacted monomers. Following this, a series of three stages of weight loss occurred between 140 ℃ and 800 ℃, with a total weight loss of 22.3%, dominated by the partial graphitisation of the phenolic resin and the generation of water vapour, carbon monoxide, and hydrogen. During this graphitisation process, the loss of water vapour, carbon monoxide, and hydrogen should result in sample weight loss as reflected by three sub-stages (the maximum weight loss rate for stage I at ~ 240 ℃, stage II at ~ 450 ℃ and stage III at ~680 ± 20 ℃). Most water vapour and carbon monoxide is generated from the carbon precursor in stage I, between ~ 140 and~ 260 ℃, with only ~ 4% weight loss. Bulk carbonisation occurs within stage II, the maximum weight loss rate being ~ 50 ℃ lower than carbonisation of the resin without the presence of the iron catalyst [63]. This weight loss is mainly related to the decomposition of surface oxides. Notably, the catalysed graphitisation temperature for NTCM in stage III from 600 to 800 ℃ was ~ 30 ℃ higher than the CM blank, indicating the $C_{60}$ was comparably more stable than the resin. There was no additional rapid weight loss, similar to that observed for $C_{60}$, and such behaviour implies that the phenolic resin limits the functional groups on the surface of the template from being fully oxidised. However, since only trace amounts of $C_{60}$ have been introduced to the resultant monolith, the TG curve of NTCM shown in Figure 3.2 (a) was not expected to show this relatively small loss. During the heat treatment to produce the NTCM, Fe(III) was reduced to metallic Fe, inducing the subsequent localised graphitisation of the monolith [69]. The excess $FeCl_3$ has a relatively low melting point and will vaporise at ~315 ℃ [70]. The vapour consists of the dimer $Fe_2Cl_6$, which increasingly dissociates into the monomeric $FeCl_3$ at higher temperature, in competition with its reversible decomposition to give $FeCl_2$ and chlorine gas [70]. $FeCl_2$ is eventually reduced to iron when the carbonisation temperature reaches above 900 ℃. No significant weight loss took place at temperatures higher than 800 ℃, in good agreement with other RF based materials [71-73].

### 3.3.2 Structure and morphology

FE-SEM of the monolith rods in cross-section revealed that the synthesised NTCM material possessed both abundant macro- and mesopores (Figure 3.3 (b)-(d)). The macroporous structure reproduced the closely packed silica gel template (Figure 3.3 (a)) exhibiting an interconnected open pore network. The macropore generating template particles were randomly oriented and closely packed within the phenolic resin mixture under gravitational force, before the resin was solidified. The diameter of macropores on average shrank by ~ 13% (Figure 3.3 (c)) in relation to the silica gel template particles (Figure 3.3 (a)). The main reason for this was the dehydrogenation and decomposition of oxygen-containing species, leading to the densification of the carbon walls during the thermal treatment and a reduction in the concentration of micropores. The degree of shrinkage seen herein is in good agreement with a previous study [62], and importantly, despite this shrinkage, there were no visible external or internal cracks seen throughout the prepared monoliths.

A high-magnification image (Figure 3.3 (d)) shows the coarse surface texture and presence of irregular mesoporous structure upon the inner wall of the macropores within the NTCM samples. These features could result from the effect the hydrophobic $C_{60}$ surface layer of the template particles has upon its inclusion within the RF resin mixture, as no such structure was seen with the CM blank, which used simply bare silica templates. In the case of NTCM, the inner pore surfaces appeared considerably smoother in texture, including those materials produced within the previous work of Liang *et al*., and Eltmimi *et al.* [55, 62].
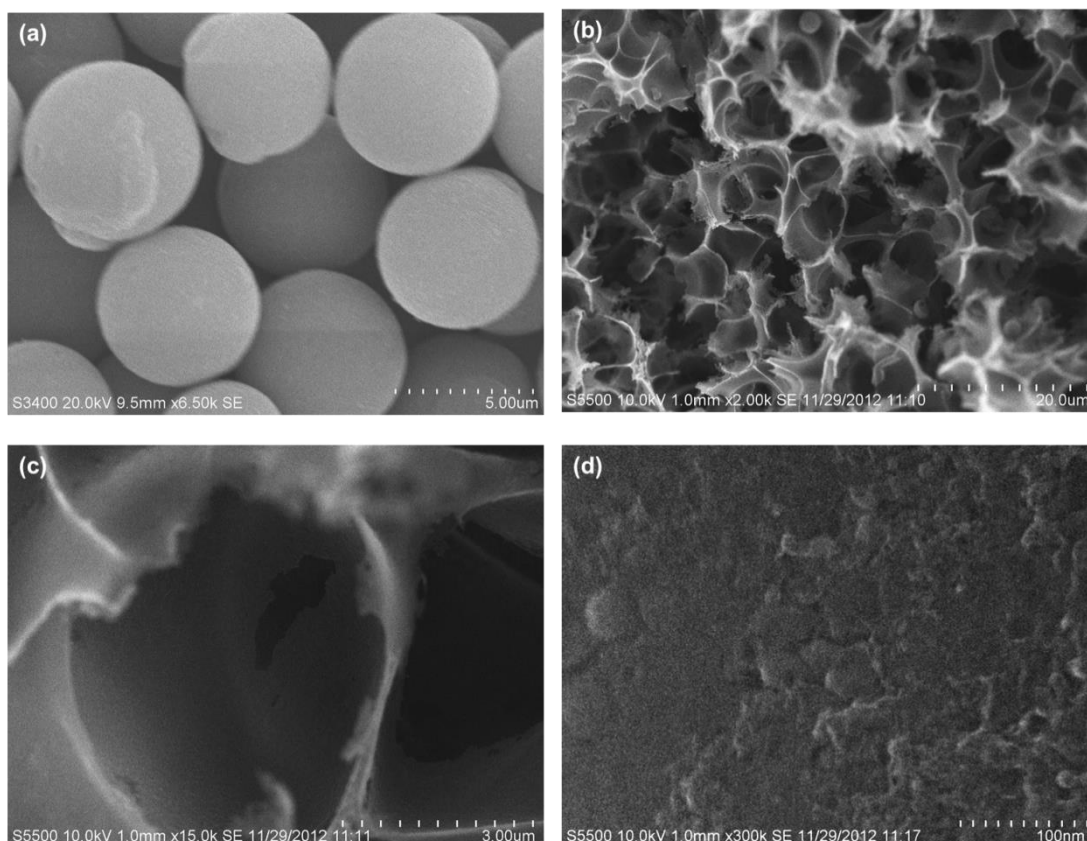
***Figure 3.3:*** *(a) SEM image of 5 μm FMS, FE-SEM image of (b) overall structure of NTCM, (c) macroporous structure and (d) mesoporous structure on NTCM macroporous wall.*

TEM analysis of both the NTCM and CM blank samples was also performed. TEM images of NTCM (Figure 3.4 (b)) appeared to confirm the absence of visible $C_{60}$ aggregates upon the walls of the NTCM material, and supported the process of partial graphitisation of NTCM, as there were few obvious graphite strips woven into the carbon mass. However, in contrast, for the CM blank without incorporated $C_{60}$, the degree of graphitisation appeared to be higher, as confirmed by the presence of a high concentration of graphite ribbons (Figure 3.4 (a)).
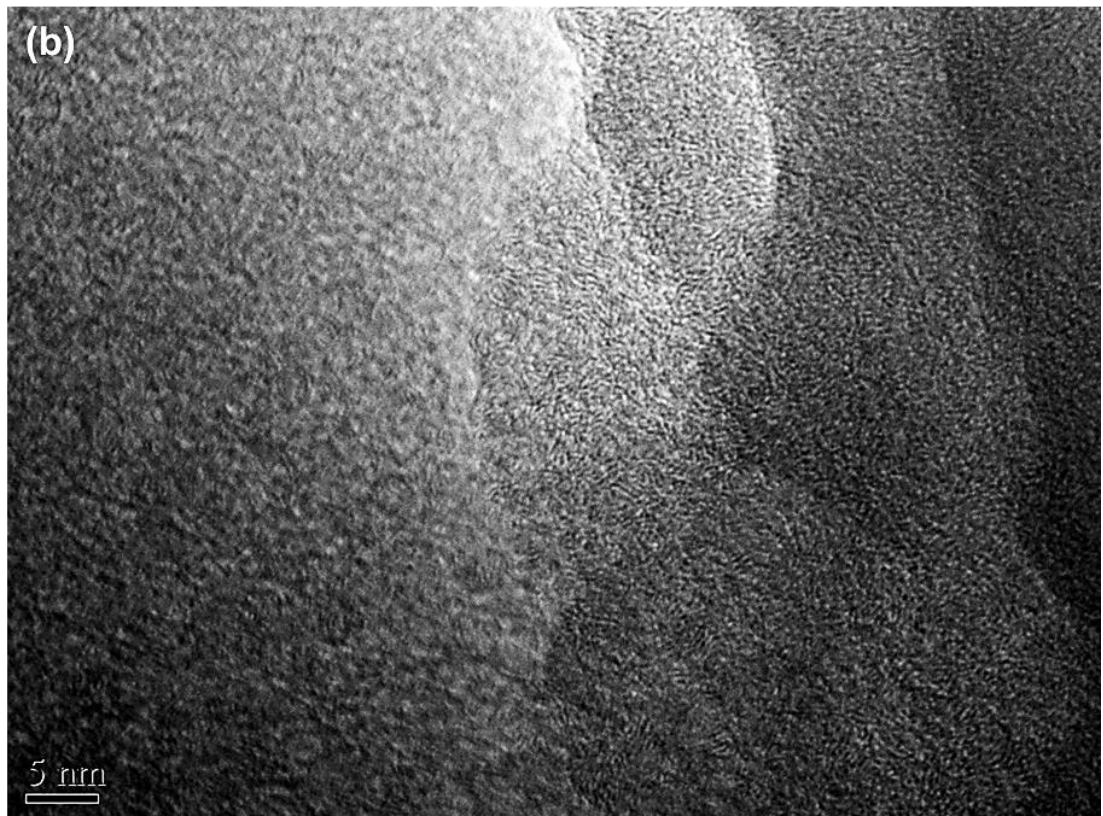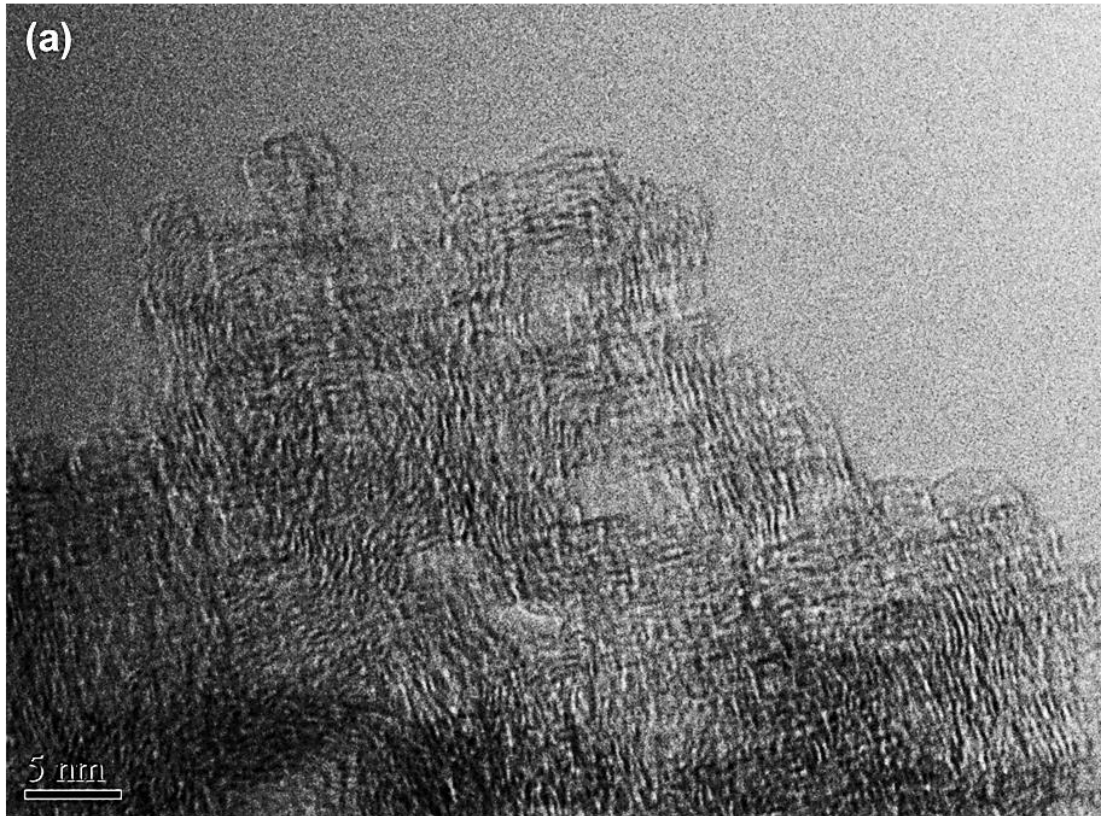
**Figure 3.4:** *TEM images of (a) CM blank and (b) NTCM.*

The EDX analysis confirmed the elements presented in CM blank and NTCM as summarised in Table 3.2 and Table 3.3, respectively. The carbon content was $94 \pm 2$ wt.% for NTCM, compared to $86 \pm 3$ wt.% for the CM blank. The EDX analysis also revealed an oxygen content of $4 \pm 1$ wt.% for the NTCM, which was considerably less than for the CM blank material, at $10 \pm 2$ wt.%. There were no detectable iron impurities within the samples. This was an important finding since the presence of iron, even at a trace level is involved in electron transfer occurring at the monolith surface, affecting the response and reproducibility of such carbon monoliths if used as electrodes [74]. The presence of trace Si ($< 1\%$) is a result of incomplete removal of the template during the HF treatment, which can be reduced further through further exposure to HF. The EDX analysis confirmed there were no traces of nitrogen present in either CM blank or NTCM samples, in the latter case indicating the all the primary or secondary amines on the silica template were sacrificed during the carbonisation.

*Table 3.2: EDX analysis of CM blank.*

| | $T_{accumulation}$ (min) | $C^a$ (%) | $O^a$ (%) | $Si^a$ (%) | $Cu^a$ (%) | $Pb^a$ (%) | Total (%) |
|---|---|---|---|---|---|---|---|
| **Spot 1** | 5 | 88.51 | 8.85 | 0.03 | 2.40 | 0.20 | 100.00 |
| **Spot 2** | 5 | 87.19 | 8.81 | 0.16 | 3.49 | 0.36 | 100.00 |
| **Spot 3** | 5 | 82.48 | 12.27 | 0.02 | 4.75 | 0.48 | 100.00 |
| **Mean** | | 86.06 | 9.98 | 0.07 | 3.55 | 0.34 | 100.00 |
| **Std. deviation** | | 3.17 | 1.99 | 0.08 | 1.18 | 0.14 | |

[a]All elements analysed is normalised.

*Table 3.3: EDX analysis of NTCM.*

| | $T_{accumulation}$ (min) | $C^a$ (%) | $O^a$ (%) | $Si^a$ (%) | $Cu^a$ (%) | Total (%) |
|---|---|---|---|---|---|---|
| **Spot 1** | 5 | 96.07 | 3.34 | 0.01 | 0.59 | 100.00 |
| **Spot 2** | 1 | 92.05 | 5.55 | 0.01 | 2.38 | 100.00 |
| **Spot 3** | 1 | 94.09 | 3.84 | 0.05 | 1.96 | 100.00 |
| **Mean** | | 94.09 | 4.24 | 0.02 | 1.64 | 100.00 |
| **Std. deviation** | | 2.01 | 1.16 | 0.02 | 0.94 | |

[a]All elements analysed is normalised.

## 3.3.3 Porosity and surface area

As shown in Figure 3.5 (a) and (b), the nitrogen adsorption/desorption isotherm of the CM blank and NTCM exhibited type IV isotherms, showing polymolecular adsorption in the mesoporous media. The adsorption hysteresis revealed the presence of a capillary condensation process in cylindrical pores with two openings. The geometry of pores can be estimated from the hysteresis loop form. Thus, the hysteresis loop for isotherms for both CM blank and NTCM belong to type B, which is characterised by the steep slope in the adsorption plot in the region close to the saturation pressure, and the steep slope for the desorption plot in the region of mid-range pressures. Such forms of hysteresis can be an indication of cylindrical pores with bottle-shape structures (wide openings and narrow "necks"), or slit-type pores [75]. Furthermore, the absence of a sharp condensation/evaporation step, or a pronounced hysteresis loop for both isotherms implied that there was no ordered structure or narrow pore size distribution within the mesoporous carbon materials. Capillary condensation for both materials started at medium relative pressures, $P/P_0$ ~ 0.45, suggesting the skeleton pores in these carbons were mainly composed of mesopores. Pore diameters for the CM blank and NTCM estimated using the Barrett-Joyner-Halenda method [76] were 10.7 and 6.1 nm, respectively.
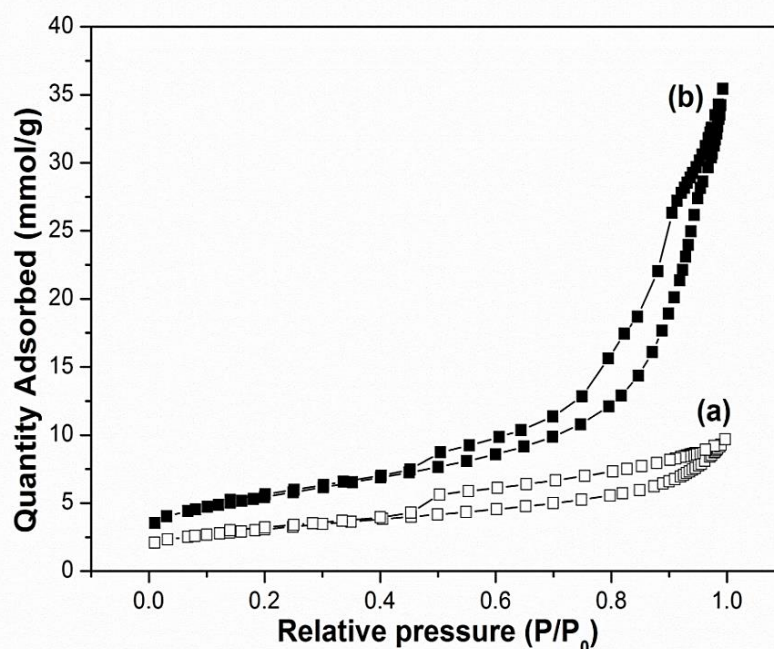


***Figure 3.5:*** *Nitrogen adsorption/desorption isotherms of (a) CM blank and (b) NTCM.*

For both isotherms, the first plateau was observed at relatively low $P/P_0$ values (~ 0.15) showing that both materials possessed some microporous structure as shown in Table 3.4. Subsequently, the total micropore volume derived from the $t$-plot was 0.028 and 0.016 $cm^3/g$ for the NTCM and the CM blank (average, $n = 3$), respectively. It is also clear from the isotherms seen, that the adsorption uptake at relative pressures below 0.05 $P/P_0$, was higher for the NTCM sample, indicating a higher degree of adsorption within the micropores. This finding shows that the introduction of fullerenes appeared to result in the formation of a greater concentration of micropores. Considering the van der Waals diameter of a fullerene molecule (~ 1.1 nm) [77], the partial decomposition of fullerenes (shown earlier by TGA) should theoretically result in the formation of pores with an average diameter below 2 nm.

The BET specific surface areas, evaluated at $P/P_0$ from 0.05 to 0.25, taking an average of three sample sets each, were calculated as $272 \pm 32$ $m^2/g$ and $435 \pm 23$ $m^2/g$ for the CM blank and NTCM, respectively (Table 3.4). The total pore volume was significantly higher for NTCM namely 1.24 $cm^3/g$, compared to 0.42 $cm^3/g$ for the CM blank. As the only difference between NTCM and the CM blank was the use of the FMS templates, it was likely therefore that the observed differences in both surface area and pore volumes, should stem firstly from the impact of the FMS surface upon the close formation of the polymer around the FMS template, and subsequently and perhaps more importantly from its impact upon the generation of a higher concentration of micropores within the macropore walls during carbonisation. These data are summarised within Table 3.4.

***Table 3.4:*** *Structural characteristics of NTCM using CM blank as a reference (n = 3).*

| Samples | $S_{BET}$[a] (m²/g) | $V_{total}$[b] (cm³/g) | $D_{meso}$[c] (nm) | $V_{micro}$[d] (cm³/g) |
|---|---|---|---|---|
| CM-blank | $272 \pm 32$ | $0.42 \pm 0.08$ | $6.54 \pm 0.68$ | $0.016 \pm 0.004$ |
| NTCM | $435 \pm 23$ | $1.24 \pm 0.08$ | $11.93 \pm 0.38$ | $0.028 \pm 0.001$ |

[a] The Brunauer-Emmett-Teller (BET) method was used to calculate the specific surface areas at relative pressure of $P/P_o = 0.01$-$0.30$. [b] Calculated by the $N_2$ amount adsorbed at the highest $P/P_o$ (~0.99). [c] The Barett-Joyner-Halenda method was used to calculate mesopore diameter from the adsorption branches of the isotherms. [d] Micropore volumes were calculated by the t-plot.

## 3.3.4 Raman spectroscopy

Based on the pioneering work of Tuinstra *et al.* [78], Raman spectroscopy was applied for the NTCM and CM blank samples, and compared to the Raman spectrum of commercial graphite (Figure 3.6). The Raman signature of NTCM exhibited three major peaks, as commonly observed for carbon nanotubes and other carbon materials, i.e., the $sp^3$ and $sp^2$ carbon phases coexisting in the sample as shown in Figure 3.6 (c). The positions of these peaks remained almost constant batch to batch. The D band, the disorder band, is located around 1350 cm$^{-1}$, which is active in Raman as the result of the imperfections or loss of hexagonal symmetry in the carbon structure [69]. Therefore, this band has been used to evaluate the degree of imperfection or crystallinity of graphite [69]. The G band, common to all $sp^2$ carbon forms, observed around 1580 cm$^{-1}$, corresponds to the Raman active $2E_{2g}$ mode of a two-dimensional network structure, i.e. the C-C bond stretching, in all carbon and graphitic materials [69].
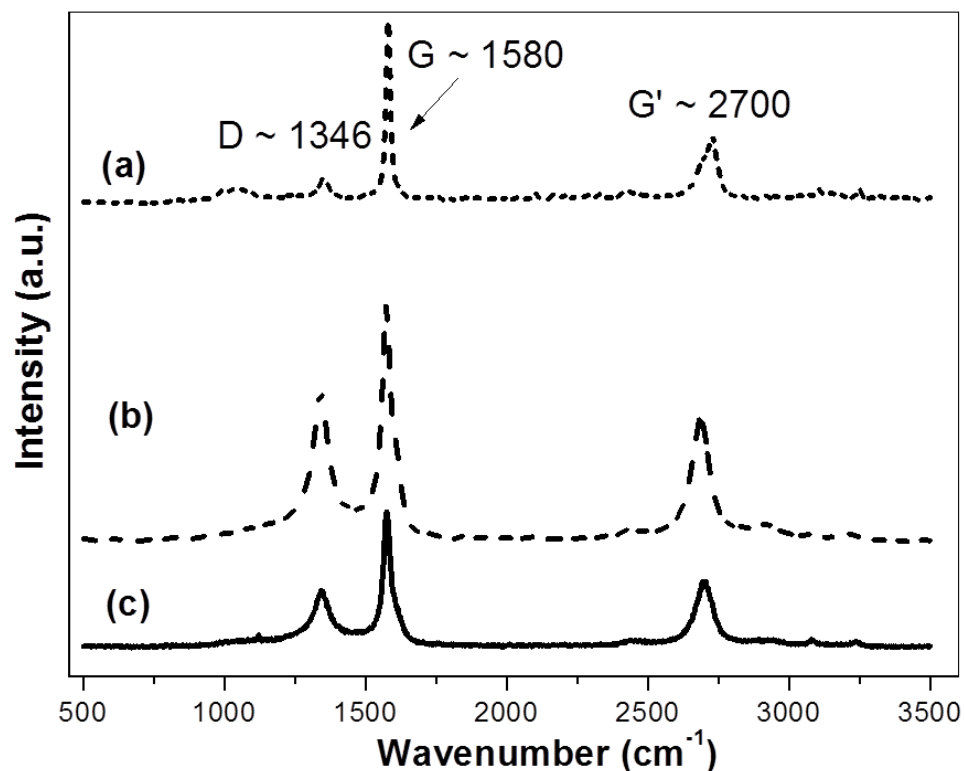


***Figure 3.6:*** *Raman spectrum of (a) commercial graphite, (b) CM blank and (c) NTCM.*

Previous studies have revealed that intensity ratio of the D to the G band, $R$, ($R = I_D/I_G$) was inversely proportional to the in-plane crystallite sizes ($L_a$) [78, 79]. The $R$ value of NTCM was 0.43, which is lower than the value of the CM blank (0.64), but still much higher than the value of commercial graphite (0.14). These results again confirmed that the NTCM was still only partially graphitised, although the degree of graphitisation was improved using the FMS template. Graphitisation must be carried out at temperature 2000 $^{o}$C or higher to achieve an R value close to commercial graphite, whereas in this work NTCM was only carbonised under 1250 $^{o}$C to preserve its mesoporous structure.

## 3.3.5 Chromatographic application

It was a great challenge to clad the carbon monolith which could operate under high pressure without the eluent leaching out of the material. In earlier works, carbon monolithic rods were cladded using heat-shrinkable Teflon tubing and then encapsulated encased rods in HPLC column housing with epoxy glue. [55, 62] There was a concern that the glue inside of the Teflon tubing could leach into the mobile phase and cause instability, and the life time of such a cladding approach was rather short since the seal between the Teflon tubing and the carbon monolithic materials was not very stable under high pressure. Therefore, several epoxy glues with known compositions were tested for their hardness and stability in HPLC mobile phase solvents, including methanol and acetonitrile. 5 Min. Permatex® general purpose epoxy and Permatex® Plastic Weld were found to be the suitable glues among the others which have minimum swelling in the testing organic solvents. The cladding procedure was developed eventually with a suitable glue and in-house modified PEEK HPLC column seen Section 3.2.5 for details. However, the CM blank column had only 7 days lifetime due to the swelling of 5 Min. Permatex® general purpose epoxy crashed the carbon monolith inside of the column. Permatex® Plastic Weld resin stayed the same therefore this is the glue should be used for coating the entire surface of the CM blank rod.

Due to the strong adsorption of aromatic analytes on carbon based sorbents, ideally strong solvents need to be used as the mobile phase [80]. The polarity of the solvent only affects the solubility of analyte in the mobile phase but does not have

any influence on the retention [81]. The weak solvents for carbon based columns usually have low molecular weight and high polarity, such as water, methanol and acetonitrile, whereas the strong solvents are heavy and/or aromatic molecules, such as chloroform, benzene and xylene [81]. Dichloromethane is one of the most frequently used solvents [55]. Unfortunately, the glue used was not stable in strong solvents such as hexane or dichloromethane [82]. As a result, the CM column was tested with methanol as a mobile phase, which could cause poor separation efficiency.

Some important information regarding the quality and properties of the prepared carbon monolith can be obtained from column liquid chromatographic evaluation [62]. Firstly, the retention behaviour of this carbon monolith can be obtained from a separation of a phenolic mixture under reversed phase mode as shown in Figure 3.7. Table 3.5 showed the calculated chromatographic parameters obtained from the chromatogram as shown in Figure 3.7. The efficiency of this column was rather poor and the run time was over 100 minutes for the separation of just three components. This was due to the presence of micropores (according to the BET result) as well as strong hydrophobic and $\pi$-$\pi$ interaction between the carbon phase and analytes [82]. However, the chromatogram (Figure 3.7) demonstrated there was reasonable selectivity for phenols on this column as compared to previously obtained results [62].

**Table 3.5:** *Chromatographic parameters obtained from the separation of three phenol derivatives on a CM blank column (Figure 3.7).*

| Analytes | $k'$ | $A$ | $N$/m | $^aR_s$ | Log p | $k'$ PGC [83] | $pK_a$ |
|---|---|---|---|---|---|---|---|
| **2-*tert*-butyl-4-methylphenol** | 2.25 | - | 173.6 | - | 3.97 | 0.57 | 11.72 |
| **Phenol** | 21.23 | 9.45 | 180.2 | 0.90 | 1.46 | 0.30 | 9.99 |
| **4-methylphenol** | 56.17 | 1.65 | 253.6 | 0.40 | 1.94 | 0.76 | 10.10 |

[a] The selectivity and resolution are calculated for two adjacent peaks, respectively, i.e. the resolution between 2-*tert*-butyl-4-methylphenol and phenol is calculated and written in the second row belonging to phenol and so on.

[b] The retention factor for the same analyte obtained on the porous graphitic carbon column from reference .

[c] $t_0$ = 0.883 min
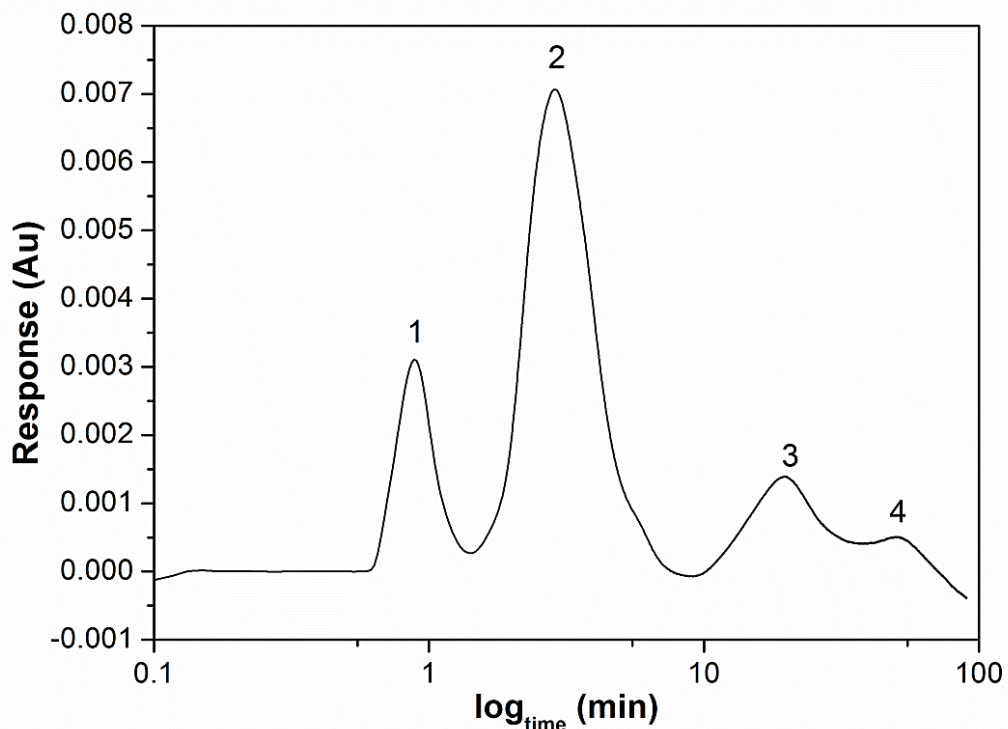
***Figure 3.7:*** Chromatogram of three phenol derivatives on a CM blank column *(74.5 × 4 mm O.D., 5 μm). Conditions: mobile phase 90 : 10, methanol : water at flow rate of 1 mL/min at isocratic mode, injection volume 10 μL, UV detector at 280 nm and column temperature ambient. Peaks: (1) System peak, (2) 2-tert-butyl-4-methylphenol, (3) phenol and (4) 4-methylphenol.*

The calculated results (Table 3.5) showed the retention order of the three phenols on the CM blank column, which were not in exactly similar order to that on a porous graphic carbon column (PGC, or Hypercarb) [83]. The CM blank column exhibited no correlation between the retention of phenols and their hydrophobicity and pKa values. Such phenomenon was exactly same as observed on the similar column previously prepared by Eltmimi *et al.* [62]. The peak of phenol eluted second after 2-*tert*-butyl-4-methylphenol, whereas it eluted first on PGC column. Phenol on the CM blank column eluted slower, which could be due to hydrogen bonding between analyte and oxygen contained functional groups on the stationary phase. The resolutions for phenol and 4-methylphenol were less than 1.5 between the adjacent peak, which were indicatored that the sample components were not well ('baseline') separated (Table 3.5). However, the values of selectivities for the all analytes were greater than 1 which is independent of flow rate.

Secondly, the retention behaviour of the CM blank column was demonstrated for five different analytes with three different concentrations of methanol as mobile phase under reversed phase modes as shown in Figure 3.8. The logarithms of the retention factors (log$k$) of phenols on CM blank column presented an almost linear relationship with increases in methanol concentration. The plots of the log$k$ of phenols versus the content of methanol were V-shaped with the inflection point at an 80% content of methanol in the mobile phase on the microdispersed stick of detonation nanodiamonds (MSDN) column (Figure 3.9 (a))[83]. The retention order of phenols on MSDN column was dependent on the acidity of the phenols rather than the content of organic solvent in the mobile phase, i.e. higher the acidity of the analyte longer the retention. Such retention behaviour was caused by a large number of oxygen contained functional groups on the surface of MSDN, including carboxyl, carbonyl and hydroxyl [84]. The comparable experiment was also carried out on a PGC column in the literature as shown in Figure 3.9 (b) [83]. The log$k$ of phenols on PGC is inversely proportional to the concentration of methanol in the mobile phase [42]. This is because the nonpolar nature of the graphite surface and the sorbent is characterised by hydrophobic interaction which is considered a reverse phase mechanism for the retention of phenols. The relationship between log$k$ and the contents of methanol on the CM blank column was completely different from MSDN and has the similar trend of similar PGC. More points were needed to confirm this trend; however the life time of the column was rather short to carry out the further study.
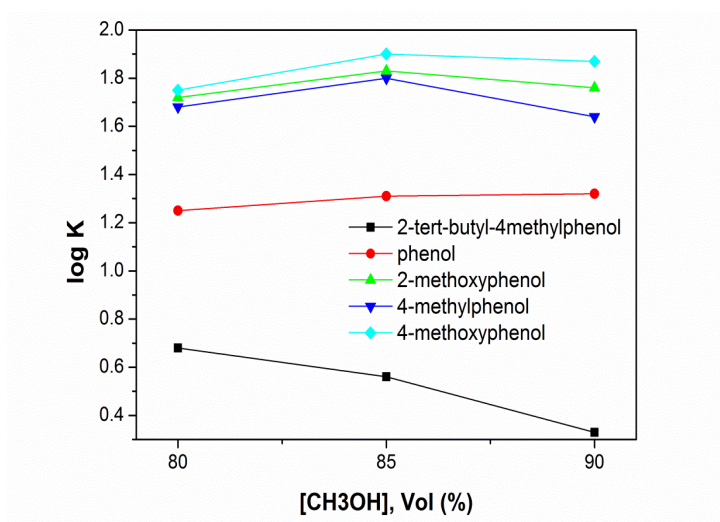


*Figure 3.8: Retention behaviour of phenols on CM column.*
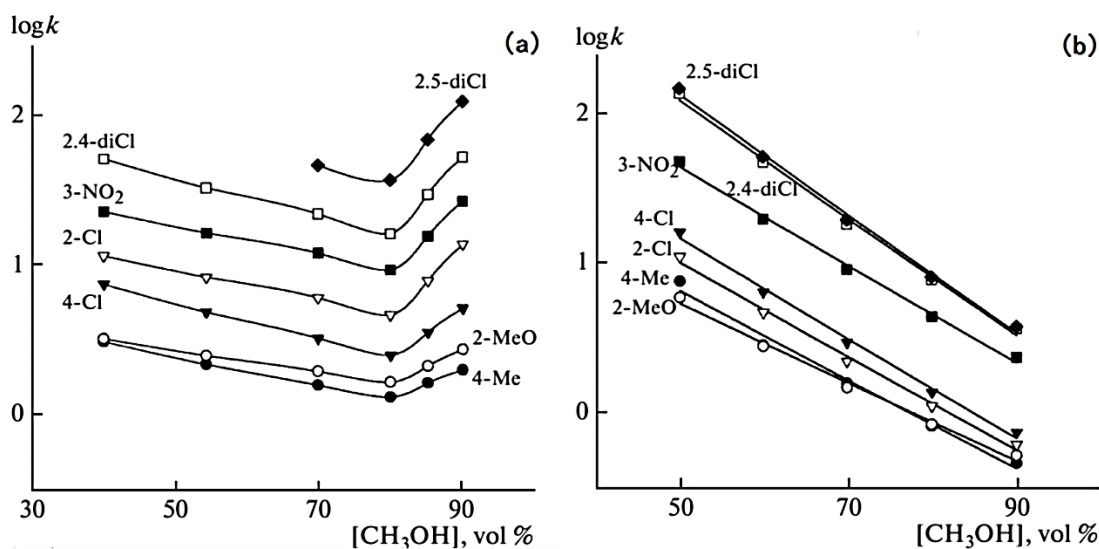
**Figure 3.9:** *Retention behaviour of phenols on (a) MSDN and (b) PGC column (Reproduced from [83]).*

Finally, the dependence of the column back pressure on the flow rate was studied. Figure 3.10 shows a plot of the pressure versus the mobile phase which is directly proportion al to flow rate. Therefore, the plot proved again there were no cracks or significant internal cavities presented within the monolithic rod and uniformity in the porous structure. Column permeability is one of the most important characteristics describing the column properties. Term permeability refers to the column packed with a stationary phase (particles or monolith) and describes how easy the mobile phase through the packing materials. The permeability of column can be calculated by Equation 3.5 as shown in Table 3.1. According to this equation, it can be seen that the flow of the mobile phase through the column is directly proportional to the pressure across the column and inversely proportional to the mobile phase viscosity and the length of the column. The permeability was found to be $6.5 \times 10^{-11}$ cm$^2$ for the CM blank monolith (74.5 $\times$ 4 mm I.D.) with 5 μm macroporous flowthrough channel, whereas the permeability for similar carbon monolith (80 $\times$ 3.4 mm I.D.) with 10 μm macroporous flowthrough channel was found to be $1.588 \times 10^{-8}$ cm$^2$ [55]. The permeability for the CM blank column was approximately 250 times smaller than the literature value, which showed the good correlation with the flowthrough channel being twice small [85]. At the same time, this value was very close to the Chromolith Performance columns which was $7.7 \times 10^{-10}$ cm$^2$ reported by Guiochon's group [55].
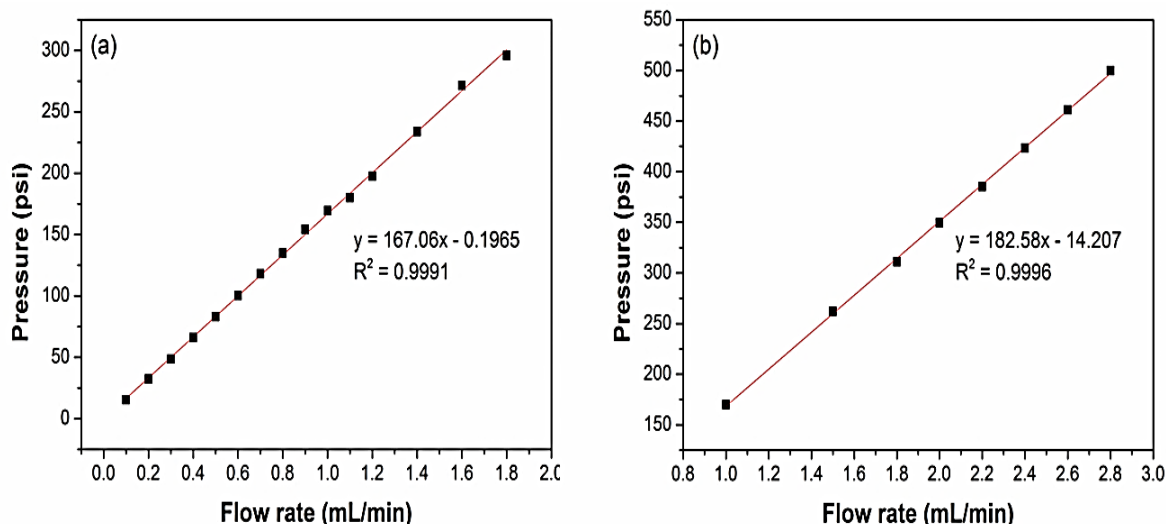
**Figure 3.10:** *Plot of the pressure versus the mobile phase flow rate (a) low flow rate (b) high flow rate (90% methanol as mobile phase).*

The NTCM was not suitable for the purpose of separation due to the presence of micropores [86]. Also the NTCM was too fragile to be cladded into a column and had a higher volume in micropores compared with the CM blank. The run time required was even longer to separate the same compounds as shown Figure 3.9. Therefore, it was not deemed necessary to further evaluate its chromatographic application.

## 3.3.6 Electrochemical measurement

Based on the similarity between the Raman signature of NTCM and multi-walled carbon nanotubes (MWCNTs), a series of experiments was conducted to assess the applicability of NTCM material as a substrate for electrode modifications. MWCNTs have been used very extensively for numerous important biosensing platforms and carbon monolithic substances have also been proven as useful materials for probing direct bioelectrochemistry and selective detection of hydrogen peroxide [74].
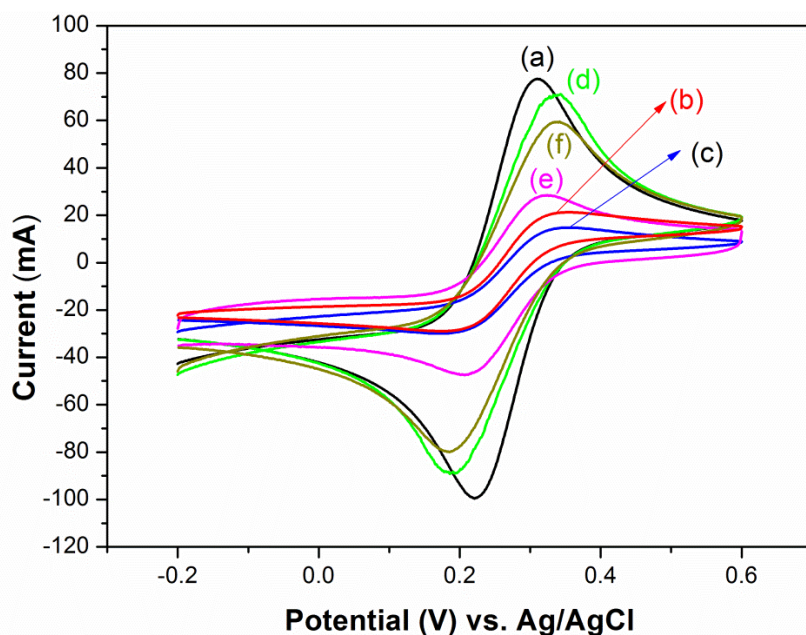
***Figure 3.11:*** *CVs of (a) GCE, (b) Nafion/GCE, (c) graphite/Nafion/GCE, (d) C$_{60}$/Nafion/GCE, (e) CM blank/Nafion/GCE and (f) NTCM/Nafion/GCE.*

The electrochemical behaviour of a glassy carbon electrode modified with NTCM or CM was first evaluated by cyclic voltammetry and compared to that of the GCE modified with pristine C$_{60}$ or graphite. Studying the electrochemical performance of such materials is helpful to understand their chemical composition and morphology [87]. With Fe(CN)$_6^{3-/4-}$ as a redox probe, the cyclic voltammograms of the modified GCEs exhibited quasi-reversible behaviour, as , as ΔEp (peak separation between the anodic and cathodic peak) was noticeably greater than the theoretical value of 59 mV for a reversible electrochemical process. Considering the ΔEp value obtained for each modified electrode, the NTCM modified GCE (Figure 3.11 (f)) resembled the C$_{60}$ modified GCE (Figure 3.11 (b)), whereas the CM modified GCE (Figure 3.11 (e)) resembled the graphite modified GCE (Figure 3.11 (c)). Furthermore, the response current to Fe(CN)$_6^{3-/4-}$ of the NTCM modified GCE (Figure 3.11 (f)) was higher compared to the CM modified GCE (Figure 3.11 (e)), implying a higher porosity and surface area of the resulting film.

Following the above comparison, the modification of a BDD electrode with the new NTCM material was investigated. The BDD was selected because it exhibits very high potentials for both oxygen and hydrogen evolution [88]. The BDD film has attracted considerable interest in electrochemistry for use as active electrodes

due to its superior chemical, physical, and mechanical inertness. Figure 3.12 A (a) shows a cyclic voltammogram of a bare BDD electrode in 0.1 M KCl solution, once again containing $Fe(CN)_6^{3-/4-}$ (10 mM) as a probe.
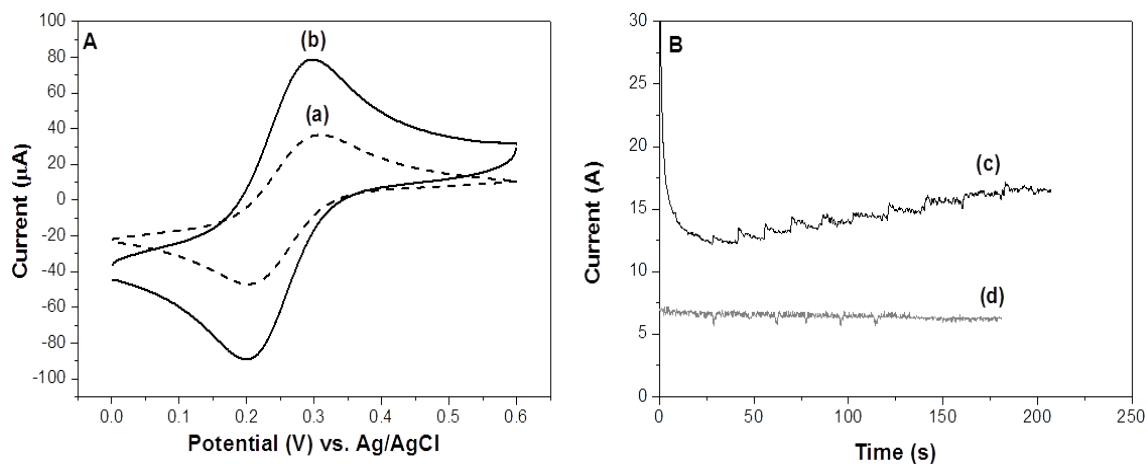


***Figure 3.12:*** *(A) CVs of (a) bare BDD electrode and (b) NTCM modified BDD electrode (scan rate, 0.1 V/s). (B) Amperometric response (I vs. t) of (c) the NTCM modified BDD electrode and the bare BDD electrode (d) to successive addition of 5 μM hydrogen peroxide. The electrodes were poised at +1.4 V vs. Ag/AgCl with 20 mM phosphate buffer pH 7 as the supporting electrolyte.*

A quasi-reversible process was also observed for the BDD electrode modified with NTCM (Figure 3.12 A, (b)). Of interest was the lower $\Delta E_p$ value of 91 mV, compared to 95 mV of the pristine BDD electrode (Figure 3.12 A, (a)). This is a quasi-reversible process because $\Delta E_p$ is greater than the theoretical value of 59 mV for a reversible electrochemical process. Nevertheless, this peak separation value was similar to or even smaller than the literature values obtained with BDD electrodes [89]. Such a result illustrated the relatively rapid electron-transfer rate at the NTCM modified diamond-solution interface. Given the above observation and to further demonstrate the potential applicability of NTCM in electrochemistry fields, the NTCM modified BDD electrode was then applied to the detection of hydrogen peroxide, a small molecule which plays an important role in clinical and analytical chemistry. The NTCM modified BDD electrode was able to detect hydrogen peroxide with a detection limit of below 300 n*M* (Figure 3.12 B, (c)) whereas the pristine BDD electrode was not responsive to this target compound (Figure 3.12 B, (d)).

111

## 3.4 Conclusion

In brief, nanotemplated trimodal carbon monolithic materials were successfully synthesised using the fullerene modified silica gel as solid templates and resorcinol /formaldehyde as a carbon precursor, with Fe (III) as a localised graphitisation catalyst. The nanotemplated monolith possessed both macropore and narrowly distributed mesopores, and increased micropores with $sp^3$ and $sp^2$ carbon phases coexistent in the samples. Furthermore, their textural properties such as BET specific surface area, pore volume, and pore size were increased for NTCM in comparison with the CM blank. All NTCM had a high specific sure area, high mesopore volume, and narrow size distributed mesopores. These NTCM materials are likely to find their use in a variety of applications including biomolecule adsorptions, catalyst supports, drug delivery, or electrode materials.

## 3.5 References

1. J. Lee, J. Kim, T. Hyeon, Recent progress in the synthesis of porous carbon materials. *Advanced Materials* **18**, 2073 (2006).
2. C. Liang, Z. Li, S. Dai, Mesoporous carbon materials: Synthesis and modification. *Angew. Chem.-Int. Edit.* **47**, 3696 (2008).
3. A. H. Lu, G. P. Hao, Q. Sun, X. Q. Zhang, W. C. Li, Chemical Synthesis of Carbon Materials With Intriguing Nanostructure and Morphology. *Macromol. Chem. Physic* **213**, 1107 (2012).
4. R. Ryoo, S. H. Joo, M. Kruk, M. Jaroniec, Ordered Mesoporous Carbons. *Advanced Materials* **13**, 677 (2001).
5. Y. Meng *et al.*, Ordered mesoporous polymers and homologous carbon frameworks: Amphiphilic surfactant templating and direct transformation. *Angew. Chem.-Int. Edit.* **44**, 7053 (2005).
6. A. Taguchi, J. H. Smatt, M. Linden, Carbon monoliths possessing a hierarchical, fully interconnected porosity. *Advanced Materials* **15**, 1209 (2003).
7. Z. G. Shi, Y. Q. Feng, L. Xu, S. L. Da, M. Zhang, Synthesis of a carbon monolith with trimodal pores. *Carbon* **41**, 2677 (2003).
8. Y. Wang, S. Tao, Y. An, Superwetting monolithic carbon with hierarchical structure as supercapacitor materials. *Microporous Mesoporous Mat.* **163**, 249 (2012).
9. X. R. Wen *et al.*, Three-dimensional hierarchical porous carbon with a bimodal pore arrangement for capacitive deionization. *Journal of Materials Chemistry* **22**, 23835 (2012).
10. C. Liang, S. Dai, G. Guiochon, A graphitized-carbon monolithic column. *Analytical Chemistry* **75**, 4904 (2003).
11. Z. G. Shi, F. Chen, J. Xing, Y. Q. Feng, Carbon monolith: Preparation, characterization and application as microextraction fiber. *J. Chromatogr. A* **1216**, 5333 (2009).

12. Y. S. Hu *et al.*, Synthesis of hierarchically porous carbon monoliths with highly ordered microstructure and their application in rechargeable lithium batteries with high-rate capability. *Adv. Funct. Mater.* **17**, 1873 (2007).

13. G. P. Hao *et al.*, Structurally Designed Synthesis of Mechanically Stable poly(benzoxazine-co-resol)-based porous carbon monoliths and their application as high-performance $CO_2$ capture sorbents. *Journal of the American Chemical Society* **133**, 11378 (2011).

14. A. H. Lu, J. H. Smatt, S. Backlund, M. Linden, Easy and flexible preparation of nanocasted carbon monoliths exhibiting a multimodal hierarchical porosity. *Microporous Mesoporous Mat.* **72**, 59 (2004).

15. S. Álvarez, A. B. Fuertes, Synthesis of macro/mesoporous silica and carbon monoliths by using a commercial polyurethane foam as sacrificial template. *Materials Letters* **61**, 2378 (2007).

16. L. Y. Xu, Z. G. Shi, Y. Q. Feng, Preparation of a carbon monolith with bimodal perfusion pores. *Microporous Mesoporous Mat.* **115**, 618 (2008).

17. A. H. Eltmimi *et al.*, Preparation, characterisation and modification of carbon-based monolithic rods for chromatographic applications. *Journal of Separation Science* **33**, 1231 (2010).

18. M. Sevilla, A. B. Fuertes, Fabrication of porous carbon monoliths with a graphitic framework. *Carbon* **56**, 155 (2013).

19. D. C. Harris, *Quantitative chemical analysis*. (W.H. Freeman and Company, New York, 7th ed., 2006).

20. Y. Huang *et al.*, One-step hydrothermal synthesis of ordered mesostructured carbonaceous monoliths with hierarchical porosities. *Chemical Communications*, 2641 (2008).

21. S. A. Al-Muhtaseb, J. A. Ritter, Preparation and Properties of Resorcinol–Formaldehyde Organic and Carbon Gels. *Advanced Materials* **15**, 101 (2003).

22. S. Zhang, L. Li, A. Kumar, *Materials characterization techniques*. (CRC Press Taylor & Francis Group, Boca Raton, 2009), pp. 290-291.

23. M. Egashira, K. Hoshii, T. Araki, Y. Korai, I. Mochida, Effects of fullerene addition on the carbonization of synthetic naphthalene isotropic pitch. *Carbon* **36**, 1739 (1998).

24. F. J. Maldonado-Hodar, C. Moreno-Castilla, J. Rivera-Utrilla, Y. Hanzawa, Y. Yamada, Catalytic graphitization of carbon aerogels by transition metals. *Langmuir* **16**, 4367 (2000).

25. N. Wiberg, A. F. Holleman, E. Wiberg, *Inorganic Chemistry*. (Academic Press, San Diego, 1st ed., 2001).

26. A. Oberlin, Transformation of ingraphitizable carbon by thermal treatment in presence of iron. *Carbon* **9**, 39 (1971).

27. M. Audier, A. Oberlin, M. Oberlin, M. Coulon, L. Bonnetain, Morphology and crystalline order in catalytic carbons. *Carbon* **19**, 217 (1981).

28. C. Lin, J. A. Ritter, Effect of synthesis pH on the structure of carbon xerogels. *Carbon* **35**, 1271 (1997).

29. X. He *et al.*, Porous graphitized carbon monolith as an electrode material for probing direct bioelectrochemistry and selective detection of hydrogen peroxide. *Analytical Chemistry* **84**, 2351 (2012).

30. S. J. Gregg, K. S. W. Sing, *Adsorption, surface area, and porosity*. (Academic Press Inc, Ltd., London, 1967), pp. 144-149.

31. E. P. Barrett, L. G. Joyner, P. P. Halenda, The determination of pore volume and area distributions in porous substances. 1. computation from nitrogen isotherms. *Journal of the American Chemical Society* **73**, 373 (1951).

32. R. Qiao, A. P. Roberts, A. S. Mount, S. J. Klaine, P. C. Ke, Translocation of $C_{60}$ and its derivatives across a lipid bilayer. *Nano Letters* **7**, 614 (2007).

33. F. Tuinstra, J. L. Koenig, Raman spectrum of graphite. *Journal of Chemical Physics* **53**, 1126 (1970).

34. M. S. Dresselhaus, A. Jorio, M. Hofmann, G. Dresselhaus, R. Saito, Perspectives on carbon nanotubes and graphene raman spectroscopy. *Nano Letters* **10**, 751 (2010).

35. L. Pereira, Porous graphitic carbon as a stationary phase in HPLC: Theory and applications. *Journal of Liquid Chromatography & Related Technologies* **31**, 1687 (2008).

36. H. Colin, C. Eon, G. Guiochon, Reversed-phase liquid-solid chromatography on modified carbon black. *J. Chromatogr. A* **122**, 223 (1976).

37. C. West, C. Elfakir, M. Lafosse, Porous graphitic carbon: A versatile stationary phase for liquid chromatography. *J. Chromatogr. A* **1217**, 3201 (2010).

38. O. N. Fedyanina, P. N. Nesterenko, Regularities of chromatographic retention of phenols on microdispersed sintered detonation nanodiamond in aqueous—organic solvents. *Russian Journal of Physical Chemistry A* **84**, 476 (2010).

39. B. V. Spitsyn *et al.*, The physical-chemical study of detonation nanodiamond application in adsorption and chromatography. *Diamond and Related Materials* **19**, 123 (2010).

40. O. N. Fedyanina, P. N. Nesterenko, Regularities of Chromatographic Retention of Phenols on Microdispersed Sintered Detonation Nanodiamond in Aqueous-Organic Solvents. *Russian Journal of Physical Chemistry A* **84**, 476 (2010).

41. F. Švec, T. B. Tennikova, Z. Deyl, *Monolithic materials: preparation, properties, and applications, 1$^{st}$ ed.* (Elsevier, Amsterdam, 2003).

42. G. Guiochon, Monolithic columns in high-performance liquid chromatography. *J. Chromatogr. A* **1168**, 101 (2007).

43. Z. Wang, Z. Lu, X. Huang, R. Xue, L. Chen, Chemical and crystalline structure characterizations of polyfurfuryl alcohol pyrolyzed at 600 ℃. *Carbon* **36**, 51 (1998).

44. J. H. T. Luong, K. B. Male, J. D. Glennon, Boron-doped diamond electrode: synthesis, characterization, functionalization and analytical applications. *Analyst* **134**, 1965 (2009).

45. M. Hupert *et al.*, Conductive diamond thin-films in electrochemistry. *Diamond and Related Materials* **12**, 1940 (2003).

# Chapter 4

# Porous Carbon Monoliths as Multifunctional Adsorbents for Organic Pollutants

*"Beyond a doubt truth bears the same relation to falsehood as light to darkness."*

Leonardo da Vinci

# Abstract

Three different classes of small aromatic molecules, ubiquitous and harmful environmental pollutants in water systems, were used as modal analytes for the adsorption study of carbon monoliths in both rod and powder form, respectively. Selected organic molecules included the simplest polyaromatic compound (naphthalene), phenolic compounds (phenol, 2-chlorophenol and bisphenol A (BPA)) and a basic dye (methylene blue (MB)).

Initially, phenolic compounds were used for a proof-of-concept SPE study using CMs in rod form (10 mm long by 3 mm O.D. and ~10 mg/rod). A tailored SPE procedure was developed for these carbon monolithic rods. Adsorption kinetics for NTCM revealed unique selectivity and higher adsorption capacity in comparison with CM blank. Naphthalene and benzoic acid were used to confirm the retention behaviour of the carbon monolithic rods. However, neither of CM blank or NTCM rod was suitable to be used as SPE media because of the slow adsorption kinetics and poor recoveries of analytes (maximum recovery < 40 % in acetonitrile) at room temperature. NTCM showed more size recognition, hydrophobicity, hydrogen bonding and $\pi$-$\pi$ interaction effect than CM blank according to its overall higher adsorption capacity and lower recovery results.

Later, in order to minimise the capillary diffusion effects of CMs, both of them were crushed into powders for a dynamic batch adsorption of MB and were also investigated using the pseudo-first and second-order kinetics. CM blank outperformed NTCM with a maximum capacity of 127 mg/g compared to ~80-100 mg/g for NTCM. The Langmuir isotherm model was applicable for describing the binding data for MB on CM blank indicating the homogeneous surface of this material. The Gibbs free energy of - 15.22 kJ/mol estimated for CM blank unravelled the spontaneous nature of this adsorbent for MB and appreciably fast adsorption than the other sorbents. In contrast, the adsorption isotherm of NTCM followed the Freundlich model, which hinted toward the formation of multilayers with surface heterogeneity to reflect the incorporation of $C_{60}$ in the polymer network. Both pH and temperature exhibited only a modest effect on the adsorption of MB onto CM blank and NTCM. The desorption of MB from CM blank using acetonitrile was very

effective with over 94 % of MB desorbed from CM blank within 10 min to allow the reusability of this porous carbon material. In contrast, acetonitrile was less effective than ethanol in desorbing MB from NTCM. The two solvents were incapable of completely desorbing MB on commercial granular coal-derived activated carbon.

## Aim

The goal of this work was to understand the adsorption performance of two emerging nanomaterials: unmodified CM blank and nanotemplated NTCM in rod and powder form, respectively, in an aqueous environment. The carbon monolithic rods were evaluated using phenolic compounds, naphthalene and benzoic acid as the model analytes. In this study, the tailored SPE procedure using carbon monolithic rods was developed. The adsorption capacity and mechanism of phenolic compound were investigated. The carbon monolithic powder was intensively studied using MB as a model analyte for demonstration of dye removal. In the MB study, the effects of contact time, analyte concentration, pH, temperature and reusability were investigated in order to identify the most favourable sorbent for MB contaminant removal from water. These studies enabled identification of suitable way to use carbon monoliths as SPE sorbents.

## 4.1 Introduction

SPE is one of the most widespread sample preparation techniques for extraction and pre-concentration of non-volatile liquid samples in recent years [1-3]. It has many advantages over liquid-liquid extraction including decreased organic solvent usage, increased extraction efficiency, and good selectivity of specific analytes in a mixture [4]. The SPE process can be carried out either on-line or off-line. It is not only used in extraction and pre-concentration of several analytes at the same time to achieve detection limits that are as low as legislation requires, but also to purify the sample and minimize the interferences or undesired compounds in a complex sample during its analysis. These complex samples can be environmental, food, beverage, pharmaceutical and biological in nature [5]. It consequently helps to improve the separation, increase the detection limit, increase the accuracy and precision, as well as lengthening the lifetime of the separation columns. SPE sorbents are usually

classified into three categories: chemically bonded silica-based, macroporous polymers, and graphitised carbon based. [6] The most commonly used sorbents are silica- and polymer - base. Silica-based materials have unavoidable presence of polar silanol groups which result in relatively narrow pH stability range (pH = 2 - 8). Though polymer-based supports are usually a viable alternative to silica sorbents, they swell in organic solvents and most of them only operate in the low concentration of organic or non-organic solvent, i.e. aqueous solutions. For instance, carbon materials have a long history of use in adsorption of polar organic compounds from active carbon [7] to graphitized carbon blacks [8]. Lately, porous PGC, HyperSep™ Hypercarb, Supelclean ENVI-Carb Plus have been used as alternative sorbents. Therefore in recent years, the search for new selective and effective adsorbents still remains one the most important challenges of SPE, sample enrichment and passive sampling.

Carbon monoliths have emerged only recently in the field of solid phase extraction after being popular in many the other areas of research, such as energy storage [9], super-capacitors [10], working electrodes [11] and heterogeneous catalyst supports [12] as well as early attempts in the application of HPLC stationary phases [13, 14]. They can be alternative sorbents to conventional silica and polymer based sorbents owing to their high surface area, thermal stability, chemical inertness (absence of swelling in most organic solvents, operate in pH range 1-14) and the possibility of chemical surface modification. The versatile nature of graphitised carbon's unique retention behaviour enables the extraction of the polar analytes based on hydrophobic, electron delocalisation and weak ionic exchange mechanism under the appropriate conditions (solvents, pH and temperature) [4, 15, 16]. The monolithic material exhibits lower hydraulic resistance, higher permeability, higher efficiency and faster mass transfer in comparison to particular materials in terms of its separation performance [17, 18]. These features arise from the monolithic material which has the bimodal interconnected porous structure and high porosity. Their integrated porous structure also minimises the packing issues. Moreover, they have high affinity for the polar compounds with partial / high solubility solutes and inert surface properties because of their graphitic compositions.

118

## 4.1.1 Analytes of interest

The presence of large amounts of phenol and derivatives thereof in water sources constitute a serious threat to human and water quality [19]. Phenolic compounds are very harmful to living organisms, even at low concentrations due to their toxicity and carcinogenicity properties. Thus, it is important to remove phenols from the water stream before they can harm any living organisms [20]. The Environmental Protection Agency has set a limit of 0.1 mg/L of phenol in wastewater. The World Health Organisation is stricter on phenol regulation. It sets a limit of 0.001 mg/L as the amount of phenol concentration in drinking water [12]. Trace analysis of such polar micro-pollutants (phenols and the other degradation products) with partial/ high solubility in water are still a remaining challenge, the conventional n-alkylsilica ($C_2$, $C_8$ and $C_{18}$) and polymer-based sorbents (mainly PS-DVB) are not retentive enough to allow percolation of a high enough volume of sample before breakthrough occurs [5]. An alternative sorbent owning good selectivity, rapid adsorption and desorption and chemical/thermal inert surfaces are highly in demand for SPE of phenols.

MB is an important basic dye used for printing calico, dyeing cotton and leather and could cause various harmful effects such as eye burns, irritation to the gastrointestinal tract and to the skin [21]. In brief, over 100,000 types of dyes have been used for industrial applications in textile, pulp and paper, pharmaceuticals, tannery, etc. [22]. Dyes used in the textile industry must have a high chemical and photolytic stability; therefore, biodegradation or biological treatment of such dyes is very difficult, time-consuming and ineffective. Currently, the textile industry uses over 10,000 different dyes with an annual consumption of $7 \times 10^5$ ton and their eventual discharge into waste streams poses a serious environmental problem [23]. Even if they are degraded, their degradation products are still toxic, carcinogenic, and teratogenic for living organisms [24]. Besides the undesirable colour in waste water, their breakdown products also exhibit a mutagenic or carcinogenic effect on human beings and their ingestion can cause severe damage to organisms. Several methods have been attempted to remove or remediate dye-contaminated wastes and adsorption is a low-cost and effective method for the removal of dyes from aqueous solutions [22]. Various organic and inorganic adsorbents including modified graphite

powder and emerging graphene have been attempted for the removal of organic dyes from aqueous waste waters [24, 25]. However, such adsorbents usually suffer from difficulties in their regeneration and separation from the waste stream. In particular, activated carbon (AC) with high surface areas (700-1,500 m$^2$/g) is highly effective for the removal of dyes, pigments and other inorganic/organic pollutants [26]. However, AC regeneration typically involves drying at elevated temperature, i.e., it is costly and causes partial destruction of this material.

The chapter describes the applicability of two emerging nanomaterials developed recently for the removal of phenols and MB from solution. CMs in rod form were used for the investigation of SPE performance of phenol and its derivatives. Naphthalene and benzoic acid were also used to confirm the retention behaviour of these sorbents. CMs in powder forms were also used for the further study of adsorption kinetics and equilibrium isotherms of MB. Carbon monoliths have been used as the stationary phase for HPLC [27] [13] or electrode materials [11] which was discussed in Chapter 3. This study is the first demonstration of the use of CM and NTCM to remove these toxic pollutants and unravel an effective procedure for their regeneration. The binding capacity and kinetics of NTCM powder are also compared with those of CM blank powder. For comparison, commercial AC was also utilised for MB removal in this study.

## 4.2 Experimental

### 4.2.1 Reagents and materials

As described in Chapter 3, Section 3.2.1 with the following additions. Phenol ($\geq$ 99 wt. %), 2-chlorophenol ($\geq$ 99 wt. %), bisphenol A (BPA)($\geq$ 99 wt. %), benzoic acid ($\geq$ 99 wt. %), naphthalene ($\geq$ 99 wt. %), anhydrous methylene blue (MB) ($\geq$ 99 wt. %), anhydrous sodium acetate ($\geq$ 99 wt. %), acetic acid ($\geq$ 99.7 vol. %), sodium tetraborate (99 wt. %) and sodium hydroxide (99.99 wt. %) were all obtained from Sigma-Aldrich (Dublin, Ireland). For investigation of pH effects on adsorption performance, 20 m$M$ sodium acetate buffer solution, pH 4.5, 20 m$M$ PBS, pH 7.5 and 20 m$M$ sodium borate, pH 10.5 were prepared as solvents for the preparation of methylene blue solution with desirable pH. Acetonitrile (ACN) (HPLC grade, 99.9 Wt. %) and methanol (MeOH) (HPLC grade, 99.9 wt. %) was purchase from Fisher

Scientific (Dublin, Ireland). CM blank and NTCM were in-house prepared and more details were described in Chapter 3, Section 3.2.3. Granular coal-based activated carbon (AC) (AquaSorb 2000) was obtained from Jacobi Carbons (Birkenhead, UK). This AC material has a BET specific surface area of 1,100 $m^2$/g. All reagents were of analytical grade with and used as received and without purification.

A 1000 mg/L phenol standard stock solution was prepared by dissolving 100 mg of phenol into a 100 mL volumetric flask using acetonitrile or methanol depending on the mobile phase used for analysis. This stock solution was used to prepare 1, 5, 10, 20, 30, 40 and 50 mg/L phenol calibration standards in water as well as in each corresponding organic solvent used for recovery. A six-point calibration curve for phenol was established for average peak area of two injections ($\mu$V*sec) vs phenol concentration [phenol] using RP-HPLC. 30 mL of the working solutions containing 30 mg/L phenol was prepared by dilution with water for kinetics study. 2-chlorophenol, BPA, naphthalene and benzoic acid were also prepared in the same manner. The parameters for each calibration curve are summarised in Table 4.6. These solutions were sonicated for 30 min. All solutions store at 4 $\mathrm{^{\circ}C}$ after use. For pH adjustments, formic acid was used.

A 4 mM MB standard stock solution was prepared by dissolving ~ 0.128 g of MB into a 100 mL volumetric flask using 20 mM PBS, pH 7.5. The MB calibration standards were prepared by dilution of the stock solution to 1.25, 2.5, 5, 10 and 20 $\mu$M in the same buffer solution. A calibration curve was established for MB absorbance at 660 nm ($Abs_{660\ nm}$) vs. MB concentration [MB] using UV-Vis spectroscopy. This provided a straight line (up to 20 $\mu$M) with a slope of 0.062 $Abs_{660\ nm}/\mu$M [MB]. 30 mL aqueous solutions containing different concentrations of MB (100-1500 $\mu$M) were prepared by dilution from the stock solution using the same manner.

*Table 4.6:* *Analytical parameters of calibration curves for each analyte in different organic solvents measured by RP-HPLC.*

| Analyte | Solvent | Calibration curve | Linearity (mg/L) | $r^2$ | LOD (mg/L) | LOQ (mg/L) |
|---|---|---|---|---|---|---|
| phenol | $H_2O$ | y = 3789.1x + 2590.1 | 1-100 | 0.9999 | 0.05 | 0.17 |
| | ACN | y = 3795.1x + 2172.5 | 1-100 | 0.9999 | 0.03 | 0.10 |
| 2-chlorophenol | $H_2O$ | y = 10663x - 1644.6 | 1-100 | 0.9998 | 0.05 | 0.15 |
| | ACN | y = 10396x - 26199 | 1-100 | 0.9990 | 0.03 | 0.10 |
| BPA | $H_2O$ | y = 4866.4x + 790.7 | 0.5-50 | 0.9995 | 0.08 | 0.27 |
| | ACN | y = 4817.8x + 398.06 | 0.1-50 | 0.9999 | 0.17 | 0.57 |
| naphthalene | $H_2O$ | y = 34659x + 3598.1 | 5-100 | 0.9913 | 0.64 | 2.13 |
| benzoic acid | $H_2O$ | y = 63.017x + 878.16 | 1-100 | 0.9997 | 0.04 | 0.10 |

## 4.2.2 Instrumentation

As described in Chapter 2, Section 2.3.2 with the following additions. The absorbance of each MB solution was measured by a Shimadzu UV-1800 UV-Vis spectrophotometer (Kyoto, Japan). A Stuart® linear reciprocating SSL2 shaker (Staffordshire, UK) was set at 200 rpm for adsorption/desorption study. The moisture in each carbon monolithic sorbent was removed by placing into an individual test tube then placed in a TurboVap® automated evaporation system after washing step. The analyte contained in the sorbent was subsequently concentrated in order to improve % recovery. A Shimadzu uHPLC Nexera® system (Kyoto, Japan) equipped with a binary pump (LC30AD), online degasser (DGU-20A$_5$), autosampler (SIL-30AC), column oven (CTO-30A) and a diode array detector (SPD-20AV) was used for qualitative and quantitative analysis of the modal analytes.

To avoid the contamination of phenols, no detergents or plastic containers were used. Glassware used in all work was pre-silanised by initial cleaning with a 50:50 v/v methanol/water solution, followed by one rinse with 10% v/v dichlorodimethylsilane in dichloromethane, two rinses with dichloromethane, followed by two rinses of methanol and water, respectively. This procedure was applied to all sample vials, volumetric flasks, conical flasks and HPLC sample vials to minimize adsorption of some chemicals to glass walls. Amber HPLC sample vials were used where possible to reduce photo-degradation of samples during analysis. All vials were used once and discarded after the analysis was complete. Any

glassware to be reused for samples was rigorously washed with a 50:50 v/v methanol/water solution and then 100% purified water between preparations and dried in vacuum oven. All containers used for methylene blue solutions were of polypropylene to minimize the dye adsorption.

## 4.2.3 Adsorption study of phenolic compounds

### 4.2.3.1 Adsorption kinetics of phenols

The adsorption of phenols on the carbon monolithic sorbent was studied in batch mode. The sorbent loading was 10 mg per 30mL of above described working solutions in a 100 mL conical flask with a glass stop. Then the flask was shaken for up to 1460 min. Unless otherwise indicated, the binding experiments were performed at ambient temperature, $22 \pm 1$ ℃ and without pH adjustment. A small amount of sample (500 μL) was taken by an autopipette every 10 min for the first 100 min, then every 30 min for the second 120 min, then every 60 min for 180 min and finally left overnight (~ 16 h) and sampled the following morning. The RP-HPLC analysis was performed immediately after the sampling. From the calibration curve of each analytes, the amount of analyte bound (mg) was then calculated and each analyte adsorption in mg/g of sample was determined. Beside the polar phenolic compounds, benzoic acid and naphthalene was also used to further investigate the complicated retention behaviour of CMs. The adsorption capacity of phenols on the adsorbent is calculated as $q = V(C_o\text{-}C_t)/m,$ where $V$ is the solution volume (mL), $C_o$ is the initial MB concentration (mg/1000 mL), $C_t$ is the phenols concentration in the solution (mg/1000mL) at a given time ($t$, $min$), and $m$ is the adsorbent mass ($g$).

### 4.2.3.2 Desorption of phenols

After adsorption, all rods were place in a 2 mL glass vial with a tinfoil septum screw cap which contained 1 mL of water for washing off the occluded amount of analyte for 1 h. Then the moisture of each rod was removed by TurboVap at 15 psi, gentle nitrogen flow and 40 ℃ water bath for 1h after washing step. For the other conventional SPE cartridge, this step can be achieved by flush air through the cartridge on the scaffold for ~ 30 min [28]. The rods were then transferred into a clean 2 mL glass vial which contained 1 mL of 100 % acetonitrile. The sample vial

was sealed with Teflon tapes and then placed in a 77 ℃ water bath for 1 h. If the other temperature was used, it will be specified. The elute was transferred into a 2 mL HPLC brown vial and cooled in the sample tray for HPLC analysis, i.e. 1$^{st}$ recovery. Repeated the elution procedure by continuing adding 1 mL of fresh acetonitrile every 1 h until they were free from the analytes, i.e. no analyte peak was observed in the chromatogram. The rods were considered ready for next adsorption uses.

### 4.2.3.3 RP-HPLC analysis

The concentrations of each analyte were measured using a RP-HPLC. The injection volume was 10 μL, with detection by UV at 280 nm (phenol, 2-chlorophenol and BPA, respectively) or 254 nm (naphthalene) or 220 nm (benzoic acid) using a SPD -20AV diode array detector and cell temperature at 40 $^{o}$C. The number of injection was two and the average of peak area was used for the calculation of the amount of phenol adsorbed by substitute into the calibration plots. The mobile phase was 50 v/v % acetonitrile with 1 v/v % formic acid, isocratic, at a flow rate of 1 mL/min. The temperature of the autosampler was 4 $^{o}$C, sampling speed was 5.0 μL/sec and rinse solution for the injection needle was same as mobile phase without formic acid. The column oven was 40 $^{o}$C and temperature limit (maximum) was 45 $^{o}$C. The data was collected and analysed by Empower 2. A monometric type octadecyl silica column (Waters symmetry C$_{18}$ column, 100 mm $\times$ 4.6 mm I.D., 3.5 μm) was used for RP-HPLC separation.

## 4.2.4 Adsorption and desorption study of methylene blue

### 4.2.4.1 Adsorption kinetics of methylene blue

The adsorption capacity of MB on the adsorbent, $q$ was calculated using same aforementioned formula in Section 4.2.3.1. The adsorption kinetics were investigated using the pseudo-first-order and pseudo-second-order models as shown in Table 4.7. The concentration of active sites on the surface of the adsorbent greatly outnumbers the MB molecule concentration, i.e., only the dye concentration significantly affects the adsorption rate, so the reaction behaves more like a first or second order reaction (pseudo).

#### 4.2.3.2 Langmuir isotherms

For each initial dye concentration ($C_o$), the amounts of MB adsorbed at a given time, $q_t$, can be related to $C_t$ as shown in Table 4.7. Non-linear regression analysis was then applied to estimate the values for $q_e = V(C_o-C_e)/m$, $k_1$, and $k_2$. A plot of $q_e$ vs. $C_e$, the residual concentration in the solution, was then performed to validate the applicability of the Langmuir isotherm equation, $q_e = q_{max}.K_L C_e/(1+K_L C_e)$ where $q_{max}$ is the Langmuir constant related to maximum adsorption capacity and $K_L$ is the Langmuir constant related to binding energy of the adsorption system as discussed later. The $q_{max}$ value was then used for the estimation of the specific surface area (SSA) of CM blank and NTCM as $(q_{max}/MW) \times \alpha_{MB} \times N_{Avo}$ where MW is the molecular weight of MB, $\alpha_{MB}$ is the occupied surface area of one MB molecule (~1.3 nm$^2$, assuming the MB molecule is lying flat on the adsorbent surface, 17.0 x 7.6 ~130 Å$^2$) and $N_{Avo}$ is the Avogadro number ($6.023 \times 10^{23}$ /mol).

*Table 4.7:* *Pseudo-first-order and pseudo-second-order adsorption kinetics.*

| | | |
|---|---|---|
| **Pseudo-first-order kinetics** | $\frac{dC}{dt} = -k_1 C$  or  $C = C_o e^{-k_1 t}$ | (1) |
| | where $k_1$ (min$^{-1}$) = the rate constant | |
| | $q_t$ = the amounts of dye adsorbed at a given time | |
| | $q_t = q_e (1 - e^{-k_1 t})$ | (2) |
| | *where* $q_e = V C_o /m$: the amounts of dye adsorbed at equilibrium | |
| | $C_o$ = initial concentration of MB | |
| | $m$ = amount of the adsorbent | |
| | $V$ = volume of the MB solution | |
| **Pseudo-second-order-kinetics** | $\frac{dC}{dt} = -k_1 C^2$ or $\frac{1}{C} - \frac{1}{C_o} = k_1 t$ | (3) |
| | $q_t = \frac{q_e C_o k_1 t}{1+C_o k_1 t} = \frac{q_e^2 k_2 t}{1+q_e k_2 t}$ | (4) |
| | $k_2 = (m /V) k_1$ | |

12 mL of working solutions with different concentration of MB were added to ground samples (12 mg) of CM blank and NTCM, respective and shook. Samples with AC were rotated with MB for a longer time period of up to 3 h. Small samples (300 µL) were taken every 30 s for the first 3 min and then at 4, 5, 10, 15, 20, and 40 min and up to 3 h for AC. These samples were immediately centrifuged at 12,000 rpm and the supernatants (after centrifugation) were tested (diluted 10–100 $\times$ depending on the concentration of MB) for the residual concentration of MB left in

solution, following any MB binding to the adsorbents, and compared to the starting concentration. From the calibration curve of MB, the amount of MB bound (mg) was then calculated and the MB adsorption in mg/g of sample was determined. Unless otherwise indicated, the binding experiments were performed at ambient temperature, $22 \pm 1$ ℃ and neutral pH. For the Langmuir isotherm plots extra $q_e$ vs $C_e$ points (in addition to those calculated from the adsorption isotherms) were determined by the addition of different concentrations of MB to the adsorbents for 16 h (i.e. end point determination).

### 4.2.3.3 Desorption of methylene blue

Desorption of MB from AC and CMs was performed using 100% ethanol or acetonitrile. In the serial desorption experiment for powdered CMs, MB containing ethanol or acetonitrile was removed by centrifugation and fresh ethanol or acetonitrile was added every 2 min to prevent the re-adsorption of MB onto the absorbent. The supernatants were analysed by UV-Vis spectroscopy.

# 4.3 Results and discussion

## 4.3.1 Characteristics of Carbon Monoliths

The CM blank skeleton was constructed by a series of mesopores with irregular shapes except for a few micropores on the walls. The inner pore surfaces of the CM sample were smoother in texture (Figure 4.13(a)–(d)). The CM sample also exhibited a higher degree of graphitisation as attested by the presence of a high density of graphite ribbons in comparison with NTCM. The carbon content was $86 \pm 3$ wt % and the oxygen content was $10 \pm 2$ wt % for CM blank whereas these values were $94.09 \pm 2.01$ wt % and $4.24 \pm 1.16$ wt % respectively for NTCM as estimated by energy-dispersive X-ray spectroscopy. Other characterisation results including Raman spectroscopy, BET specific surface area and porosity of CMs were described in more detail in Chapter 3, Section 3.3.2 – 3.3.4.
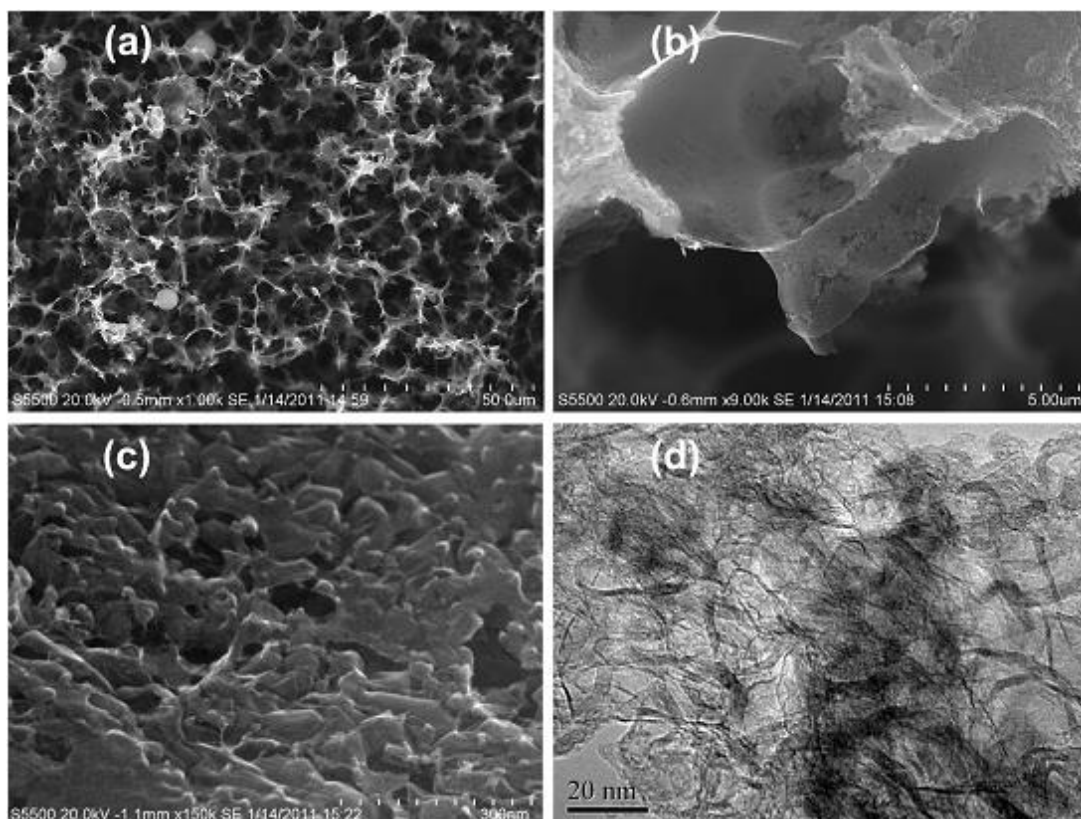
***Figure 4.13:*** *FE-SEM images of (a) macroporous networks, (b) macroporous walls, (c) mesoporous structure of CM blank; and (d) TEM image of CM blank.*

## 4.3.2 Adsorption kinetics of phenolic compounds

Extraction time is an essential parameter affecting the method sensitivity in SPE [28]. It was expected that the hierarchical porous structure and the oxygen containing groups in the carbon monolithic sorbent could lead to a reasonably faster adsorption rate and unique chemical selectivity. Furthermore, the residue of $C_{60}$ on the macroporous wall in NTCM resulted in higher levels of micro-porosities and slightly a more hydrophobic surface than for the CM blank. The different physicochemical properties of CM blank and NTCM were discussed in Chapter 3. The adsorption study results could further indicate these different features between these two carbon monolithic sorbents. The adsorption kinetics of phenol, 2-chlorophenol, BPA, naphthalene and benzoic acid with the same initial concentrations (30 mg/L) and sorbent loading (10mg adsorbent /30mL of adsorbate solution) onto CM blank and NTCM rods, respectively. These were studies as function of contact time in order to find out the equilibration time as well as kinetic mechanism (Figure 4.14).
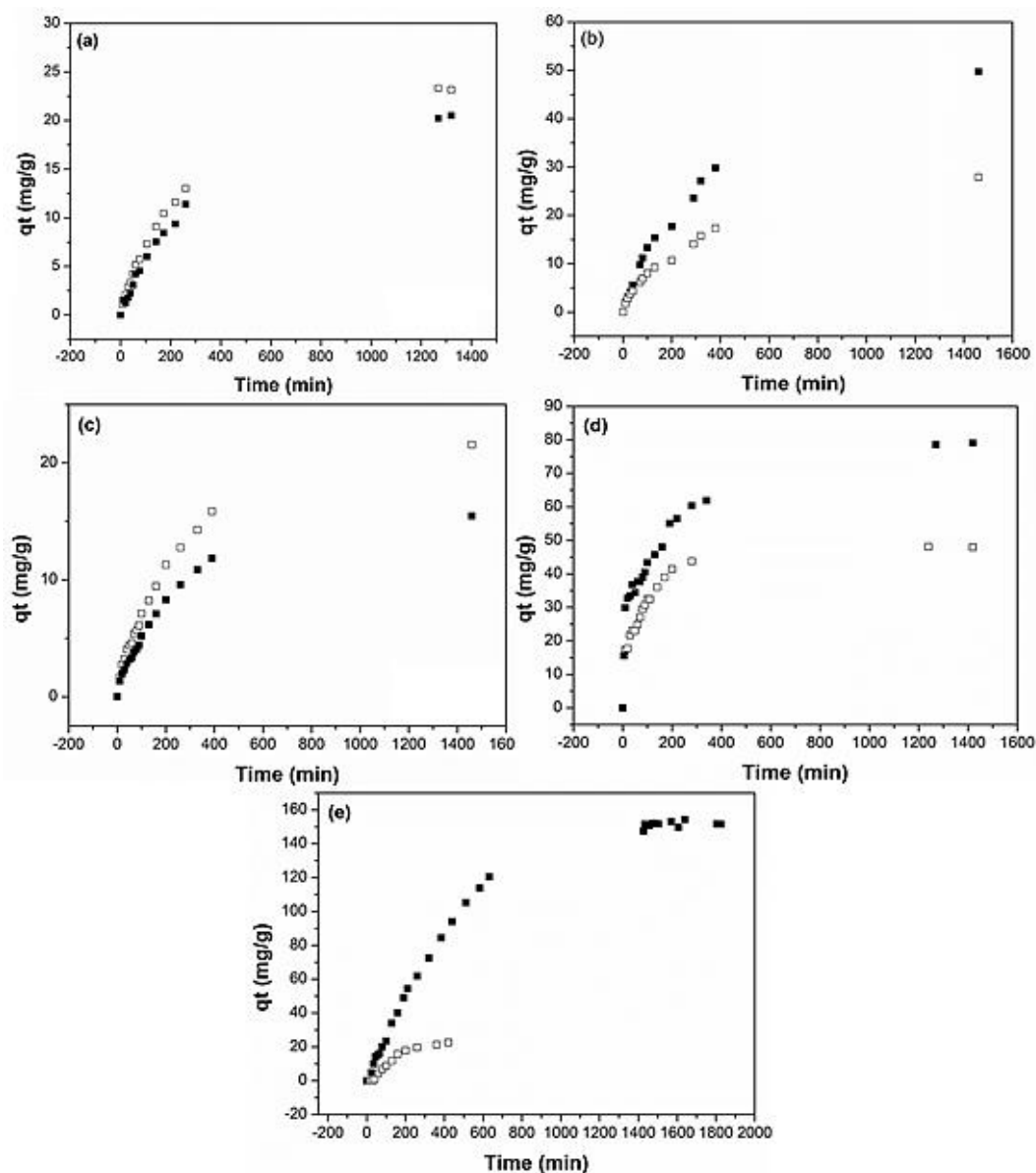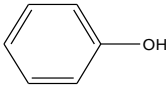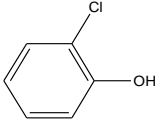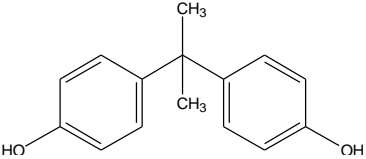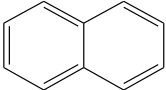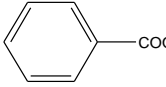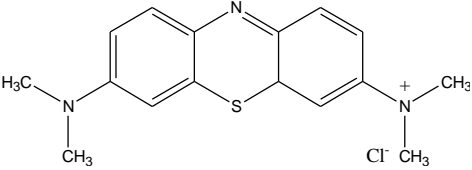
***Figure 4.14:*** *Adaption kinetics of (a) phenol, (b) 2-chlorophenol, (c) BPA, (d) naphthalene and (e) benzoic acid (without any pH adjustment) onto (□) CM blank and (■) NTCM.*

Figure 4.14 showed different maximum adsorption capacity q values over all these five adsorbates. The order of q value of each analytes using CM blank and NTCM is same: benzoic acid > naphthalene > 2-chlorophenol > phenol > and BPA. There was reasonable correlation between this order to the order of pKa as shown in Table 4.8. This indicated that the retention properties of CMs were different from those of classical non-polar phases. Such phenomenon was also observed from PGC column [29]. Benzoic acid was the most favourable adsorbate among the other analytes to the NTCM due to the presence of higher amount of basic surface oxygen groups and micropores contributed higher specific surface area than CM blank. This result

implied the formation of electron donor-accepter complexes on the surface of NTCM. The amount of benzoic acid adsorbed by NTCM was ~ 8 times greater than CM blank. BPA adsorbed the least onto CMs. Overall, the q values for each analyte obtained from NTCM were greater than from CM blank due to higher specific surface area of NTCM, except for BPA. Such results were not completely unexpected since biphenyl molecules tended to be staggered when present in the aqueous phase [29]. The sorbent used needs to have higher adsorption energy to compete with BPA rotational strain energy in order to achieve the closer contact with the sorbent surface. CM blank showed a higher degree of graphitisation than NTCM (Chapter 3) so that it had higher adsorption energy than NTCM.

***Table 4.8:*** *Chemical structures, molecular weights and physical properties of the model analytes [30-32].*

| Analyte | Chemical structure | Molar mass (g/mol) | log p | pKa at 25 °C |
|---|---|---|---|---|
| phenol | (structure: phenol, C6H5–OH) | 94.11 | 1.46 | 9.89 |
| 2-chlorophenol | (structure: 2-chlorophenol, Cl and OH on benzene) | 128.56 | 2.17 | 8.52 |
| bisphenol A (BPA) | (structure: bisphenol A) | 228.29 | 3.30 | 9.59 |
| naphthalene | (structure: naphthalene) | 128.17 | 3.30 | 43.00 |
| benzoic acid | (structure: benzoic acid, C6H5–COOH) | 122.12 | 1.87 | 4.20 |
| methylene blue (MB) | (structure: methylene blue, $Cl^-$ counter ion) | 320 | 0.9 | 3.80 |

Benzoic acid as the most acidic among the other model analytes thus it was used to investigate the ion exchange properties of the adsorbents with and without pH adjustment. The sorption capacity of benzoic acid onto CM blank at pH 1.75 was slightly higher than at pH 3.55, as shown in Figure 4.15. Such results indicated the charge interaction between benzoic acid and CM blank was very weak, even for the acidic species. Naphthalene as a representative of polyaromatic hydrocarbons was also used to explore the electron localisation effect on the graphitic CMs surfaces. The rapid uptake was observed in the initial adsorption stage for both CMs. After 50 min, more naphthalene was adsorbed by NTCM due to the residue of $C_{60}$ which might have the ability of molecular recognition [33]. Thus, NTCM adsorbed phenols mainly via size recognition, hydrophobic interaction, and $\pi$-$\pi$ stacking. It also has geometrical recognition ability along with very weak ion exchange capability due to the basic oxygen containing functional groups. These retention mechanisms can be further confirmed by desorption studies.
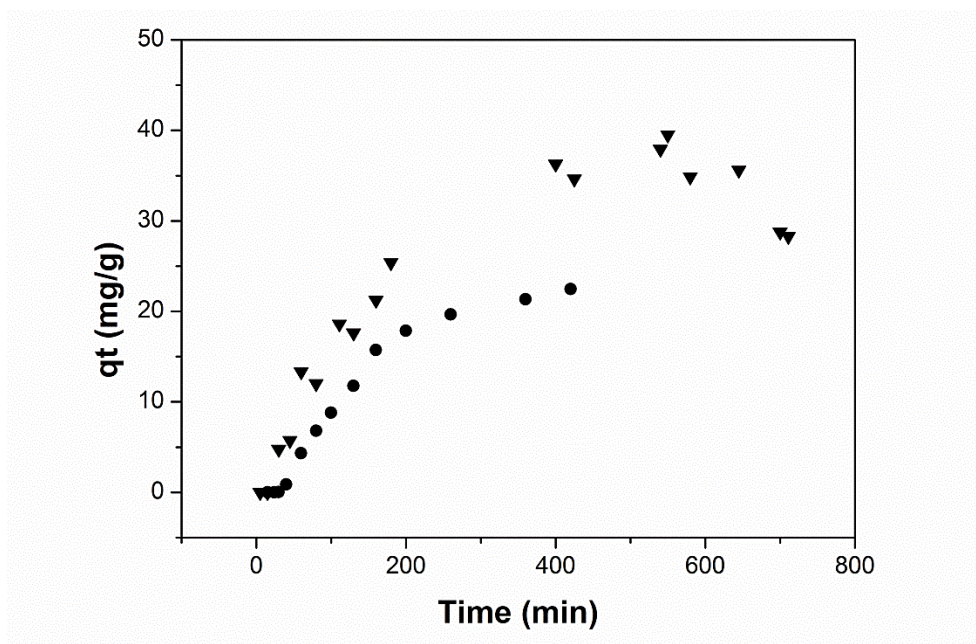


**Figure 4.15:** *pH effect on the binding kinetics of benzoic acid on CM blank rod at two different pHs: (▼) pH 1.75 and (●) pH 3.55.*

Kinetic mechanism of phenols adsorption occurs on the rod form sorbent through the following steps [34]:

1. Adsorbate molecules across the liquid film surrounding the porous adsorbent by external diffusion,

2. Adsorbate molecules associate with the adsorption site,

3. Adsorbate molecules diffuse into the adsorbate by internal capillary diffusion.

After 1460 min, the equilibrium of the analyte was not quite reached, therefore, either the adsorption kinetic model or Langmuir isotherm equation can be applied to these adsorption kinetics data. The slow adsorption kinetic of phenols on the rod was due to the hydrophobic nature of carbon, the presence of micropores and large cross section of the rod, $A = \pi \times r^2 = 3.14 \times 1.5^2 = 7.07$ mm$^2$. The kinetics can be speeded up by minimising the dimension of the sorbents to shorten the diffusion distance or enlarge the flow-through pore (Chapter 5). Much fast kinetics of MB onto ground CMs were observed in Section 4.3.1.

According to the literature, most of ACs adsorbed phenolic compounds, based on their basic surface oxygen groups, form electron donor-acceptor complex between adsorbates and adsorbents. Moreover, carbon crystal basal plane edge providing $\pi$-electron rich regions may also play an important role as well. Table 4.9 summarises the comparison of phenol adsorption capacities by various types of adsorbents used in the literature. It is quite obvious that the adsorption capacities of both CM blank and NTCM were lower than those reported for most sorbents, therefore either these sorbents were suitable for SPE. The adsorption capacity of phenol by CMs can be improved by pre-treatment with strong bases, such as potassium hydroxide [35]. Alternatively, the rod can be ground into powder to minimise the diffusion distance.

*Table 4.9:* *The maximum phenol adsorption capacity of various types of adsorbents.*

| Adsorbent | Maximum adsorption capacity (mg/g) | References |
|---|---|---|
| **CM blank** | 23.2 | Present work |
| **NTCM** | 20.5 | Present work |
| **Activated coconut shell** | 205.8 | [36] |
| **Samla coal** | 13.3 | [37] |
| **Coconut charcoals ACG40** [a] | 200.0 | [38] |
| **Duolite S861 resin** [a] | 96.1 | [39] |

[a] Commercial adsorbents

## 4.3.3 Desorption of phenolic compounds

The HPLC analysis restricted the type of solvents that can be used for desorption of phenols, i.e. extreme pH solution (e.g. potassium hydroxide or nitric acid etc.) or strong organic solvents (e.g. acetone etc.) which cannot be used as they will cause damage to the column. Therefore, acetonitrile was used, which is compatible with the mobile phase. In all water wash step, there was a very minor amount of phenols (< 0.3 % of the intimal amount), which was occluded by either CM blank or NTCM. The Turbovap drying step was introduced to pre-concentrate the analytes and shorten desorption duration since the slow adsorption kinetics were observed previously (Section 4.3.2). Furthermore, increasing temperature usually can decrease the solution viscosity and shorten the elution time due to enhanced diffusion rate of desorption solvent, which penetrated into the internal porous structure to elute the adsorbate off. PGC columns are often used for high temperature HPLC [40]. Therefore, a temperature close to the boiling point of the solvent used for desorption was applied for maximising the desorption amount of phenols. The maximum amount of phenols from $1^{st}$ recovery at room temperature (RT) and at 77 $^o$C was compared in the suitable solvents as shown in Table 4.10. The recoveries for all phenols at 77 $^o$C were much higher than at RT. For all phenols, the CM blank showed slight higher recovery than NTCM. The results implied that the affinity between CM blank and phenols was slighter weaker than NTCM due to less amount of micropores present. The highest $1^{st}$ recovery value was obtained from 2-chlorophenol by CM blank because that CM blank has higher amount of oxygen content which can delocalise electrons and, thereby, withdrawing electrons from the conjugation system of the graphite plane, consequently reduced the $\pi$-$\pi$ interaction effect. The 2-chlorophenol is the most acidic among the other phenols and NTCM showed slight strong affinity to it, thus NTCM has slightly more basic oxygen contained groups on the surface. Therefore, NTCM showed more size recognition, hydrophobicity, hydrogen bonding and $\pi$-$\pi$ interaction effect than CM blank. The high temperature recoveries of phenols from CMs are not practicable due to the toxicity of phenols and ideally the recoveries should be carried out at room temperature and neutral pH. However, the maximum recovery of phenols from CMs was < 50 % in acetonitrile at room temperature again confirmed either these sorbents were suitable for SPE.

**Table 4.10:** *The comparison of the amount of phenols from 1ˢᵗ recovery at room temperature (RT) and at 77 °C in 1 mL of acetonitrile.*

| Adsorbate | Adsorbent | Recovery (%) | |
|---|---|---|---|
| | | RT, 1 h | 77 °C, 1 h |
| phenol | CM blank | 5.68 | 99.64 |
| | NTCM | 3.42 | 98.70 |
| 2-chlorophenol | CM blank | 10.09 | 64.23 |
| | NTCM | 7.25 | 62.22 |
| BPA | CM blank | 49.32 | 101.93 |
| | NTCM | 31.36 | 96.62 |

## 4.3.4 Adsorption kinetics of methylene blue

Several experiments were carried out for the study of adsorption kinetics of MB on CM blank and NTCM powders. Figure 4.16 shows $q_t$ versus time ($t$) for different concentrations of MB on such adsorbents. The adsorption capacity of CM blank increased and reached equilibrium within 5 min. In excess of 10 min of contact time was required for the $q_t$ value of NTCM to reach the plateau, in particular at high initial MB concentrations. The first and second order models can be a utilised for describing the adsorption data as attested by the higher correlation factors of ($R^2$) for CM blank and NTCM, (Table 4.11). The equilibrium or contact time of the MB - NTCM binding (Figure 4.16B) was significantly longer than that of MB – CM blank (Figure 4.16A) and such behaviour could be attributed to the difference in their pore sizes (10.7 nm for CM blank and 6.1 nm for NTCM, presented  with BET results in Chapter 3, Section 3.3.3), structure and oxygen contents of such two carbon materials (10 ± 2 wt. % for CM blank vs. 4 ± 1 wt. % for NTCM refer to EDX results in Chapter 3, Section 3.3.2). CM blank also showed a higher degree of graphitisation and its inner pore surfaces appeared considerably smoother in texture. The presence of oxygen was expected to promote hydrogen bonding interaction between MB and the absorbent, which in turn favoured the binding of MB onto CM blank over NTCM. In contrast, the adsorption of MB to AC was much slower and the contact time required for the $q_t$ value of AC to reach the plateau was several hours particularly at high initial MB concentrations. It should be noted that the binding capacity for MB on AC was higher than on CMs, confirming higher surface area (1,100 m²/g) and higher MB binding (280 mg/g) of this carbon material than the

the other two sorbents as indicated by the manufacturer (AquaSorb 2000, Birkenhead, U.K.) [41].
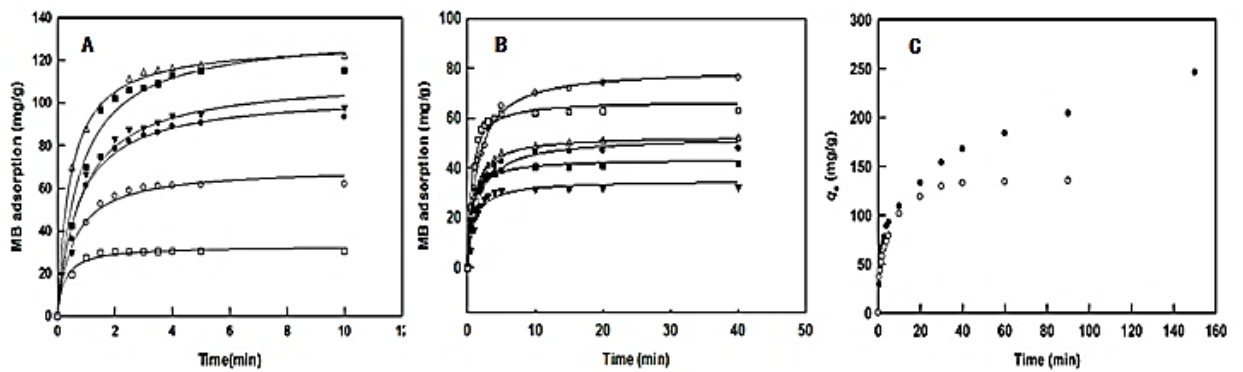


**Figure 4.16:** *Adsorption kinetics at different concentrations (μM) of methylene blue (MB) (A) CM blank: bottom to top 96, 196, 302, 386, 776, and 1150; (B) NTCM bottom to top 100, 200, 302 , 404 , 611, and 854;and (C) on AC, bottom to top, 424 and 1221. The solid lines were obtained by fitting the data using the pseudo-second-order kinetics.*

**Table 4.11:** *Estimate kinetic parameters of the two adsorption isotherm for MB.*

| CM blank | Equation | Para-meter | Methylene Blue concentration ($\mu M$) | | | | | |
|---|---|---|---|---|---|---|---|---|
| | | | 96 | 196 | 302 | 386 | 776 | 1150 |
| Pseudo 1st order | $q_t = q_e(1-e^{-k_1 t})$ | $q_e$ | 30.4 | 61.6 | 90.2 | 95.7 | 115 | 115 |
| | | $k_1$ | 2.13 | 1.26 | 1.07 | 0.99 | 1.49 | 1.01 |
| | | $R^2$ | 0.999 | 0.999 | 0.996 | 0.988 | 0.984 | 0.993 |
| Pseudo 2nd order | $q_e=(q_e^2 k_2 t)/(1+q_e k_2 t)$ | $q_e$ | 32.7 | 69.6 | 84.3 | 112 | 131 | 129 |
| | | $k_2$ | 0.119 | 0.0256 | 0.0127 | 0.0109 | 0.0096 | 0.0174 |
| | | $R^2$ | 0.985 | 0.988 | 0.990 | 0.974 | 0.975 | 0.998 |

| NTCM | Equation | Para-meter | Methylene Blue concentration ($\mu M$) | | | | | | | |
|---|---|---|---|---|---|---|---|---|---|---|
| | | | 100 | 200 | 202 | 302 | 404 | 611 | 854 | 1251 |
| Pseudo 1st order | $q_t = q_e(1-e^{-k_1 t})$ | $q_e$ | 31.9 | 40.3 | 47.1 | 49.5 | 48.7 | 62.3 | 72.3 | 78.8 |
| | | $k_1$ | 0.716 | 0.903 | 0.497 | 0.828 | 0.731 | 1.06 | 0.513 | 1.5 |
| | | $R^2$ | 0.992 | 0.995 | 0.993 | 0.996 | 0.966 | 0.998 | 0.987 | 0.993 |
| Pseudo 2nd order | $q_e=(q_e^2 k_2 t)/(1+q_e k_2 t)$ | $q_e$ | 34.7 | 43.5 | 52.2 | 53.6 | 52.8 | 66.9 | 79.9 | 77.5 |
| | | $k_2$ | 0.030 | 0.033 | 0.013 | 0.024 | 0.021 | 0.026 | 0.0093 | 0.094 |
| | | $R^2$ | 0.954 | 0.988 | 0.973 | 0.988 | 0.998 | 0.975 | 0.995 | 0.988 |

## 4.3.5 Langmuir and Freundlich Adsorption Isotherms

The Langmuir adsorption isotherm was then applied to describe the adsorption process by plotting $q_e$ vs $C_e$, the equilibrium or residual concentration of MB in the solution (Figure 4.17). This adsorption isotherm, with some rational basis, assumes that the adsorbent surface consists of active sites with uniform energy for the formation of a monolayer [42]. The Langmuir constant is also related to the Gibbs free energy ($\Delta G^o$) of sorption reaction as $\Delta G^o = -RT\ln K_L$ where $T=$ absolute temperature (295 K) and $R$ (the gas constant) $= 8.314$ J.mol$^{-1}$.K$^{-1}$. The negative value of the free energy indicates the feasibility of the process and the spontaneous nature of the adsorption. At low adsorbate concentrations ($K_L C_e \ll 1$), the Langmuir model becomes a linear isotherm ($q_e = q_{max} K_L C_e$) and follows Henry's law. Alternatively, at high adsorbate concentrations ($1 + K_L C_e \sim K_L C_e$), it predicts a constant monolayer sorption capacity, i.e., $q_e = q_{max}$ [42].
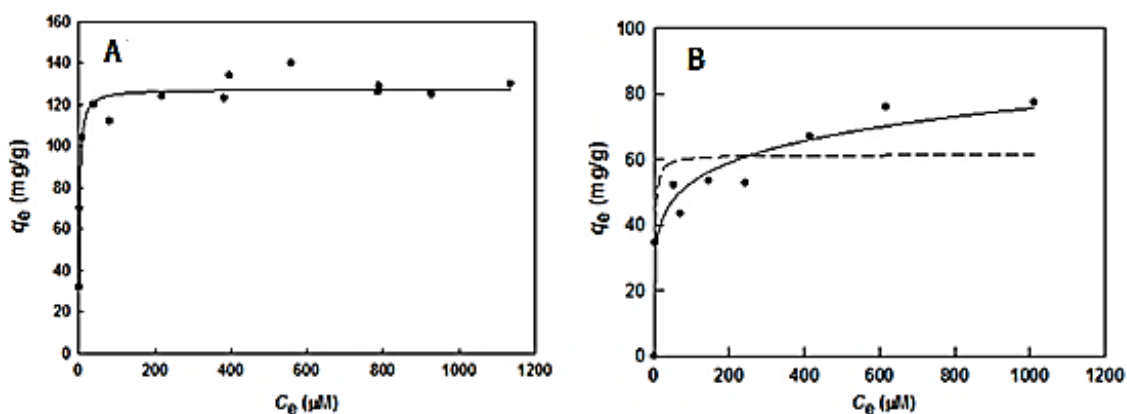


***Figure 4.17:*** *(A) Langmuir adsorption isotherm of methylene blue on CM blank and (B) Freundilich adsorption isotherm of the dye on NTCM.*

Nonlinear regression analysis was performed to estimate the Langmuir constants since the linearisation of the Langmuir model tends to fit experimental data better at higher concentrations [43] and might violate the error variance and normality assumptions of standard least squares [44]. Other modified Langmuir models such as Radke-Prausnitz isotherm [45], and Langmuir-Freundlich (Sips equation) [46] were not attempted in this study since they involve more than two fitting parameters with no physical meaning or rational basis.

The Langmuir isotherm model (Figure 4.17) appeared to well represent the binding data for MB on CM blank as estimating from the obtained correlation coefficients $R^2$ (Table 4.12), indicating the homogeneous nature of CM blank. The amount of MB loading on CM blank was found to be 127.53 mg/g, faster binding kinetics and its affinity to MB binding than the other nanosorbents such as NCC [32], as reflected by higher $q_{max}$ and a very steep initial slope of the isotherm. It should be noted that $C_e^* = 1/K_L$, the equilibrium concentration at which the loading is 50% of the maximum capacity, was estimated to be 2.02 μM for CM blank. The Gibbs free energy ($\Delta G^o = -RT\ln K_L$) was estimated at -15.22 for CM to confirm the spontaneous nature of the adsorption of CM for this dye (Table 4.12).

**Table 4.12:** *Estimated adsorption parameters of Langmuir and Freundlich isotherms at room temperature.*

| Adsorption model | CM blank | NTCM |
|---|---|---|
| **Langmuir** $$q_e = \frac{q_{max}K_LC_e}{1 + K_LC_e}$$ | $q_{max}$= 127.53 mg/g (SE = 2.11) $K_L = 0.496$ μM$^{-1}$ (SE = 0.082) $R^2 = 0.957$ $\Delta G^o$ = -15.22 kJ/mol | $q_{max}$= 61.52 mg/g (SE = 25.51) $K_L = 0.538$ μM$^{-1}$ (SE = 0.462) $R^2 = 0.758$ |
| **Freundlich** $$q_e = K_FC_e^{1/n}$$ | n/a | $K_F = 26.11$ μM$^{-1}$ (SE =3.755) $1/n = 0.154$ (SE =0.025) $R^2 = 0.955$ |

SE: standard error; n/a: not applicable; $\Delta G^o$ (Gibbs free energy) = $-RT\ln K_L$, where T= absolute temperature (295 K), $R$ (the gas constant) = 8.314 J.mol$^{-1}$.K$^{-1}$.

It would be possible to saturate CM blank adsorbent with MB at low and high concentrations, corresponding to very low residual MB in the solution. This was a critical finding since the aim of the regulatory authorities is always to try to limit the maximum concentration of pollutants such as organics, metals, etc. By way of comparison, the binding of MB on *Polyalthia longifolia* (Ashoka) seed powder is time-consuming [47], taking over 60 min and its binding capacity for MB is below 10 mg/g. The $q_{max}$ values of CM blank compare favourably with those obtained for

AC obtained from different sources, ranging from a few mg/g to hundred mg/g. Significantly, the monolayer sorption capacity of AC prepared from pea shell for MB is as high as 246.9 mg/g [48]. However, the equilibrium time is 40 and 100 min at concentrations of 100 and 150 mg/L, respectively, and 180 min for higher concentrations (200, 250, 300, and 350 mg/L) [47]. Also, in this study the value of $q_{max}$ for granular coal based AC (AquaSorb 2000) approached 300 mg/g, but the equilibrium time was in the order of hours at 384 mg/L.

The adsorption isotherm of NTCM, however, was not governed by the Langmuir model which is reflected by a very low correlation coefficient ($R^2$) and high standard errors for the estimated parameters, $q_{max}$ and $K_L$ (Table 4.12). Also, the estimated $q_{max}$ value was 61.52 mg/g, which is significantly below the observed experimental data. The binding kinetics were satisfactorily described by the simple Freundlich model [49]. The estimated Freundlich $K_F$ constant of 26.11/$\mu$M was an approximate indicator of adsorption capacity and $1/n = 0.154$ or $n$ (index of heterogeneity) = 6.5 confirmed a favourable adsorption process ($n$ = >1-10). This model, unlike the Langmuir isotherm, does not indicate a finite uptake capacity of NTCM for MB. This could be >80 mg/g. The $q_{max}$ value of NTCM should range from 80 to 110 mg/g, as estimated by nonlinear extrapolation. It should also be observed that this model has been widely used to present the adsorption isotherm of pollutants onto activated carbons or other adsorbents to describe non-ideal sorption on heterogeneous surfaces as well as for multilayer sorption. The adsorption isotherm of NTCM, as described by the Freundlich model [49], indicated surface heterogeneity of the adsorbent which might reflect the incorporation of $C_{60}$ in the polymer network before carbonisation. The Freundlich model also implies a multilayer surface mechanism, i.e., the hydrophobic interaction between the adsorbate and adsorbent forms the first layer followed by the dipole-dipole interaction between adsorptive molecules and the adsorbates at the secondary layer. An additional contributing factor to the formation of multilayers could also be the dimerisation of MB when its concentration exceeds c. 7 $\mu$M [50].

On the basis of a rectangular volume of dimensions $1.7 \times 0.76 \times 0.325$ nm [51-53], the projected area of MB has been given previously as 1.35 nm$^2$, 1.32 nm$^2$, and 1.30

nm$^2$ and in this work will be taken as 1.30 nm$^2$. Thus, it is very unlikely that MB is able to fill in micropores of the adsorbent (< 2 nm) and the sorption should occur in mesopores and macropores. Nevertheless, the two -N(CH$_3$)$_2$ groups of this dye should be able to protrude into such micropores to display hydrophobic interaction and hydrogen bonding with the walls of such micropores. In macropores and mesopores, the sorption depends not only upon the fluid wall attraction but also on the attractive interactions between the MB molecules, leading to possible multilayer adsorption. Based on the $q_{max}$ estimated from the Langmuir model for CM blank (Table 4.12), and the observed value of at least 80 mg/g for NTCM, the surface area of 312 m$^2$/g, and 196 to 270 m$^2$/g was estimated for CM blank and NTCM. The surface area estimated by BET (272 $\pm$ 32 m$^2$/g) was in agreement with the MB adsorption procedure for CM blank (312 m$^2$/g).

Of interest was the comparison of the performance of CM blank obtained in this study versus the other materials reported in the literature. Spent mushroom substrate, a renewable biowaste was used as an adsorbent to remove MB from aqueous solution [54]. The adsorption kinetics is governed by the pseudo-second-order model with a maximum adsorption capacity of 63.5 mg/g at 303 K. The equilibrium time ranges from 25–100 min and is dependent on the initial MB concentration. A review paper of Sharma *et al* [55] presents AC derived from various natural or agricultural wastes which have been used as dye adsorbents with their adsorption capacity ranging from 2–600 mg/g. Foo and Hameed also provide an overview of dye removal via AC adsorption process [56].

## 4.3.6 The effects of pH and temperature

CM blank was chosen for further investigation into pH and temperature effects as well as to its plausible regeneration on the basis of binding kinetics and binding capacity. The sorption capacity was also identical at three different pHs: 4.5 (20 mM sodium acetate), 7.5, and 10.5 (20 mM sodium borate), indicating that there was no noticeable charge interaction between MB and CM blank (Figure 4.18 A). Such results were not completely unexpected since the MB surface with pK$_a$ of 3.8 was predominantly neutral and did not participate in ionic/electrostatic interaction with

hydrophobic and neutral CM blank. Thus, CM blank adsorbed MB mainly via hydrophobic interaction, $\pi$-$\pi$ stacking and hydrogen bonding.
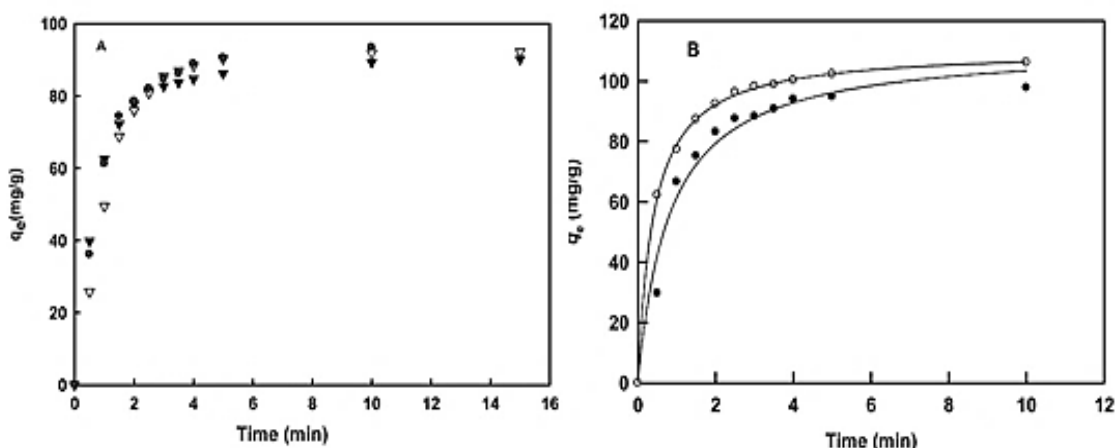


***Figure 4.18:*** *(A) The pH effect on the binding kinetics of methylene blue (MB) on CM blank at three different pHs: (▼) pH 4.5, (●) pH 7.5 and (∇) pH 10.5. (B) The temperature effect on the binding kinetics of methylene blue on CM blank: (●) 25 °C, and (○) 60 °C.*

As described earlier, kinetics of MB onto CM blank followed the pseudo-second-order model, suggesting that the rate-limiting step might be chemisorption. The adsorption capacity of CM blank slightly increased with the increase of adsorption temperature to 60 °C (Figure 4.18B). Considering the apparent activation energy of MB adsorption on CM using the Arrhenius equation, $k_2 = k_o\, e^{-Ea/RT}$, where $k_2$ is the pseudo-second-order rate constant defined in Table 4.7, $k_o$ is the temperature dependent factor, $E_a$ is the apparent activation energy of the adsorption, $R$ is the gas constant and $T$ is the adsorption absolute temperature. The activation energy was estimated to be 18.52 kJ/mol, compared to 27.63 kJ/mol for the adsorption of MB onto bamboo charcoal [57]. It is also noticed that the contact time of MB adsorbed onto bamboo charcoal requires several hours to reach equilibrium. Apparently, increasing temperature decreased the solution viscosity, leading to an enhanced diffusion rate of adsorptive molecules across the external boundary layer and in the internal pores. From a practical viewpoint, the adsorption of MB on CM blank should be carried out at room temperature and neutral pH.

## 4.3.7 Desorption of methylene blue

The desorption using 1 M potassium hydroxide or nitric acid as described for the desorption of MB onto AC was not effective [58], thus, this approach was not considered in this study. The desorption of MB adhered on CM blank by ethanol was rapid at room temperature, however, only 50% of MB was desorbed and increasing desorption temperature up to 60 °C did not accelerate the desorption process (Figure 4.19A). In this serial desorption, MB containing ethanol was removed by centrifugation and fresh ethanol was added every 2 min to prevent the re-adsorption of MB onto CM blank and the desorption aliquots collected at different time interval were shown in Figure 4.20A. Apparently, ethanol was only capable of effecting the desorption of MB adhered on the CM blank surface, not in the macro and mesopores (Figure 4.19A). Finally, desorption of MB adhered on CM blank by acetonitrile using the above protocol even at room temperature was most effective, with ~95% of the MB desorbed in the first 10 min (Figure 4.19A). Such a result confirmed that acetonitrile could remove the MB from the CM blank surface, macro- and mesopores as shown in Figure 4.20B. In contrast, the desorption of MB from AC was not very effective as only 42 and 42% of MB was desorbed with ethanol and acetonitrile, respectively (Figure 4.19B). It should be noted that AC regeneration typically involves drying the carbon followed by heat treatment at 500 - 900 °C. This procedure is costly and causes partial cracking and charring of the activated carbon, resulting in up to a 20% loss of adsorptive capacity due to a decrease in surface area [59].
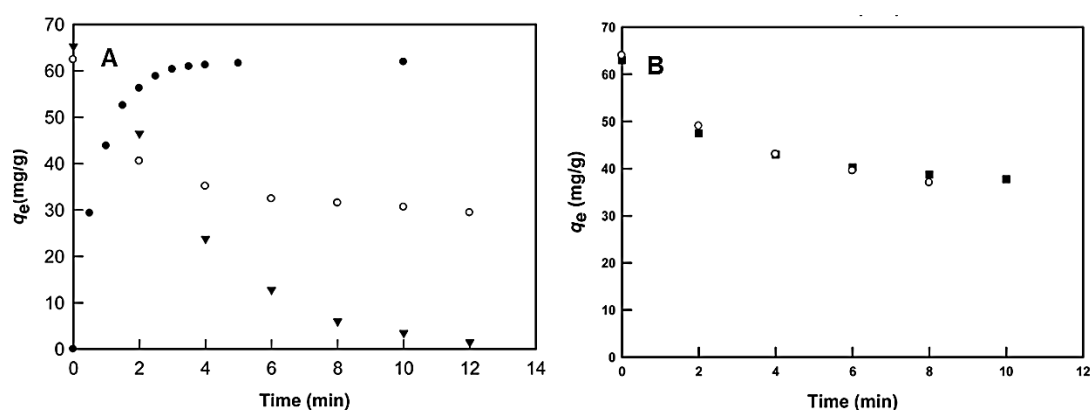


**Figure 4.19:** (A) Time course for the desorption of 4 mL methylene blue (MB 200 μM) adsorbed on CM blank (4 mg) by ethanol (○) and acetonitrile (▼) at room temperature compared to its adsorption isotherm for the adsorption of 4 ml of methylene blue (MB 200 μM) adsorbed on CM blank (●).(B) Time course for the

desorption of 4 ml of methylene blue (MB 200 μM) adsorbed on AC (4 mg) by ethanol (○) and acetonitrile (■).
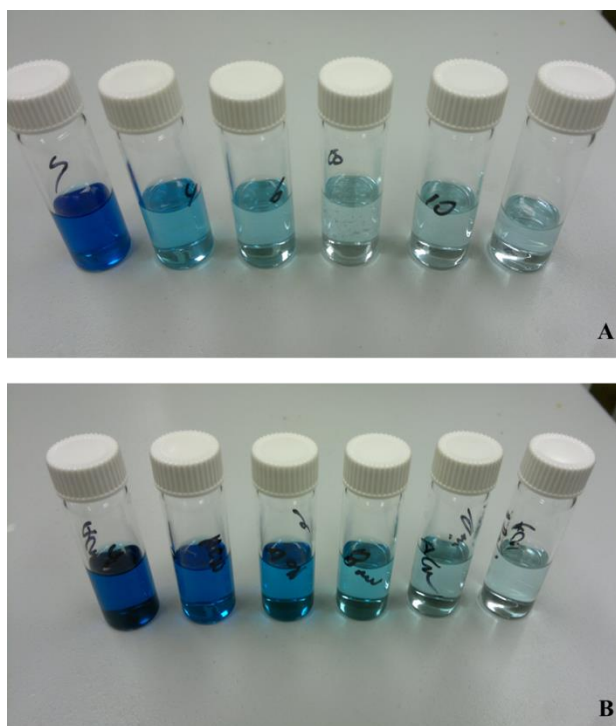


*Figure 4.20: The photograph of the time course for the desorption of 4 mL methylene blue (MB 200 μM) adsorbed on CM blank (4 mg) by ethanol methylene blue (MB) was desorped in (A) ethanol (B) in acetonitrile (from left to right) at 2, 4, 6, 8, 10 and 12 min.*

## 4.4 Conclusion

In conclusion, the applications of CMs in rod and in powder form as SPE sorbents have been demonstrated using phenolic compounds and MB, respectively. Both CM blank and NTCM rods showed slow adsorption kinetics and low adsorption capacity due to the dimension of the rod and presence of micropore. The retention between NTCM and phenols was mainly via size recognition, hydrophobic interaction, $\pi$-$\pi$ stacking. It also has geometrical recognition ability along with very weak hydrogen bonding and ion exchange capability due to the basic oxygen contained functional group. Significantly, carbon monoliths when ground into powder with a higher accessible surface area can be designed with a controlled dimension and shape in order to to facilitate their reusability avoiding laborious separation from the treated waste stream such as was experienced with AC powder. The test model MB was

adsorbed and easily desorbed from CM blank powders. These results demonstrated the potential use of this promising material as SPE sorbent. It can be easily prepared from inexpensive and abundant materials for the removal of recalcitrant contaminants in water and waste waters for water purification. Magnetic nanoparticles [60] and/or $TiO_2$ [61] can be readily prepared and incorporated into carbon monoliths via adsorption to facilitate the process design and perform both adsorption and photocatalytic remediation of this blue dye as well as other organic pollutants.

# 4.5 References

1. I. Liska, Fifty years of solid-phase extraction in water analysis - historical development and overview. *J. Chromatogr. A* **885**, 3-16 (2000).
2. M. C. Hennion, Solid-phase extraction: method development, sorbents, and coupling with liquid chromatography. *J. Chromatogr. A* **856**, 3-54 (1999).
3. C. W. Huck, G. K. Bonn, Recent developments in polymer-based sorbents for solid-phase extraction. *J. Chromatogr. A* **885**, 51-72 (2000).
4. M. C. Hennion, Graphitized carbons for solid-phase extraction. *J. Chromatogr. A* **885**, 73-95 (2000).
5. N. Fontanals, R. M. Marce, F. Borrull, New materials in sorptive extraction techniques for polar compounds. *J. Chromatogr. A* **1152**, 14-31 (2007).
6. J. S. Fritz, Recent developments in the separation of inorganic and small organic ions by capillary electrophoresis. *J. Chromatogr. A* **884**, 261-275 (2000).
7. M. W. Jung, K. H. Ahn, Y. Lee, K. P. Kim, J. S. Rhee, J. T. Park, K. J. Paeng, Adsorption characteristics of phenol and chlorophenols on granular activated carbons (GAC). *Microchemical Journal* **70**, 123-131 (2001).
8. B. Altenbach, W. Giger, Determination of Benzene- and Naphthalenesulfonates in Wastewater by Solid-Phase Extraction with Graphitized Carbon Black and Ion-Pair Liquid Chromatography with UV Detection. *Analytical Chemistry* **67**, 2325-2333 (1995).
9. D. Lozano-Castello, J. Alcaniz-Monge, M. A. de la Casa-Lillo, D. Cazorla-Amoros, A. Linares-Solano, Advances in the study of methane storage in porous carbonaceous materials. *Fuel* **81**, 1777-1803 (2002).
10. V. Ruiz, C. Blanco, R. Santamaría, J. M. Ramos-Fernández, M. Martínez-Escandell, A. Sepúlveda-Escribano, F. Rodríguez-Reinoso, An activated carbon monolith as an electrode material for supercapacitors. *Carbon* **47**, 195-200 (2009).
11. X. He, L. Zhou, E. P. Nesterenko, P. N. Nesterenko, B. Paull, J. O. Omamogho, J. D. Glennon, J. H. T. Luong, Porous graphitized carbon monolith as an electrode material for probing direct bioelectrochemistry and Selective Detection of Hydrogen Peroxide. *Analytical Chemistry* **84**, 2351-2357 (2012).
12. T. A. Nijhuis, A. E. W. Beers, T. Vergunst, I. Hoek, F. Kapteijn, J. A. Moulijn, Preparation of monolithic catalysts. *Catalysis Reviews-Science and Engineering* **43**, 345-380 (2001).

13. A. H. Eltmimi, L. Barron, A. Rafferty, J. P. Hanrahan, O. Fedyanina, E. Nesterenko, P. N. Nesterenko, B. Paull, Preparation, characterisation and modification of carbon-based monolithic rods for chromatographic applications. *Journal of Separation Science* **33**, 1231-1243 (2010).
14. C. Liang, S. Dai, G. Guiochon, A graphitized-carbon monolithic column. *Anal.Chem* **75**, 4904-4912 (2003).
15. M. C. Carneiro, L. Puignou, M. T. Galceran, Comparison of silica and porous graphitic carbon as solid-phase extraction materials for the analysis of cationic herbicides in water by liquid chromatography and capillary electrophoresis. *Anal. Chim. Acta* **408**, 263-269 (2000).
16. L. Pereira, Porous graphitic carbon as a stationary phase in HPLC: Theory and applications. *Journal of Liquid Chromatography & Related Technologies* **31**, 1687-1731 (2008).
17. G. Guiochon, Monolithic columns in high-performance liquid chromatography. *J. Chromatogr. A* **1168**, 101-168 (2007).
18. A. Namera, A. Nakamoto, T. Saito, S. Miyazaki, Monolith as a new sample preparation material: Recent devices and applications. *Journal of Separation Science* **34**, 901-924 (2011).
19. A. Bhatnagar, Removal of bromophenols from water using industrial wastes as low cost adsorbents. *Journal of Hazardous Materials* **139**, 93-102 (2007).
20. B. Özkaya, Adsorption and desorption of phenol on activated carbon and a comparison of isotherm models. *Journal of Hazardous Materials* **129**, 158-163 (2006).
21. *Accessed on 01/07/2013, Executive Summary Methylene Blue: Exposure and Toxic.Effects,http://ntp.niehs.nih.gov/ntp/htdocs/Chem_Background/ExecSumm/ MethyleneBlue/MethBlue_exp_toxeffects.html.*
22. G. Ghanizadeh, G. Asgari, Adsorption kinetics and isotherm of methylene blue and its removal from aqueous solution using bone charcoal. *Reaction Kinetics Mechanisms and Catalysis* **102**, 127-142 (2011).
23. J. D. Joshi, V. Jabali, S. Sangita, C. C. Patel, A. B. and Patel, Photo degradation of p-nitrophenol in presence of semiconductor. *Asian Journal of Chemistry* **16**, 1069 - 1075 (2004).
24. T. Liu *et al.*, Adsorption of methylene blue from aqueous solution by graphene. *Colloids and Surfaces B: Biointerfaces* **90**, 197-203 (2012).
25. C.-h. Huang, R.-a. Doong, D. Gu, D. Zhao, Dual-template synthesis of magnetically-separable hierarchically-ordered porous carbons by catalytic graphitization. *Carbon* **49**, 3055-3064 (2011).
26. Y. C. Sharma, Optimization of Parameters for Adsorption of Methylene Blue on a low-cost activated carbon. *Journal of Chemical and Engineering Data* **55**, 435-439 (2010).
27. C. Liang, S. Dai, G. Guiochon, A graphitized-carbon monolithic column. *Analytical Chemistry* **75**, 4904-4912 (2003).
28. C. Lacey, G. McMahon, J. Bones, L. Barron, A. Morrissey, J. M. Tobin, An LC-MS method for the determination of pharmaceutical compounds in wastewater treatment plant influent and effluent samples. *Talanta* **75**, 1089-1097 (2008).
29. C. West, C. Elfakir, M. Lafosse, Porous graphitic carbon: A versatile stationary phase for liquid chromatography. *J. Chromatogr. A* **1217**, 3201-3216 (2010).
30. A. Dabrowski, P. Podkoscielny, Z. Hubicki, M. Barczak, Adsorption of phenolic compounds by activated carbon - a critical review. *Chemosphere* **58**, 1049-1070 (2005).

31. C. A. Staples, P. B. Dorn, G. M. Klecka, S. T. O'Block, L. R. Harris, A review of the environmental fate, effects, and exposures of bisphenol A. *Chemosphere* **36**, 2149-2173 (1998).
32. X. He, K. B. Male, P. N. Nesterenko, D. Brabazon, B. Paull, J. H. T. Luong, Adsorption and desorption of methylene blue on porous carbon monoliths and nanocrystalline cellulose. *ACS Appl. Mater. Interfaces* **5**, 8796-8804 (2013).
33. M. Baba, Y. Kowaka, U. Nagashima, T. Ishimoto, H. Goto, N. Nakayama, Geometrical structure of benzene and naphthalene: Ultrahigh-resolution laser spectroscopy and ab initio calculation. *Journal of Chemical Physics* **135**, (2011).
34. C. Sarici-Ozdemir, Adsorption and desorption kinetics behaviour of methylene blue onto activated carbon. *Physicochemical Problems of Mineral Processing* **48**, 441-454 (2012).
35. V. K. Gupta, R. Jain, M. Shrivastava, A. Nayak, Equilibrium and Thermodynamic Studies on the Adsorption of the Dye Tartrazine onto Waste "Coconut Husks" Carbon and Activated Carbon. *Journal of Chemical and Engineering Data* **55**, 5083-5090 (2010).
36. A. T. Mohd Din, B. H. Hameed, A. L. Ahmad, Batch adsorption of phenol onto physiochemical-activated coconut shell. *Journal of Hazardous Materials* **161**, 1522-1529 (2009).
37. M. Ahmaruzzaman, D. K. Sharma, Adsorption of phenols from wastewater. *Journal of Colloid and Interface Science* **287**, 14-24 (2005).
38. B. Singh, S. Madhusudhanan, V. Dubey, R. Nath, N. B. S. N. Rao, Active carbon for removal of toxic chemicals from contaminated water. *Carbon* **34**, 327-330 (1996).
39. M. Otero, M. Zabkova, A. E. Rodrigues, Comparative study of the adsorption of phenol and salicylic acid from aqueous solution onto nonionic polymeric resins. *Separation and Purification Technology* **45**, 86-95 (2005).
40. M. C. Pietrogrande, A. Benvenuti, F. Dondi, Temperature effect on HPLC retention of PCBs on porous graphitic carbon. *Chromatographia* **51**, 193-198 (2000).
41. *Accessed on 06/09/2013, AquaSorb 2000-granular coal based activated carbon, Technical Data Sheet, www.jacobi.net.*
42. I. Langmuir, The adsorption of gases on plane surfaces of glass, mica and platinum. *Journal of the American Chemical Society* **40**, 1361-1403 (1918).
43. E. Richter, W. Schutz, A. L. Myers, Effect of adsorption equation on prediction of multicomponent multicomponent adsorption equilibria by the ideal adsorbed solution theory. *Chemical Engineering Science* **44**, 1609-1616 (1989).
44. D. A. Ratkowsky, *Handbook of Nonlinear Regression Models.* (Marcel Dekker, New York, 1990).
45. C. J. Radke, J. M. Prausnitz, Thermodynamics of multi-solute adsorption from dilute liquid solutions. *Aiche Journal* **18**, 761-+ (1972).
46. R. Sips, On the structure of a catalyst surface. *Journal of Chemical Physics* **16**, 490-495 (1948).
47. K. S. Mundhe, A. B. Gaikwad, R. C. Torane, N. R. Deshpande, R. V. Kashalkar, Adsorption of methylene blue from aqueous solution using Polyalthia longifolia (Ashoka) seed powder *Journal of Chemical and Pharmaceutical Research* **4**, 423-436 (2012).
48. U. Gecgel, G. Ozcan, G. C. Gurpinar, Ü. Geçgel, G. Özcan, G. Ç. Gürpınar, Removal of methylene blue from aqueous solution by activated carbon prepared from pea shells (pisum sativum). *Journal of Chemistry* **2013**, 9 pages (2013).

49. H. M. F. Freundlich, Über die Adsorption in Lösungen *Zeitschrift für Physikalische Chemie* **57**, 385-470 (1906).

50. K. Bergmann, C. T. Okonski, A spectroscopic study of methylene blue monomer, dimer, and complexes with montmorillonite. *Journal of Physical Chemistry* **67**, 2169-2177 (1963).

51. J. J. Kipling, R. B. Wilson, Adsorption of methylene blue in the determination of surface areas. *Journal of Applied Chemistry* **10**, 109-113 (1960).

52. C. E. J. Johnson, paper presented at the 131st National Meeting of the American Chemical Society, April 7-12 1957.

53. M. Kalousek, R. Blagnik, Issledovanie monolekulyarnykh plenok. 3.prebor dlya izucheniya monomolekulyarnykh plenok, adsorbirovannykh na granitse razdela rtut-voda. *Collection of Czechoslovak Chemical Communications* **20**, 782-788 (1955).

54. T. G. Yan, L. H. Li, L. J. Wang, A Simple Nickel Activation Process for Electroless Nickel-Phosphorus Plating on Carbon Fiber. *BioResources* **8**, 340-349 (2013).

55. P. Sharma, H. Kaur, M. Sharma, V. Sahore, A review on applicability of naturally available adsorbents for the removal of hazardous dyes from aqueous waste. *Environ. Monit. Assess.* **183**, 151-195 (2011).

56. K. Y. Foo, B. H. Hameed, An overview of dye removal via activated carbon adsorption process. *Desalin. Water Treat.* **19**, 255-274 (2010).

57. Y. Zhu, D. Wang, X. Zhang, Q. Hongdong, Adsorption removal of methylene blue from aqueous solution by using bamboo charcoal. *Fresenius Envir. Bulletin* **18**, 369-376 (2009).

58. M. A. Rahman, S. M. Ruhul Amin, A. M. Shafiqul Alam, Removal of methylene blue from waste water using activated carbon prepared from rice husk. *Dhaka Univ. J. Sci.* **60**, 185-189 (2012).

59. R. Berenguer, J. P. Marco-Lozar, C. Quijada, D. Cazorla-Amoros, E. Morallon, Comparison among Chemical, Thermal, and Electrochemical Regeneration of Phenol-Saturated Activated Carbon. *Energy & Fuels* **24**, 3366-3372 (2010).

60. R. Liu, X. Shen, X. Yang, Q. Wang, F. Yang, Adsorption characteristics of methyl blue onto magnetic $Ni_{0.5}Zn_{0.5}Fe_2O_4$ nanoparticles prepared by the rapid combustion process. *J Nanopart Res* **15**, 1-11 (2013).

61. K. M. Joshi, V. S. Shrivastava, Removal of methylene blue dye aqueous solution using photocatalysis. *Int. J. Nano Dim.* **2**, 241-252 (2012).

# Chapter 5

# Development and Characterisation of Laser Cut Carbon Monolithic Discs

*"An experiment is a question which science poses to Nature and a measurement is the recording of Nature's answer."*

Max Planck

## Abstract

It is important to keep the integrity of carbon based porous structures as well as to be able to tailor-make them into desirable shapes to enable targeted applications. A simple set up using a 1.5 kW $CO_2$ laser in continuous wave mode (CW) was implemented to cut fragile and porous CM blank and NTCM rods into discs with prescribed thickness and good integrity (laser secioned carbon monoliths (LCMs)). Changes in structure, porosity and composition of these LCMs were induced by the efficient thermal energy afforded by CW $CO_2$ laser irradiation under the controlled conditions. The main effects observed after laser cutting were extensively studied. FE-SEM images confirmed that the resulting LCMs exhibited a more open, interconnected macroporous structure and smoothed mesopores to a depth of approximately 5 $\mu$m, while the structure of the middle section was kept intact. Minimal change in chemical composition was confirmed by X-ray photoelectron spectroscopy (XPS). Raman spectroscopy revealed a modest increase in the graphitic content on the cross sections of LCM discs, which considerably improved their electrical conductivity. The integration of open macroporous cross section, hierarchical porous body and high mesoporosity makes these materials highly efficient for small polar organic molecule removal through physisorption, with unique selectivity and kinetics compared with scalpel sectioned discs. The model analytes used were phenol and bisphenol A (BPA). The same batches of carbon monolithic samples cut by scalpel were used to prepare the LCM blank and LNTCM samples. Characterisation and application results determined from scalpel cut carbon monoliths (SCMs) were used as reference for comparison with results determined with LCMs and LNTCMs.

## Aim

The aim of this work was to develop a controllable, reproducible and facile method to cut fragile carbon monolithic rods into discs using a CW 1.5 kW $CO_2$ laser, without damage to the porous structure. The impacts of the laser beam upon different types of carbon monolithic materials' surfaces (CM blank and NTCM) were studied. The possible enhancement of the properties of these promising carbon monolithic materials for adsorption of aromatic molecules was also to be investigated.

147

## 5.1. Introduction

The development of novel porous carbon based monolithic materials is a topical area of research within the fields of analytical chemistry and material science over the last decade. They have found diverse applications in chromatography [1, 2], SPE [3], energy storage [4], as catalytical supports [5] and within electrochemistry [6] owing to their high specific surface area, interconnected porous structure, low hydraulic resistance, unique retention mechanism and excellent thermal/chemical stability. Most of these applications require the carbon monolith to be of a certain shape for adaptation into a flow-through device. Though various chemical synthetic techniques were developed for tailoring microscopic properties such as pore size, pore shape, pore connectivity and pore surface reactivity, there are few studies carried out on development of tailoring a bulk monolithic material into various suitable macroscopic forms such as fibres, thin films and rods for development of actual applications. In general, most carbon monoliths are cut by a scalpel or knife for their use in flow through applications. Such mechanical cutting methods are not very suitable as they tend to cause deformations or cracks within the porous structure; hence the monolithic materials subsequently lose their integrity and openness for future use. In addition such methods are unable to form the carbon monolith into more complicated shapes, and their dimensional reproducibility is also not of a high standard. An alternative and superior cutting technique is needed to overcome these difficulties, in order to satisfy the growing interest in the use of carbon monolithic materials.

Recently, several groups have reported the synthesis of carbon monolith replicas from silica monoliths in order to achieve various macroscopic shapes with tunable pore sizes and structures [7-10]. The unique property of the silica monolith presents an excellent template for carbon replicas. Zhang and his co-workers developed a nanocasting method to prepare size and porosity controlled carbon replicas from hierarchical silica monoliths [10]. They moulded the silica templates into the required shapes and sizes and carbonised the sucrose-filled silica monolith, and subsequently removed the silica frameworks by NaOH. The corresponding carbon monolithic replicas were in various shapes including cylinders, triangles, squares, loops, and pentagons with reverse microstructures to the parent silica monolithic

templates, as shown in Figure 5.1. Such nanocasting approaches require precise control of the loading of the precursor in the mesoporous channels of the templates [11]. More details about nanocasting can be found in Section 1.3.1, Chapter 1.
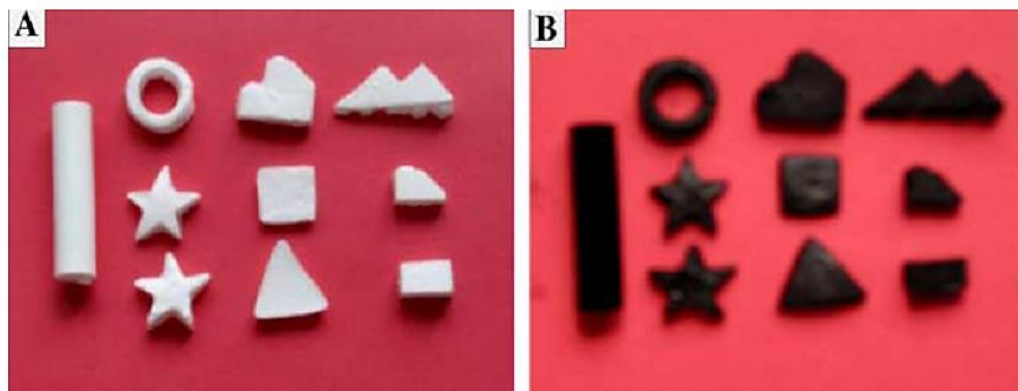


**Figure 5.1:** *Photograph of (A) the silica templates and (B) the corresponding carbon replicas. (Reproduced from [10] )*

In the search for more efficient, more flexible and reproducible fabrication strategies, laser processing is an attractive option for achieving prescribed dimensions of monoliths for various applications. Laser is an acronym of "Light Amplification by Stimulated Emission of Radiation" [12]. It provides a coherent and monochromatic source of electromagnetic radiation that can propagate in a straight line with negligible divergence. According to practical applications, laser material processing can be classified into four major categories, which include forming (manufacturing of near net-shape or finished products), joining (welding, brazing, etc.), machining (cutting, drilling, etc.) and surface engineering (processing confined only to the near-surface region) (Figure 5.2). These application areas are defined by specific combinational regions of power density (irradiance) and exposure/interaction time (residence time) [13]. The various processes can be achieved by varying of the irradiance and residence time to heat, melt and/or vaporise the target material. Many groups use laser processing for microfluidic chip fabrications. For instance, Sinton group reported how they employed multiple passes of a commercial $CO_2$ laser at low power (1.8 W) and low speed to cut Teflon film as part of their microfluidic chips fabrication.
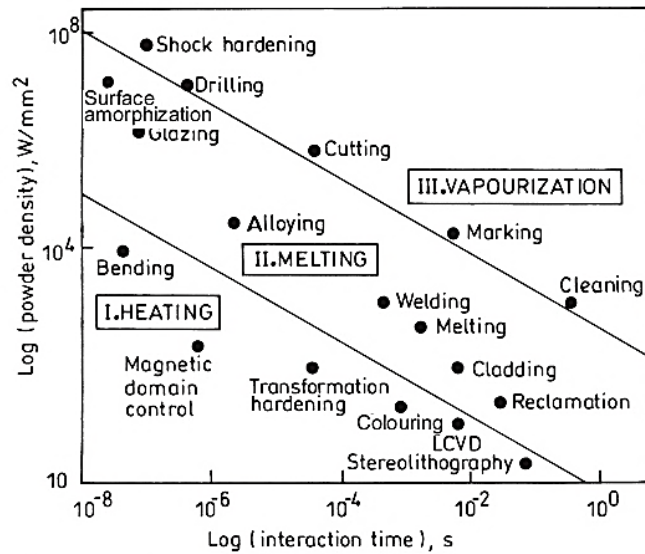
*Figure 5.2*: *Process map of laser power density as a function of interaction time for different laser material processing methods (Reproduced from [13]).*

The increasing demand for use of laser material processing can be attributed to several unique advantages, namely high productivity, ability to automate, non-contact nature, elimination of finishing operations, reduced processing cost, improved product quality, greater material utilisation and minimised heat affected zone [13]. Figure 5.3 shows another classification of the laser material processing techniques based on materials' phase/state changes.
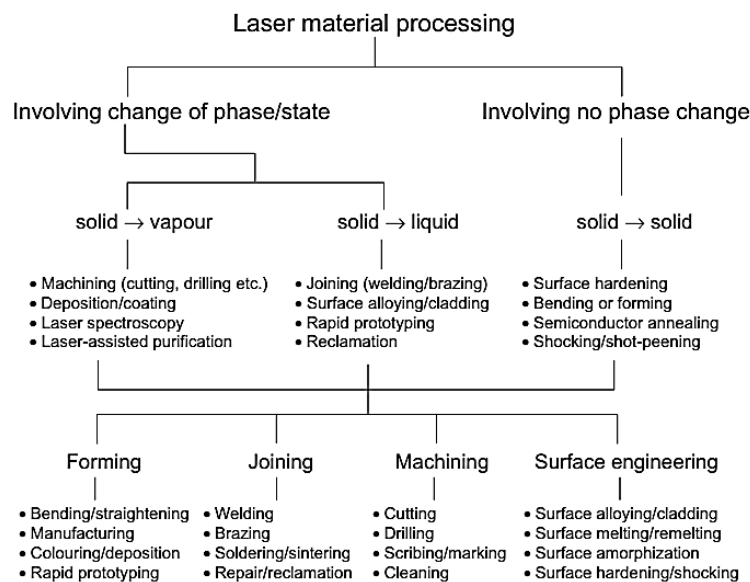


*Figure 5.3:* *Classification of laser material processing based on phase/state changes (reproduced from [13]).*

The following work focused on the high power density vaporisation regime which requires a substantial amount of energy to be induced in a reasonably short period of time to trigger phase transformation and microstructure. The $CO_2$ laser is one of the most powerful lasers for cutting due to its wide output power range, typically $1 - 10$ kW. Thus it is a practical solution to this type of process in compassion to the Nd : YAG laser option [13]. The $CO_2$ laser is particularly suited for this application because of its high power output and stability, which allows for deeper penetration. These characteristics align well with the focus of this study, which is to use the laser beam as a heating source to induce carbon phase transformation from solid to vapour.

This Chapter presents the first report of using a $CO_2$ laser as an alternative tool to cut carbon monolith into discs. The ablation by laser beam can be considered as high temperature applied onto the carbon monolithic rods and subsequently vaporise a thin layer of sample to form a disc. Thus the main effects of laser ablation in the cross sections of two types of carbon monolithic discs (LCM blank and LNTCM) were intensely studied using various characterisation techniques. Moreover, their potential application as new selective sorbent materials for adsorption of organic molecules (phenol and BPA), in comparison with their scalpel cut carbon monolithic counterparts was also investigated.

## 5.2 Experimental

### 5.2.1 Reagents and materials

As described in Chapter 4, Section 4.2.1 with the following additions. Phenol ($\geq$ 99 wt. %) and bisphenol A ($\geq$ 99 wt. %) were all obtained from Sigma-Aldrich (Dublin, Ireland). Acetonitrile and methanol were purchased from Fisher. Acetonitrile (HPLC grade, 99.9 wt. %) were purchased from Fisher Scientific (Dublin, Ireland). All reagents were of analytical grade with and used as received and without purification. All solvents used were high-performance liquid chromatography (HPLC) grade or higher for phenol and BPA adsorption. The commercial silica-based monolithic rods consisted of a silica-skeleton modified with $C_{18}$ groups and activated carbon (MonoTrap RCC18) were obtained from GL Sciences (Tokyo, Japan) and used as received. MonoTrap rods were in hollow

cylindrical shape (5 × 2.9 mm O.D, 1 mm channel), ~8mg, with 150 m$^2$/g surface area.

## 5.2.2 Instrumentation

The physiochemical properties of the laser cut carbon monoliths were fully characterised using the following techniques. The surface morphology of the LCM discs was examined using a Hitachi S-5500 FE-SEM (Dallas, TX, USA) at an accelerating voltage of 10 kV for achieving high-resolution SEM images of their surfaces. The surface compositions of the LCMs were examined using X-ray photoelectron spectroscopy (XPS). The XPS spectra were recorded using a Kratos AXIS-165 electron spectrometer, with monochromatic Al Kα radiation of energy 1486.6 eV. Each spectrum was the accumulation of three scans. High resolution spectra were taken at fixed pass energy of 20 eV, 0.05 eV step size and 100 ms dwell time per step. Surface charge was efficiently neutralised by flooding the sample surface with low energy electrons. Core level binding energies were corrected using C 1s peak at 284.5 eV as the charge reference [14]. For construction and fitting of synthetic peaks of high resolution spectra, a mixed Gaussian-Lorenzian function with a Shirley type background subtraction were used. Raman spectra were obtained using a Horiba JobinYvon LabRam 800HR with a CCD detector (New Jersey, USA). The Raman argon ion laser used was the Innova 70-C-2, made by Coherent (Santa Clara, USA). The laser power was 6 mW with an excitation wavelength of 514.5 nm. A magnification of ×50 on the objective lens was used both to focus the laser beam and to collect the backscattering radiation. The exposure time of all spectra recorded was 10 s.

A Rofin DC015 slab $CO_2$ laser with a maximum power output of 1.5 kW in the far infrared region (10.6 $\mu$m wavelength) was used for cutting the carbon monolithic rods. A DT205LR Handheld Tachometer LCD Display tachometer (Shimpo, Instruments, Itasca, Illinois, USA) was used to measure the rotation speed of a rotary motor which rotated the samples during cutting.

### 5.2.3 $CO_2$ laser cutting of cylindrical carbon monoliths

The experiments were conducted on a in-house prepared CM blank and NTCM rods. Each rod was mounted in a fitted glass tube using epoxy glue in order to be able to be held in a chuck and rotated by the motor later for the ablative cutting operation. The work-pieces, approximately 20 mm long and 3 mm in diameter were cut using a Rofin DC015 slab $CO_2$ laser in continuous wave mode. In continuous wave mode the output power of the laser beam is constant over time. The laser has a maximum power output of 1.5 kW in the far infrared region (10.6 $\mu$m wavelength). Both pulsing and continuous wave laser operation modes were available. The simple continuous wave mode (CW) was used in order to avoid the cumbersome design of the experiment for pulsed mode. Preliminary trials revealed that rotating the samples resulted in homogeneous and clean cuts. Subsequent to the preliminary test an optimisation study resulted in the following parameters being used for the final study: average power of 90 W, feed rate of 100 mm/min and rotational speed of 100 rpm/min. The estimated ablation distance is 0.1 mm. An additional 0.1 mm was added to the desired sample thickness e.g. for a final thickness of the LCM disc to be 2 mm, a 2.1 mm feed was used to compensate for the vaporised material. Argon at a pressure of 0.2 bars was used as an assist gas to minimise heating affected zoom by increasing the cooling rates, and preventing back-spattering of ablated particles capable of damaging the laser optics. The operation of this laser system was controlled by a Rofin laser control unit which was used to control laser beam peak power, duty cycle, and pulse repetition frequency. The work-piece was rotated with a DC motor fixed to a table moving perpendicular to the laser irradiation direction. The maximum rotational speed was 2500 rpm. Rotational speed was checked with a DT205LR Handheld Tachometer LCD Display tachometer (Shimpo, Instruments, and Itasca, Illinois, USA). A schematic of the laser processing set-up is shown in Figure 5.4. The Gaussian laser beam output was focused on the work-piece surface providing a laser spot size of 90 μm for all experiments. The power was set to 90 W for the laser cutting operation. The power density used can be calculated according to $(90/\pi\ 0.045^2) = 1.42 \times 10^4$ W/mm$^2$. The minimum laser beam spot size of 90 μm was employed in order to maximize the cooling rates since smaller heat affected areas result in higher cooling rates. The laser beam was perpendicular to the work-piece to maximise laser beam absorbance [15]. The tangential (100 rpm/min) and

linear velocities (100 mm/min) of the sample's rotation and feed were calculated based on the laser spot overlapping for the full coverage of the process surface.
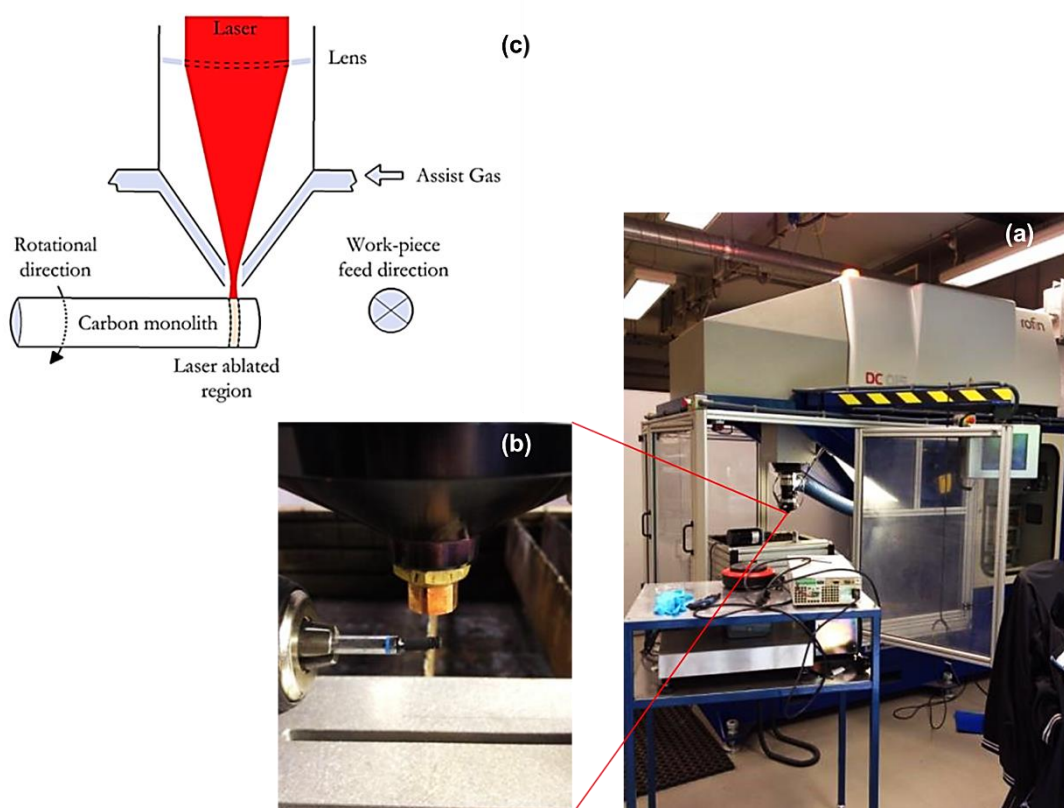


*Figure 5.4: (a) A photograph of the overall set-up of carbon monolith sectioned by $CO_2$ laser, (b) showing glass tubing mounted carbon monolith rod holed by a rotary motor under the laser nozzle (c) a schematic of the $CO_2$ laser cutting carbon monolith.*

## 5.2.4 Characterisation of LCM

For FE-SEM sample preparations, all of the samples were prepared by slicing approximately 2 mm in thickness a cross section of carbon monolith using a scalpel while keeping the laser ablated section intact. The scalpel cut section was then loaded onto a normal carbon film grid. Once the side of the laser processed carbon monolith was imaged, as 'a laser sectioned sample', then approximately 1 mm in thickness of the sample was sliced off to image it again, as 'a scalpel cut sample'. For XPS and Raman sample preparations, all of the samples were dried 40 $^o$C under vacuum for 16 h to remove any physically adsorbed moisture before the spectroscopic analysis.

## 5.2.5 Adsorption study of phenol

The details and methods of phenol and BPA sample preparation, adsorption kinetics of phenol and BPA, desorption of phenol and BPA and detection by RP-HPLC analysis were described in Section 4.2.3.

# 5.3   Results and discussion

## 5.3.1 CW $CO_2$ laser cut CM

The intense heat that a laser beam produces on solid matter enables it to create precise and uniform cutting of materials, which is distinct when compared to the conventional mechanical method [13]. Laser cutting in this study operates by the direction of the output of the laser at the material, then elevating the temperature rapidly on the carbon monolith surface to reach its vaporisation point, thereby leaving the surface of the cut edge with a high quality finish. Photography of the LCM blank and SCM blank are shown in Figure 5.5 (a) and (b), respectively. With a view to obtaining 2 mm thick discs, the SCM blank crumbled after scalpel cutting while the LCM blank disc maintained the required disc shape and structure after the laser cutting.
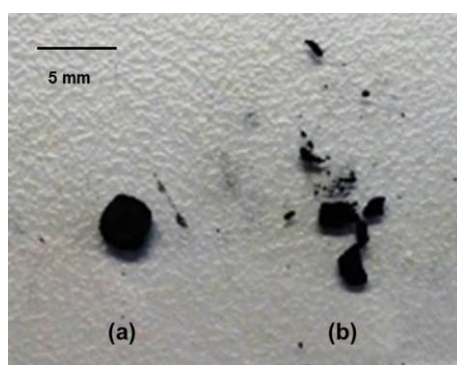


***Figure 5.5:*** *Photograph of (a) LCM blank disc (2 × 3 mm I.D.) and (b) attempted SCM blank disc (2 × 3 mm I.D.).*

The pros and cons of laser and scalpel cut carbon monolithic rods are summarised in Table 5.1. The use of $CO_2$ laser cutting of carbon monolithic materials has many advantages over traditional scalpel cutting, including being a more flexible process, rapid/automatic prototyping of desirable size/shape, producing a smoother surface finish, less contamination caused by cutting tools, and is reproducible. In addition,

the high thermal energy laser beam could be an alternative means for increasing the degree of graphitisation and oxygen functional groups on the processed surfaces, which will be described in more detail in Section 5.3.3 and 5.3.4. According to a previous porosity study in Section 3.3.3, these carbon monoliths have high porosities, i.e. volume density is low, the minimum power was required only 6 % of the output power, i.e. 90 W, respectively.

***Table 5.1:*** *The summary of the pros and cons of laser cut (LCMs) and scalpel cut carbon monolithic rods (SCMs).*

| | Laser cutting (LCMs) | Scalpel cutting (SCMs) |
|---|---|---|
| **Pros** | Smooth and even surface, high reproducibility, controllable shape and size, minimum damage to the porous structure; efficient (10 discs were processed within 3 min via manual loading of samples), increase the graphitic feature, certain percentage of oxygen included functional groups and reduce contaminations. | Easy, cheap and typically no dramatic chemical composition changes. |
| **Cons** | High capital costs | Uneven surface (the carbon material could be fractured after the certain amount of force was applied on the material surface since it is rather brittle.), not reproducible, damage to the porous structure and ease of sample breakage or cracking, time consuming and possible increase of contaminations. |

One of the major parameters for proving the reproducibility of this laser cutting process is the thickness of each of the LCMs. A Vernier calipers was used for a direct reading of the thickness of the processed discs.The thickness of five randomly selected inter-day prepared LCM blank discs was measured by Vernier calipers with 0.01 mm accuracy as shown in Table 5.2. There was no significant difference in thickness between LCM blank and LNTCM discs. The average thickness of 6 LCM blank discs was $2.003 \pm 0.004$ cm. For most industrial and academic applications, this 95% confidence range is acceptable and would allow for fluid tight integration of the monolith within flow through devices.

*Table 5.2:* *Thickness measurements for five carbon monolithic discs*

| LCM blank samples | Thickness (cm) |
|:---:|:---:|
| 1 | 2.00 |
| 2 | 2.01 |
| 3 | 2.00 |
| 4 | 2.01 |
| 5 | 2.00 |
| 6 | 2.00 |
| **Average thickness** | $2.03 \pm 0.004$ |

## 5.3.2 Structure and morphology of LCMs

A series of SEM micrographs revealed distinguishing features of the laser heating on a well-defined three-dimensional structure from the cross sections of laser sectioned CM blank and NTCM discs, and comparison with non-laser sectioned scalpel cut counterparts as shown in Figure 5.6. The laser sectioned materials showed porous structures within the cross section which were more integrated, flatter and without any broken fragments or cracks.

In the heat transfer theory by thermal conductivity, a temperature gradient was generated by molecular transfer of heat in a continuous medium without consideration of heat transfer by diffusion of materials [16]. For porous materials, their thermal conductivity coefficient was mostly dependent on their volume density and the thermophysical properties of the media which filled in their cavities and pores [17]. The effective thermal conductivity of these materials is also partially dependent on the size and form of the pores and cavities [18]. Since the porous structure was not ordered within the carbon monoliths, i.e. the pores and cavities with either fully closed volumes or completed interconnected open channels, heat transfer in such materials show some different phenomena at pores/cavities and points of direct contact as transfer occurs by conductivity. Heat transfer occurs in the air medium of the pores and cavities by both conductivity and radiation. The contribution of the random heat transfer increases with increase in pores and cavity size. As both carbon skeleton and air have low thermal conductivity [19, 20], the laser ablation showed minimal heat affected zones present in the samples after ablative cutting. Approximately 0.1 mm of carbon monolith at the tip of the rod was

vaporised. The overall structures for the most part kept their integrity. All macropores maintained similar shapes and sizes after laser ablation, except they became more opened and the depth of the processed microstructure could be seen to be approximately 5 $\mu$m. Those channels were probably caused by relatively rapid high temperature/pressure $CO_2$ stream induced during the laser ablation [21]. Tobes *et al.* also observed the surface opening of the inner tubes in carbon fibre after the liquid phase oxidative treatments [22]. The mesopores/micropores with irregular shapes on the laser sectioned samples were visibly diminished in comparison with the scalpel sectioned samples (Figure 5.6 (b), (d), (f) and (h)).

The CM blank possessed the full coverage of an ordered nodular pattern on the carbon skeleton which could have been induced by molten carbon spheroidisation due to the high surface tension (Figure 5.6 (d)). The nodular pattern shown in CM blank samples was created possibly due to the rapid cooling rate occurring immediately after a sintering process. These balls solidified quickly under the assistance of argon gas. Such phenomenon was also observed from sintered iron-graphite powder mixture [23]. As discussed in Chapter 3, the thermal resistance of NTCM is higher than CM blank due the existence of $C_{60}$ residue in NTCM. As shown in Figure 5.6 (h), the skeleton of laser sectioned NTCM was much smoother than CM counterpart which indicated that the degree of carbon melting and perhaps cooling rate was less than with the CM blank. In the other words, the depth of molten layer was shallower in NTCM.
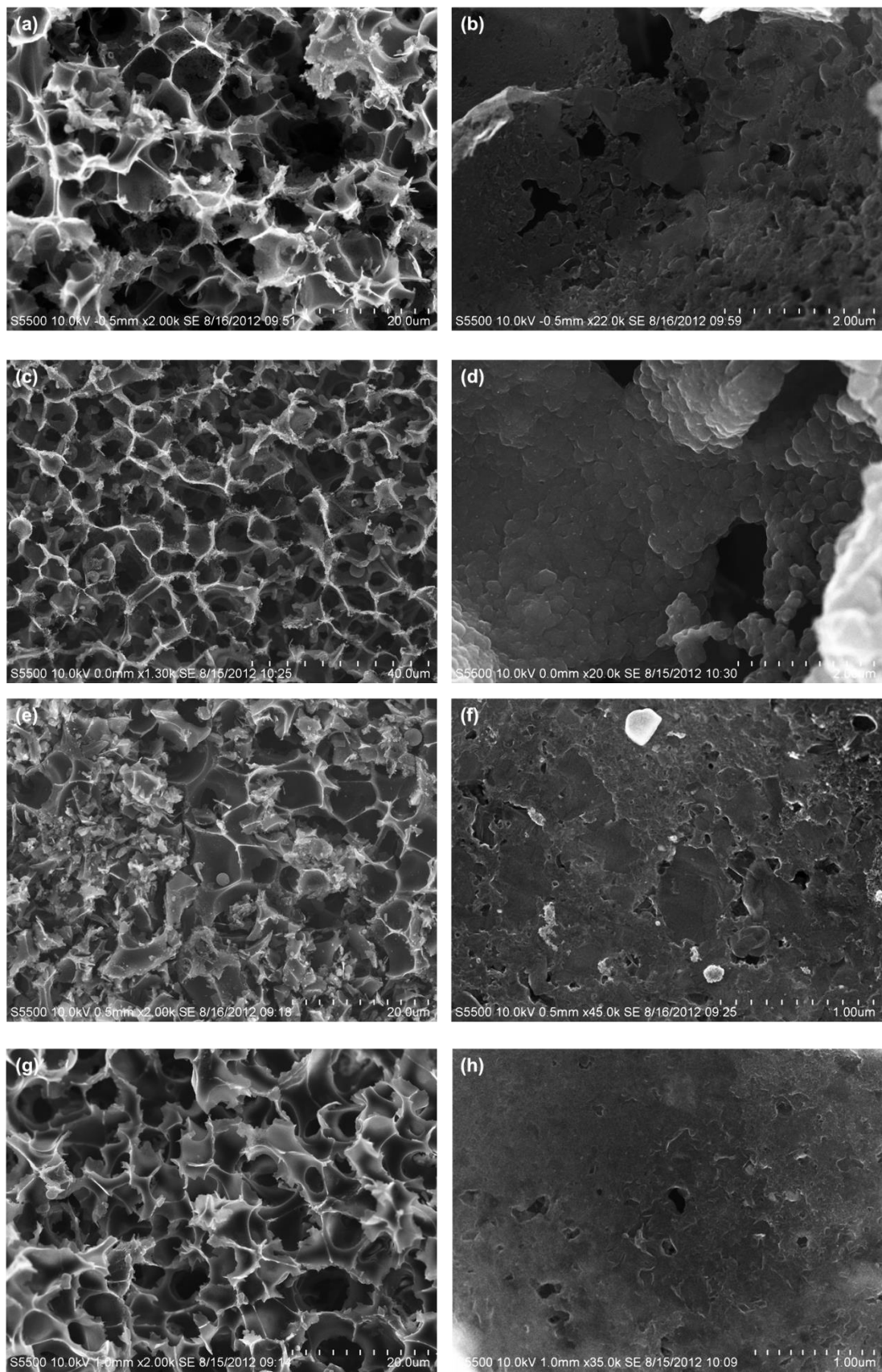
***Figure 5.6:*** *FE-SEM images of scalpel sectioned CM blank (a) macroporous structure and (b) mesoporous structure; laser sectioned CM blank (c) macroporous structure and (d)*

*mesoporous; scalpel sectioned NTCM (e) macroporous structure and (f) mesoporous structure; laser sectioned NTCM (g) macroporous structure and (h) mesoporous, with different magnifications.*

The higher magnification SEM showed the smooth surface texture and the presence of irregular mesoporous structure on the inner wall of the macropore within the NTCM (Figure 5.7 (a) and (b)). In addition, there were also few same size circular ~ 200 nm macropores among the mesopores (Figure 5.7 (c) and (d)). This structure has not previously been identified in literature. However, it is postulated that these circular pores were heating annealing holes possibly caused by heat from the vapour state of carbon penetration to heterogeneous surfaces of NTCM, for example $CO_2$ gas evolved from boiled liquidified graphite with fast cooling process.
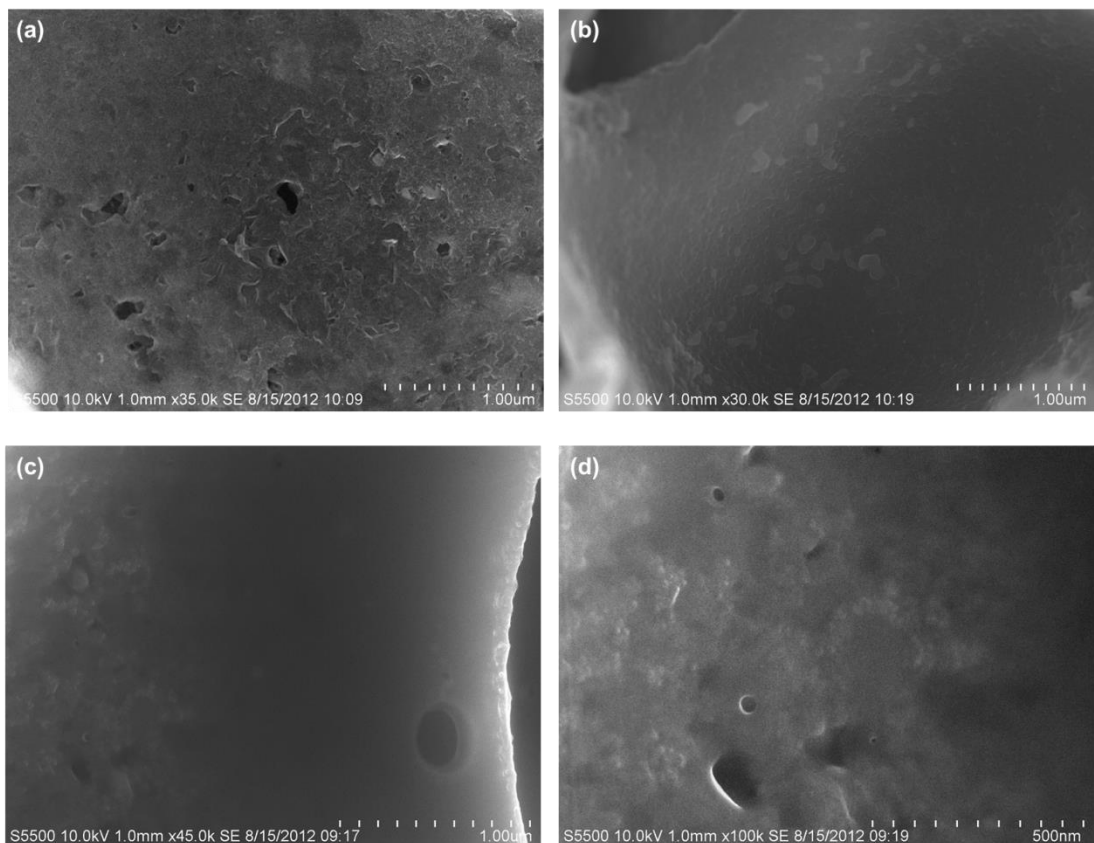


**Figure 5.7:** *High magnification of* FE-SEM images of (a) - (d) mesoporous structure of LNTCM.

### 5.3.3 X-ray photoelectron spectroscopy

The surface modification of carbon surface is rather challenging, owing to its chemical and thermal inertness. One of the most common approaches involves oxidizing the carbon surface with acid or ozone to achieve oxygenated functional groups, such as carboxylic acids, esters, or quinones [24]. However, the drawbacks of such oxidation processes are that the resultant carbon materials have low bonding densities, and damaged surface or porous structure [25, 26]. It was interesting to determine if there are any extra oxygen functional groups on these LCM cross sections subsequently created by this laser ablation process at atmospheric condition, i.e. not in vacuum condition and with low Ar gas flow during the laser cutting process. This approach can be considered similar to high temperature thermal treatment taking place on the cross sections. Secondly, the existing surface oxygen groups on carbon materials can possibly be decomposed by heating to produce CO and $CO_2$ at different temperatures. As a consequence of the decomposition of the acidic groups [14, 27], $CO_2$ evolves at low temperatures. The evolution of CO occurs at higher temperatures and is originated by further oxidation of basic or neutral groups such as phenols, ethers and carbonyls [14, 27]. It is very important to understand the transformation of the existing oxygenated functional groups.

As previously mentioned LCMs have a sandwich-like hybrid structure. EDX technique was no longer suitable for such detection because the X-ray beam penetrates more than 5 μm into this material. Thus, XPS technique was an ideal technique for the analysis of the surface elemental compositions and atomic configuration within 0 to 10 nm of samples' surface which was well within the laser abrasive layers [28].

Survey XPS spectra of LCM blank gave three strong signals from oxygen, carbon and iron while SCM blank showed only have oxygen and carbon, as seen in Figure 5.8. The sign of trace iron in LCM blank was likely to be due to contamination from lying on the laser stage after being cut, which could possibly be removed by water washing. The detection limit of the XPS was < 0.1 atomic %.
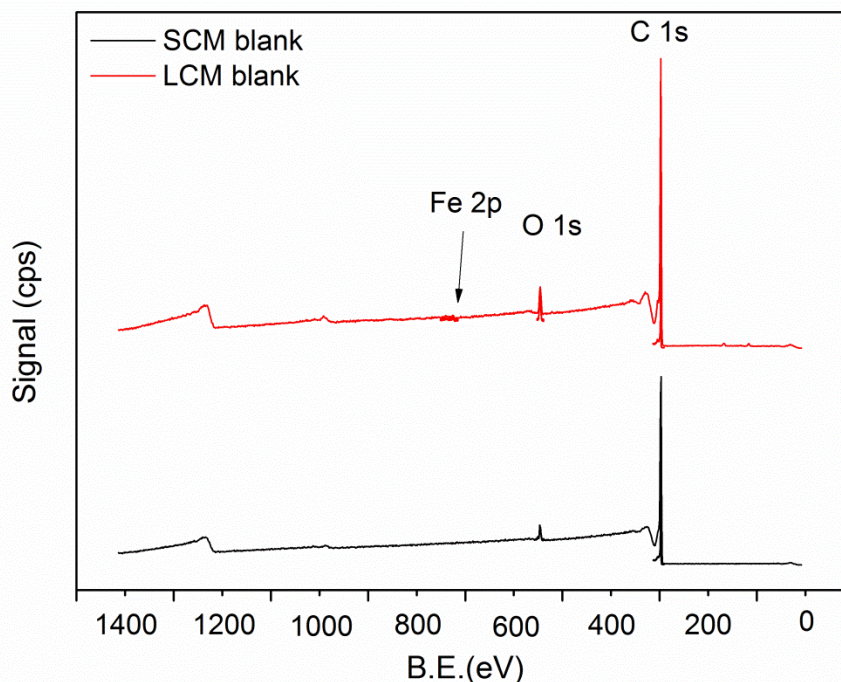
***Figure 5.8:*** *XPS survey spectrum of SCM blank and LCM blank.*

Table 5.3 – Table 5.6 show the high-resolution XPS spectra of the cross sections of scalpel cut/laser cut CM blank and NTCM samples, respectively, with compositions, BE (binding energy), FWHM (full width at half maximum of peak) and RSF (relative sensitivity factor) values and % conc. (percentage atomic concentration). Rows highlighted in grey correspond to overall concentration. Rows below these show the synthetic components and most likely species responsible for them. The binding energies were assigned using C 1s at 284.5 eV as charge reference for all of the samples [29].

The oxygen content was found to be 4.2 % in the LCM blank which was 1.6 % more than that in the SCM blank. These oxygen-containing surface groups were formed by reaction with oxidizing gases from the air surrounding the carbon monolith rods (e.g. $O_2$, and $CO_2$) [30]. The percentage of carbon with different functional groups in the LCM blank was slightly lower than for the SCM blank except for C-O which was 7.1 % in LCM blank compared with 5.4 % in SCM blank. Meanwhile, there was 1.8 % less carbon in LCM blank. Therefore, it can be predicted that 1.7 % of the carbon converted to C-O after laser ablation and that 0.1 % of carbon was converted to $CO/CO_2$ and evolved during the laser cutting process.

162

**Table 5.3:** *Compositions from a high resolution XPS spectrum of SCM blank.*

| Name | B. E (eV) | FWHM (eV) | R. S. F. | % Conc. | Assigned Functional groups |
|------|-----------|-----------|----------|---------|----------------------------|
| **O 1s** | 533.3 | 3.1 | 2.93 | 2.6 | |
| **C 1s** | 284.5 | 0.8 | 1 | 97.4 | |
| **O 1s_1** | 530.6 | 1.6 | 2.93 | 0.4 | Oxides |
| **O 1s_2** | 532.0 | 1.7 | 2.93 | 1.2 | From organic |
| **O 1s_3** | 533.5 | 1.4 | 2.93 | 1.0 | From organic |
| **C 1s_1** | 284.5 | 0.7 | 1 | 61.8 | Hydrocarbon |
| **C 1s_2** | 285.2 | 1.3 | 1 | 13.1 | C-C |
| **C 1s_3** | 286.3 | 1.3 | 1 | 5.4 | C-O |
| **C 1s_4** | 287.6 | 1.5 | 1 | 5.1 | C=O |
| **C 1s_5** | 289.3 | 1.5 | 1 | 4.5 | O-C=O |
| **C 1s_6** | 291.0 | 1.5 | 1 | 4.0 | Shake up satellites, pi to pi* |
| **C 1s_7** | 292.5 | 1.8 | 1 | 2.3 | Shake up satellites, pi to pi* |
| **C 1s_8** | 294.4 | 2.0 | 1 | 1.2 | Shake up satellites, pi to pi* |

**Table 5.4:** *Compositions from a high resolution XPS spectrum of LCM blank.*

| Name | B. E (eV) | FWHM (eV) | R. S. F. | % Conc. | Assigned Functional groups |
|------|-----------|-----------|----------|---------|----------------------------|
| O 1s | 532.9 | 3.2 | 2.93 | 4.2 | |
| C 1s | 284.5 | 0.6 | 1 | 95.6 | |
| Fe 2p | 711.6 | 1.1 | 16.4 | 0.2 | |
| **O 1s_1** | 531.0 | 1.6 | 2.93 | 0.8 | Oxides |
| **O 1s_2** | 532.0 | 1.7 | 2.93 | 1.6 | From organic |
| **O 1s_3** | 533.8 | 1.8 | 2.93 | 1.8 | From organic |
| **C 1s_1** | 284.5 | 0.5 | 1 | 60.2 | Hydrocarbon |
| **C 1s_2** | 285.2 | 0.9 | 1 | 11.7 | C-C |
| **C 1s_3** | 286.3 | 1.3 | 1 | 7.1 | C-O |
| **C 1s_4** | 287.6 | 1.5 | 1 | 4.0 | C=O |
| **C 1s_5** | 289.4 | 1.5 | 1 | 3.7 | O-C=O |
| **C 1s_6** | 291.0 | 1.5 | 1 | 4.2 | Shake up satellites, pi to pi* |
| **C 1s_7** | 292.3 | 2.0 | 1 | 3.4 | Shake up satellites, pi to pi* |
| **C 1s_8** | 294.5 | 1.9 | 1 | 1.4 | Shake up satellites, pi to pi* |
| **Fe 2p_1** | 712.1 | 3.8 | 16.4 | 0.09 | Fe 2p 3/2: $Fe^{+3}$, $Fe^{+2}$ |
| **Fe 2p_2** | 716.1 | 3.1 | 16.4 | 0.04 | Fe 2p 3/2: satellite $Fe^{+2}$ |
| **Fe 2p_3** | 719.1 | 3.3 | 16.4 | 0.02 | Fe 2p 3/2: satellite $Fe^{+3}$ |
| **Fe 2p** | 724.5 | 3.6 | 16.4 | 0.05 | Fe 2p 1/2: $Fe^{+3}$, $Fe^{+2}$ |
| **Fe 2p** | 727.7 | 3.0 | 16.4 | 0.02 | Fe 2p 1/2: satellite $Fe^{+2}$ |
| **Fe 2p** | 733.0 | 4.0 | 16.4 | 0.01 | Fe 2p 1/2: satellite $Fe^{+3}$ |

The C 1s XPS line shape in graphite, graphite-like carbon nanotubes, and vitreous carbons is highly asymmetric [31]. As shown in Figure 5.9, both SCM blank and LCM blank samples displayed this asymmetry peak, which was a good indication of the overall graphitic nature of these carbon monoliths [32]. Each have identical C 1s peaks and these peaks are attributed as follows: C 1s_1 (284.5 eV, undamaged

alternant hydrocarbon structure, SP$^2$), C 1s_2 (285.2 eV, damaged alternant hydrocarbon structure, SP$^3$), C 1s_3 (286.3 eV, C-O), C 1s_4 (287.6 eV, carbonyl groups C=O), C 1s_5 (289.3 eV, O-C=O) and C 1s_6-8 (291.4, 292.5 and 294.4 eV, pi to pi* shake-up of C1-3) [29]. These features are consistent with previous studies for graphite and graphite-like materials [29, 32, 33].
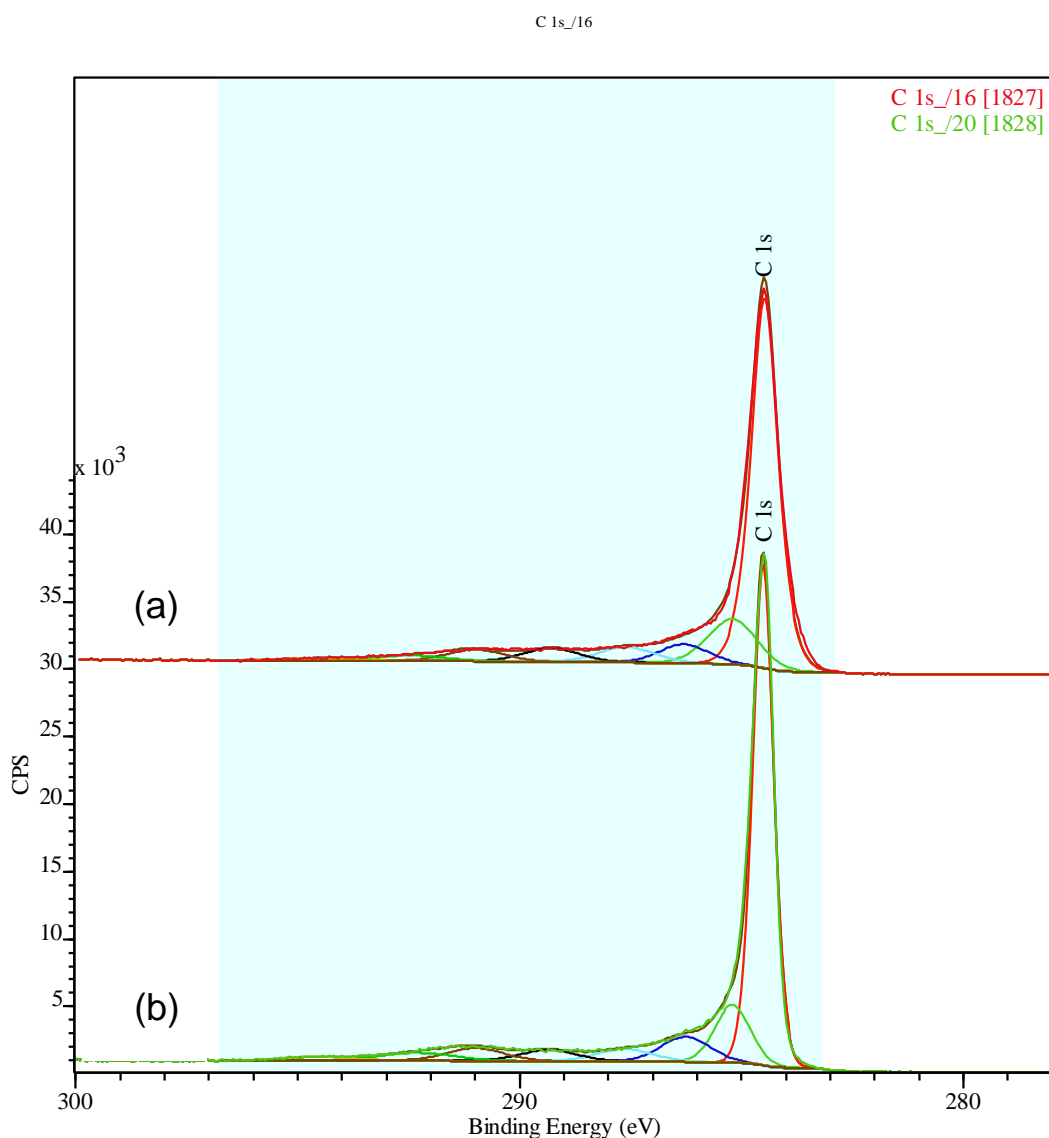


***Figure 5.9:*** *XPS spectra of C 1s and deconvolution curves obtained for (a) LCM blank and (b) SCM blank.*

The XPS spectrum (Figure 5.10) showed the contamination of iron within the LCM blank, in the form of iron dust stuck on the LCM blank (not chemically bonded) surface. Curve fitting was applied which indicated that there were two main pieces of information about the chemical state of the Fe that could be discerned. First, Fe 2p$^{3/2}$

at ~ 712 eV characteristic of Fe in +3 state, more likely to be FeO(OH), $Fe_2O_3$. There is some intensity at ~719 eV which is the characteristic satellite of $Fe^{+3}$ state. Secondly, there is also some intensity seen at ~ 716 eV which is characteristic of the satellite of $Fe^{+2}$ which would appear ~709-710 eV. Due to poor spectra, the corresponding principle peak for $Fe^{+2}$ cannot be distinguished from Fe +3 broad peak (FWHM = 3.8 eV)
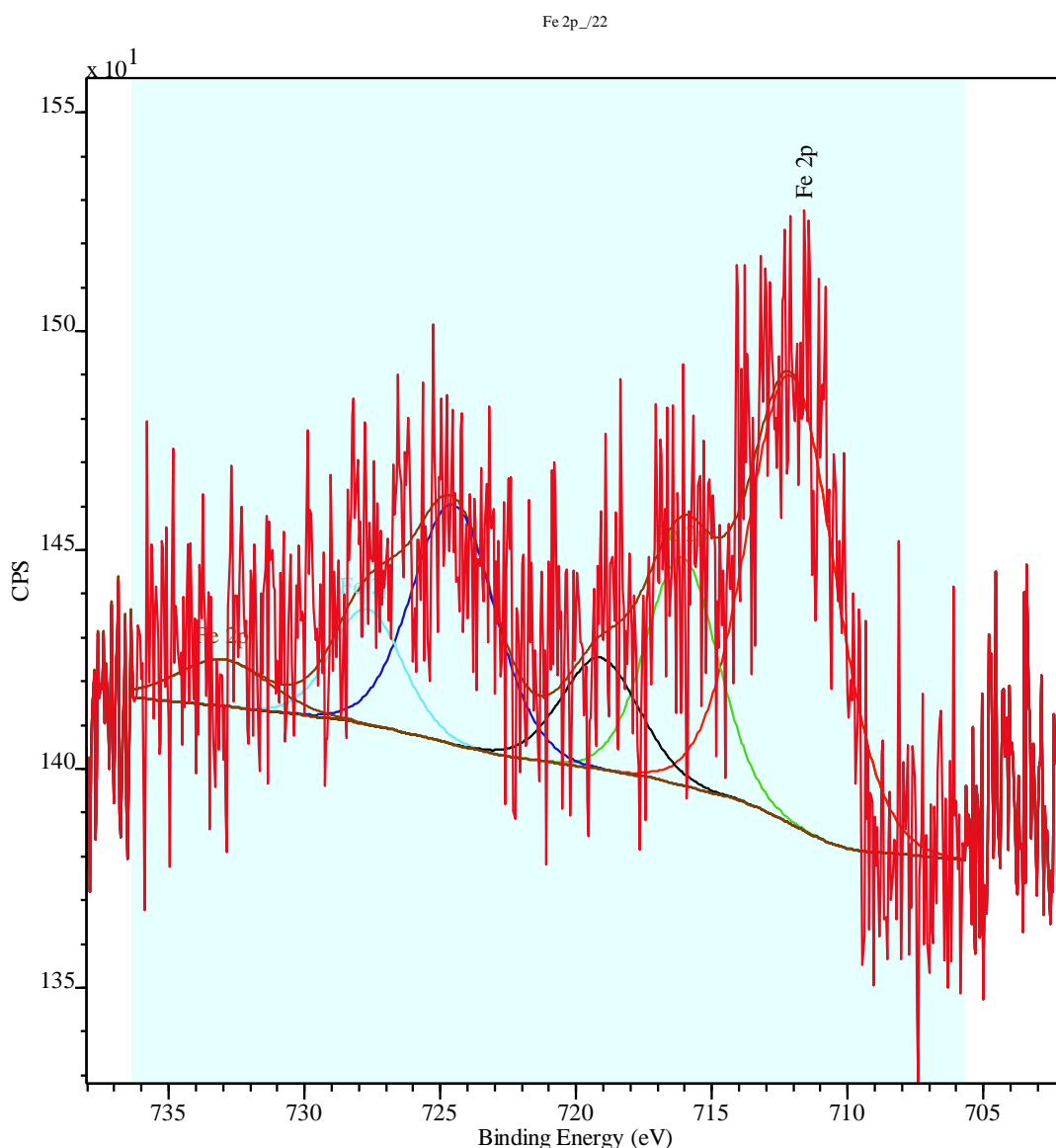


**Figure 5.10:** *XPS spectra of Fe 2p and deconvolution curves obtained for LCM blank.*

The main peaks of XPS survey spectra in LNTCM and SNTCM were all most identical as LCM blank and SCM blank. Survey spectra of LNTCM showed the sample containing oxygen, carbon, silica and iron while for SNTCM only showed oxygen, carbon and silica (Figure 5.11). The exact same amount of silica in both

165

samples is because the surface area of NTCM was higher than CM blank. This observation highlighted that the diffusion effect was slower in NTCM through the micro-, meso- and macroporous structure than in CM through the meso- and macroporous structure only. Interestingly, the similar amount of silica residue was also observed by Taguchi and his co-works [34]. 6 h HF was not enough to completely remove silica complete from the sample and longer HF treatment was needed to completely remove the silica templates.
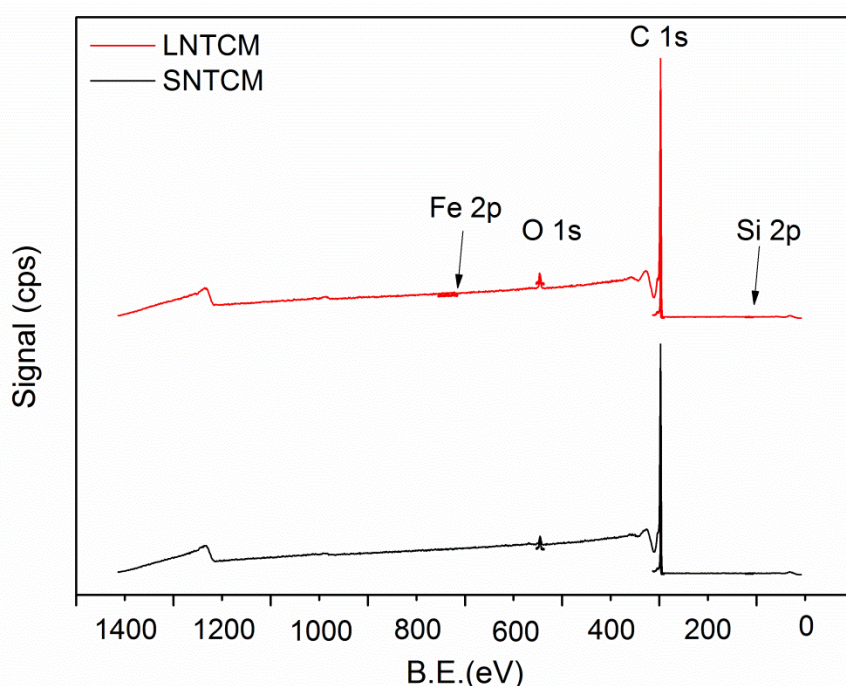


***Figure 5.11:*** *XPS survey spectra of LNCM and SNTCM.*

Iron was again the only difference in composition between laser treated and non-laser treated samples which again pointed to the fact that this was due to their contamination. There was only 0.2 % difference in % concentration of O 1s which was 8 times less than the O 1s change that occurred in LCM blank sample. Because of the heterogeneous nature of NTCM, it requires more heat than CM blank to be decomposed as shown in the TGA curves, previously presented in Section 3.3.1, Chapter 3. After the laser radiation on the surface of NTCM, the total amount of C was almost same as SNTCM, which again indicated it has better thermal stability than CM blank. 2.8 % of C=C/C-H was increased while 1 % of C-C, 0.6 % of C-O and 0.6 % O-C=O were decreased in LNTCM (Table 5.6), compared with NTCM (Table 5.5). Therefore, there was 2.2 % of C-C, C-O and O-C=O converted into

166

C=C/C-H in LNTCM samples, which could be sign of increasing in the $sp^3$ and $sp^2$ carbon phases. The Raman spectroscopy results further confirmed this prediction, as shown in the following Section 5.3.4.

**Table 5.5:** *Compositions from a high resolution XPS spectrum of SNTCM.*

| Name | B. E (eV) | FWHM (eV) | R. S. F. | % Conc. | Assigned Functional groups |
|------|-----------|-----------|----------|---------|----------------------------|
| **O 1s** | 533.3 | 3.1 | 2.93 | 1.8 | |
| **C 1s** | 284.5 | 0.7 | 1 | 98.3 | |
| **Si 2p** | 101.6 | 0.2 | 0.817 | 0.2 | |
| **O 1s_1** | 532.9 | 2.8 | 2.93 | 1.2 | From organic |
| **O 1s_2** | 531.1 | 2.3 | 2.93 | 0.6 | From organic |
| **C 1s_1** | 284.5 | 0.7 | 1 | 60.7 | Hydrocarbon |
| **C 1s_2** | 285.2 | 1.4 | 1 | 10.9 | C-C |
| **C 1s_3** | 286.2 | 1.5 | 1 | 7.5 | C-O |
| **C 1s_4** | 287.6 | 1.5 | 1 | 4.7 | C=O |
| **C 1s_5** | 289.0 | 1.5 | 1 | 3.8 | O-C=O |
| **C 1s_6** | 290.7 | 2.0 | 1 | 6.1 | Shake up satellites, pi to pi* |
| **C 1s_7** | 292.4 | 1.5 | 1 | 3.1 | Shake up satellites, pi to pi* |
| **C 1s_8** | 294.5 | 1.5 | 1 | 1.5 | Shake up satellites, pi to pi* |
| **Si 2p** | 101.8 | 2.0 | 0.817 | 0.2 | SiOx |

**Table 5.6:** *Compositions from a high resolution XPS spectrum of LNTCM.*

| Name | B. E (eV) | FWHM (eV) | R. S. F. | % Conc. | Assigned Functional groups |
|------|-----------|-----------|----------|---------|----------------------------|
| O 1s | 533.3 | 3.4 | 2.93 | 1.7 | |
| C 1s | 284.5 | 0.7 | 1 | 98.1 | |
| Si 2p | 101.6 | 0.2 | 0.817 | 0.2 | |
| Fe 2p | 719.9 | 0.1 | 16.4 | 0.1 | |
| O 1s_1 | 533.2 | 2.2 | 2.93 | 1.0 | From organic |
| O 1s_2 | 531.2 | 2.2 | 2.93 | 0.7 | From organic |
| C 1s_1 | 284.5 | 0.5 | 1 | 63.5 | Hydrocarbon |
| C 1s_2 | 285.2 | 1.0 | 1 | 11.9 | C-C |
| C 1s_3 | 286.3 | 1.3 | 1 | 6.5 | C-O |
| C 1s_4 | 287.7 | 1.5 | 1 | 4.1 | C=O |
| C 1s_5 | 289.4 | 1.5 | 1 | 3.2 | O-C=O |
| C 1s_6 | 291.2 | 2.0 | 1 | 6.2 | Shake up satellites, pi to pi* |
| C 1s_7 | 293.1 | 2.0 | 1 | 1.9 | Shake up satellites, pi to pi* |
| C 1s_8 | 294.8 | 1.5 | 1 | 0.8 | Shake up satellites, pi to pi* |
| Si 2p_1 | 101.7 | 1.4 | 0.817 | 0.1 | SiOx |
| Si 2p_2 | 103.4 | 2.0 | 0.817 | 0.1 | $SiO_2$ |
| Fe 2p_1 | 711.5 | 5.6 | 16.4 | 0.1 | Fe 2p 3/2: $Fe^{+3}$, $Fe^{+2}$ |
| Fe 2p | 724.6 | 3.4 | 16.4 | 0 | Fe 2p 1/2 |

The XPS spectra of C 1s for LNTCM blank and SNTCM are shown in Figure 5.9. All of these extrapolated peaks had the same binding energy as LCM blank and SCM blank but differed in signal counts.

C 1s_1930/10
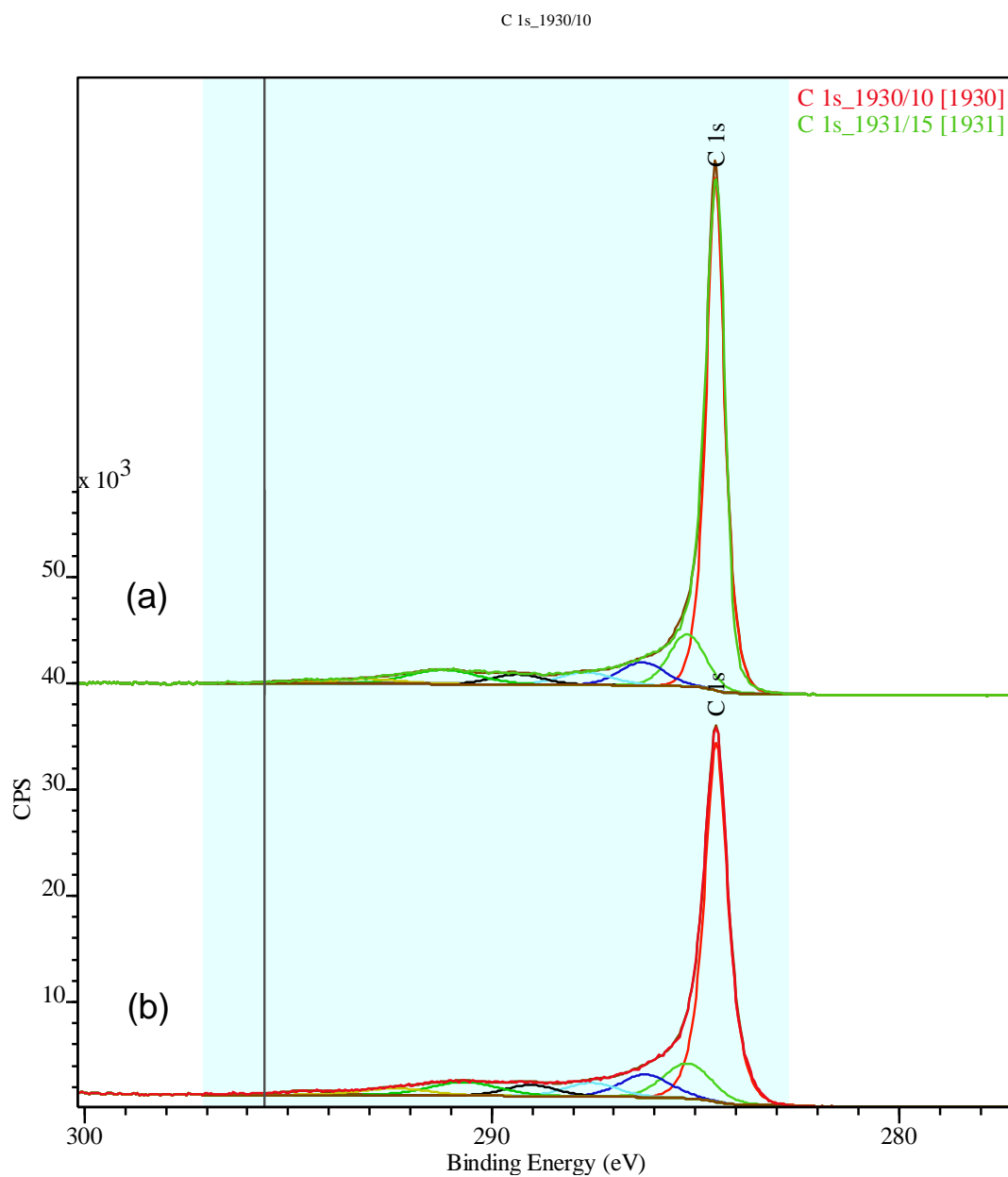


*Figure 5.12: XPS spectra of C 1s and deconvolution curves obtained for (a) LNTCM blank and (b) SNTCM.*
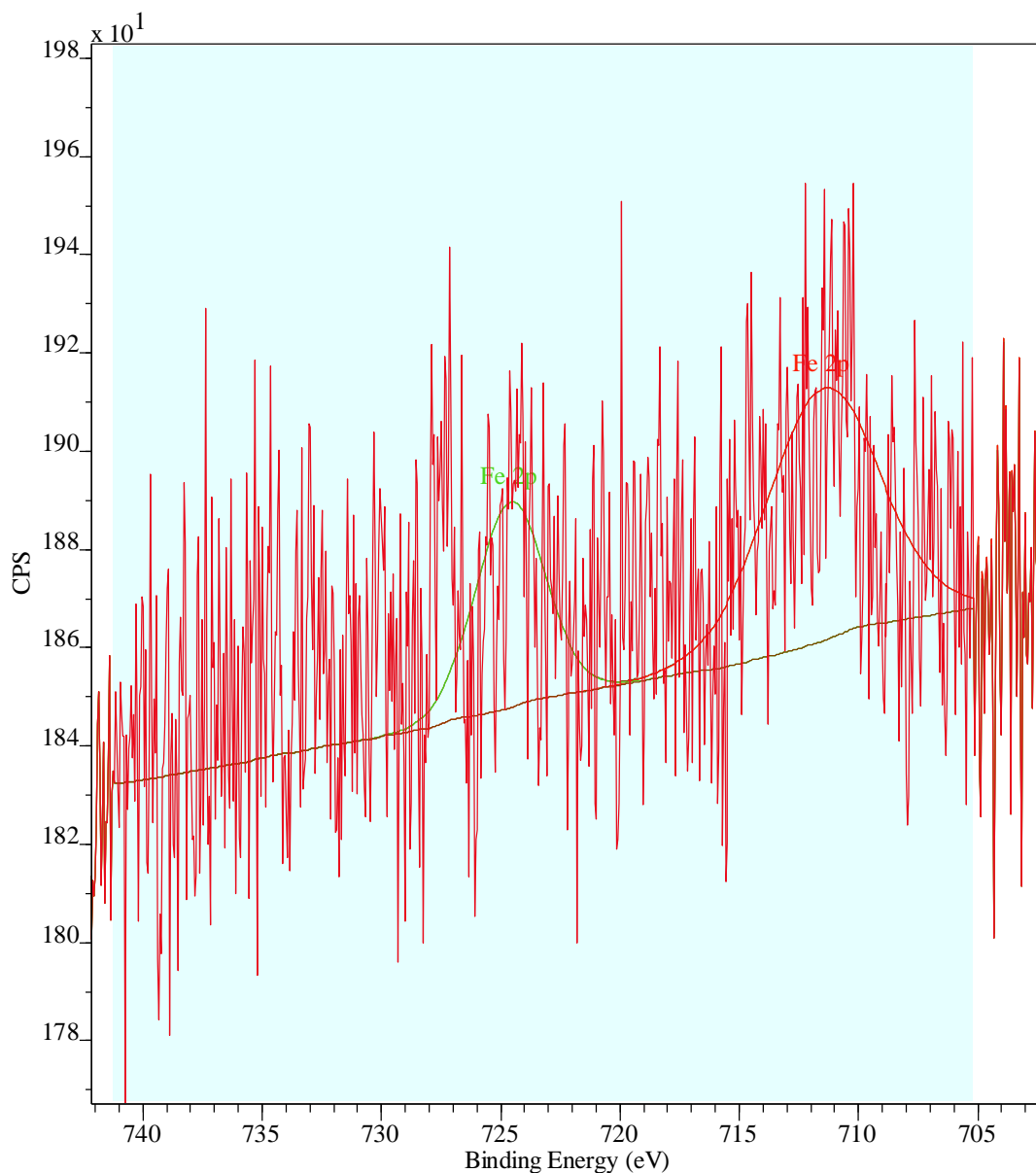
**Figure 5.13:** *XPS spectra of Fe 2p and deconvolution curves obtained for for LNTCM.*

The XPS spectrum of Fe 2p for LNTCM (Figure 5.13) was similar to that from LCM blank (Figure 5.10). Therefore, the same contamination on the sample was caused by lying on the laser stage.

## 5.3.4 Raman spectroscopy

The effect of the laser ablation to all LCM samples in the aspect of graphitisation has been studied using Raman spectroscopy. The Raman spectrum for each LNTCM and LCM blank was acquired and compared to that of NTCM and CM blank in

Figure 5.14. The commercial graphite again was used as a reference sample. All of the spectra distinctly showed the three characteristic peaks of graphite peaks, i.e., the $sp^3$ and $sp^2$ carbon phases coexisting in the samples (Figure 5.14). The disordered (or amorphous) D-band at ~1350 cm$^{-1}$, reflects the imperfection or loss of hexagonal $A_{1g}$ symmetry in the carbon structure [35]. The G (graphite) band, is common to all $sp^2$ carbon materials, at ~1580 cm$^{-1}$, it corresponds to the Raman active $E_{2g}$ mode of a two-dimensional network structure, i.e. an in-plane C-C bond stretching motion in all carbon and graphitic materials [35]. The G' band is a second order peak, at 2700 cm$^{-1}$, and is a criterion for the crystallinity of graphite [31, 36].
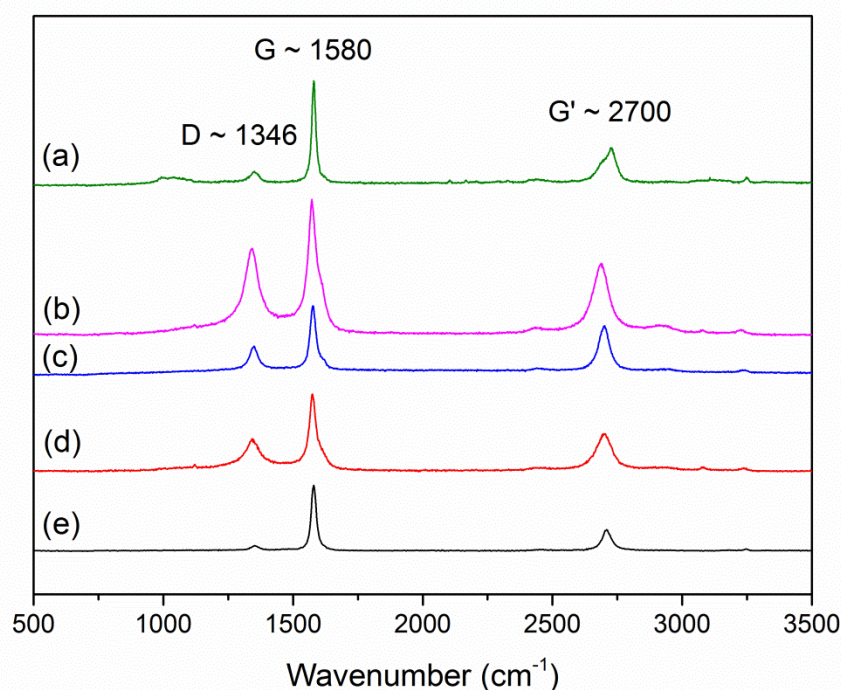


***Figure 5.14:*** *Raman spectrum of (a) commercial graphite, (b) SCM blank, (c) LCM blank, (d) SNTCM and (e) LNTCM.*

Previous studies have revealed that intensity ratio of the D to the G band, R, ($R = I_D/I_G$) was inversely proportional to the in-plane crystallite sizes ($L_a$) [37, 38][37, 38][37, 38][36, 37][35, 36] [35, 36]. The intensity of the D band is in all samples lower than that of the G band, suggesting that the carbon monoliths have a certain amount of graphitic content. However, the R values varied over all samples as shown in Table 5.7. The estimated R value of LNTCM was 0.07, compared with 0.41 for

NTCM and 0.10 for commercial graphite. The estimated $R$ value of LCM blank was 0.37, compared with 0.63 for CM blank. Obviously, the degree of graphitisation was increased after the laser cutting process; especially for the resulting LNTCM which was almost fully graphitised whereas LCM blank was still partially graphitised with a slight improvement in the degree of graphitisation degree. From this it can be concluded that the laser beam can provide above $2,000^o\,C$ or higher to achieve an $R$ value close to commercial graphite. This increase comes with an associated loss of meso-/micropore in the heat affected zone in the LNTCMs, i.e. decrease in surface area and increase in crystallinity.

*Table 5.7: R values for Raman spectra*

| Samples | $R$ values |
|---|---|
| **Commercial graphite** | 0.10 |
| **SCM blank** | 0.63 |
| **LCM blank** | 0.37 |
| **SNTCM** | 0.41 |
| **LNTCM** | 0.07 |

## 5.3.5 Adsorption study

The sandwich like structures in the LCMs (opened interconnected macroporous structure on laser cut surface and intact hierarchical central region) creates a great challenge to use the conventional surface area and porosity measurements, such as nitrogen adsorption and mercury intrusion porosimetry (MIP). All these techniques can only provide information for materials that have only one type of porous structure throughout (i.e. either micro-, meso-, macropores or bimodal or trimodal). The LCMs have two types of porous structures, i.e. macropores only in the cross section (~ 5 μm) and hierarchical pores in the middle section (~ 1.99 mm). Phenol showed reasonable retention on CM blank column (Section 3.3.5, Chapter 3) and strong affinity with carbon monolithic sorbents (Section 4.3.3, Chapter 4). As a derivative of phenol, the molecule size of BPA is considered to be twice as big as that of phenol. The adsorption study using those two different molecules demonstrated the effects of change that occurred in the morphology and surface chemistry of laser cut carbon monolithic discs. According to XPS results discussed in Section 5.3.3, more oxygen containing surface groups were introduced thus

enhancing the wettability for polar solvents such as water and making the surface more reactive [4].

The adsorption kinetics plots of $q_t$ (mg/g) versus time (min) for scalpel sectioned carbon monolithic rod (CM blank and NTCM), laser sectioned CMs (LCM and LNTCM) and MonoTrap using phenol and BPA as a modal analyte are shown in Figure 5.15 and Figure 5.16, respectively. Their adsorption performance indirectly showed the differences in surface chemistry and morphology between laser sectioned and non-laser sectioned carbon monoliths as well as the commercially available carbon coated silica monolithic sorbent MonoTrap.

Since both LNTCM and LCM blank have improved their graphitisation degree, graphite-like carbon is essentially hydrophobic in nature, its affinity to polar solvents, such as water, is low whereas to nonpolar solvents, such as acetone, is high [30]. The amounts of phenol adsorbed by LCMs were only slightly decreased due to the lack of meso-/micropores in the external surface after laser section as well as increase in graphitic carbon, i.e. nonpolar surface. The amount of phenol was adsorbed mainly due to the middle section of carbon monolith which still maintained the original morphology (trimodal porous structure), since LNTCM still adsorbed slightly more phenol than LCM blank (Figure 5.15). The enhanced accessibility of the middle section of carbon monolith due to the interconnected macroporous network is deemed to ease the adsorption of analytes. However, the kinetics of both LCMs for approximately the first 100 min overlapped. This might be caused by the air in the enlarged macropores of LCMs repelling the analyte that penetrated into the middle section and decreased adsorption affinity due to the morphology changes. Meanwhile, the MonoTrap showed no sign of adsorption of phenol as the $C_{18}$ group has only slight retention of phenol. The adsorbent dose should be increased so that more adsorption sites will be available to gain a higher percentage removal of phenol, i.e. greater than 1 mg of adsorbent vs. 1 mL of analyte [39].
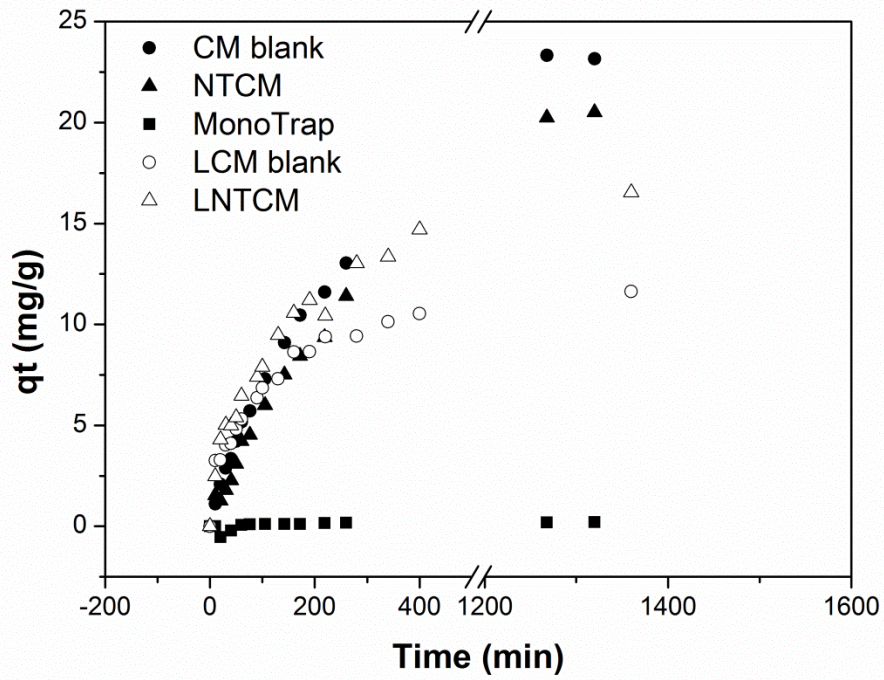
***Figure 5.15:*** *Adsorption kinetics at 30 ppm of phenol on scalpel sectioned carbon monolithic rod (● CM blank and ▲ NTCM), laser sectioned CMs (○ LCM and Δ LNTCM) and ■ MonoTrap. Inserted: Rescaled adsorption kinetics at 30 ppm of phenol on laser sectioned CMs (○ LCM and Δ LNTCM) and ■ MonoTrap.*
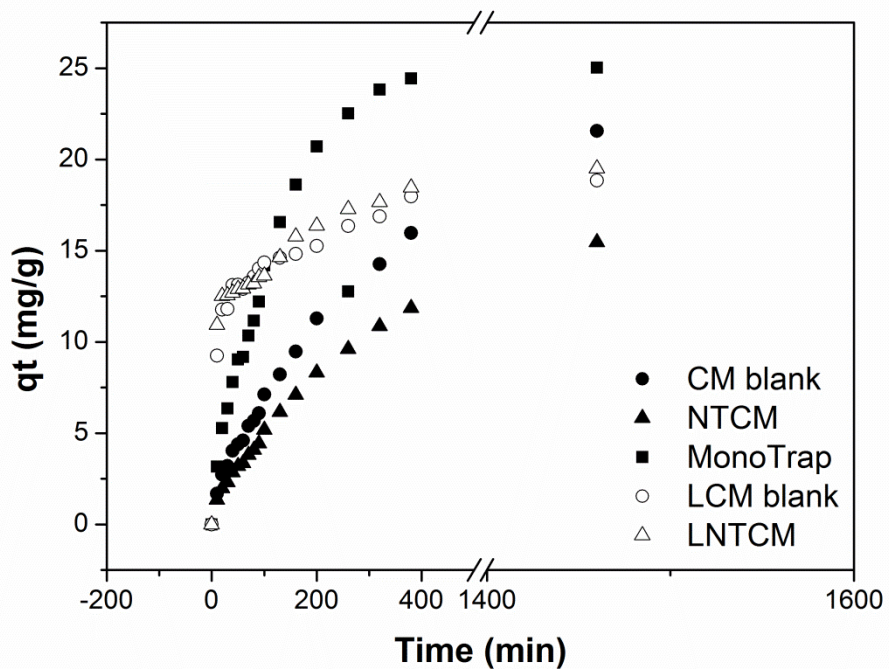


***Figure 5.16:*** *Adsorption kinetics at 30 ppm of BPA on scalpel sectioned carbon monolithic rod (CM blank and NTCM), laser sectioned CMs (LCM and LNTCM) and MonoTrap.*

MonoTrap had the highest adsorption capacity and reasonably fast kinetics for adsorbing BPA among all the other carbon monolithic sorbents due to its large macropores which resulted in a more open porous structure and the highest surface area (Figure 5.16). Figure 5.16 showed that the kinetics plots of LCM blank and LNTCM were identical and indicate that these two carbon sorbents had similar surface chemistry and porous structure after laser section. They had the fastest adsorption rate for the first 10 min and they adsorbed ~ 9.2 and 10.9 mg/g, respectively, whereas it took the second fastest kinetics sorbent MonoTrap 70 min of contact time to reach a similar adsorption capacity (~ 10.3 mg/g). Such kinetic results further confirmed the laser ablation smoothed most of meso- and micropores on the surface of LCMs and subsequently reduced the equilibrium time to the analyte. In addition, it also indicated the surface chemistry, i.e. functional groups on these resultant carbon monolithic discs were identical which has already been discussed in Section 5.3.3. LNTCM was modestly more hydrophobic than LCM blank. The adsorption capacity of LNTCM was increased from ~ 15 mg/g to ~20 mg/g because of the laser ablation resulting in a more opened macroporous structure on the cross section that allowed more analyte to pass into the middle tri-modal porous structure section. After 20 min the kinetics of LCMs reduced indicating that the analyte went through the laser modified macroporous section and was penetrating the middle section. Therefore the improved kinetics after laser section is only due to more opened porous structure on the cross section and the middle section maintained the same functionality as before laser ablation. The adsorption for BPA could be further improved by increasing the sorbent loading.

## 5.2 Conclusion

In this Chapter, $CO_2$ laser was used as a useful tool to section carbon monolithic discs into desirable thickness with approximately 1 mm ablation distance. The LCM discs were fully characterised using various physiochemical characterisation techniques. FE-SEM showed the integrated, interconnected and crack free porous structures. In addition, there are distinguished features of the surface of LCMs, such as elimination of mesopores and smoothness of the surface of the resultant materials within the 5 μm heat effect zone from laser ablation which were also observed. XPS revealed modestly increased oxidation degree on all LCMs surfaces. The improved

degree of graphitisation was confirmed by Raman spectroscopy. The materials and laser methodologies presented here should have great potential for the rapid development of new sorbent materials for microfluidic devices which require fast adsorption kinetics and exact shape/size to fit into the devices. This work has demonstrated that the CW $CO_2$ would be highly amenable to further platform development in applications where novel carbon monolithic materials are required with the potential to overcome many of the current problems regarding creation of desirable macroscopic shapes.

## 5.5 References

1. R. Wu, L. G. Hu, F. J. Wang, M. L. Ye, H. Zou, Recent development of monolithic stationary phases with emphasis on microscale chromatographic separation. *J. Chromatogr. A* **1184**, 369-392 (2008).
2. F. Svec, E. C. Peters, D. Sykora, J. M. J. Frechet, Design of the monolithic polymers used in capillary electrochromatography columns. *J. Chromatogr. A* **887**, 3-29 (2000).
3. F. Wei, Y.-Q. Feng, Methods of sample preparation for determination of veterinary residues in food matrices by porous monolith microextraction-based techniques. *Anal. Methods* **3**, 1246-1256 (2011).
4. Y. Wang, S. Tao, Y. An, Superwetting monolithic carbon with hierarchical structure as supercapacitor materials. *Microporous Mesoporous Mat.* **163**, 249-258 (2012).
5. T. A. Nijhuis, A. E. W. Beers, T. Vergunst, I. Hoek, F. Kapteijn, J. A. Moulijn, Preparation of monolithic catalysts. *Catalysis Reviews-Science and Engineering* **43**, 345-380 (2001).
6. Y. Zhao, M.-b. Zheng, J.-m. Cao, X.-f. Ke, J.-s. Liu, Y.-p. Chen, J. Tao, Easy synthesis of ordered meso/macroporous carbon monolith for use as electrode in electrochemical capacitors. *Materials Letters* **62**, 548-551 (2008).
7. S. Álvarez, A. B. Fuertes, Synthesis of macro/mesoporous silica and carbon monoliths by using a commercial polyurethane foam as sacrificial template. *Materials Letters* **61**, 2378-2381 (2007).
8. M.-M. Titirici, A. Thomas, M. Antonietti, Replication and coating of silica templates by hydrothermal carbonization. *Adv. Funct. Mater.* **17**, 1010-1018 (2007).
9. A. H. Lu, F. Schueth, Nanocasting: A versatile strategy for creating nanostructured porous materials. *Advanced Materials* **18**, 1793-1805 (2006).
10. Z. G. Shi, Y. Q. Feng, L. Xu, S. L. Da, M. Zhang, A template method to control the shape and porosity of carbon materials. *Carbon* **42**, 1677-1682 (2004).
11. H. Yang *et al.*, A Simple Melt Impregnation Method to Synthesize Ordered Mesoporous Carbon and Carbon Nanofiber Bundles with Graphitized Structure from Pitches. *The Journal of Physical Chemistry B* **108**, 17320-17328 (2004).
12. A. L. Schawlow, C. H. Townes, Infrared and optical masers. *Physical Review* **112**, 1940-1949 (1958).

13. J. D. Majumdar, I. Manna, Laser processing of materials. *Sadhana-Acad. Proc. Eng. Sci.* **28**, 495-562 (2003).
14. M. J. Bleda-Martinez, D. Lozano-Castello, E. Morallon, D. Cazorla-Amoros, A. Linares-Solano, Chemical and electrochemical characterization of porous carbon materials. *Carbon* **44**, 2642-2651 (2006).
15. T. Mahank, PhD thesis, Pennsylvania State University (2004).
16. R. H. S. Winterton, *Heat transfer.* (Oxford University Press, Oxford New York, 1997).
17. D. Zhou, C. Y. Zhao, Experimental investigations on heat transfer in phase change materials (PCMs) embedded in porous materials. *Applied Thermal Engineering* **31**, 970-977 (2011).
18. P. E. Khizhnyak, A. V. Chechetkin, A. P. Glybin, Thermal conductivity of carbon black. *Journal of Engineering Physics* **37**, 1073-1075 (1979).
19. M. Wiener, G. Reichenauer, S. Braxmeier, F. Hemberger, H. P. Ebert, Carbon Aerogel-Based High-Temperature Thermal Insulation. *International Journal of Thermophysics* **30**, 1372-1385 (2009).
20. R. I. Baxter, R. D. Rawlings, N. Iwashita, Y. Sawada, Effect of chemical vapor infiltration on erosion and thermal properties of porous carbon/carbon composite thermal insulation. *Carbon* **38**, 441-449 (2000).
21. A. G. Straatman, N. C. Gallego, B. E. Thompson, H. Hangan, Thermal characterization of porous carbon foam - convection in parallel flow. *International Journal of Heat and Mass Transfer* **49**, 1991-1998 (2006).
22. M. L. Toebes, J. M. P. van Heeswijk, J. H. Bitter, A. Jos van Dillen, K. P. de Jong, The influence of oxidation on the texture and the number of oxygen-containing surface groups of carbon nanofibers. *Carbon* **42**, 307-315 (2004).
23. K. Murali, A. N. Chatterjee, P. Saha, R. Palai, S. Kumar, S. K. Roy, P. K. Mishra, A. R. Choudhury, Direct selective laser sintering of iron-graphite powder mixture. *J. Mater. Process. Technol.* **136**, 179-185 (2003).
24. C. Liang, Z. Li, S. Dai, Mesoporous carbon materials: Synthesis and modification. *Angew. Chem.-Int. Edit.* **47**, 3696-3717 (2008).
25. J. L. Bahr, J. M. Tour, Covalent chemistry of single-wall carbon nanotubes. *Journal of Materials Chemistry* **12**, 1952-1958 (2002).
26. M. B. Martinhopkins, R. K. Gilpin, M. Jaroniec, Studies of the surface heterogeneity of chemically modified porous carbons by gas solid chromatography. *J. Chromatogr. Sci.* **29**, 147-152 (1991).
27. F. Rodriguez-Reinoso, M. Molina-Sabio, Textural and chemical characterization of microporous carbons. *Adv. Colloid Interface Sci.* **76**, 271-294 (1998).
28. S. Zhang, L. Li, A. Kumar, *Materials characterization techniques.* (CRC Press Taylor & Francis Group, Boca Raton, 2009), pp. 290-291.
29. D.-Q. Yang, E. Sacher, Carbon 1s X-ray Photoemission Line Shape Analysis of Highly Oriented Pyrolytic Graphite: The Influence of Structural Damage on Peak Asymmetry. *Langmuir* **22**, 860-862 (2005).
30. F. Rodríguez-Reinoso, The role of carbon materials in heterogeneous catalysis. *Carbon* **36**, 159-175 (1998).
31. T. Belin, F. Epron, Characterization methods of carbon nanotubes: a review. *Mater. Sci. Eng. B-Solid State Mater. Adv. Technol.* **119**, 105-118 (2005).
32. C. Pham-Huu, N. Keller, V. V. Roddatis, G. Mestl, R. Schlogl, M. J. Ledoux, Large scale synthesis of carbon nanofibers by catalytic decomposition of ethane on nickel nanoclusters decorating carbon nanotubes. *Physical Chemistry Chemical Physics* **4**, 514-521 (2002).

33. H. Darmstadt, C. Roy, S. Kaliaguine, S. H. Joo, R. Ryoo, Pore structure and graphitic surface nature of ordered mesoporous carbons probed by low-pressure nitrogen adsorption. *Microporous Mesoporous Mat.* **60**, 139-149 (2003).

34. A. Taguchi, J. H. Smatt, M. Linden, Carbon monoliths possessing a hierarchical, fully interconnected porosity. *Advanced Materials* **15**, 1209-1211 (2003).

35. F. J. Maldonado-Hodar, C. Moreno-Castilla, A. F. Perez-Cadenas, Surface morphology, metal dispersion, and pore texture of transition metal-doped monolithic carbon aerogels and steam-activated derivatives. *Microporous Mesoporous Mat.* **69**, 119-125 (2004).

36. H. M. Heise, R. Kuckuk, A. K. Ojha, A. Srivastava, V. Srivastava, B. P. Asthana, Characterisation of carbonaceous materials using Raman spectroscopy: a comparison of carbon nanotube filters, single- and multi-walled nanotubes, graphitised porous carbon and graphite. *Journal of Raman Spectroscopy* **40**, 344-353 (2009).

37. F. Tuinstra, J. L. Koenig, Raman spectrum of graphite. *Journal of Chemical Physics* **53**, 1126-1130 (1970).

38. M. S. Dresselhaus, A. Jorio, M. Hofmann, G. Dresselhaus, R. Saito, Perspectives on Carbon Nanotubes and Graphene Raman Spectroscopy. *Nano Letters* **10**, 751-758 (2010).

39. J. E. Kilduff, T. Karanfil, Y. P. Chin, W. J. Weber, Adsorption of natural organic polyelectrolytes by activated carbon: A size-exclusion chromatography study. *Environmental Science & Technology* **30**, 1336-1343 (1996).

# Chapter 6

# Final Conclusion and Future Work

*"There are no secrets to success. It is the result of preparation, hard work learning from failure."*


Max Planck

## 6.1 Final conclusion

This thesis presented a systematic study of the development of a nanotemplated carbon monolith (NTCM), followed with comprehensive characterisation using various physical and chemical techniques and finally explored its potential applications including solid phase extraction of environmental pollutants (phenols and methylene blue) within aqueous phases and electrode support materials. NTCMs were prepared using $C_{60}$-fullerene modified silica gels as hard templates embedded in resorcinol/phenol carbon precursor with metal catalyst for localised graphitisation was undertaken. A blank carbon monolith (CM blank) was prepared using a bare silica template for comparison of graphitic character, specific surface area and extraction performance. The resultant monoliths, NTCM, possessed graphitic features, hierarchical porous structures, increased micropores and high surface areas.

These monoliths were free from both the hydrolysis instability and the swelling problems in comparison with conventional n-alkyl silica and organic polymer sorbents. Furthermore, being carbon monolithic materials they have the flexibility to be used either in rods, powder or disc form by simply cut with scalpel knife, grinding by pestle and mortar or section ablation with a CW $CO_2$ laser. A CW $CO_2$ laser can be successfully used as a method to cut fragile and porous carbon monolithic materials into the required sizes and shapes with intriguing morphology and structure. The resulted sandwich-like LCMs after laser ablation can be easily modified with size controlled gold nanoparticles in order to introduce the unique adsorption to any biomolecules for potentially using as electrode materials/electroadsorption. According to the separation of mixed phenol using in-house prepared CM blank column, the separation efficacy was rather poor. NTCM was too fragile to be cladded into a column for HPLC evaluation. Besides, it has even higher microporous volume which suggests not to use it for RP-HPLC stationary phases according to literature [86]. However, the selectivity and adsorption performance of NTCM were evaluated in both rod and powder form using a series of phenols and methylene blue compared with carbon monolith blank.

## 6.2 Future work

Suggested future work will involve surface modification of the resultant carbon monolith to enhance the adsorption performance as well as using different synthetic strategies to achieve highly ordered and controlled carbon monoliths. Instead of modifying the hard template with $C_{60}$ to achieve unique selectivity, the existing CM blank can easily be modified with melamine during its carbonisation procedure for introducing nitrogen groups on the surface. Wu *et al.* have proposed this simple nitrogen surface functionalisation strategy and have achieved ~ 20.6 wt% nitrogen contents with carbon nitride as a major contribution on their ordered mesoporous carbon under a low temperature carbonisation (~ 500 $^{\circ}$C) [90]. Upon carbonisation, a high concentration of surface nitrogen containing groups can be generated, which can alter the CM blank surface to be more hydrophilic and dispersible in an aqueous environment for accelerating its adsorption kinetics. The nitrogen-containing functional groups could possibly be generated uniformly with high surface coverage on the frameworks, rendering the resultant carbon monoliths more versatile in adsorption performance, such as heavy metal ions removal and $CO_2$ capture.

The laser sectioned discs hold several advantages compared with carbon monolithic discs cut by scalpel knife. In Chapter 5, LCMs showed reasonable fast adsorption kinetics, integrated structure and desirable and precisely controlled thickness. They can be easily integrated into centrifugal microfluidic devices for pre-concentration of organic pollutants as shown in Figure 6.1.
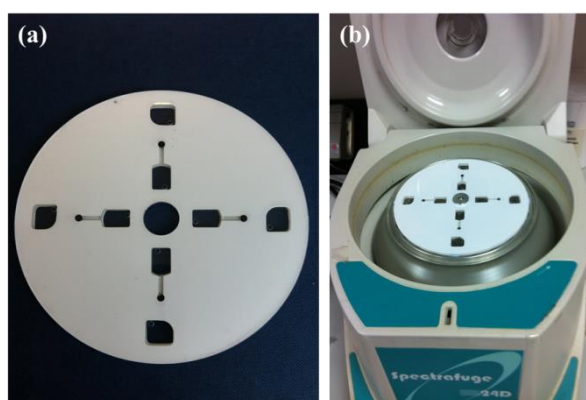


***Figure 6.1:*** *Photograph of (a) carbon monolithic disc integrated microfluidic disc and (b) CD extractions were performed in a centrifuge.*

With respect to the LCM disc modification, an investigation of introduction of size controlled gold nanoparticles by electrodeposition can be carries out. The correlation between particles size and the electrodepostion time, concentration of gold solution, suitable protein/enzyme and the other parametersare needed. This could lead to a new class of biosensors development using Au LCM as a working electrode [74].

1.  H. W. Kroto, J. R. Heath, S. C. O'Brien, R. F. Curl, R. E. Smalley, C60: Buckminsterfullerene. *Nature* **318**, 162-163 (1985).
2.  K. Jinno, R. S. o. Chemistry., *Separation of fullerenes by liquid chromatography*. (Royal Society of Chemistry, Cambridge, 1999).
3.  J. M. Millar, K. M. Creegan, J. L. Robbins, W. K. Robbins, R. D. Sherwood, P. J. Tindall, D. M. Cox, Chromatographic separations of fullerenes: discovery and characterization of C60 mono-epoxide. *Inorganic Chemicals and Reactions* **59**, 317-331 (1993).
4.  J. C. Fetzer, Mechanisms of fullerene separations. *Analytical Chemistry* **76**, 342A-342A (2004).
5.  Y. Saito, H. Ohta, K. Jinno, Design and characterization of novel stationary phases based on retention behavior studies with various aromatic compounds. *Journal of Separation Science* **26**, 225-241 (2003).
6.  Y. Saito, H. Ohta, K. Jinno, Peer Reviewed: Chromatographic Separation of Fullerenes. *Analytical Chemistry* **76**, 266 A-272 A (2004).
7.  C. S. Chang, T. G. Den, C. C. Chen, S. L. Lee, Stationary phases 44: Chromatographic separation of naturally occurring dehydroiso-alpha-lapachone derivatives with C-60-fullerene stationary phase. *Hrc-Journal of High Resolution Chromatography* **20**, 624-628 (1997).
8.  K. Jinno, K. Tanabe, Y. Saito, H. Nagashima, R. D. Trengove, Retention behavior of calixarenes with various $C_{60}$ bonded silica phases in microcolumn liquid chromatography. *Section Title: Organic Analytical Chemistry* **34**, 175-177 (1997).
9.  C. D. Tran, S. Challa, Fullerene-impregnated ionic liquid stationary phases for gas chromatography. *Analyst* **133**, 455-464 (2008).
10. L. A. Kartsova, A. A. Makarov, New fullerene-based stationary phases for gas chromatography. *Journal of Analytical Chemistry* **59**, 724-729 (2004).
11. R. M. Vallant *et al.*, Development and application of $C_{60}$-fullerene bound silica for solid-phase extraction of biomolecules. *Analytical Chemistry* **79**, 8144-8153 (2007).
12. K. Boeddi *et al.*, Use of fullerene-, octadecyl-, and triaconthyl silica for solid phase extraction of tryptic peptides obtained from unmodified and in vitro glycated human serum albumin and fibrinogen. *Journal of Separation Science* **32**, 295-308 (2009).
13. P. Innocenzi, G. Brusatin, Fullerene-based organic-inorganic nanocomposites and their applications. *Chem. Mat.* **13**, 3126-3139 (2001).
14. M. Prato, [60] Fullerene chemistry for materials science applications. *Journal of Materials Chemistry* **7**, 1097-1109 (1997).
15. H. W. Kroto, J. R. Heath, S. C. O'Brien, R. F. Curl, CM: Buckminsterfullerene. *Physics & chemistry of fullerenes: a reprint collection*, 8 (1993).

16. E. H. L. Falcao, F. Wudl, Carbon allotropes: beyond graphite and diamond. *Journal of Chemical Technology & Biotechnology* **82**, 524-531 (2007).
17. F. Wudl, The chemical-properties of Buckminsterfullerene ($C_{60}$) and the birth and infancy fulleroids. *Accounts of Chemical Research* **25**, 157-161 (1992).
18. H. L. Anderson *et al.*, in *2nd International winterschool on electronic properties of novel materials, Progress in fullerene research; Chemistry*. (World Scientific , River Edge, NJ 1994), pp. 13-18.
19. G. D. Panagiotou, M. D. Tzirakis, J. Vakros, L. Loukatzikou, M. Orfanopoulos, C. Kordulis, A. Lycourghiotis, Development of [60] fullerene supported on silica catalysts for the photo-oxidation of alkenes. *Applied Catalysis A: General* **372**, 16-25 (2010).
20. Y. Liu, Y. Feng, S. Da, Y. Chen, Preparation and evaluation of C60 bonded silica phase for high performance liquid chromatography. *Se Pu* **16**, 115-117 (1998).
21. Y. Feng, Y. Hu, J. Li, Y. Liu, S. Da, Y. Chen, Separation of calixarenes and calixcrowns with a $C_{60}$ bonded silica stationary phase in normal-phase liquid chromatography. *Journal of Instrumental Analysis* **19**, 1-4 (2000).
22. F. Wudl, Fullerene materials. *Journal of Materials Chemistry* **12**, 1959-1963 (2002).
23. Y. Saito, H. Ohta, H. Terasaki, Y. Katoh, H. Nagashima, K. Itoh, K. Jinno, Microcolumn LC separation of polycyclic aromatic hydrocarbons with a chemically bonded C60 stationary phase. *Inorganic Analytical Chemistry* **16**, 192-195 (1995).
24. Y. Saito, H. Ohta, H. Terasaki, Y. Katoh, H. Nagashima, K. Jinno, Separation of polycyclic aromatic hydrocarbons with a C60-bonded silica phase in microcolumn liquid chromatography. *Organic Analytical Chemistry* **18**, 569-572 (1995).
25. K. Jinno, K. Tanabe, Y. Saito, H. Nagashima, Separation of polycyclic aromatic hydrocarbons with various C-60 fullerene bonded silica phases in microcolumn liquid chromatography. *Analyst* **122**, 787-791 (1997).
26. K. Jinno, K. Fukuoka, J. C. Fetzer, W. R. Biggs, Buckminsterfullerene as a stationary phase in liquid chromatography. *Journal of Microcolumn Separations* **5**, 517-523 (1993).
27. K. Jinno, K. Yamamoto, J. C. Fetzer, W. R. Biggs, C60 as a stationary phase for microcolumn liquid chromatographic separation of polycyclic aromatic hydrocarbons. *Journal of Microcolumn Separations* **4**, 187-190 (1992).
28. C.-S. Chang, C.-H. Wen, T.-G. Den, Stationary Phases 45[(1)]: Chromatographic Separation of High Energetic Materials with $C_{60}$-Fullerene Stationary Phase. *Propellants, Explosives, Pyrotechnics* **23**, 111-113 (1998).
29. G. P. Miller, Reactions between aliphatic amines and [60] fullerene: a review. *Comptes Rendus Chimie* **9**, 952-959 (2006).
30. S. Brunauer, P. H. Emmett, E. Teller, Adsorption of Gases in Multimolecular Layers. *Journal of the American Chemical Society* **60**, 309-319 (1938).
31. L. L. Gumanov, G. A. Volkov, A. V. Shastin, B. L. Korsounskii, Preparation and properties of sorbents based on silica gel containing covalently linked fullerene $C_{60}$. *Russian Chemical Bulletin* **45**, 768-770 (1996).
32. I. Taylor, A. G. Howard, Measurement of primary amine groups on surface-modified silica and their role in metal-binding. *Anal. Chim. Acta* **271**, 77-82 (1993).

33. J. Nawrocki, The silanol group and its role in liquid chromatography. *J. Chromatogr. A* **779**, 29-71 (1997).

34. R. S. Ruoff, D. S. Tse, R. Malhotra, D. C. Lorents, Solubility of fullerene ($C_{60}$) in a variety of solvents. *The Journal of Physical Chemistry* **97**, 3379-3383 (1993).

35. A. Goel, J. B. Howard, J. B. Vander Sande, Size analysis of single fullerene molecules by electron microscopy. *Carbon* **42**, 1907-1915 (2004).

36. D. M. Cox *et al.*, Characterization of $C_{60}$ and $C_{70}$ Clusters. *Journal of the American Chemical Society* **113**, 2940-2944 (1991).

37. G. Angelini, O. Ursini, F. Cataldo, Synthesis of fullerene-silica hybrid materials. *Journal of Radioanalytical and Nuclear Chemistry* **284**, 179-187 (2010).

38. B. Buszewski, M. Jaroniec, R. K. Gilpin, Studies of physicochemical and chromatographic properties of mixed amino-alkylamide bonded phases. *J. Chromatogr. A* **673**, 11-19 (1994).

39. C. S. Chang, T. G. Den, C. C. Chen, S. L. Lee, Stationary Phases. Part 44. Chromatographic separation of naturally occurring dehydroiso- Î±-lapachone derivatives with C60-fullerene stationary phase. *Section Title: Organic Analytical Chemistry* **20**, 624-628 (1997).

40. A. Simon, T. Cohen-Bouhacina, M. C. Porté, J. P. Aimé, C. Baquey, Study of Two Grafting Methods for Obtaining a 3-Aminopropyltriethoxysilane Monolayer on Silica Surface. *Journal of Colloid and Interface Science* **251**, 278-283 (2002).

41. D. F. Siqueira Petri, G. Wenz, P. Schunk, T. Schimmel, An Improved Method for the Assembly of Amino-Terminated Monolayers on $SiO_2$ and the Vapor Deposition of Gold Layers. *Langmuir* **15**, 4520-4523 (1999).

42. O. N. Fedyanina, P. N. Nesterenko, Regularities of Chromatographic Retention of Phenols on Microdispersed Sintered Detonation Nanodiamond in Aqueous-Organic Solvents. *Russian Journal of Physical Chemistry A* **84**, 476-480 (2010).

43. E. Forgacs, T. Cserhati, Retention strength and selectivity of porous graphitized carbon columns. Theoretical aspects and practical applications. *Section Title: Organic Analytical Chemistry* **14**, 23-29 (1995).

44. E. Heftmann, *Chromatography: fundamentals and applications of chromatographic and electrophoretic methods*. (Elsevier Scientific, Amsterdam, 1983).

45. G. Marko-Varga, D. Barceló, Liquid chromatographic retention and separation of phenols and related aromatic compounds on reversed phase columns. *Chromatographia* **34**, 146-154 (1992).

46. J. Lee, J. Kim, T. Hyeon, Recent progress in the synthesis of porous carbon materials. *Advanced Materials* **18**, 2073-2094 (2006).

47. C. Liang, Z. Li, S. Dai, Mesoporous carbon materials: Synthesis and modification. *Angew. Chem.-Int. Edit.* **47**, 3696-3717 (2008).

48. A.-H. Lu, G. P. Hao, Q. Sun, X. Q. Zhang, W. C. Li, Chemical Synthesis of Carbon Materials With Intriguing Nanostructure and Morphology. *Macromol. Chem. Physic* **213**, 1107-1131 (2012).

49. R. Ryoo, S. H. Joo, M. Kruk, M. Jaroniec, Ordered mesoporous carbons. *Advanced Materials* **13**, 677-681 (2001).

50. Y. Meng, D. Gu, F. Q. Zhang, Y. F. Shi, H. F. Yang, Z. Li, C. Z. Yu, B. Tu, D. Y. Zhao, Ordered mesoporous polymers and homologous carbon frameworks: Amphiphilic surfactant templating and direct transformation. *Angew. Chem.-Int. Edit.* **44**, 7053-7059 (2005).

51. A. Taguchi, J. H. Smatt, M. Linden, Carbon monoliths possessing a hierarchical, fully interconnected porosity. *Advanced Materials* **15**, 1209-1211 (2003).
52. Z. G. Shi, Y. Q. Feng, L. Xu, S. L. Da, M. Zhang, Synthesis of a carbon monolith with trimodal pores. *Carbon* **41**, 2677-2679 (2003).
53. Y. Wang, S. Tao, Y. An, Superwetting monolithic carbon with hierarchical structure as supercapacitor materials. *Microporous Mesoporous Mat.* **163**, 249-258 (2012).
54. X. R. Wen, D. S. Zhang, L. Y. Shi, T. T. Yan, H. Wang, J. P. Zhang, Three-dimensional hierarchical porous carbon with a bimodal pore arrangement for capacitive deionization. *Journal of Materials Chemistry* **22**, 23835-23844 (2012).
55. C. Liang, S. Dai, G. Guiochon, A graphitized-carbon monolithic column. *Analytical Chemistry* **75**, 4904-4912 (2003).
56. Z. G. Shi, F. Chen, J. Xing, Y. Q. Feng, Carbon monolith: Preparation, characterization and application as microextraction fiber. *J. Chromatogr. A* **1216**, 5333-5339 (2009).
57. Y. S. Hu, P. Adelhelm, B. M. Smarsly, S. Hore, M. Antonietti, J. Maier, Synthesis of hierarchically porous carbon monoliths with highly ordered microstructure and their application in rechargeable lithium batteries with high-rate capability. *Adv. Funct. Mater.* **17**, 1873-1878 (2007).
58. G. P. Hao *et al.*, Structurally Designed Synthesis of Mechanically Stable Poly(benzoxazine-co-resol)-Based Porous Carbon Monoliths and Their Application as High-Performance $CO_2$ Capture Sorbents. *Journal of the American Chemical Society* **133**, 11378-11388 (2011).
59. A.-H. Lu, J. H. Smatt, S. Backlund, M. Linden, Easy and flexible preparation of nanocasted carbon monoliths exhibiting a multimodal hierarchical porosity. *Microporous Mesoporous Mat.* **72**, 59-65 (2004).
60. S. Álvarez, A. B. Fuertes, Synthesis of macro/mesoporous silica and carbon monoliths by using a commercial polyurethane foam as sacrificial template. *Materials Letters* **61**, 2378-2381 (2007).
61. L. Y. Xu, Z. G. Shi, Y. Q. Feng, Preparation of a carbon monolith with bimodal perfusion pores. *Microporous Mesoporous Mat.* **115**, 618-623 (2008).
62. A. H. Eltmimi, L. Barron, A. Rafferty, J. P. Hanrahan, O. Fedyanina, E. Nesterenko, P. N. Nesterenko, B. Paull, Preparation, characterisation and modification of carbon‐based monolithic rods for chromatographic applications. *Journal of Separation Science* **33**, 1231-1243 (2010).
63. M. Sevilla, A. B. Fuertes, Fabrication of porous carbon monoliths with a graphitic framework. *Carbon* **56**, 155-166 (2013).
64. D. C. Harris, *Quantitative chemical analysis*. (W.H. Freeman and Company, New York, ed. 7th, 2006).
65. Y. Huang, H. Cai, D. Feng, D. Gu, Y. Deng, B. Tu, H. Wang, P. A. Webley, D. Zhao, One-step hydrothermal synthesis of ordered mesostructured carbonaceous monoliths with hierarchical porosities. *Chemical Communications*, 2641-2643 (2008).
66. S. A. Al-Muhtaseb, J. A. Ritter, Preparation and Properties of Resorcinol–Formaldehyde Organic and Carbon Gels. *Advanced Materials* **15**, 101-114 (2003).
67. S. Zhang, L. Li, A. Kumar, *Materials characterization techniques*. (CRC Press Taylor & Francis Group, Boca Raton, 2009), pp. 290-291.

68. M. Egashira, K. Hoshii, T. Araki, Y. Korai, I. Mochida, Effects of fullerene addition on the carbonization of synthetic naphthalene isotropic pitch. *Carbon* **36**, 1739-1747 (1998).

69. F. J. Maldonado-Hodar, C. Moreno-Castilla, J. Rivera-Utrilla, Y. Hanzawa, Y. Yamada, Catalytic graphitization of carbon aerogels by transition metals. *Langmuir* **16**, 4367-4373 (2000).

70. N. Wiberg, A. F. Holleman, E. Wiberg, *Inorganic Chemistry*. (Academic Press, San Diego, ed. 1st, 2001).

71. A. Oberlin, Transformation of ingraphitizable carbon by thermal treatment in presence of iron. *Carbon* **9**, 39-42 (1971).

72. M. Audier, A. Oberlin, M. Oberlin, M. Coulon, L. Bonnetain, Morphology and crystalline order in catalytic carbons. *Carbon* **19**, 217-224 (1981).

73. C. Lin, J. A. Ritter, Effect of synthesis pH on the structure of carbon xerogels. *Carbon* **35**, 1271-1278 (1997).

74. X. He, L. Zhou, E. P. Nesterenko, P. N. Nesterenko, B. Paull, J. O. Omamogho, J. D. Glennon, J. H. T. Luong, Porous Graphitized Carbon Monolith as an Electrode Material for Probing Direct Bioelectrochemistry and Selective Detection of Hydrogen Peroxide. *Analytical Chemistry* **84**, 2351-2357 (2012).

75. S. J. Gregg, K. S. W. Sing, *Adsorption, surface area, and porosity*. (Academic Press Inc, Ltd., London, 1967), pp. 144-149.

76. E. P. Barrett, L. G. Joyner, P. P. Halenda, The determination of pore volume and area distributions in porous substances. 1. computation from nitrogen isotherms. *Journal of the American Chemical Society* **73**, 373-380 (1951).

77. R. Qiao, A. P. Roberts, A. S. Mount, S. J. Klaine, P. C. Ke, Translocation of C60 and Its Derivatives Across a Lipid Bilayer. *Nano Letters* **7**, 614-619 (2007).

78. F. Tuinstra, J. L. Koenig, Raman spectrum of graphite. *Journal of Chemical Physics* **53**, 1126-1130 (1970).

79. M. S. Dresselhaus, A. Jorio, M. Hofmann, G. Dresselhaus, R. Saito, Perspectives on Carbon Nanotubes and Graphene Raman Spectroscopy. *Nano Letters* **10**, 751-758 (2010).

80. L. Pereira, Porous graphitic carbon as a stationary phase in HPLC: Theory and applications. *Journal of Liquid Chromatography & Related Technologies* **31**, 1687-1731 (2008).

81. H. Colin, C. Eon, G. Guiochon, Reversed-phase liquid-solid chromatography on modified carbon black. *J. Chromatogr. A* **122**, 223-242 (1976).

82. C. West, C. Elfakir, M. Lafosse, Porous graphitic carbon: A versatile stationary phase for liquid chromatography. *J. Chromatogr. A* **1217**, 3201-3216 (2010).

83. O. N. Fedyanina, P. N. Nesterenko, Regularities of chromatographic retention of phenols on microdispersed sintered detonation nanodiamond in aqueous—organic solvents. *Russian Journal of Physical Chemistry A* **84**, 476-480 (2010).

84. B. V. Spitsyn, S. A. Denisov, N. A. Skorik, A. G. Chopurova, S. A. Parkaeva, L. D. Belyakova, O. G. Larionov, The physical-chemical study of detonation nanodiamond application in adsorption and chromatography. *Diamond and Related Materials* **19**, 123-127 (2010).

85. F. e. Švec, T. B. Tennikova, Z. e. Deyl, *Monolithic materials: preparation, properties, and applications, 1st ed*. (Elsevier, Amsterdam, 2003).

86. G. Guiochon, Monolithic columns in high-performance liquid chromatography. *J. Chromatogr. A* **1168**, 101-168 (2007).

87. Z. Wang, Z. Lu, X. Huang, R. Xue, L. Chen, Chemical and crystalline structure characterizations of polyfurfuryl alcohol pyrolyzed at 600 ℃. *Carbon* **36**, 51-59 (1998).

88. J. H. T. Luong, K. B. Male, J. D. Glennon, Boron-doped diamond electrode: synthesis, characterization, functionalization and analytical applications. *Analyst* **134**, 1965-1979 (2009).

89. M. Hupert, A. Muck, J. Wang, J. Stotter, Z. Cvackova, S. Haymond, Y. Show, G. M. Swain, Conductive diamond thin-films in electrochemistry. *Diamond and Related Materials* **12**, 1940-1949 (2003).

90. Z. X. Wu, P. A. Webley, D. Y. Zhao, Post-enrichment of nitrogen in soft-templated ordered mesoporous carbon materials for highly efficient phenol removal and CO2 capture. *Journal of Materials Chemistry* **22**, 11379-11389 (2012).